学位論文

An Observational Study of the Origin of Spiral Structures with High Resolution Imaging of Nearby Spiral Galaxies

（ 近傍渦巻銀河の高分解能撮像による
渦状腕構造の起源の観測的研究 ）

平成 27 年 12 月 博士 (理学) 申請

東京大学大学院理学系研究科
天文学専攻

橋場 康人

An Observational Study of the Origin of Spiral Structures with High Resolution Imaging of Nearby Spiral Galaxies

Thesis by

Yasuhito Hashiba

Department of Astronomy, School of Science,
The University of Tokyo

Submitted in December, 2015

Abstract

The density wave theory for quasi-stationary spiral structures in galaxies has been widely accepted because it seemingly explains why spiral structures are sustained over a billion years. This theory predicts a systematic gradient of stellar age across spiral arms. On the other hand, recent theoretical studies suggest that spiral arms are not stationary, but short-lived and recurrently formed. In this case, the systematic gradient of stellar age is not observed. In fact, there have been a growing number of observational studies that gave evidence against the density wave theory. Therefore, the comprehensive understanding is needed.

In Part I, we investigated the difference of spatial offsets between gas arms and star forming regions in 12 nearby spiral galaxies with two prominent spiral arms. This method has been applied to a number of galaxies in previous studies, but it depends on the tracers of gas and galaxies whether the offsets predicted by the density wave theory are observed. We traced star forming regions with Hα images and dust lanes as a sign of molecular gas arms with I−H or I−K color images whose resolution is higher than that of radio data used by previous studies. We found that bar structures is related to the offsets. Five of 12 galaxies, which have the bar radii larger than 3 kpc, showed almost no offsets. Our results suggested that the reason for no offsets may be explained by the effects of corotation resonance and elliptical orbits nearly parallel to the spiral arms. Therefore, we need other methods to trace older star formation histories than Hα emission (i.e., 10 Myr) in order to verify the density wave theory in such galaxies.

In Part II, we verified the density wave theory in NGC 4321, which is one of the galaxies without clear offsets between dust lanes and star forming regions in Part I. In addition, previous studies have found no differences not only in the distribution of molecular gas and HII regions, but also in the distribution of HII regions and UV star-forming sources with the ages over 100 Myr. However, the angular resolution used in previous works might not be high enough to reject the density wave considering that the spiral arms are located near the corotation resonance. Therefore, we used the HST high resolution imaging data to investigate the difference between the distributions of young and old stellar clusters. We detected resolved stellar clusters with the WFC3/UVIS F555W image

and separated the clusters into the following three samples with the WFPC2 F675W and F658N images; young (Age $\lesssim$ 6 Myr), middle (6 Myr $\lesssim$ Age $\lesssim$ 10 Myr) and old (Age $\gtrsim$ 10 Myr). We investigated the azimuthal distributions of three cluster samples around the southern spiral arm. We succeeded in discovering an observational evidence to support the density wave, i.e., the old cluster sample is distributed downstream of the young cluster sample.

There is a possibility that the conventional method with molecular gas and Hα emission could not detect the predicted offsets in spiral galaxies with relatively large bar structures because the arms are located near the corotation resonance. The new method with resolved old stellar clusters (Age $\gtrsim$ 10 Myr) is essential to discover the evidence for the density wave in such galaxies.

Contents

Chapter 1

Introduction

Galaxy, which is a gravitationally bound system of stars, gas, dust, and other forms of matter, is a fundamental unit of the Universe. It is estimated that the observable Universe includes more than 100 billion galaxies (Gott et al. 2005). According to the Galaxy Zoo project, more than half of massive galaxies at low redshift have spiral structures (Lintott et al. 2011, Willett et al. 2013). Generally, star formation occurs mainly in spiral galaxies, in particular along spiral arms. Therefore, the origin of spiral structures is important not only for understanding star and galaxy formation, but also for understanding the Universe itself.

1.1 Classification of Spiral Galaxies

Hubble (1926) divided galaxies into three major types: elliptical, spiral, and irregular. In the de Vaucouleurs (1959) classification which is an elaboration and extension of the Hubble (1926) scheme, galaxies are classified into different types according to barrishness (E, S0, S, SA, SB, I), openness of arms/disk-bulge ratio (a, b, c, d, m), and rings or s shapes (r, s). There are four main classes: E for elliptical galaxies, S0 for lenticular galaxies, S for spiral galaxies, and I for irregular galaxies. In spiral galaxies, SB galaxies are barred spirals, SA galaxies are unbarred spirals, and SAB galaxies have intermediate bar strength or mixed barrred and unbarred characteristics. The classification from Sa to Sd is based on several criteria: (1) disk-bulge ratio (decreasing in the size and luminosity of the bulge from Sa to Sd galaxies), (2) pitch angle of spiral arms (spiral arms tighter in Sa galaxies), (3) nature of spiral arms (HII regions and young bright stars/clusters are more easily recognized in Sd galaxies), and (4) gas content (increasing from Sa to Sd galaxies). The (r) galaxy has an inner ring, and the (s) galaxy is the pure spiral type, where the arms begin from a central bulge or ends of a bar.

Elmegreen & Elmegreen (1987) classified spiral galaxies into 12 Arm Classes (AC) according

to the morphology of spiral arms. The 12 AC are divided into the three main types: flocculent spirals for AC 1−3, multiple-arm spirals for AC 4−9, and grand design spirals for AC 10−12 (e.g., Elmegreen et al. 2011). The grand design spirals have two long symmetric arms dominating the optical disk. The flocculent spirals have fragmented arms and lack both the strength and continuity of grand design spirals. The multiple-arm spirals have characteristics of both grand design and flocculent spirals.

1.2 Origin of Spiral Structures

Beautiful and fascinating structures of spiral galaxies have a mystery called "Winding Dilemma" (e.g., Wilczynski 1896). We know now that a material rotating in the inner side of a galaxy has a faster angular speed than that in the outer side from observational results of the flat rotation curve. However, if spiral arms were rotating with the same speed as materials, they would be wound up quickly. Therefore, we cannot explain why the spiral structure is sustained over a billion years. In order to solve the issue, there are mainly two contrary hypotheses.

1.2.1 Quasi-Stationary Spiral Structures

The density wave theory (Lin & Shu 1964) describes the spiral structures as quasi-stationary density waves. In this theory, the spiral structure is considered to be a periodic compression and rarefaction of the surface density that propagates through the disk in the same way that waves propagate on the water surface. Lin & Shu (1964) derived the dispersion relation of the density waves for a rotating disk and hypothesized that spiral structures rigidly rotate and remain unchanged over many orbital periods.

Stars in a rotating disk have two frequencies of orbital motion: the angular frequency of circular rotation Ω and the radial epicyclic frequency κ. There exist important resonances: $\Omega_P = \Omega$ (corotation resonance), $m(\Omega_P - \Omega) = \kappa$ (ILR; Inner Lindblad Resonance), and $m(\Omega_P - \Omega) = -\kappa$ (OLR; Outer Lindblad Resonance), where Ω_P is the pattern frequency of the gravitational potential and m is the number of the arms. These resonances occur at specific radii in the differentially rotating disk. The location and the existence of these radii, called the corotation and Lindblad radii, depend on the rotation speed and the pattern speed. At the corotation radius, the star and the gravitational potential rotate with the same speed. At the Lindblad radii, the stellar epicyclic frequency is equal to the frequency at which the star encounters the gravitational potential minima (i.e., density maxima). The density wave only exists between the ILR and OLR because of the resonance with stellar epicyclic motion.

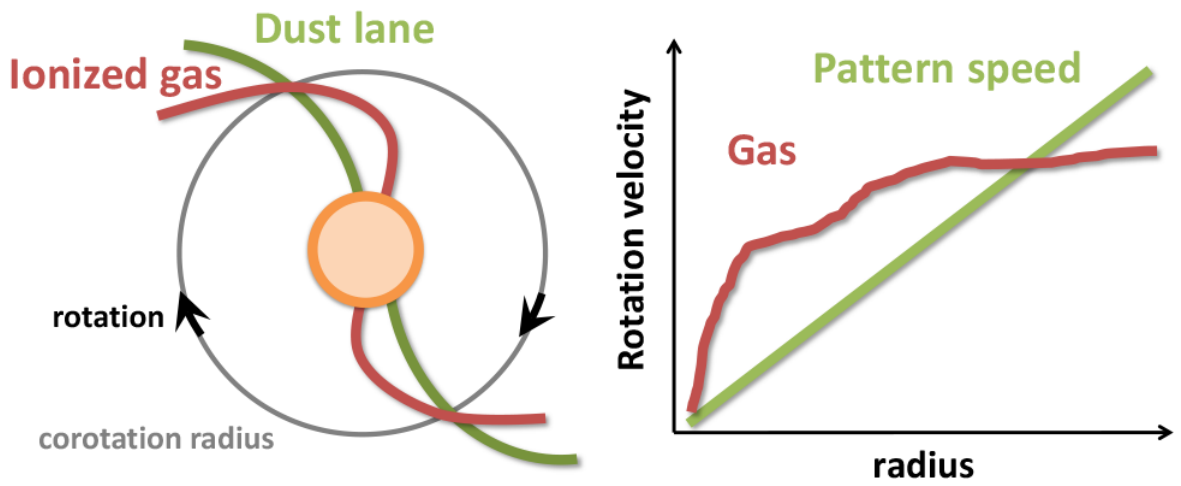

Figure 1.1: The positions of dust lanes and ionized gas in a spiral disk (left panel), and the rotational velocity of gas and the pattern speed of spiral potential (right panel) predicted by the density wave theory. The density wave theory predicts systematic radial dependence of offsets between dust lanes and star forming regions, as a result of star formation due to the interaction between spiral potential with rigid rotation and gas with differential rotation.

This theory predicts large-scale galactic shock waves along spiral arms (Fujimoto 1968, Roberts 1969). As illustrated in Figure 1.1, gas with differential rotation passes through the spiral potential minima with rigid rotation inside the corotation radius. The gas with a subsonic velocity is accelerated toward the spiral potential minimum and enters the potential minimum with a supersonic velocity. The supersonic flow of the gas makes a galactic shock and is decelerated. Then, the gas is strongly compressed, and star formation is induced by the gravitational collapse. When the gas leaves the shock region, it is quickly decompressed, and star formation ceases. In this situation, the observable picture of spiral structure should be arranged in the following way. A dust lane (or gas arm) represents the location of the galactic shock. HII regions, OB associations and relatively young stars are displaced from the dust lane according to their ages.

Although the density wave theory by Lin & Shu (1964) seems to explain quasi-stationary spiral structure, there are some problems. For example, this theory cannot be applied to loosely wound spiral arms strictly due to the tight-winding approximation. In addition, the density waves radially propagate with the group velocity in a few galactic rotations and eventually disappear due to absorption at the Lindblad resonances (Lynden-Bell & Kalnajs 1972). To solve the problems, a modal approach to various morphologies of spiral galaxies has been developed (e.g., Bertin et al.1989 a,b). However, it is still unclear that quasi-stationary spiral structure really exists, since the modal theory requires some assumptions.

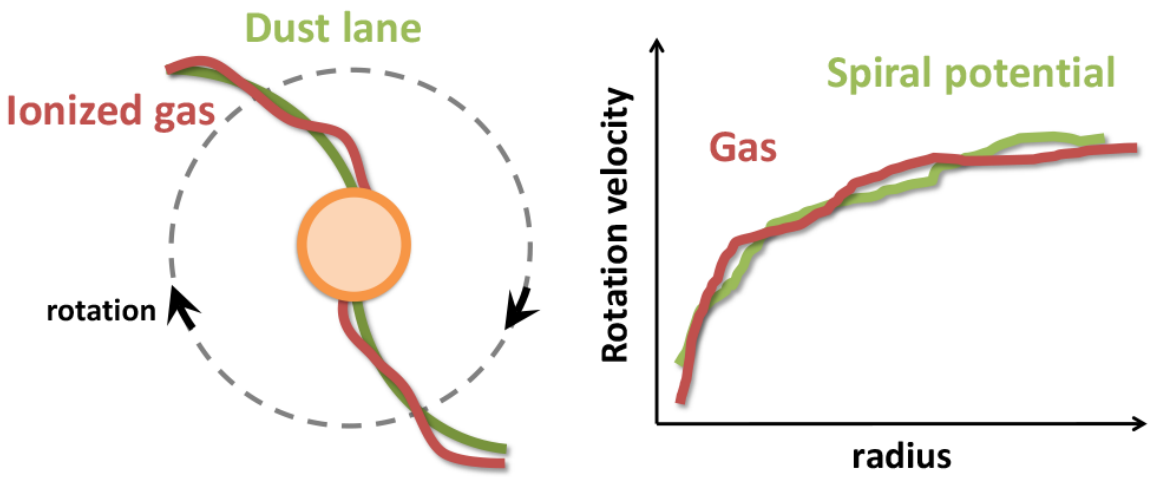

Figure 1.2: The positions of dust lanes and ionized gas in a spiral disk (left panel), and the rotational velocity of gas and spiral potential (right panel) predicted by the recent theoretical studies of spiral structures by time-dependent multi-dimensional numerical simulations. In this case, systematic radial dependence of offsets between dust lanes and star forming regions is not observed.

1.2.2 Non-Stationary Spiral Structures

Almost all the recent theoretical studies of spiral structures by time-dependent multi-dimensional numerical simulations have been unable to prove the existence of the stationary spiral structures. These studies support that spiral structures are not stationary, but more dynamical structures, i.e., they are short-lived and recurrently formed (e.g., Fujii et al. 2011, Wada et al. 2011, Grand et al. 2012a, b, Baba et al. 2013, D'Onghia et al. 2013). Sellwood & Carlberg (1984), using pioneering two-dimensional N-body simulations of the stellar disks with the number of particles ($N = 2 \times 10^4$), showed that spiral structures fade after less than 10 galactic rotations because the stellar disks kinematically heat up with time and become too stable against the development of nonaxisymmetric structure. On the other hand, Fujii et al. (2011), using three-dimensional N-body simulations with a sufficiently high number of particles (e.g., $N = 3 \times 10^6$), showed that spiral structures can survive for more than 10 Gyr although they are short-lived and recurrently formed.

In these studies, both gas and spiral potential differentially rotate at any radii as illustrated in Figure 1.2. Therefore, in contrast to the galactic shock mentioned in the above section, gas is always subsonic relative to the spiral potential. In this situation, gas falls into the spiral potential minimum from both sides, and forms condensations lead to the star formation (see Figure 8 in Wada et al. 2011). As a result, systematic radial dependence of offsets between dust lanes (or gas arms) and star forming regions, which is predicted by the density wave theory, is not observed.

1.3 Observational Studies

There have been a number of observational studies to test whether galaxies have quasi-stationary or non-stationary spiral structures. However, it is difficult to obtain a comprehensive understanding from these studies because different results have been reported depending on methods and galaxies. Here, we introduce some representative methods.

1.3.1 Angular Offsets between Gas Arms and Star Forming Regions

The density wave theory for quasi-stationary spiral structures predicts systematic radial dependence of offsets between dust lanes (gas arms) and star forming regions. Early observational studies have showed existence of the angular offsets in some nearby spiral galaxies (e.g., Mathewson et al. 1972, Rots 1975, Vogel et al. 1988). On the other hand, recent studies with a number of spiral galaxies have reported that not all galaxies show the systematic radial dependence of the offsets (e.g., Egusa et al. 2009, Tamburro et al. 2008, Foyle et al. 2011, Martínez-García & Puerari 2014). Most of the observational studies have detected the angular offsets between atomic hydrogen (HI) or molecular (CO) gas and Hα or 24 μm emission. Egusa et al. (2009), using CO and Hα, found the systematic radial dependence of the offsets in 5 out of 13 spiral galaxies. On the other hand, Foyle et al. (2011) reported that none of 12 spiral galaxies have the systematic angular offsets between HI and 24 μm emission.

1.3.2 Age Distribution of Stellar Clusters

Stellar age gradients across spiral arms are also predicted by the density wave theory. In this case, old stellar clusters are located on the more downstream side than young ones. Since Hα emission serves as a tracer of stellar clusters not older than 10 Myr (Leitherer et al. 1999), methods to trace older stellar populations are more effective for the test of the density wave theory than the above method.

• Azimuthal color gradients

There have been a number of studies with multi-band imaging to investigate color gradients resulting from stellar age gradients across spiral arms. (e.g., Beckman & Cepa 1990, González & Graham 1996, Martínez-García et al. 2009, Martínez-García & González-López lira 2013). Martínez-García & González-López lira (2013), using optical and near-infrared surface photometry, found that 7 out of 13 spiral galaxies show evidence of color gradients predicted by the density wave theory.

• **Stellar cluster complexes**

Several studies have examined age distribution of young stellar cluster complexes (e.g., Grosbøl & Dottori 2009, Sánchez-Gil et al. 2011, Ferreras et al. 2012, Cedrés et al. 2013). Sánchez-Gil et al. (2011) mentioned that grand design spiral galaxies such as NGC 628, NGC 4321 and NGC 5194 show age gradients in star forming regions younger than 10 Myr. On the other hand, Ferreras et al. (2012) found no offsets between HII regions and UV star-forming sources with the ages over 100 Myr in NGC 4321.

• **Resolved stellar populations**

There have been some studies to detect individual stars or clusters and measure their ages with the Hubble Space Telescope (HST) high resolution imaging data. For example, Scheepmaker et al. (2009) investigated age distribution of stellar clusters in NGC 5194, which is located at 8.4 Mpc. Kim et al. (2012) investigated age distribution of stars in NGC 5236, which is located at 4.6 Mpc. Both of them showed the results in general agreement with the density wave theory, i.e., older stellar populations are distributed downstream of spiral arms in comparison with younger ones. On the other hand, Choi et al. (2015) investigated spatially resolved star formation histories (SFHs) in NGC 3031, which is located at 3.8 Mpc. The resulting SFHs showed no systematic age gradient across the spiral arm. Although this method enables us to test the density wave theory with high accuracy, objects are restricted to face-on spiral galaxies closer than $\sim$ 20 Mpc. There are only a few studies which have examined stellar age distribution around spiral arms so far.

1.3.3 Radial Dependence of Pattern Speed

In addition to the above studies with morphological features, the density wave theory has been tested kinematically. It is predicted that quasi-stationary spiral structures have a constant pattern speed, in contrast to a radially decreasing pattern speed for non-stationary spiral structures. The Tremaine-Weinberg method (Tremaine & Weinberg 1984) has been used to measure the pattern speed with the continuity equation which relates the pattern speed to the velocity and surface density. In recent studies, by extending the method to allow for the measurement of a radial dependent pattern speed, the evidence for radial variation in the pattern speed has been reported (e.g., Merrifield et al. 2006, Meidt et al. 2008, 2009, Speights & Westpfahl 2011, 2012). These studies found radially decreasing pattern speeds, which seems to be consistent with non-stationary spiral structures, in some spiral galaxies (e.g., NGC 1068, NGC 1365, NGC 3031, NGC 5194, NGC 5457). However, it is not clear whether the pattern speed varies continuously or consists of multiple radial areas, each with a constant pattern speed.

1.4 Objectives and Approaches

The density wave theory for quasi-stationary spiral structures has been widely accepted because it seemingly explains why spiral structures are sustained over a billion years. The theory predicts stellar age gradients across spiral arms, as a result of star formation due to the interaction between spiral potential with rigid rotation and gas with differential rotation. On the other hand, recent theoretical studies of spiral structures by numerical simulations support that spiral structures are not stationary, but short-lived and recurrently formed. In this case, the systematic gradient of stellar age across spiral arms is not observed. In fact, there have been a growing number of observational studies which gave evidence against the density wave theory. Surprisingly, such studies suggest that even grand design spiral galaxies may have non-stationary spiral structures. However, in the observational studies, which have investigated the morphological features predicted by the density wave theory, the results are different depending on methods and galaxies. Therefore, in this thesis, we will verify the density wave theory with the following two approaches in order to obtain comprehensive understanding about the results in such studies.

There are two representative works against the density wave theory, Foyle et al. (2011) and Ferreras et al. (2012). Foyle et al. (2011) investigated angular offsets between gas traced by HI and star forming regions traced by 24 μm emission, and found the systematic angular offsets in none of 12 spiral galaxies. This method has been applied to a number of galaxies in previous studies, but the results may depend on the tracers of gas and star forming regions. In fact, Louie et al. (2013) suggested that both HI and 24 μm emission are not ideal for tracers to measure the offsets. On the other hand, Egusa et al. (2009), using CO and Hα, found the systematic radial dependence of the offsets in 5 out of 13 spiral galaxies. In addition, they also found no offsets in 2 galaxies. Therefore, in Part I of this thesis, we will examine the difference of offsets between CO and Hα among various galaxies.

Ferreras et al. (2012) investigated stellar age gradients across spiral arms using stellar populations with the ages over 100 Myr in NGC 4321. This galaxy has been also investigated offsets between molecular gas and star forming regions in Egusa et al. (2009). Ferreras et al. (2012) and Egusa et al. (2009) found no evidence for the density wave theory in the spiral arms, i.e., no offset from molecular gas to stellar populations with the ages over 100 Myr. This result seems to strongly support non-stationary spiral structures, considering that NGC 4321 is one of the most famous grand design spiral galaxies. However, since Ferreras et al. (2012) used unresolved stellar cluster complexes, it is worth investigating the age distribution of resolved stellar clusters. Therefore, in Part II of this thesis, we will verify the density wave theory in NGC 4321 with high resolution imaging data.

1.5 Structure of This Thesis

This thesis consists of two parts. In Part I (Chapter 2 − 8), we investigate the difference of offsets between molecular gas arms and star forming regions in 12 nearby spiral galaxies. We trace dust lanes as a sign of molecular gas arms. This enables us to use optical and near-infrared imaging data with higher angular resolution than radio data.

In Part II (Chapter 9 − 15), we verify the density wave theory in NGC 4321 with high resolution imaging data. The southern spiral arm has been observed using the HST with the multiband filters including Hα. We detect resolved stellar clusters and investigate the azimuthal distributions of the young and old stellar clusters against the dust lane. Finally, we give conclusions in Chapter 16.

Part I

The Offsets between Dust Lanes and Star Forming Regions

Chapter 2

Introduction of Part I

2.1 Review of Previous Studies

The density wave theory for quasi-stationary spiral structures predicts systematic radial dependence of offsets between dust lanes (gas arms) and star forming regions. Early observational studies have showed existence of the angular offsets in some nearby spiral galaxies (e.g., NGC 224 − Loinard et al. 1996; NGC 3031 − Rots 1975; NGC 4254 − Egusa et al. 2004; NGC 4321 − Rand 1995; NGC 5194 − Mathewson et al. 1972, Vogel et al. 1988, García-Burillo et al. 1993, Rand & Kulkarni 1990). Here, we review recent studies with offsets between gas arms and star forming regions.

2.1.1 Offset Method

Egusa et al. (2004) estimated a timescale for star formation (t_{SF}) and a pattern speed of the spiral density wave (Ω_P) from radial dependence of angular offsets between molecular clouds traced by CO(J=1-0) and star forming regions traced by Hα emission in NGC 4254. They referred to this method as "Offset method". We show the schematic diagram in Figure 2.1. When we define the angular offset between molecular clouds and star forming regions as θ, it is written with

$$\theta = (\Omega_{gas} - \Omega_P) \times t_{SF}$$

where Ω_{gas} is the angular velocity of gas. In this equation, θ is described as a linear function of Ω_{gas} assuming that t_{SF} and Ω_P are constant over a certain radial region. Therefore, by plotting θ against Ω_{gas} and fitting a line, we can determine both Ω_P and t_{SF} at the same time.

The offset method has been applied to a number of nearby spiral galaxies. However, it depends on galaxies or tracers of gas and star forming regions whether the systematic offsets predicted by the density wave theory are observed. Egusa et al. (2009, hereafter E09) used CO(J=1-0) and

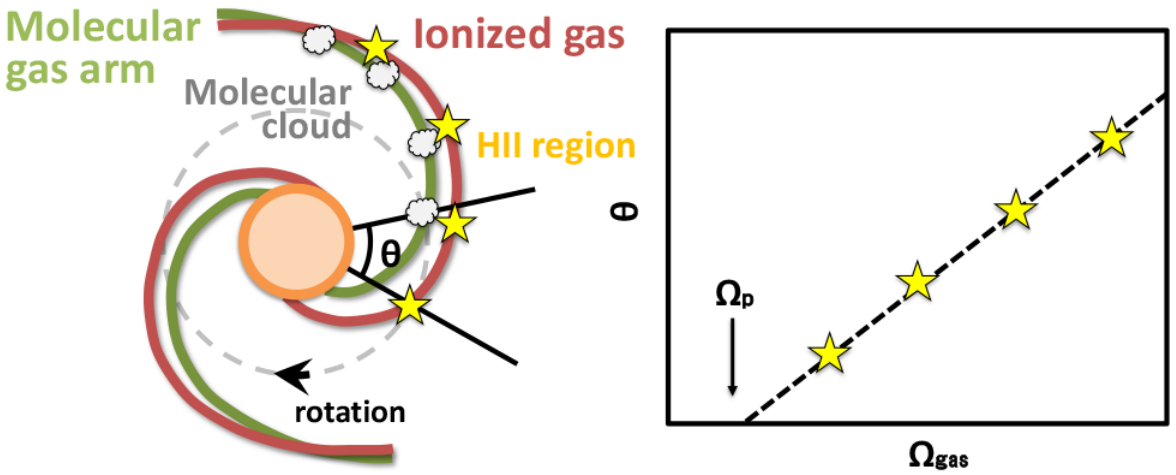

Figure 2.1: A schematic diagram of "Offset method" which was proposed by Egusa et al. (2004, 2009). When we define the angular offset between molecular clouds and HII regions as θ, it is described as a linear function of the angular velocity of gas Ω_{gas} assuming that the timescale for star formation (t_{SF}) and the angular velocity of spiral pattern (Ω_P) are constant in a certain radial region.

Hα imaging data of 13 nearby spiral galaxies to determine t_{SF} and Ω_P. They found systematic offsets in accordance with the density wave theory in 5 galaxies (NGC 628, NGC 4254, NGC 4303, NGC 5194, and NGC 5457), but found no offsets in 2 galaxies (NGC 4321 and NGC 5248), and ambiguous offsets (i.e., non-systematic offsets) in 5 galaxies (NGC 3184, NGC 3938, NGC 4736, NGC 6181, and NGC 6946). The work by E09 depended on by-eye estimation to select the peaks of emission lines. On the other hand, Tamburro et al. (2008, hereafter T08) developed an algorithmic technique. They have succeeded in measuring both Ω_P and t_{SF} from angular offsets between HI and 24 μm emission in 14 nearby spiral galaxies (NGC 628, NGC 925, NGC 2403, NGC 2841, NGC 3031, NGC 3184, NGC 3351, NGC 3521, NGC 3621, NGC 3627, NGC 5055, NGC 5194, NGC 6946, and NGC 7793). However, there is a great discrepancy between their results of t_{SF}, T08 ($1 \leq t_{SF} \leq 4$ Myr) and E09 ($5 \leq t_{SF} \leq 30$ Myr). In addition, Foyle et al. (2011, hereafter F11), which used the same methods and data as T08, reported that none of 12 nearby spiral galaxies (NGC 628, NGC 2403, NGC 2841, NGC 3031, NGC 3351, NGC 3521, NGC 3621, NGC 3627, NGC 5055, NGC 5194, NGC 6946, and NGC 7793) have systematic angular offsets, although they found some evidences of the offsets between CO(J=2-1) and 24 μm emission in NGC 6946 and NGC 5194, and between CO(2-1) and UV emission in NGC 628. Recently, Martínez-García & Puerari (2014) investigated angular offsets between CO(2-1) and 24 μm emission in 3 nearby spiral galaxies (NGC 628, NGC 3627 and NGC 5194) which exhibit bi-symmetric spiral structures by a two-dimensional Fourier analysis in F11 sample

galaxies. They suggested that NGC 628 and NGC 5194 show the angular offsets resembling the theoretical expectations of the density wave theory.

Louie et al. (2013) tried to clarify the cause of this surprising discrepancy of the results among previous studies by comparing offsets among four emission tracers (CO, HI, Hα, and 24 μm) in NGC 5194. They found large offsets between CO and Hα, but small offsets between HI and 24 μm emission. They suggested that both HI and 24 μm emission are not ideal for tracers to measure the offsets, because HI emission traces gas photo-dissociated by recent star formation (Allen 2002) and 24 μm emission is sensitive to dusts heated by young and old stellar populations (Liu et al. 2011).

2.1.2 Galaxies with Systematic or Non-Systematic Offsets

There has been a number of studies to test the density wave theory observationally so far. However, there are not so many galaxies which have been frequently suggested that they are consistent with the density wave theory (e.g., NGC 628, NGC 5194). In fact, it is controversial whether the systematic offsets predicted by the density wave theory are observed in NGC 5194. Louie et al. (2013) found large and ordered offsets between Hα and CO(1-0) with higher angular resolution data than E09 and F11 in NGC 5194, but could not make sure whether the offsets show systematic radial dependence due to the substantial scatter.

Here, we explain the difficulty in verifying whether galaxies show the systematic offsets by using the offset method. The offset method assumes that gas rotates in a circular orbit and a timescale for star formation is constant. However, these assumptions are not necessarily satisfied even in galaxies that the systematic radial dependence of the offsets has been found in previous studies. We show the HST Advanced Camera for Surveys (ACS) image of NGC 5194[*1] (Mutchler et al. 2005) in Figure 2.2. We see that embedded HII regions (red color) are located on the dust lane, which is about 200 pc width, with no significant offsets. If we assume the density wave, there is a possibility that (1) gas rotates in a non-circular orbit, i.e., an elliptical orbit nearly parallel to the spiral arm (e.g., Kuno & Nakai 1997; Aalto et al. 1999) and (2) a timescale for star formation is too short to detect clear offsets ($t_{SF} \lesssim$ a few Myr) (e.g., Elmegreen 2007). In addition, we see that large HII regions are sparsely distributed downstream of the dust lane and small HII regions are distributed everywhere regardless of the dust lane. If we assume the density wave, there is a possibility that (3) stellar cluster complexes with strong Hα emission are sparsely distributed downstream of the dust lane and they have different ages younger than 10 Myr (Leitherer et al.

[*1] The false-color image was constructed by ourselves with the HST multi-color ACS mosaic of NGC 5194 https://archive.stsci.edu/prepds/m51/

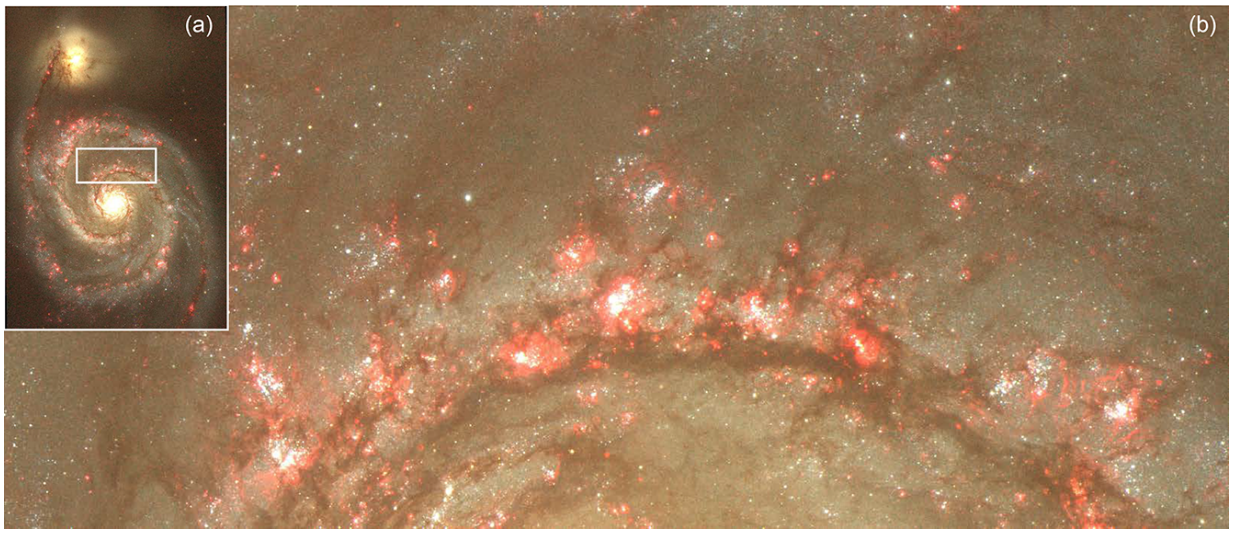

Figure 2.2: (a) The false-color image constructed from the HST multi-color ACS mosaic of NGC 5194. The RGB image is composed of B (blue), V (green), I and emphasized Hα (red). (b) The enlarged image of the northern inner arm surrounded by a white rectangle in (a). The image size is $60'' \times 140''$ and the pixel scale is $0''.05$.

1999), (4) not all stellar clusters were born on the dust lane (e.g., secondary star formation) and (5) a timescale for star formation is not necessarily constant ($\sim$ 1 Myr $< t_{SF} <$ $\sim$ 10 Myr). If the timescale for star formation is constant, the systematic offsets may be able to be detected when we measure the offsets by selecting stellar clusters of similar ages. In E09, five galaxies showed the systematic offsets between CO and Hα. We infer that these galaxies have a number of stellar cluster complexes of similar ages with strong Hα emission. In fact, the offsets in some galaxies had a large variance (see their Figure 6). Therefore, we should consider ages of stellar clusters in order to detect the systematic offsets clearly.

In E09, five galaxies showed ambiguous offsets between CO and Hα. These galaxies had non-systematic offsets, but most of their offsets were positive, i.e., HII regions were distributed downstream of molecular clouds (see their Figure 5). As mentioned above, even if galaxies have quasi-stationary spiral structures predicted by the density wave theory, it is not necessarily possible to detect the systematic offsets clearly, unless we consider ages of stellar populations with Hα emission. Therefore, we suggest that it is difficult to make sure whether galaxies with non-systematic offsets are consistent or inconsistent with the density wave theory by using the offset method. In this part, we do not aim to discern whether galaxies have systematic or non-systematic offsets because studies to investigate stellar age distribution need special imaging data (e.g., multi-band, high angular resolution) and are difficult to deal with a large number of galaxies.

2.1.3 Galaxies with No Offsets

In E09, two galaxies with bar structures (NGC 4321 and NGC 5248) showed no offsets between CO and Hα in their arm regions. E09 mentioned several possible reasons for no offsets: (1) material arms (i.e., non-stationary spiral structure), (2) corotation resonance, and (3) elliptical orbits nearly parallel to the spiral arms. In the case of NGC 5248, they suggested that (3) can partially explain the reason for no offsets because Yuan & Yang (2006) has calculated strong inward streaming motions along the spiral arm assuming that the disk is predominantly driven by a large-scale bar found by Jogee et al. (2002). On the other hand, in the case of NGC 4321, they suggested that (1) would be the most plausible reason, because some offsets were found close to the bar region, where orbits should have higher ellipticity than in the arm region, and the arm region was located inside the corotation radii that have been estimated in previous studies. NGC 4321 also showed no offset between young and old stellar populations with the ages over 100 Myr in Ferreras et al. (2012), which strongly supports that this galaxy has non-stationary spiral structure.

The method to investigate offsets between molecular gas arms and star forming regions is effective to find candidates of galaxies which may have non-stationary spiral structures. In addition, examining the properties of such galaxies will help us to understand the origin of spiral structures.

2.2 Overview of Part I

In this part, we investigate the difference of offsets between molecular gas arms and star forming regions in 12 nearby spiral galaxies. We aim to find candidates of galaxies which may have non-stationary spiral structures and examine their properties. We trace dust lanes as a sign of molecular gas arms with I−H or I−K color images. This enables us to use optical and near-infrared imaging data with higher angular resolution than radio data used by previous studies.

We explain the advantage for tracing dust lanes with I−H or I−K color images in Chapter 3. We show the sample galaxies and the data in Chapter 4. We select 11 nearby spiral galaxies from a sample of Knapen et al. (2003) with I, K and Hα band images, besides NGC 5194 with the HST I and H-band images. In addition, we use optical data (I and Hα band images) from the fifth delivery of the Spitzer Data from the "The Spitzer Infrared Nearby Galaxies Survey" (SINGS) (Kennicutt et al. 2003). In Chapter 5, we describe how to measure offsets between dust lanes and star forming regions. In Chapter 6, we investigate the relation between the offsets and the bar or spiral structures. In Chapter 7, we discuss the possible reasons for no offsets. Then, we give a summary in Chapter 8.

Chapter 3

Methods

We used optical and near-infrared imaging data to trace dust lanes as a sign of molecular gas arms. Here, we describe the advantage of tracing dust lanes and the importance of near-infrared data.

3.1 Advantage of Tracing Dust Lanes

Generally, spatial resolution of radio data (e.g.,CO and HI) is lower than that of optical and near-infrared data. Louie et al. (2013) reported that CO serves as a better tracer for gas arms than HI. Most of the recent studies to measure offsets between molecular clouds and star forming regions (e.g., E09, F11) have used CO data from the Berkeley-Illinois-Maryland Association Survey of Nearby Galaxies (BIMA-SONG; Helfer et al. 2003) or the Heterodyne Receiver Array CO Line Extragalactic Survey (HERACLES; Leroy et al. 2009). The typical spatial resolutions of the data for BIMA-SONG and HERACLES are about $6''$ and $13''$, respectively. On the other hand, the resolution of optical or near-infrared imaging data taken with ground-based telescopes is limited by the seeing which is a few seconds at most. Therefore, the resolution of dust lanes traced by optical and near-infrared images is generally higher than that of molecular clouds traced by CO data.

The molecular gas arms traced by CO emission have been considered to be well correlated with dust lanes. Schinnerer et al. (2013) utilized the CO(1−0) emission with $1''$ resolution from the Plateau de Bure Interferometer Arcsecond Whirlpool Survey (PAWS) to study the relation between molecular gas traced by the CO emission and other galactic components (gas, dust, and stars) in NGC 5194. The resolution of the CO data from PAWS is better than or comparable with that of optical and near-infrared imaging data obtained from ground. For reference, we show

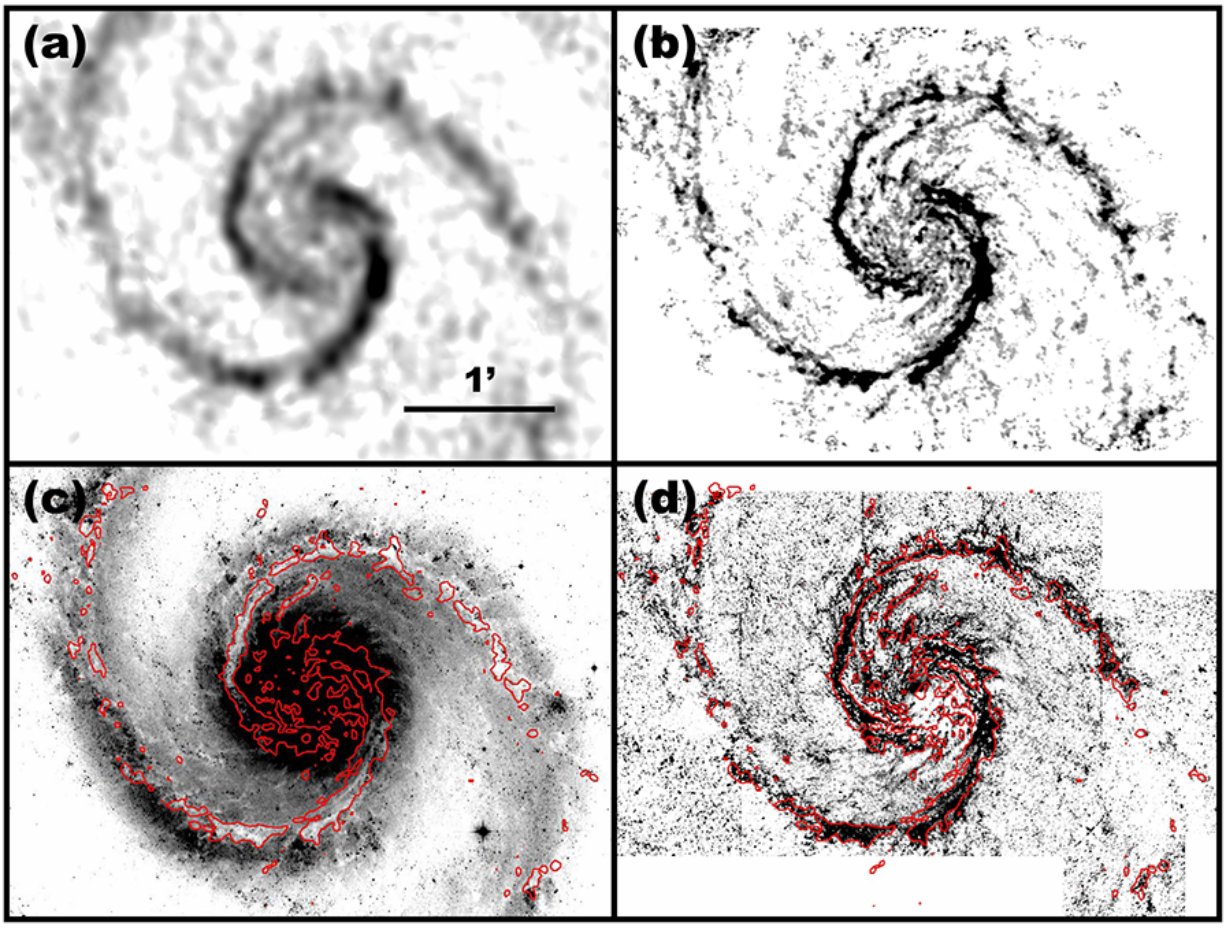

Figure 3.1: CO emission image of NGC 5194 from (a) BIMA-SONG (resolution ∼ 6") and (b) PAWS (resolution ∼ 1"). The CO contour lines overlaid on (c) I-band image obtained with the HST/ACS F814W filter, and (d) I−H color image. The H-band image was obtained with the HST/NICMOS F160W filter. All images are shown in negative representation. The box size of each image is $4' \times 3'$.

the BIMA-SONG data[*1] (resolution ∼ 6″) and the PAWS data[*2] (resolution ∼ 1″) in Figure 3.1 (a) and (b). Schinnerer et al. (2013) showed that the I−H color map is an excellent tracer of the distribution of CO emission (see their Figure 5). We show the I-band image and I−H color image with the CO contour lines from the PAWS data in Figure 3.1 (c) and (d). We used the same images as Schinnerer et al. (2013), i.e., the I-band image obtained with the HST/ACS F814W filter (Section 4.3.3) and the H-band image obtained with the HST Near Infrared Camera and Multi-Object Spectrometer (NICMOS) F160W filter (Section 4.2.2). We can confirm that dust lanes traced with the I−H color image serve as a good tracer of CO emission.

[*1] https://ned.ipac.caltech.edu/level5/March02/SONG/SONG.html
[*2] http://www2.mpia-hd.mpg.de/PAWS/PAWS/Home.html

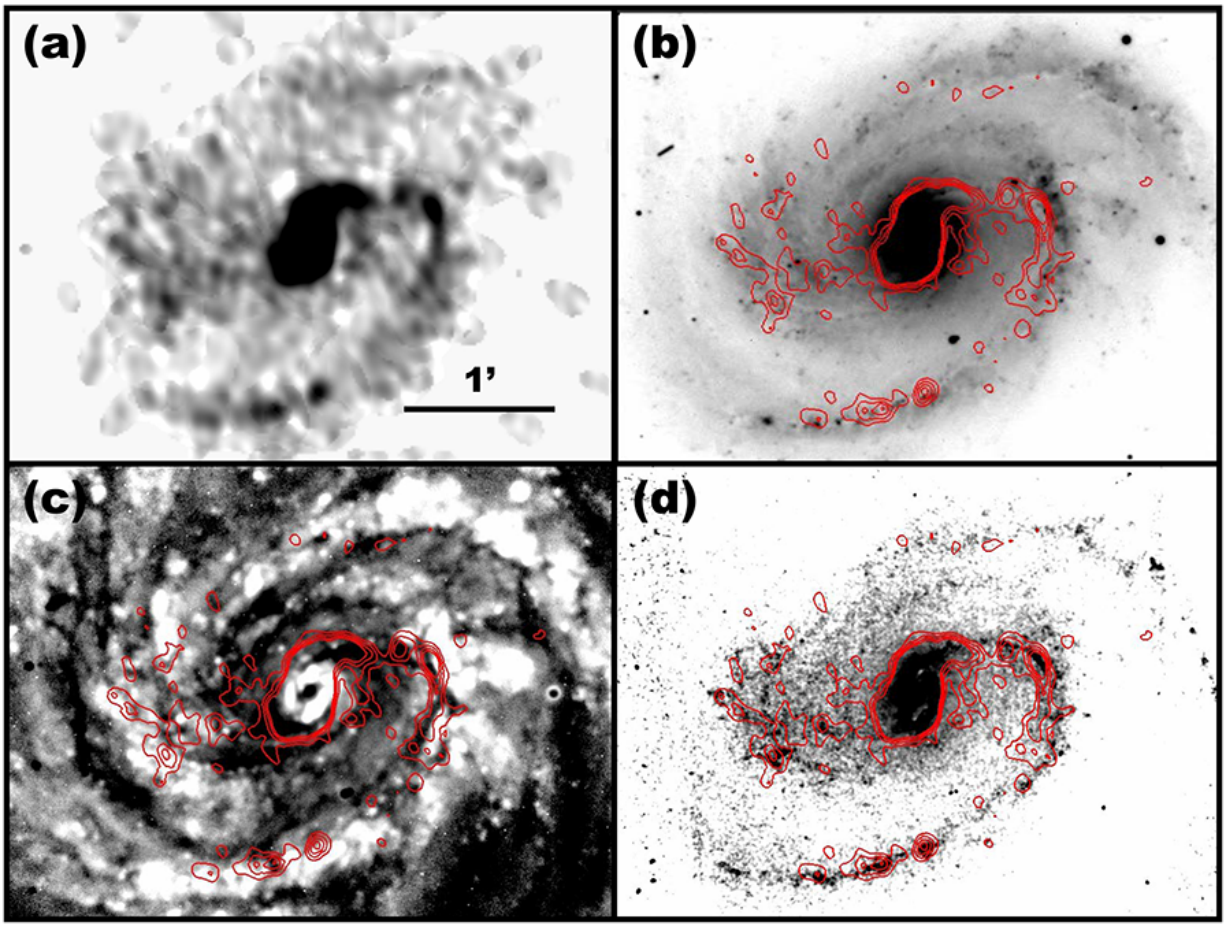

Figure 3.2: (a) CO emission image of NGC 4231 from BIMA-SONG (resolution $\sim 6''$). The CO contour lines overlaid on (b) I-band image, (c) B−I color image, and (d) I−K color image. The B and I-band were obtained from the SINGS, and the K-band was from Knapen et al. (2003). All images are shown in negative representation. The box size of each image is $4' \times 3'$.

3.2 Importance of Near-Infrared Image

Dust lanes visible in optical images have been utilized to trace the position of the spiral shock (e.g., Lynds 1970, Grosbøl et al. 1999). It has been reported that they are well correlated with CO emission, and star forming regions are located downstream of CO emission (e.g., Vogel et al. 1988, Rand & Kulkarni 1990). However, some studies found that there are offsets between CO emission and dust lanes traced by optical images. For example, CO observations in the eastern spiral arm of NGC 5236 showed that CO emission is distributed in accord, not with dust lanes, but with star forming regions (Wiklind et al. 1990, Lord & Kenney 1991). In addition, the southern CO arm in NGC 4321 also showed a better correspondence with star forming regions than dust lanes (Rand 1995). Rand (1995) mentioned that the use of a B−I color image may cause the

offsets between CO emission and dust lanes because the B−I color is so sensitive to young stellar populations and that a near-infrared color (e.g., I−K) would be better to trace dust lanes.

We investigated whether dust lanes traced with an I−K color image serve as a good tracer of CO emission in NGC 4321. We show the CO emission image from BIMA-SONG in Figure 3.2 (a) and the I-band, B−I, and I−K color images with the CO contour lines in Figure 3.2 (b), (c), and (d), respectively. We used the B and I-band images from the SINGS, and the K-band image from Knapen et al. (2003). The dust lanes are displayed in dark color on the B−I and I−K color images. We can see a great discrepancy between the dust lanes traced with the B−I and I−K color images. The dust lanes traced by the I−K color image show excellent agreement with the distribution of CO emission. On the other hand, the B−I color image is strongly affected by star forming regions with young blue stellar populations and not appropriate to trace dust lanes especially in case that young stellar populations locate on the dust lanes. Therefore, we adopt I−H or I−K color images to trace dust lanes as a sign of molecular gas arms.

Chapter 4

Sample Selection & Data

We used I, K (or H), and Hα band images to investigate the distributions of dust lanes and star forming regions. We selected 11 nearby spiral galaxies from a sample of Knapen et al. (2003). In addition, we included NGC 5194 with the HST data in our sample.

4.1 Sample Selection

Knapen et al. (2003, 2004) have carried out an optical and near-infrared imaging survey of 57 nearby spiral galaxies. They have obtained B, I, K and Hα imaging data. We selected 11 galaxies from their sample.

4.1.1 Sample Selection of Knapen et al. (2003)

Knapen et al. (2003) extracted their sample from the list of galaxies selected by Elmegreen & Elmegreen (1987). The Elmegreen & Elmegreen (1987) sample contains 708 galaxies with declination $\delta > -35^\circ$, inclination $i < 60^\circ$ and inclination-corrected diameter at 25 mag arcsec^{-2}, i.e., $D_{25} > 2$ arcmin from the Second Reference Catalogue of Bright Galaxies (RC2; de Vaucouleurs et al. 1976). The sample of 57 galaxies by Knapen et al. (2003) was extracted from the large sample primarily for analysis of the spiral arm properties according to the following items:

- Galaxies with $D_{25} > 4.2$ arcmin were selected to ensure that their spiral arms could be resolved.
- Galaxies with $\delta < -20^\circ$ were excluded to ensure the visibility from the Northern hemisphere.
- Galaxies with $i > 50^\circ$ were excluded because the spiral arms would be difficult to be resolved.

Stedman & Knapen (2001) presented the distribution diagram of the sample galaxies as a function of the morphological type, arm class, bar type, disk diameter, ellipticity, and systemic velocity.

4.1.2 Our Sample Selection

We selected 11 nearby spiral galaxies which could extract the dust lanes from 57 galaxies of Knapen et al. (2003) according to the following terms:

- Galaxies with $D_{25} \geq 5$ arcmin were selected (57 → 36 galaxies).
- Galaxies with the morphological type of Sa, Sab, Sd, Sdm and Sm including peculiar from the NASA/IPAC Extragalactic Database (NED)[*1] were excluded (36 → 23 galaxies).
- Galaxies with an inner ring structure i.e., the morphological type of (r) from NED were excluded (23 → 17 galaxies).

In addition to the above, we excluded six galaxies for other reasons. The quality of K-band image of NGC 1300 and NGC 5457 were not high enough for our purpose. We could not detect the dust lanes clearly in NGC 210, NGC 4051 and NGC 5247 due to low surface brightness of the spiral arms. In addition, we excluded NGC 6946 because of too many foreground stars.

4.1.3 Our Sample

Our sample consists of 12 galaxies including NGC 5194. The properties of our sample galaxies are summarized in Table 4.1, and the I-band images are shown in Figure 4.1. Two galaxies are barred (SB), five galaxies are unbarred (SA), and the others are mixed (SAB). Our sample includes the morphological type from Sb to Scd. As for the AC[*2], eight galaxies are classified as AC 9, two galaxies as AC 12, and the others as AC 3 and AC 5 respectively.

[*1] https://ned.ipac.caltech.edu/

[*2] Elmegreen & Elmegreen (1987) defined the AC as follows: AC 3=fragmented arms uniformly distributed around the center of the galaxy, AC 5=two symmetric, short arms in the inner regions; irregular outer arms, AC 9=two symmetric inner arms; multiple long and continuous outer arms, and AC 12=two long symmetric arms dominating the optical disk.

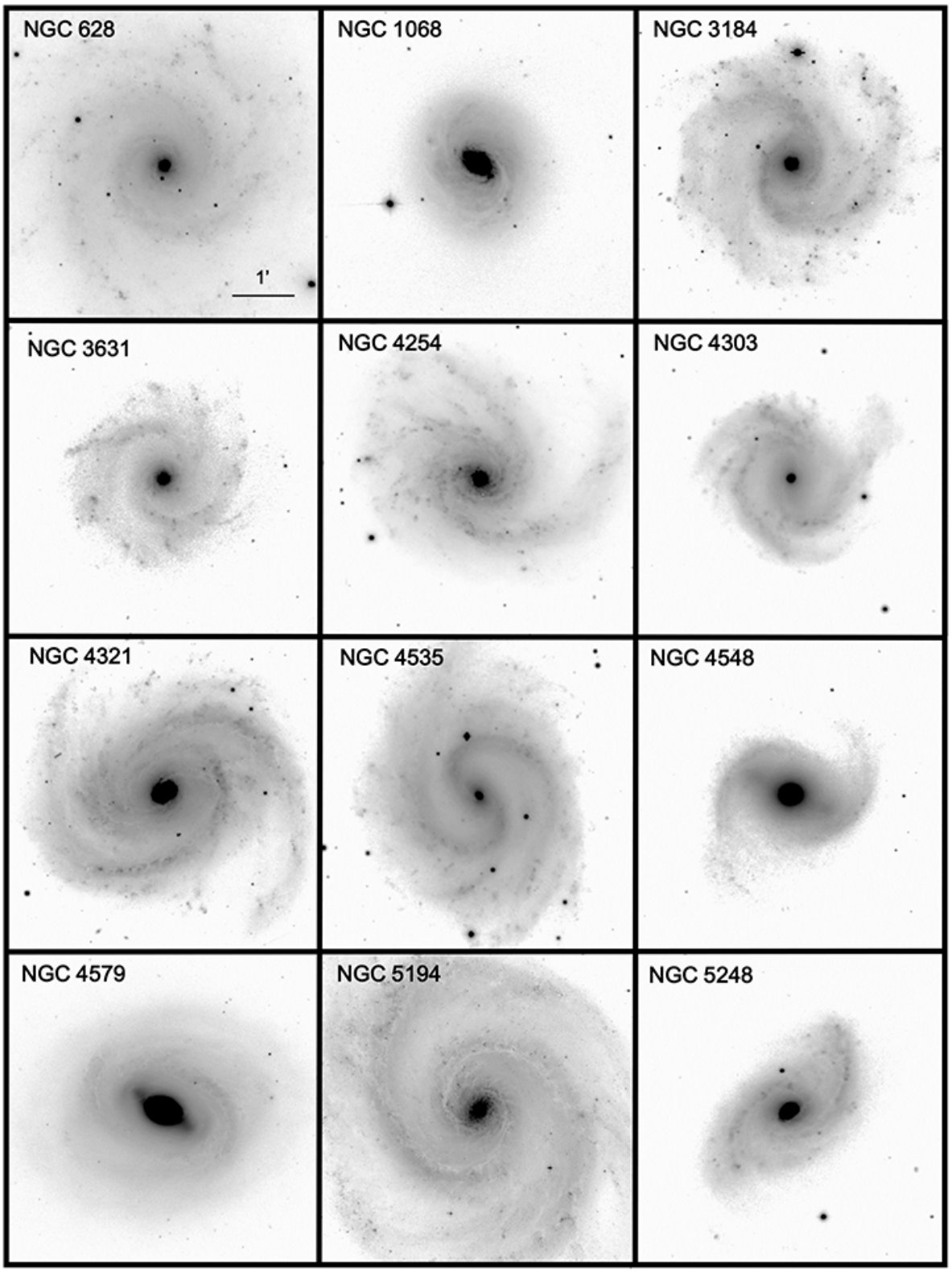

Figure 4.1: I-band images of our sample galaxies in negative representation. All images are oriented with north to the top and east to the left. The box size of all galaxies is 5' × 5'.

Table 4.1: Properties of our sample galaxies

Galaxy		Morphology	AC [1]	D [2]	D_{25} [3]	PA [4]	i [5]	RA	Dec	Redshift
NGC	Messier			(Mpc)	(′)	(°)	(°)	(J2000)	(J2000)	z
628	74	SA(s)c	9	9.7	10.5	11.8[a]	24[b]	01h36m41.7s	+15d47m01s	0.002192
1068	77	SA(rs)b	3	14.4	7.1	13[b]	33[b]	02h42m40.7s	−00d00m48s	0.003793
3184		SAB(rs)cd	9	8.7	7.4	176.4[c]	16.7[c]	10h18m16.8s	+41d25m27s	0.001975
3631		SA(s)c	9	17.5	5	150[e]	17[e]	11h21m02.9s	+53d10m10s	0.003856
4254	99	SA(s)c	9	16.8	5.4	70.9[a]	52.4[a]	12h18m49.6s	+14d24m59s	0.008029
4303	61	SAB(rs)bc	9	15.2	6.5	318[d]	27[d]	12h21m54.9s	+04d28m25s	0.005224
4321	100	SAB(s)bc	12	16.8	7.4	146[d]	27[d]	12h22m54.8s	+15d49m19s	0.005240
4535		SAB(s)c	9	16.8	7.1	28[f]	45[b]	12h34m20.3s	+08d11m52s	0.006551
4548	91	SB(rs)b	5	16.8	5.4	150[b]	37[b]	12h35m26.4s	+14d29m47s	0.001621
4579	58	SAB(rs)b	9	16.8	5.9	89.5[c]	45.7[c]	12h37m43.5s	+11d49m05s	0.005060
5194	51	SA(s)bc	12	7.7	11.2	22[d]	20[d]	13h29m52.7s	+47d11m43s	0.001544
5248		SB(rs)bc	9	12.7	6.2	109.6[a]	43[b]	13h37m32.0s	+08d53m07s	0.003839

Notes. Morphology, right ascension (RA), declination (Dec) and redshift are from NED.

(1) Arm Class from Elmegreen & Elmegreen (1987).

(2) D is the distance from the Nearby Galaxy Catalog (Tully 1988) except for NGC 3631 from Theureau et al. (2007) and NGC 5248 from Tully et al. (2009).

(3) D_{25} is the apparent major isophotal diameter measured at the surface brightness level $\mu_B = 25.0$ B-mag per square arcsecond from Third Reference Catalogue of Bright Galaxies (RC3; de Vaucouleurs et al. 1991).

(4) PA is the position angle of major axis of the disk. North is defined as 0° and east as 90°.

(5) i is the inclination angle of the disk. Face-on is defined as 0° and edge-on as 90°.

References. (a) Egusa et al. 2009; (b) Helfer et al. 2003; (c) Daigle et al. 2006; (d) Sofue et al. 1999; (e) Knapen 1997; (f) Möllenhoff & Heidt 2001

4.2 Near-Infrared Imaging Data

We used K-band imaging data for 11 galaxies and H-band imaging data for NGC 5194. The K-band imaging data were from Knapen et al. (2003). They were downloaded through the Strasbourg astronomical Data Center (CDS) catalogue service (VizieR)[*1]. On the other hand, the H-band imaging data were obtained with the HST/NICMOS. They were downloaded through the Multimission Archive at STScI (MAST)[*2]. We summarize the information about telescopes and seeing in Table 4.2, which are partially quoted from Table 2 of Knapen et al. (2003).

4.2.1 K-band Imaging Data

The images of nine galaxies were obtained using the Isaac Newton Group Red Imaging Device (INGRID; Packham et al. 2003) imager on the 4.2-m William Herschel Telescope during nights between 2000 and 2002. The INGRID camera has a 1024×1024 HAWAII detector (HgCaTe) and gives a projected pixel scale of $0''.242$ with a field of view of $4'.2 \times 4'.2$. The object images were background subtracted, bad pixel masked, flat fielded, and median combined (more details described in Knapen et al. 2003).

The images of two galaxies (NGC 628 and NGC 1068) were obtained with the PISCES (A Wide-Field, 1−2.5 μm Camera for Large-Aperture Telescopes; McCarthy et al. 2001) on the 2.3-m Bok telescope on October 18, 1999. The PISCES camera uses the same kind of array as the INGRID, but gives a projected pixel scale of $0''.5$ with a field of view of $8'.5$ in diameter. The object images were flat fielded, sky subtracted, distortion corrected, and then optimally combined (more details described in McCarthy et al. 2001). The final images have a pixel scale of $0''.242$, which is the same scale as that of the INGRID camera.

4.2.2 H-band Imaging Data

The H-band imaging data of NGC 5194 were obtained with the F160W filter of the NICMOS/NIC3 in November to December, 2005 (HST Proposal ID: Cycle 14 GO 10501, PI: Chandar, Title: Extending the Heritage: Clusters, Dust, and Star Formation in M51). The NICMOS (Viana et al. 2009) is an instrument that provides near-infrared imaging and spectroscopy from 0.8 to 2.5 μm, which was installed on the HST in February 1997. The NIC3 is equipped with a 256×256 HgCdTe Rockwell array with a pixel scale of $0''.2$ and a field of view of $51''.2 \times 51''.2$.

We used images obtained at 15 slightly overlapping pointings in a 5×3 mosaic with four

[*1] http://vizier.nao.ac.jp/viz-bin/VizieR?-source=VI/112

[*2] http://archive.stsci.edu/

exposures in each. We aligned all images relative to the ACS I-band image (Section 4.3.3) with the GEOMAP/GEOTRAN task in IRAF. Then, we combined them into one frame using the IRAF IMCOMBINE task.

4.3 Optical Imaging Data

The I-band and Hα imaging data of six galaxies were from Knapen et al. (2003). On the other hand, the imaging data of the other galaxies were from the SINGS except for the I-band imaging data of NGC 5194. The imaging data of Knapen et al. (2003) were downloaded through the VizieR. The imaging data of the SINGS were downloaded from the fifth delivery of the Spitzer Data[*1]. The I-band imaging data of NGC 5194 were obtained with the HST/ACS and downloaded through the MAST. We summarize the properties of the I-band and Hα imaging data in Table 4.2, which are partially quoted from Table 1 of Knapen et al. (2004).

4.3.1 Knapen et al. (2003) Data

Most of the I-band and Hα imaging data including the continuum data for six galaxies were obtained with the 1-m Jacobus Kapteyn Telescope (JKT) on La Palma, during a number of observing runs from 1999 to 2003. A considerable variety of cameras and CCD detectors were used, but the principal camera was an imager with a 2K $\times$ 2K SITe2 CCD and gave a projected pixel scale of $0''.331$ with an unvignetted field of view of about $10' \times 10'$. On the other hand, the I-band imaging data for NGC 4535 and the R-band imaging data (i.e., Hα continuum data) for NGC 5248 were obtained with the 2.5-m Isaac Newton Telescope (INT) on La Palma. The wide field camera has four 2K $\times$ 4K EEV CCDs and each CCD has a projected pixel scale of $0''.331$ with a field of view of $11' \times 22'$. The images were bias subtracted, flat fielded, image combined, and sky subtracted (more details described in Knapen et al. 2004). The final images have a pixel scale of $0''.242$, which is the same scale as that of the INGRID camera.

As for Hα filters, a narrow-band filter with central wavelength (λ_c) of 6594 Å and full width at half maximum (FWHM) of 44 Å was used except for NGC 3631 which was observed with a filter with λ_c of 6589 Å and FWHM of 15 Å. The continuum images for Hα emission were obtained with narrow-band filters with λ_c of 6470 Å and FWHM of 110 Å for NGC 4548, and with λ_c of 6565 Å and FWHM of 15 Å for NGC 3631, and R-band filters for the others. Although the continuum-subtracted Hα images are provided with the scaling factors, we made the continuum-subtracted images by ourselves except for NGC 3631 for which the original Hα and continuum

[*1] http://irsa.ipac.caltech.edu/data/SPITZER/SINGS/

images were not available. The details of the continuum subtraction technique for NGC 3631 were given in Rozas et al. (1996). We constructed the continuum-subtracted Hα images by scaling and subtracting the continuum images after the images with better seeing were convolved with a Gaussian kernel to match the seeing of worse quality images by using the IRAF GAUSS task. We adopted the same scaling factors as Knapen et al. (2004), which are summarized in Table 4.2.

4.3.2 SINGS Data

We used the I-band and Hα imaging data and adopted the R-band imaging data as the continuum images for Hα emission from the SINGS. The imaging data were obtained at the National Optical Astronomy Observatory (NOAO), as a part of the Legacy Project, over the course of about 3 years during 2001 to 2003. The imaging data of five galaxies were obtained with the 2K $\times$ 2K CCDs on the Kitt Peak National Observatory (KPNO) 2.1-m telescope, which provide a pixel scale of $0''.305$ and a field of view of $10' \times 10'$. On the other hand, the imaging data of NGC 628 were obtained with the 2K $\times$ 2K CCDs on the Cerro Tololo Inter-American Observatory (CTIO) 1.5-m telescope, which provide a pixel scale of $0''.433$ and a field of view of $14'.5 \times 14'.5$. The data reduction consisted of bias subtraction, flat-fielding, single image cosmic ray removal, and combination of images (more details described in the SINGS Fifth Data Delivery April 2007 USER'S GUIDE).

As for Hα filters, three narrow-band filters were used for six galaxies (λ_c [Å]/ FWHM [Å]; 6583/20 for NGC 628, 6618/74 for NGC 4254 and NGC 4579, and 6573/67 for the others). We constructed the Hα continuum-subtracted images by scaling and subtracting the R-band images from the Hα images after the images with better seeing were convolved with a Gaussian kernel to match the seeing of worse quality images by using the IRAF GAUSS task. The scaling factors we adopted are summarized in Table 4.2.

4.3.3 HST/ACS Data

The HST I-band imaging data of NGC 5194 were obtained with the F814W filter of the ACS Wide Field Camera (WFC) in January, 2005 (HST Proposal ID: Cycle 13 GO 10452, PI: Beckwith, Title: HST/ACS Mosaic of M51). The ACS (Avila et al. 2015) is a third generation instrument which was installed on the HST in March 2002. The WFC detector has two 2K $\times$ 4K SITe CCDs with a pixel scale of $\sim 0.05''$ and a field of view of $\sim 202'' \times 202''$. Four exposures of 340 seconds were obtained at six slightly overlapping pointings in a 2 $\times$ 3 mosaic. We downloaded the drizzled science data (h_m51_i_s05_drz_sci.fits) from the MAST (Mutchler et al. 2005).

Table 4.2: Properties of the imaging data

Galaxy	K (or H)		I		Hα			Continuum			
NGC	Telescope	Seeing (″)	Telescope	Seeing (″)	Telescope	Filter (λ_c/FWHM)	Seeing (″)	Telescope	Filter (λ_c/FWHM)	Seeing (″)	Scale
628	Bok	1.55	CTIO	1.3	CTIO	6583/20	2.1	CTIO	R	1.5	0.009
1068	Bok	1.64	JKT	1.4	JKT	6594/44	2.0	JKT	R	2.2	0.019
3184	WHT	0.89	KPNO	1.2	KPNO	6573/67	1.6	KPNO	R	1.3	0.046
3631	WHT	0.87	JKT	1.3	JKT	6589/15	1.3	JKT	6565/15	...	...
4254	WHT	0.82	KPNO	1.6	KPNO	6618/74	1.7	KPNO	R	1.9	0.051
4303	WHT	1.06	JKT	1.7	JKT	6594/44	1.4	JKT	R	1.3	0.042
4321	WHT	0.76	KPNO	1.1	KPNO	6573/67	1.2	KPNO	R	1.1	0.046
4535	WHT	0.77	INT	1.7	JKT	6594/44	1.9	JKT	R	1.6	0.042
4548	WHT	0.81	JKT	1.4	JKT	6594/44	1.7	JKT	6470/115	1.7	0.418
4579	WHT	0.98	KPNO	1.0	KPNO	6618/74	1.2	KPNO	R	1.3	0.046
5194	HST	...	HST	...	KPNO	6573/67	1.7	KPNO	R	1.9	0.046
5248	WHT	0.79	JKT	2.0	JKT	6594/44	1.4	INT	R	1.3	0.005

Notes.

Abbreviations for telescopes: Bok (Steward Observatory Bok 2.3-m telescope), CTIO (Cerro Tololo Inter-American Observatory 1.5-m telescope), KPNO (Kitt Peak National Observatory 2.1-m telescope), WHT (4.2-m William Herschel Telescope), JKT (1-m Jacobus Kapteyn Telescope), INT (2.5-m Isaac Newton Telescope), HST (Hubble Space Telescope)

Chapter 5

Offset Measurement

First of all, we give a brief description of our analysis with Figure 5.1 and 5.2. We trace dust lanes with an I−H or I−K color image. The color image is deprojected using the position angle and the inclination angle, and transformed into polar-coordinates (radius R, azimuth θ). We trace dust lanes by fitting a line to the peaks of the color image on the (log R, θ) plane. Then, we investigate the distribution of star forming regions with respect to the dust lanes. The continuum-subtracted Hα images are also deprojected and transformed into polar-coordinates. The sum of the Hα emission intensity within the radial region where we traced dust lanes according to the azimuth angle (θ') with respect to each dust lane is measured. We assume that spiral arms are trailing, and set the direction of rotation as the forward direction of θ'. Finally, we derive the average azimuth angle of the Hα emission intensity within the range from -50° to $+50^\circ$ as the offset ($\theta_{\rm offset}$) between the dust lane and star forming regions.

5.1 Extracting Dust Lanes

5.1.1 Image Subtraction

The K and H-band images were aligned relative to the I-band images with the GEOMAP/GEOTRAN task in IRAF. The images with better seeing were convolved with a Gaussian kernel to match the seeing of worse quality images by using the IRAF GAUSS task. We constructed the I−K or I−H color images by subtracting the K or H-band images from the I-band images after subtracting the background and converting the counts to magnitude.

As for the I and K-band imaging data from Knapen et al. (2003), the magnitude zeropoint was derived from measurements of stars in the Two Micron All-Sky Survey (2MASS) point source catalog for the K-band and the USNO-B1.0 catalog for the I-band. As for the I-band imaging data from the SINGS, we converted the counts to magnitude by the keyword PHOTFLAM and

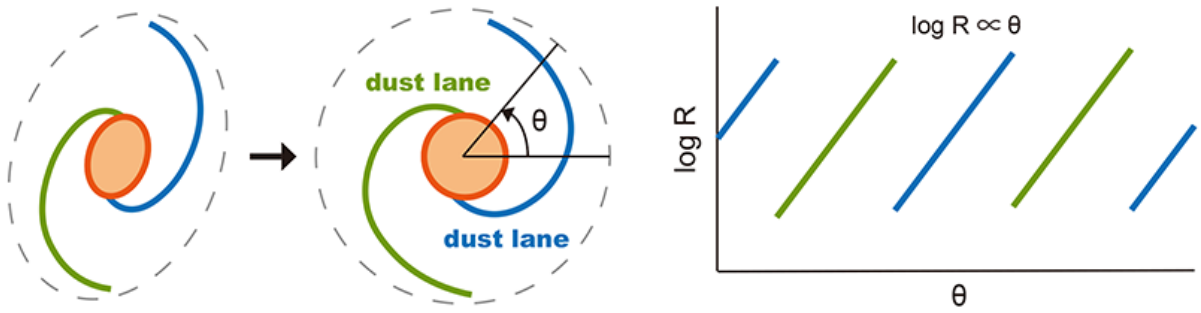

Figure 5.1: Schematic views illustrating the way of tracing dust lanes. The I−H or I−K color image is deprojected using the position angle and the inclination angle, and transformed into polar-coordinates (radius R, azimuth θ). We trace dust lanes by fitting a line to the peaks of the color image on the (log R, θ) plane.

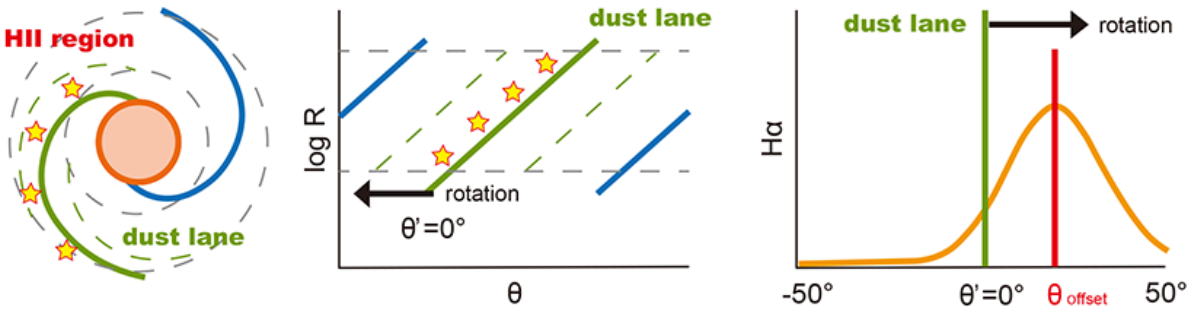

Figure 5.2: Schematic views illustrating the way of measuring offsets between dust lanes and star forming regions. The sum of the Hα emission intensity within the radial region where we traced dust lanes according to the azimuth angle (θ') with respect to the dust lane is measured. The average azimuth angle of the Hα emission intensity within the range from −50° to +50° is derived as the offset ($\theta_{\rm offset}$).

ZPOINT in the FITS header according to the following formula[*1].

$$m = -2.5 \times [\log(\text{counts} \times \text{PHOTFLAM}) - \log(\text{ZPOINT})]$$

As for the HST I and H-band imaging data of NGC 5194, we converted the counts to magnitude with the FITS header keyword PHOTFLAM and PHOTPLAM for the ACS data, and PHOTFNU for the NICMOS data according to the following formulae[*2,*3].

$$m_{AB} = -2.5 \times \log(\text{counts} \times \text{PHOTFLAM}) - 21.10 - 5 \times \log(\text{PHOTPLAM}) + 18.6921 \text{ ; [ACS]}$$

$$m_{AB} = -2.5 \times \log(\text{counts} \times \text{PHOTFNU}) + 8.9 \text{ ; [NICMOS]}$$

[*1] SINGS: The Spitzer Infrared Nearby Galaxies Survey Fifth Data Delivery April 2007 USER'S GUIDE
[*2] ACS Data Handbook, version 7.2 (Gonzaga 2014)
[*3] NICMOS Data Handbook, version 8.0 (Thatte et al. 2009)

The I−K or I−H color images of our sample galaxies are shown in Figure 5.3. As for NGC 3631, we smoothed the image by using the IRAF GAUSS task to highlight dust lanes.

5.1.2 Polar Coordinate Transformation

We deprojected the I−K or I−H color images with the IRAF GEOTRAN task by the position angle and the inclination angle listed in Table 4.1. In Appendix A, we display the deprojected color images of our sample galaxies on the (ΔRA, ΔDec) plane in the top left panels of Figure A.1 to A.12. We transformed the deprojected color images into polar-coordinates by dividing them into areas of radial width of 1 arcsecond and azimuth angle of 1 degree. We display the deprojected color images of our sample galaxies on the (log R, θ) plane in the top right panels of Figure A.1 to A.12. The abscissa shows the azimuth angle θ from 0° to 720°, which is defined as 0° toward the west and increases counterclockwise on the (ΔRA, ΔDec) plane.

5.1.3 Tracing Dust Lanes

We describe the procedure to trace dust lanes in the case of NGC 5194 with Figure 5.4. We detect peaks above a threshold in each azimuth angle as shown in the top of Figure 5.4. We plot the detected peaks with red triangles in the middle of Figure 5.4. The detected peaks contain not only areas with strong dust extinction but also areas with young stellar clusters, e.g., red supergiant clusters which are bright in near-infrared wavelengths. Therefore, we select the peaks which form in line on the upstream side of the spiral arm. Then, we trace the dust lane assuming that the pitch angle of the spiral arm is constant, i.e., a logarithmic spiral.

The equation of a logarithmic spiral in polar coordinates (r, θ) is described below with arbitrary constants a, b.

$$r = ae^{b\theta} \iff \log(r) = b\theta + \log(a) \quad (5.1)$$

We select peaks that can be approximated with the logarithmic spiral, i.e., a straight line in the (log r, θ) plane. Then, we fit the equation to the peaks by using the least squares method. We show the peaks used for fitting dust lanes with green and blue triangles and the best fit lines with green and blue dashed lines in the bottom of Figure 5.4.

In Appendix A, in the middle of Figure A.1 to A.12, the peaks we detected in our sample galaxies are shown with triangles. The peaks used for fitting dust lanes are shown with green and blue triangles, and the best fit lines are shown with green and blue dashed lines. In the bottom of Figure A.1 to A.12, the dust lanes we traced in our sample galaxies are shown with green and blue dashed lines on the deprojected color images.

The threshold of the deprojected color image and the radial region where we traced dust lanes

differ according to galaxies. We summarize the threshold and the radial region in Table 5.1. We set the threshold to be as many peaks for fitting dust lanes and as few peaks due to the fluctuation in the inter-arm regions as possible. We adjusted the threshold at an interval of 0.1 mag. When the number of the peaks for fitting dust lanes was too small, we readjusted the threshold at a minimum interval of 0.025 mag. In some galaxies, we varied the threshold according to the azimuthal angle. Two thresholds were used for NGC 3184, NGC 4321 and NGC 4535, because extinction intensities were different between two dust lanes. On the other hand, three thresholds were used for NGC 4548, because we avoided the peaks due to poor quality of the flatness in the K-band image.

As for NGC 1068 and NGC 5248, we traced only one dust lane, because extinction intensities seemed to be significantly different between two dust lanes. In both cases, there is a possibility that the background subtraction was not accurate because the field of view was smaller than the angular size of the galaxy. This might make it hard to trace the other dust lane.

5.2 Offsets between Dust Lanes and Star Forming Regions

We display the continuum-subtracted Hα images of our sample galaxies in Figure 5.5. The continuum-subtracted Hα images were aligned relative to the I-band images with the GEOMAP/GEOTRAN task in IRAF. If there were bright foreground stars around spiral arms, we masked them with apertures three to six times as large as the seeing size. We deprojected the continuum-subtracted Hα images with the IRAF GEOTRAN task by the position angle and the inclination angle listed in Table 4.1. We used the counts as Hα emission intensity without converting them to flux and correcting the contamination by [NII] emission lines.

We describe the procedure to measure the offsets between dust lanes and star forming regions in the case of NGC 5194. We show the red contour lines for the Hα emission on the deprojected I−H color images on the (ΔRA, ΔDec) and (log R, θ) planes in Figure 5.6. The dust lanes traced in the above section are shown with green and blue lines. We set the azimuth angle (θ', θ'') with respect to each dust lane, i.e., $\theta' = 0$ and $\theta'' = 0$ represent the position of each dust lane. We set the direction of rotation as the forward direction of θ' and θ''. We measure the sum of the Hα emission intensity within the radial region where we traced dust lanes according to the azimuth angle, which is defined in the following equation.

$$L_{\mathrm{H}\alpha}(\theta') = \sum_{r=\mathrm{R_{min}}}^{\mathrm{R_{max}}} H\alpha(r, \theta')$$

$H\alpha(r, \theta')$ indicates the Hα emission intensity at radius r and azimuth angle θ'. $\mathrm{R_{max}}$ and $\mathrm{R_{min}}$

Table 5.1: Threshold and radial region of dust lanes

Galaxy	Threshold	R (″)		Galaxy	Threshold	R (″)	
NGC	(mag)	Min	Max	NGC	(mag)	Min	Max
628	2.35	50	90	4535	1.2 ($\theta \leq 150°$) 1.3 ($\theta > 150°$)	45	85
1068	2.0	30	50				
3184	2.2 ($\theta \leq 200°$) 2.15 ($\theta > 200°$)	30	80	4548	1.75 ($\theta \leq 10°$) 1.8 ($10° < \theta \leq 190°$) 1.85 ($190° < \theta \leq 340°$) 1.75 ($\theta > 340°$)	60	80
3631	3.8	40	70				
4254	1.4	30	70				
4303	2.0	20	50	4579	1.325	50	90
4321	1.6 ($\theta \leq 130°$) 1.7 ($\theta > 130°$)	65	105	5194	0.9	50	90
				5248	1.6	40	100

indicate the radial region where we traced dust lanes listed in Table 5.1. We show the distribution of $L_{\mathrm{H}\alpha}(\theta')$ and $L_{\mathrm{H}\alpha}(\theta'')$ with red lines in the lower panels of Figure 5.7. We derive the average azimuth angle of the Hα emission intensity as the offset (θ_{offset}), which is defined in the following equation.

$$\theta_{\mathrm{offset}} = \frac{\sum_{\theta'=-50}^{50} \theta' L_{\mathrm{H}\alpha}(\theta')}{\sum_{\theta'=-50}^{50} L_{\mathrm{H}\alpha}(\theta')}$$

We show the θ_{offset} with magenta lines in the lower panels of Figure 5.7.

We display the continuum-subtracted Hα images on the (R, θ') and (R, θ'') planes in negative representation in the upper panels of Figure 5.7. The red solid lines indicate the average azimuth angle of the Hα emission intensity according to the radius, which is defined in the following equation.

$$\theta_{\mathrm{offset}}(r) = \frac{\sum_{\theta'=-50}^{50} \theta' H\alpha(r, \theta')}{\sum_{\theta'=-50}^{50} H\alpha(r, \theta')}$$

On the other hand, the red dashed lines indicate the peak azimuth angle of the Hα emission intensity according to the radius, i.e., $\theta_{\mathrm{max}}(r) = \mathrm{Max}\ H\alpha(r, \theta')$ $[-50° \leq \theta' \leq 50°]$.

In Appendix B, in the top of Figure B.1 to B.12, we show the red contour lines for the Hα emission of our sample galaxies on the deprojected I−K or I−H color images on the (ΔRA, ΔDec) and (log R, θ) planes. In the bottom of Figure B.1 to B.12, we show the continuum-subtracted Hα images on the (R, θ') and (R, θ'') planes and the distribution of the sum of the Hα emission intensity within the radial region where we traced dust lanes according to the azimuth angle (θ', θ'').

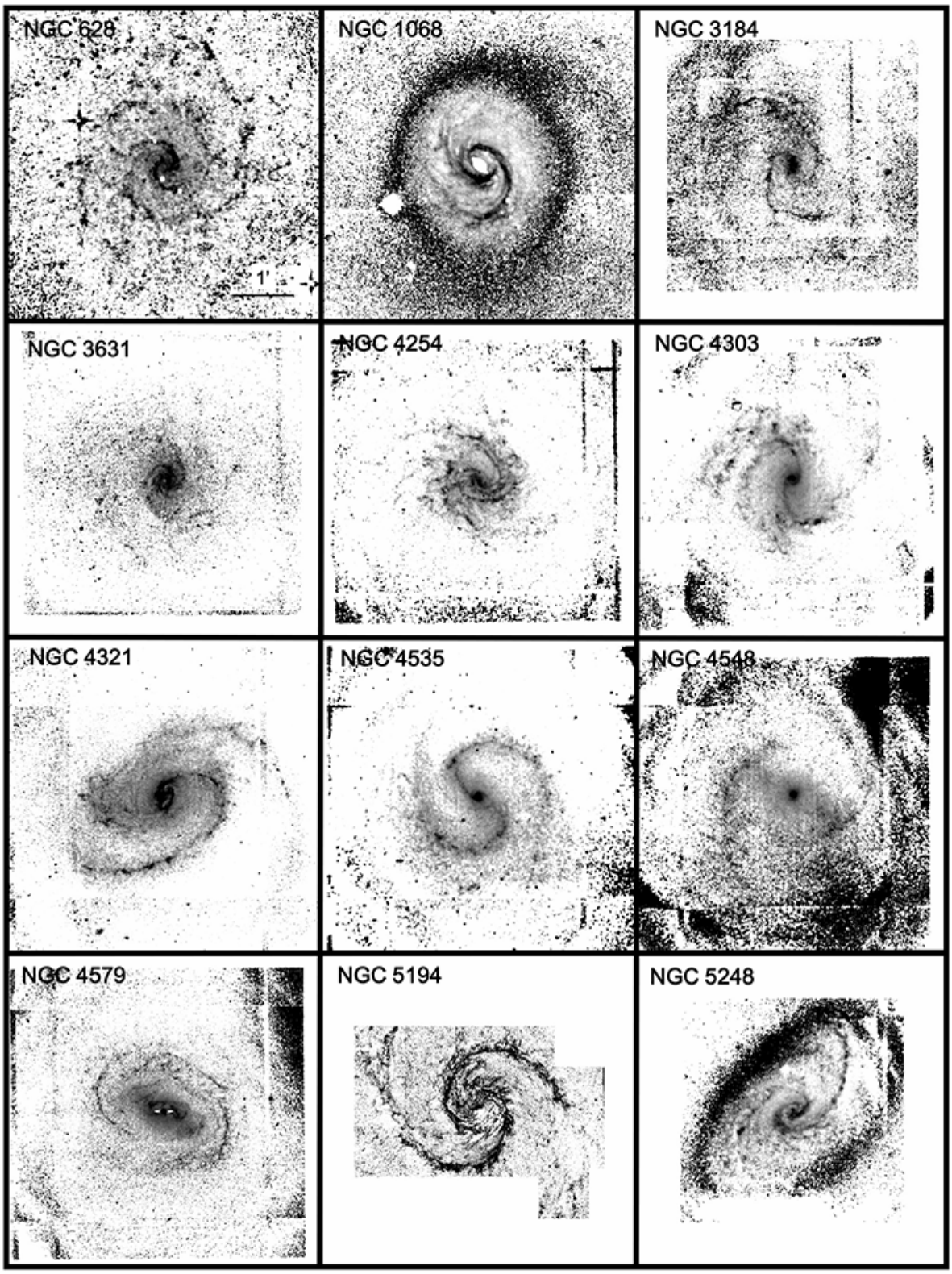

Figure 5.3: The I−K or I−H color images of our sample galaxies in negative representation. All images are oriented with north to the top and east to the left. The box size of all galaxies is $5' \times 5'$.

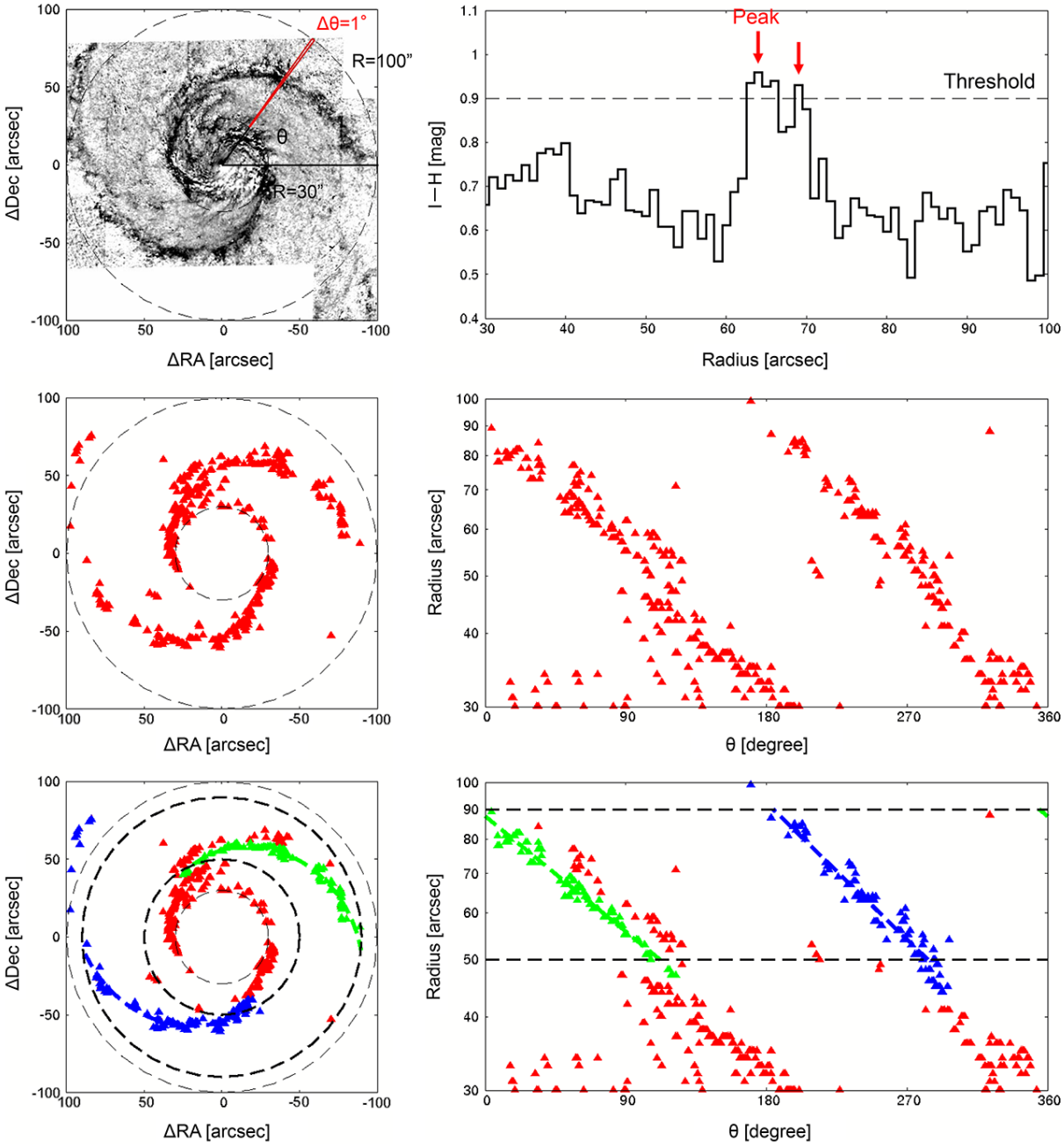

Figure 5.4: *(Top);* The deprojected I−H color image of NGC 5194 is shown in the left. The right figure shows the radial variation of I−H color at θ = 54°. In the case of NGC 5194, we detected the peaks above a threshold of 0.9 mag in the deprojected I−H color image. *(Middle);* The detected peaks plotted with red triangles on the (ΔRA, ΔDec) and (log R, θ) planes. *(Bottom);* The peaks used for fitting dust lanes are shown with green and blue triangles. The best fit lines are shown with green and blue dashed lines. The radial region between the thick black dashed lines is used when we examine the distribution of star forming regions.

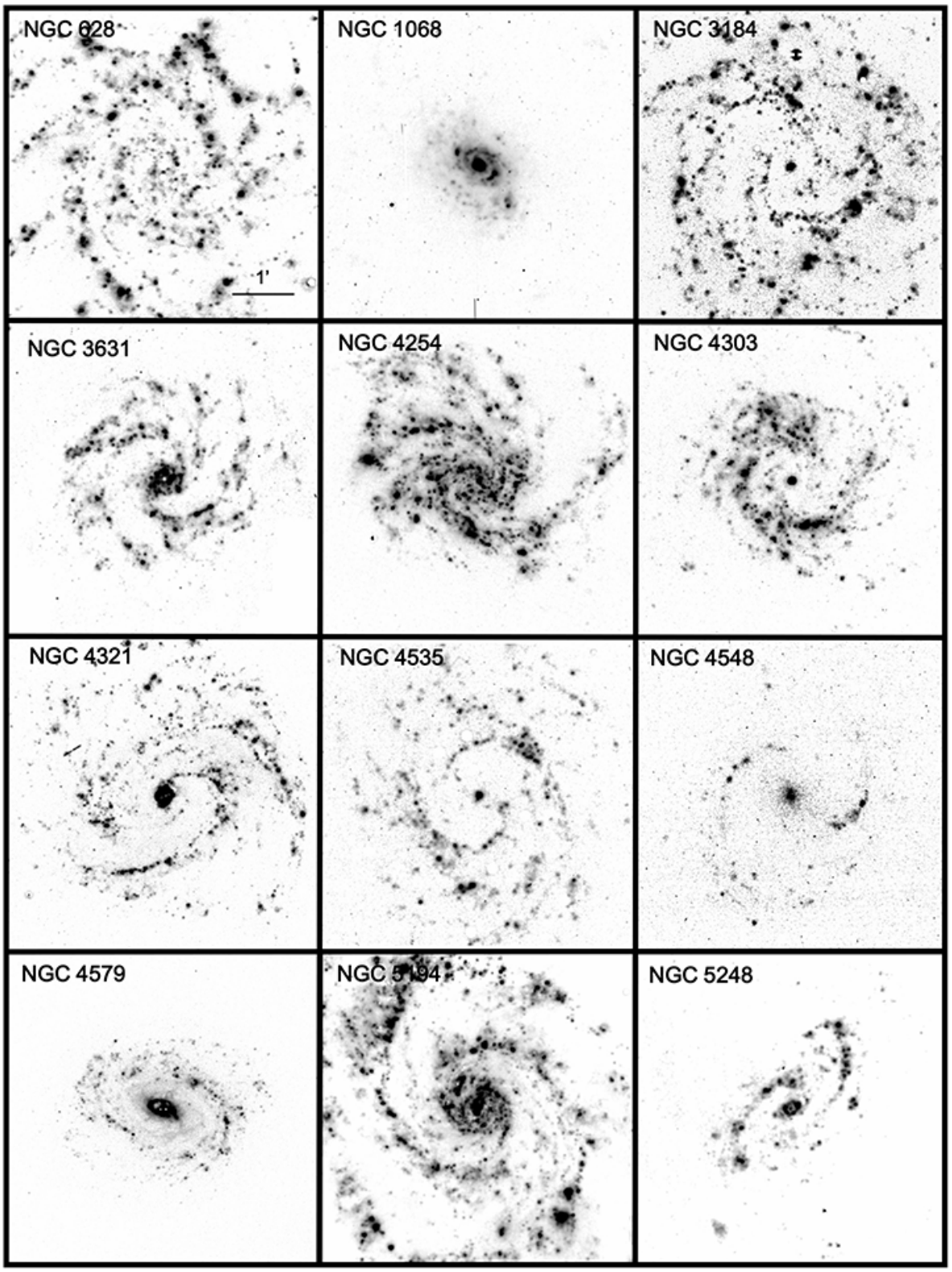

Figure 5.5: The continuum-subtracted Hα images of our sample galaxies in negative representation. All images are oriented with north to the top and east to the left. The box size of all galaxies is $5' \times 5'$.

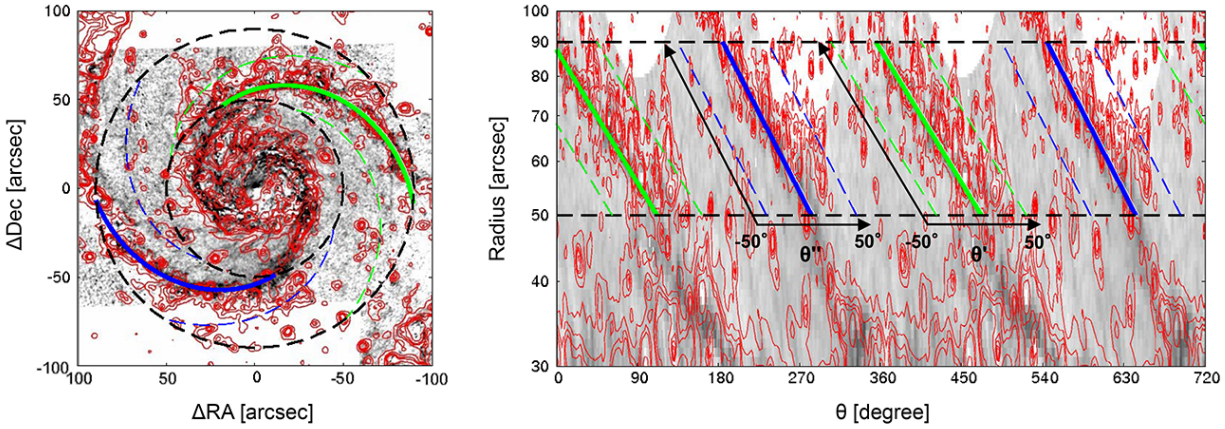

Figure 5.6: The red contour lines for the Hα emission on the deprojected I−H color images on the (ΔRA, ΔDec) and (log R, θ) planes. The dust lanes are shown with green and blue lines. The positions at the azimuth angle ± 50° with respect to the dust lanes are shown with green and blue dashed lines.

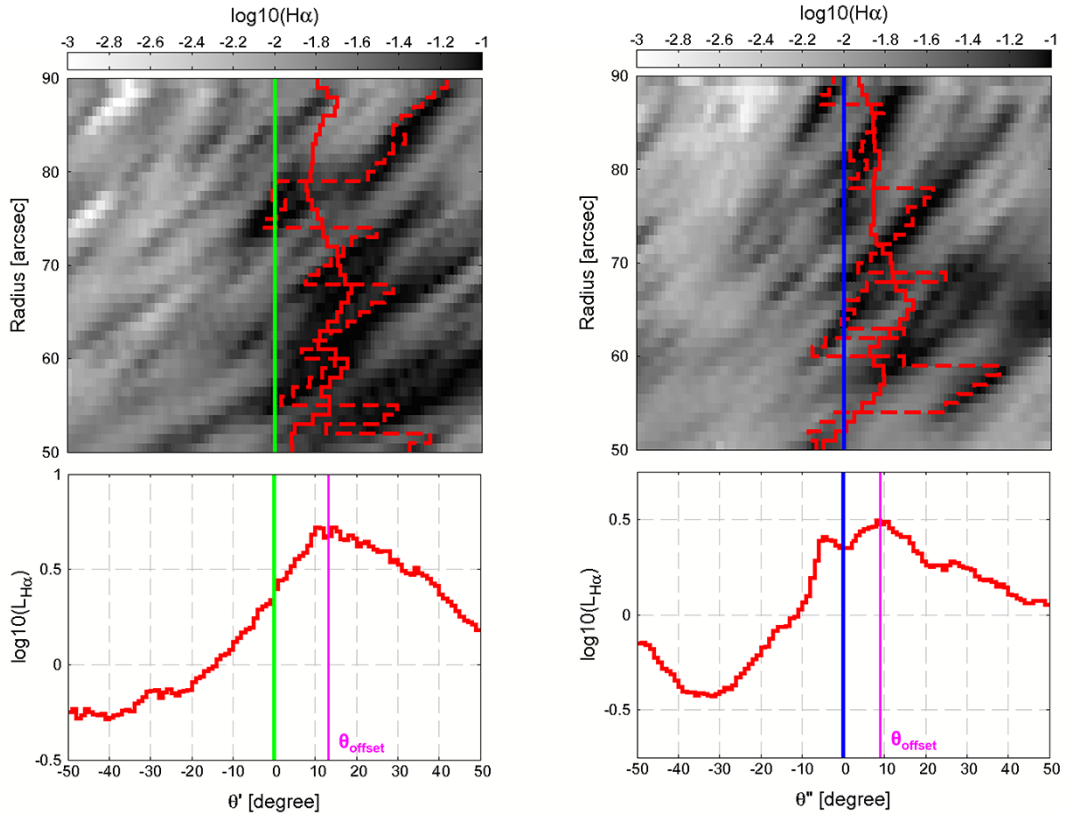

Figure 5.7: The upper panels show the continuum-subtracted Hα images on the (R, θ') and (R, θ'') planes in negative representation. The average and the peak azimuth angle of the Hα emission intensity according to the radius are shown with red solid lines and red dashed lines respectively. The lower panels show the distribution of the sum of the Hα emission intensity within the radial region where we traced dust lanes according to the azimuth angle (θ', θ''). The magenta lines show the $\theta_{\rm offset}$.

Chapter 6

Results

We derived $\theta_{\rm offset}$ in each arm of 12 sample galaxies. We describe the details of the results of individual galaxies in Appendix C. Here, we investigate the relation between $\theta_{\rm offset}$ and the bar or spiral structures.

6.1 Relation with Bar Structure

We found that the bar structure is related to $\theta_{\rm offset}$. Therefore, we classified our sample galaxies into the following three types based on the bar structure.

Type 1 : galaxies without bar structure (NGC 628, NGC 3631, NGC 4254, and NGC 5194)

Type 2 : galaxies with bar structure of the radii smaller than 3 kpc (NGC 1068, NGC 3184, and NGC 4303)

Type 3 : galaxies with bar structure of the radii larger than 3 kpc (NGC 4321, NGC 4535, NGC 4548, NGC 4579, and NGC 5248)

We judged whether the galaxy has a bar or not by referencing previous studies (more details described in Appendix C). We did not regard a nuclear bar with a radius of a few seconds as a bar. The physical scale of the bar structure depends on the distance to the galaxy listed in Table 4.1. The distances of all galaxies were measured with the Tully-Fisher relation (Tully & Fisher 1977). We adopted the distance from the Nearby Galaxy Catalog (Tully 1988) except for NGC 3631 and NGC 5248 whose distance might be largely overestimated in comparison with the mean distance in NED. As for NGC 3631, we adopted the revised distance of 17.5 Mpc from Theureau et al. (2007) instead of 21.6 Mpc from Tully (1988). As for NGC 5248, we adopted the revised distance of 12.7 Mpc from Tully et al. (2009) instead of 22.7 Mpc from Tully (1988).

Table 6.1: Relation between θ_{offset} and the bar radii

Category	Galaxy	R_{bar}		θ_{offset} (°)		
	NGC	(″)	(kpc)	Arm1	Arm2	Average
Type 1	628	...	...	8.8	9.8	9.3
	3631	...	...	14.0	8.9	11.4
	4254	...	...	10.7	6.9	8.8
	5194	...	...	13.2	9.0	11.1
Type 2	1068	16[a]	1.1	4.9	...	4.9
	3184	25[b]	1.1	9.9	3.2	6.6
	4303	30[c]	2.2	4.5	13.7	9.1
Type 3	4321	61[d]	5.0	0.6	4.1	2.4
	4535	41[d]	3.3	2.5	−1.8	0.3
	4548	62[d]	5.0	−0.3	0.2	0.0
	4579	45[c]	3.7	−0.6	3.1	1.3
	5248	71[e]	4.4	1.5	...	1.5

References.
(a) Scoville et al. 1988; (b) Elmegreen et al. 1996; (c) Laurikainen et al. 2004; (d) Kuno et al. 2007; (e) Elmegreen & Elmegreen 1985

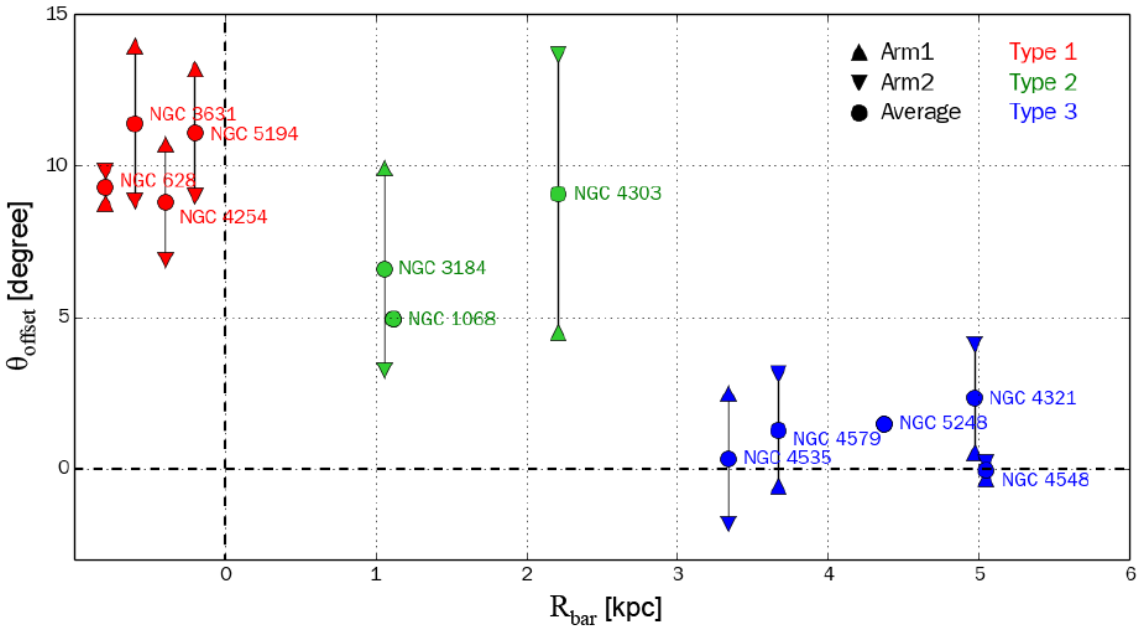

Figure 6.1: The relation between θ_{offset} and the bar radii in units of kiloparsec. Type 1 galaxies have no bar, i.e., $R_{bar} = 0$.

6.1.1 Offsets

We summarize the relation between $\theta_{\rm offset}$ and the bar radii of our sample galaxies in Table 6.1 and Figure 6.1. The average $\theta_{\rm offset}$ for Type 1, 2, and 3 galaxies are 10°, 7°, and 1°, respectively. Type 1 galaxies have $\theta_{\rm offset}$ more than 5° for all arms, while Type 3 galaxies have $\theta_{\rm offset}$ less than 5° for all arms. On the other hand, $\theta_{\rm offset}$ of Type 2 galaxies tend to be much different among arms. As for NGC 3184 and NGC 4303, one arm has $\theta_{\rm offset}$ more than 5°, and the other arm has $\theta_{\rm offset}$ less than 5°. As for NGC 1068, $\theta_{\rm offset}$ is about 5° which is between Type 1 and Type 3 galaxies.

In Type 1 and Type 2 galaxies, star forming regions with strong Hα emission tend to be located downstream of dust lanes. On the other hand, in Type 3 galaxies, star forming regions tend to be located on dust lanes.

6.1.2 Radial Distance

We summarize the relation between $\theta_{\rm offset}$ and the radial regions where we traced dust lanes in Table 6.2. We traced dust lanes by choosing the radial region where they can be approximated by a logarithmic spiral. The radial regions of all our sample galaxies are located within the radial distance from 20″ to 105″. We show the relation between $\theta_{\rm offset}$ and the radial regions in Figure 6.2. In this figure, the bar radii are also shown with magenta dashed lines. The radial regions of barred galaxies tend to be located farther from the center than those of unbarred galaxies. This tendency becomes more noticeable when we use the radial regions in unit of kpc as shown in Figure 6.3. The average radial regions for Type 1, 2, and 3 galaxies are 2.5 − 4.8 kpc, 1.6 − 3.5 kpc, and 4.1 − 7.1 kpc, respectively. The radial regions of Type 3 galaxies are located the farthest from the center. We show the relation between $\theta_{\rm offset}$ and the radial regions normalized by the isophotal radius R_{25} in Figure 6.4. The radial regions of Type 1 and 2 galaxies include the central region of $R/R_{25} \simeq 0.2$ except for NGC 3631. On the other hand, the radial regions of Type 3 galaxies are located at the region of $R/R_{25} \gtrsim 0.3$ except for NGC 4535 and NGC 5248.

The main reason that the radial regions of barred galaxies tend to be located farther from the center than those of unbarred galaxies is because we traced dust lanes located outside of the bar in most of the barred galaxies. In addition, it may be one of the reasons that the physical size of barred galaxies is generally larger than that of unbarred galaxies (Elmegreen & Elmegreen 1989, Ann & Lee 2013).

Table 6.2: Radial regions where we traced dust lanes

Category	Galaxy	R (″)		R (kpc)		R/R_{25}[a]	
	NGC	Min	Max	Min	Max	Min	Max
Type 1	628	50	90	2.4	4.2	0.16	0.29
	3631	40	70	3.4	5.9	0.27	0.47
	4254	30	70	2.4	5.7	0.19	0.43
	5194	50	90	1.9	3.4	0.15	0.27
Type 2	1068	30	50	2.1	3.5	0.14	0.23
	3184	30	80	1.3	3.4	0.14	0.36
	4303	20	50	1.5	3.7	0.10	0.26
Type 3	4321	65	105	5.3	8.6	0.29	0.47
	4535	45	85	3.7	6.9	0.21	0.40
	4548	60	80	4.9	6.5	0.37	0.49
	4579	50	90	4.1	7.3	0.28	0.51
	5248	40	100	2.5	6.2	0.22	0.54

Notes.

[a] R_{25} is the apparent major isophotal radius measured at or reduced to the surface brightness level $\mu_B = 25.0$ B-mag per square arcsecond from RC3.

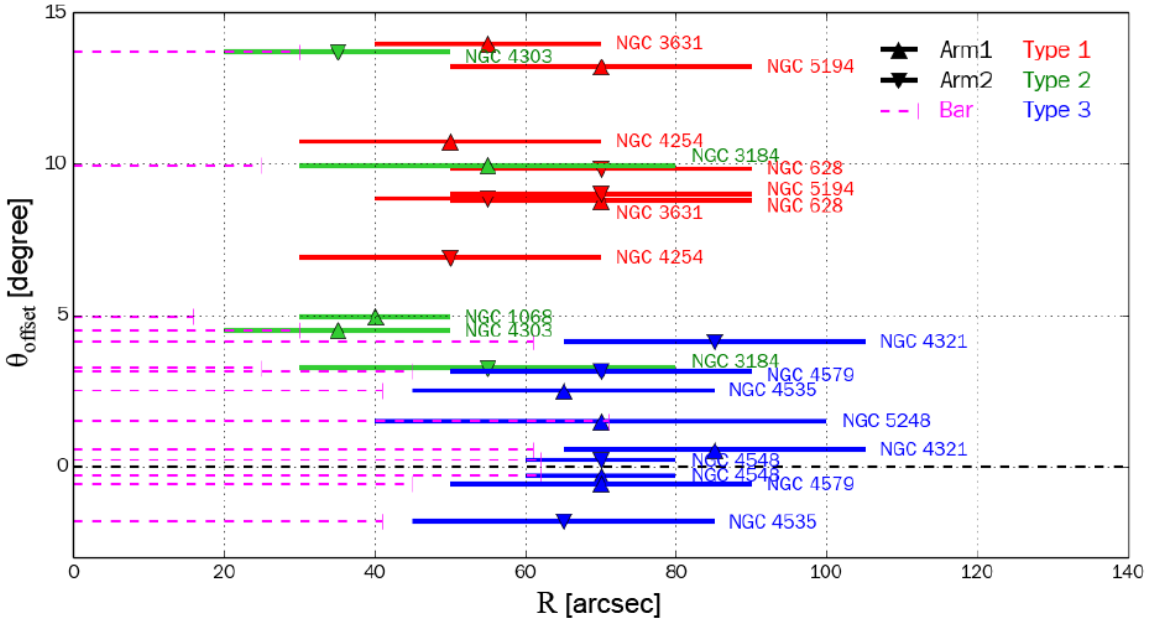

Figure 6.2: The relation between θ_{offset} and the radial regions in units of arcsecond. The bar radii are shown with magenta dashed lines.

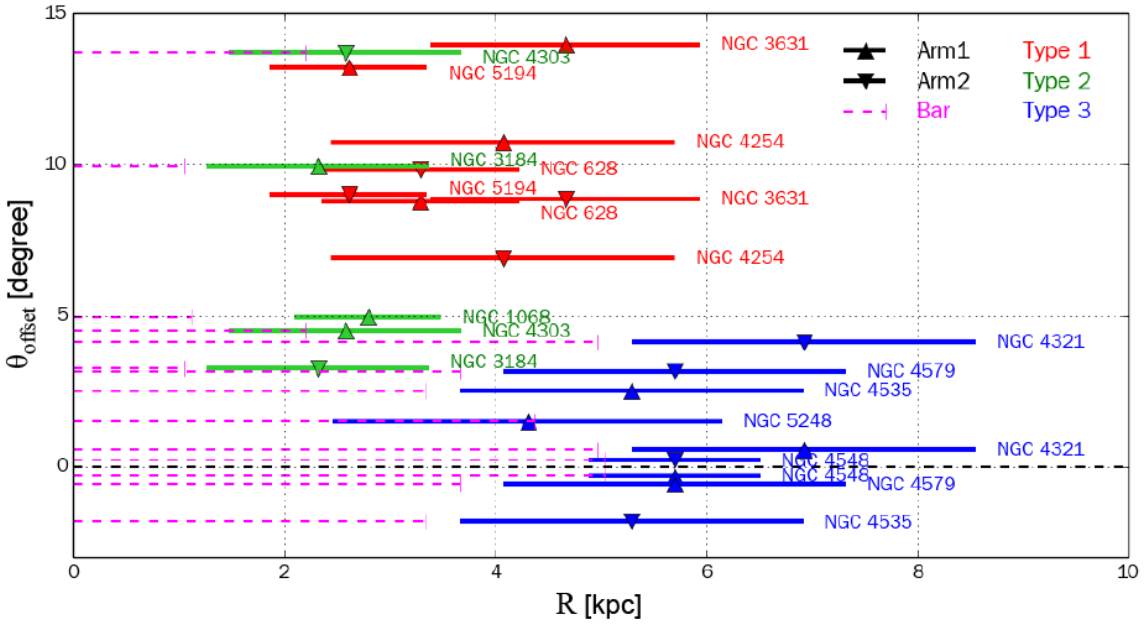

Figure 6.3: The relation between θ_{offset} and the radial regions in units of kiloparsec. The bar radii are shown with magenta dashed lines.

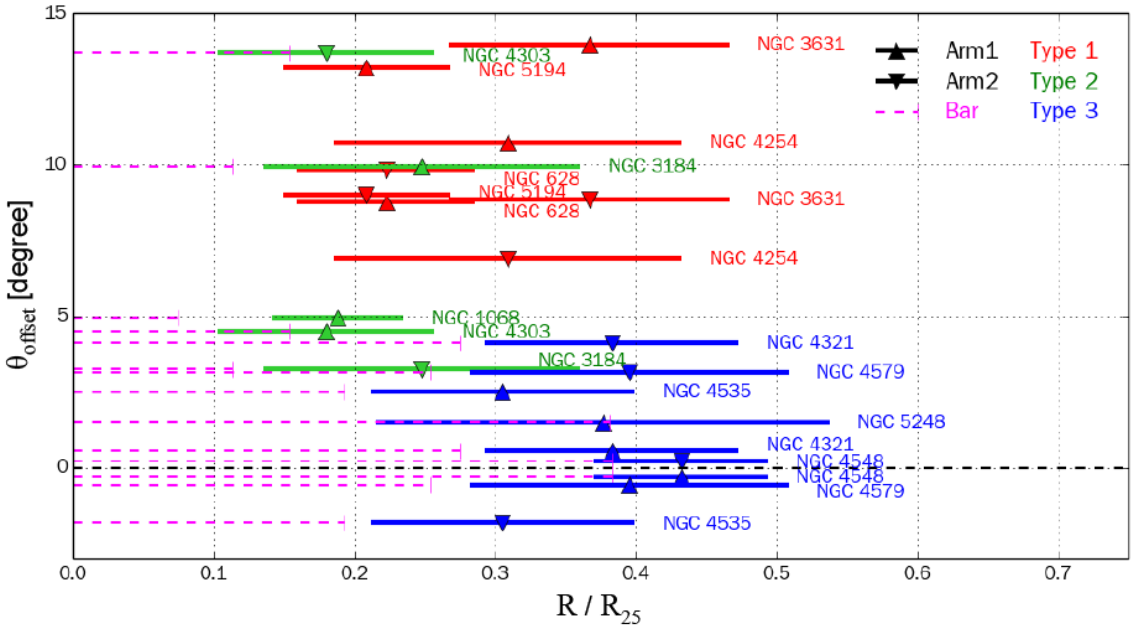

Figure 6.4: The relation between θ_{offset} and the radial regions normalized by the isophotal radii R_{25}. The bar radii normalized by the R_{25} are shown with magenta dashed lines.

6.2 Relation with Spiral Structure

In order to investigate the relationships between $\theta_{\rm offset}$ and the spiral structure, we have examined the pitch angle and arm strength. We summarize the results in Table 6.3.

6.2.1 Pitch Angle

We traced dust lanes by assuming that spiral arms have a constant pitch angle, i.e. a logarithmic spiral. The pitch angle (p) was calculated by the following equation with the constant b in equation (5.1).

$$p = \arctan b$$

The derived pitch angles of our sample galaxies are summarized in Table 6.3. The error represents the fitting error when tracing the dust lane in Section 5.1.3.

We show the relation between $\theta_{\rm offset}$ and the pitch angles in Figure 6.5. The average pitch angles of Type 1, 2, and 3 galaxies are 21°, 37°, and 25°, respectively. There seems to be no correlation between $\theta_{\rm offset}$ and the pitch angles, although some galaxies in Type 2 and Type 3 have a great difference of the pitch angle between two arms.

6.2.2 Arm Strength

We investigated the arm-interarm flux ratio in the K-band image as an indicator of the strength of the spiral arm. The K-band images of face-on galaxies serve as a tracer of the old stellar population which dominates the mass in the disk and allow a mapping of the azimuthal variation in the surface mass density (Rix & Rieke 1993). We used the K-band images from Knapen et al. (2003) except for NGC 5194 whose K-band image was obtained from the 2MASS. The images were sky subtracted, and bright foreground stars were masked. They were sampled in the same way as the polar coordinate transformation in Section 5.1.2. We derived the arm-interarm flux ratio ($I_{\rm arm/interarm}$) in each arm, which is defined in the following equation.

$$I_{\rm arm/interarm} = \frac{2\sum_{r=\mathrm{R_{min}}}^{\mathrm{R_{max}}} L(r,\theta_{\rm arm})}{\sum_{r=\mathrm{R_{min}}}^{\mathrm{R_{max}}} L(r,\theta_{\rm interarm1}) + \sum_{r=\mathrm{R_{min}}}^{\mathrm{R_{max}}} L(r,\theta_{\rm interarm2})}$$

$L(r,\theta)$ is the intensity at radius r and azimuth angle θ from the dust lane in the deprojected K-band image, i.e., $L(r,0)$ represents the intensity on the dust lane at the radius r. $\theta_{\rm arm}$ represents the θ when $\sum_{r=\mathrm{R_{min}}}^{\mathrm{R_{max}}} L(r,\theta)$ has the peak around the dust lane ($\theta = 0$). $\theta_{\rm interarm1}$ and $\theta_{\rm interarm2}$ represent the θ when $\sum_{r=\mathrm{R_{min}}}^{\mathrm{R_{max}}} L(r,\theta)$ takes the minimum on the both sides of the dust lane. $\mathrm{R_{max}}$ and $\mathrm{R_{min}}$ show the radial region where we traced dust lanes listed in Table 6.2. The values of $I_{\rm arm/interarm}$

are summarized in Table 6.3, and the relationship with $\theta_{\rm offset}$ is shown in Figure 6.6. We note that $L(r, \theta_{\rm arm})$ is affected by young stellar clusters, e.g., red supergiant clusters which are bright in near-infrared wavelengths. Therefore, the $I_{\rm arm/interarm}$ derived by our measurement should be overestimated.

Fourier transforms are an independent method for measuring arm amplitudes besides the arm-interarm flux ratio. We measured Fourier components for m = 2 by a one-dimensional discrete Fourier transformation. The Fourier component for m-mode was determined in the following equation.

$$F_m(r) = \frac{|\sum_{\theta=0}^{360-1} I(r,\theta)\exp(-2\pi i m\theta/360)|}{|\sum_{\theta=0}^{360-1} I(r,\theta)|}$$

$I(r, \theta)$ is the intensity at azimuth angle θ and radius r in the deprojected K-band image. In our definition, a spiral arm with an amplitude profile $I(\theta) = 1 + A\sin(m\theta)$ has a Fourier component for m-mode F_m equal to A/2. We derived the Fourier transform for m = 2 in each radius with the unit of arcsecond and calculated the average and standard deviation in the radial region where we traced dust lanes. The values of $F_{\rm m=2}$ are summarized in Table 6.3, and the relationship with $\theta_{\rm offset}$ is shown in Figure 6.7. The m = 2 component is the strongest for all galaxies. The standard deviations of some galaxies are large due to the fluctuation of $F_{m=2}(r)$ depending on the radius.

We see that $\theta_{\rm offset}$ has a negative correlation with both $I_{\rm arm/interarm}$ and $F_{\rm m=2}$. The average $I_{\rm arm/interarm}$ of Type 1, 2, and 3 galaxies are at 1.9, 2.1, and 2.9, respectively. On the other hand, the average $F_{\rm m=2}$ of Type 1, 2, and 3 galaxies are at 0.12, 0.14, and 0.21, respectively. This result shows that Type 3 galaxies, i.e., galaxies with relatively large bar structures, tend to have stronger m=2 spiral structures than the others. This trend is consistent with studies which have suggested that bars drive spiral density waves (e.g., Salo et al. 2010).

We note that our measurements with the K-band images have not worked well for some galaxies in Type 3. NGC 4579 has lower $I_{\rm arm/interarm}$ and smaller $F_{\rm m=2}$ than the others. We infer that this is because NGC 4579 has bright oval structure which increases the luminosity of the interarm regions. In addition, NGC 4321 and NGC 4548 have a great difference of $I_{\rm arm/interarm}$ between two arms. The high value of $I_{\rm arm/interarm}$ about 4 should be affected by young stellar clusters, because bright stellar clusters seem to be strongly concentrated on the arm.

Table 6.3: Properties of the spiral structure

Category	Galaxy	Pitch Angle[a] (°)		$I_{arm/interarm}$[b]		$F_{m=2}$[c]
	NGC	Arm1	Arm2	Arm1	Arm2	
Type 1	628	11.9 ± 0.2	13.3 ± 0.3	1.4	1.3	0.07 ± 0.02
	3631	18.1 ± 0.5	21.4 ± 1.5	2.2	2.1	0.06 ± 0.02
	4254	36.7 ± 0.4	32.4 ± 1.1	2.1	2.1	0.20 ± 0.08
	5194	16.0 ± 0.3	18.8 ± 0.3	1.6	2.1	0.16 ± 0.04
Type 2	1068	23.6 ± 0.5	...	1.6	...	0.07 ± 0.01
	3184	36.1 ± 0.7	24.8 ± 0.3	2.2	1.9	0.14 ± 0.04
	4303	53.6 ± 1.3	48.0 ± 0.8	2.5	2.4	0.21 ± 0.04
Type 3	4321	28.2 ± 0.9	25.7 ± 0.6	3.0	4.0	0.24 ± 0.14
	4535	25.3 ± 0.3	22.9 ± 0.4	2.8	2.9	0.19 ± 0.03
	4548	12.3 ± 1.3	28.4 ± 2.3	3.0	4.0	0.28 ± 0.04
	4579	19.9 ± 0.4	18.9 ± 0.4	1.4	1.5	0.10 ± 0.03
	5248	41.1 ± 0.5	...	3.4	...	0.24 ± 0.09

Notes.

[a] Pitch angle of the dust lane traced in the I − K color image.

[b] Arm-interarm flux ratio in the K-band image.

[c] Fourier transform for m = 2 in the K-band image.

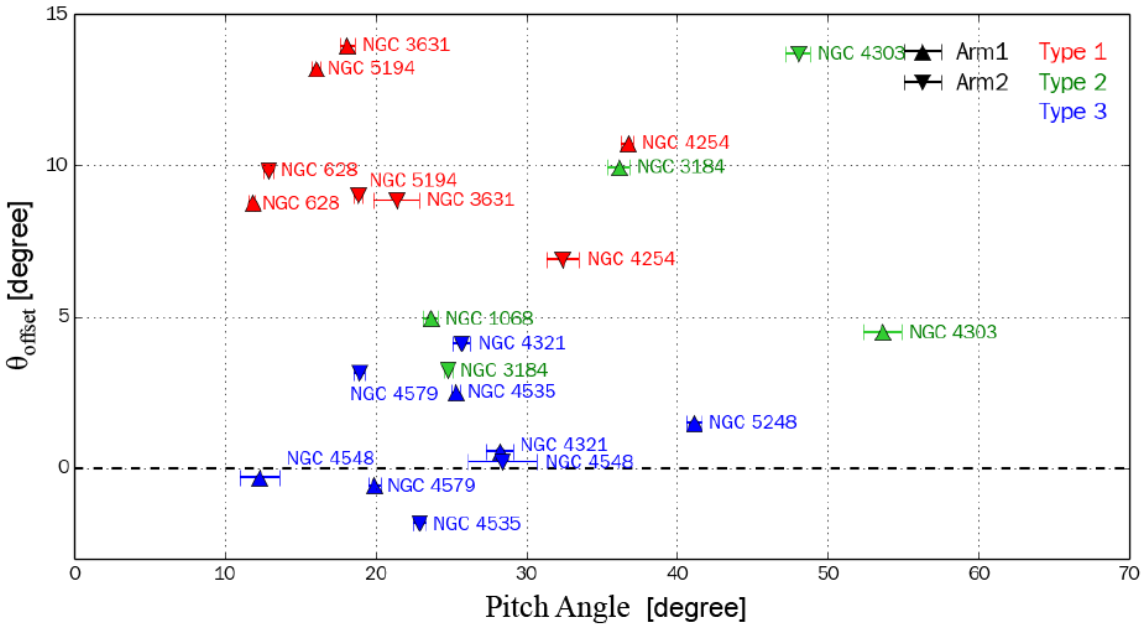

Figure 6.5: The relation between θ_{offset} and the pitch angles.

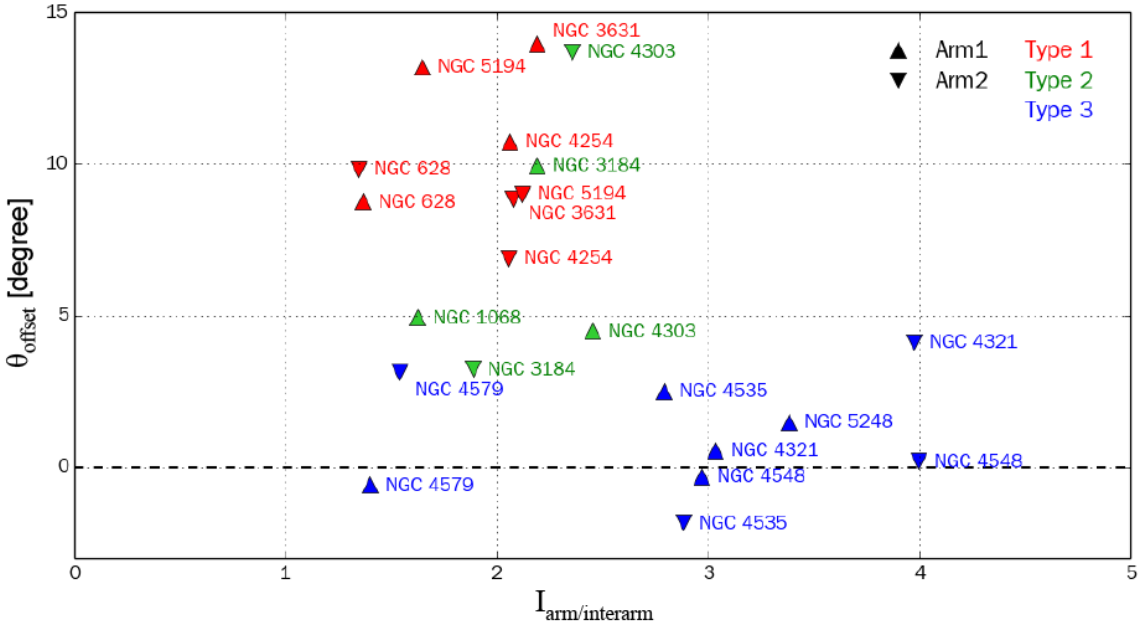

Figure 6.6: The relation between θ_{offset} and the arm/interarm flux ratio in the K-band image.

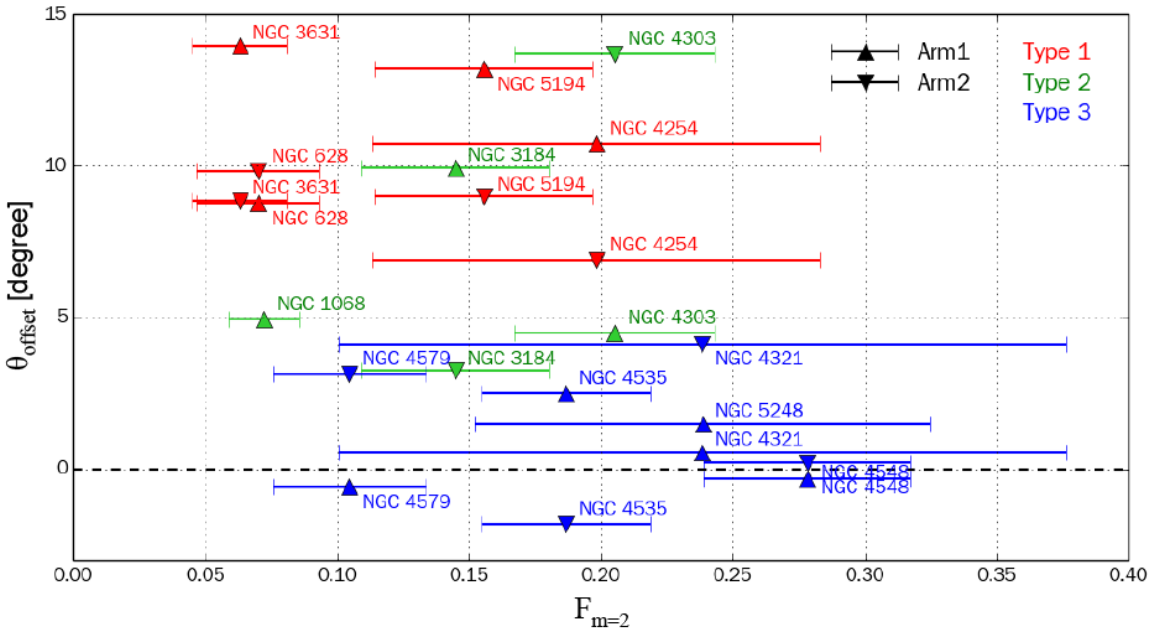

Figure 6.7: The relation between θ_{offset} and the Fourier transform for m = 2.

Chapter 7

Discussions

7.1 Comparison with the Results of E09

Seven of 12 sample galaxies are included in the sample of E09. We compared our results with those of E09.

7.1.1 Comparison with the Classification of E09

E09 classified their sample galaxies into three categories as follows:

C : galaxies with clear offsets between CO and Hα, i.e., $t_{SF} > 0$ and $\Delta\Omega_P/\Omega_P \lesssim 1$.

N : galaxies with no offsets although they have clear spiral structures.

A : galaxies with ambiguous offsets. i.e., $t_{SF} < 0$ or $\Delta\Omega_P/\Omega_P \gtrsim 1$.

We summarize the relation between their and our classifications in our sample galaxies in Table 7.1. In seven galaxies, four galaxies are classified as "C", two galaxies as "N", and one galaxy as "A". "C" galaxies include three Type 1 galaxies (NGC 628, NGC 4254, and NGC 5194) and one Type 2 galaxy (NGC 4303). "A" galaxy corresponds with one Type 2 galaxy (NGC 3184). "N" galaxies correspond with two Type 3 galaxies (NGC 4321 and NGC 5248).

"C" and "A" galaxies with positive offsets between CO and Hα are consistent with Type 1 and 2 galaxies that star forming regions with strong Hα emission tend to be located downstream of dust lanes. We do not discriminate "A" from "C" because the angular offsets are not necessarily described as a linear function of Ω_{gas} by assuming that t_{SF} is constant. On the other hand, "N" galaxies without offsets between CO and Hα are consistent with Type 3 galaxies that star forming regions with strong Hα emission tend to be concentrated on dust lanes. We newly found three "N" galaxies (NGC 4535, NGC 4548, and NGC 4579) in addition to two "N" galaxies (NGC 4321 and NGC 5248) in E09.

Table 7.1: Relation with the classification of E09

Galaxy	Category		Galaxy	Category	
NGC	This work[a]	E09[b]	NGC	This work[a]	E09[b]
628	Type 1	C	4321	Type 3	N
3631	Type 1	...	4535	Type 3	...
4254	Type 1	C	4548	Type 3	...
5194	Type 1	C	4579	Type 3	...
1068	Type 2	..	5248	Type 3	N
3184	Type 2	A			
4303	Type 2	C			

Note.

[a] "Type 1" galaxies without bar structure. "Type 2" galaxies with bar structure of the radii smaller than 3 kpc. "Type 3" galaxies with bar structure of the radii larger than 3 kpc.

[b] "C" galaxies with clear offsets between CO and Hα. "N" galaxies with no offsets. "A" galaxies with ambiguous offsets.

7.1.2 Reasons for No Offsets

E09 mentioned several possible reasons for no offsets: (1) material arms (i.e., non-stationary spiral structure), (2) corotation resonance, and (3) elliptical orbits nearly parallel to the spiral arms.

In the case of NGC 4321, they suggested that (1) would be the most plausible reason because the offsets were found in the region close to the bar where orbits should have larger ellipticity than in the arm region. In addition, the radial region where offsets were measured was within the corotation radii estimated by previous studies. On the other hand, in the case of NGC 5248, they suggested that (3) can partially explain the reason for no offsets because Yuan & Yang (2006) showed strong inward streaming motions along the spiral arms up to the radius of about 70″ assuming that the disk is predominantly driven by a large-scale bar found by Jogee et al. (2002).

Considering the properties of Type 3 galaxies with relatively large bar structures, we suggest that (2) and (3) may explain no offsets. Especially, (2) may explain no offsets outside the bar region, while (3) can explain no offset within the bar region in NGC 5248.

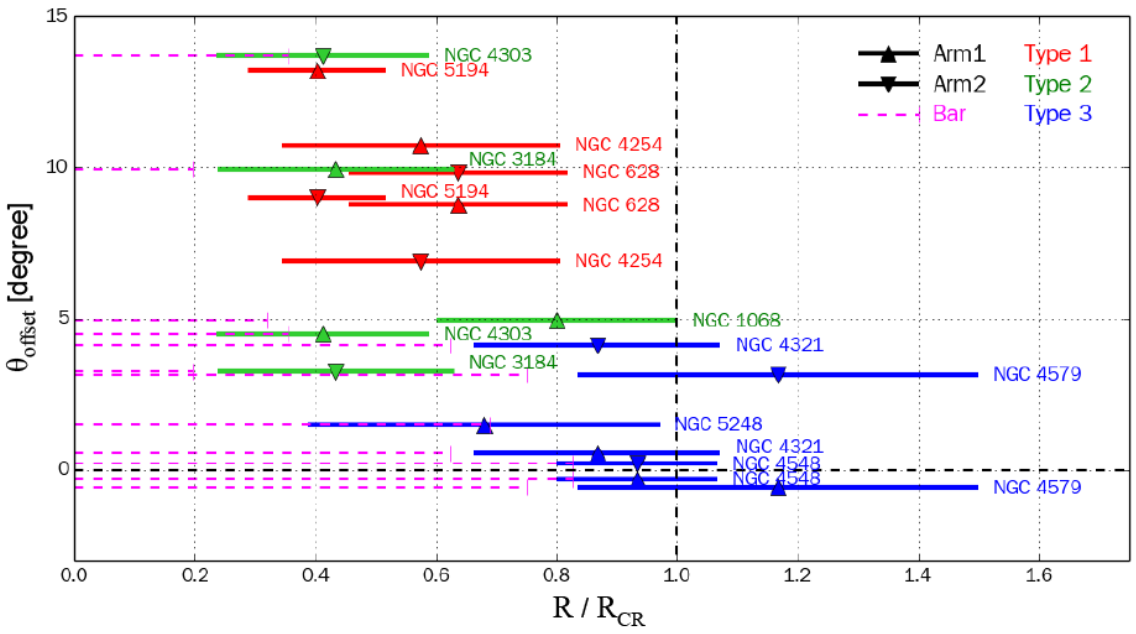

Figure 7.1: The relation between $\theta_{\rm offset}$ and the radial regions normalized by the corotation radii R_{CR} for our sample galaxies except for NGC 3631 and NGC 4535. The R_{CR} are from Table 7.2.

7.2 Relation with Corotation Radius

We investigated the relation between corotation radii and the radial regions we traced dust lanes. The corotation radii (R_{CR}) of our sample galaxies have been investigated in previous studies except for NGC 4535. We summarize the values of R_{CR} in Table 7.2. It also contains the values of Ω_P if they have been derived. We show the relation between $\theta_{\rm offset}$ and the radial regions normalized by R_{CR} except for NGC 3631 and NGC 4535 in Figure 7.1. We excluded NGC 3631 with $R_{CR} = 42''$ $\pm$ $5''$ from Fridman et al. (2001) because we found positive offsets outside the R_{CR}. In this figure, we adopted the value of R_{CR} marked with an asterisk in Table 7.2. The R_{CR} we adopted were limited to the values measured observationally. In addition, we preferentially chose the R_{CR} that Ω_P has been also measured. Otherwise, we chose the R_{CR} which was the nearest to the average.

We found a negative correlation between $\theta_{\rm offset}$ and R/R_{CR}. Both of the average R/R_{CR} of Type 1 and Type 2 galaxies are $0.4 - 0.7$ respectively. On the other hand, the average R/R_{CR} of Type 3 galaxies is $0.7 - 1.2$. In addition, the average R_{bar}/R_{CR} of Type 2 and Type 3 galaxies are about 0.3 and 0.8, respectively. This result suggests that it is difficult to detect clear offsets for galaxies with $R_{bar}/R_{CR} \gtrsim 0.6$ because they have the arms near the corotation resonance.

7.3 Comparison with Star Forming Regions Predicted by Rotation Curve and Ω_P

The reason for no offsets in Type 3 galaxies may be explained by the effect of corotation resonance. We investigated whether the distribution of star forming regions traced by Hα emission is consistent with that of star forming regions predicted by the rotation curve and Ω_P.

7.3.1 Results of Individual Galaxies

Both R_{CR} and Ω_P have been measured in previous studies in eight out of 12 sample galaxies. We could derive almost the same R_{CR} as the previous studies by using the rotation curves and Ω_P in four out of eight galaxies. We predicted positions of stellar clusters with the ages of 10 Myr assuming that they were born in the dust lanes and rotate in a circular orbit. Then, we compared the positions with the distribution of Hα emission.

We show the results for four galaxies (NGC 628, NGC 4321, NGC 4579 and NGC 5194) in Appendix D, in Figure D.1 − D.4. The top right panels show the relation between the rotation curve (red filled circle and solid line) and Ω_P (red dashed line). The rotation curves have been obtained from either Sofue et al. (1999) or Daigle et al. (2006). Sofue et al. (1999) presented high-resolution central-to-outer rotation curves from optical (Hα and [NII]) and radio (CO and HI) observations[*1]. On the other hand, Daigle et al. (2006) presented rotation curves of a part of the SINGS sample from observations of Hα emission with the Fabry-Perot of New Technology for the Observatoire du mont Mégantic (FaNTOmM)[*2]. We display the estimated positions of stellar clusters with the ages of 10 Myr by using magenta lines on the deprojected continuum-subtracted Hα images in the top left and bottom panels.

NGC 628 (M74)

This galaxy is classified as Type 1. Both of the rotation curve and Ω_P = 31 km/s/kpc were referred from Fathi et al. (2007). We adopted the same distance of 9.7 Mpc as Fathi et al. (2007). The R_{CR} was estimated at 107″ from the rotation curve and Ω_P. The arms we traced are located in the radial region of 50″ − 90″ which is inside of the corotation radius. In Figure D.1, magenta lines show the estimated positions of stellar clusters with the ages of 10 Myr. There exist many young stellar clusters with Hα emission downstream of magenta lines. It is difficult to consider that such clusters were born in the dust lanes, but this tendency is consistent with E09 that esti-

[*1] http://www.ioa.s.u-tokyo.ac.jp/~sofue/RC99/rc99.htm

[*2] http://www.astro.umontreal.ca/fantomm/sings/rotation_curves.htm

mated the t_{SF} at 28.2 ± 3.1 Myr, which is more than twice as large as t_{SF} of other galaxies in E09. We infer that such clusters were formed downstream of the dust lanes, or some parameters (e.g., rotation curve, Ω_P, i, PA) are not correct. We note that our parameters (i = 24° and PA = 11.8°) are different from Fathi et al. (2007) (i = 6.5° and PA = 19°). We confirmed that θ_{offset} does not substantially change, even if we adopt the same i and PA as Fathi et al. (2007).

NGC 4321 (M100)

This galaxy is classified as Type 3. The Ω_P was measured at 31 km/s/kpc in Canzian & Allen (1997). We adopted the rotation curve from Sofue et al. (1999), because the rotation curve used by Canzian & Allen (1997) was not available. The R_{CR} was estimated at 98″ from the rotation curve and Ω_P. The R_{CR} is the same as Canzian & Allen (1997), although our distance of 16.8 Mpc is slightly different from their distance of 17.1 Mpc. The arms we traced are located in the radial region of 65″ − 105″ which includes the corotation radius. In Figure D.2, magenta lines show the estimated positions of stellar clusters with the ages of 10 Myr. Most of the star forming regions with strong Hα emission are concentrated on the dust lanes in both arms, which is consistent with the distribution predicted by the magenta lines. The transition of θ_{offset} across the corotation radius is unclear, but Hα emission seems to be weak around the $R_{CR} \simeq 98''$ in Arm 2. We note that our parameters (i = 27° and PA = 146°) are slightly different from Canzian & Allen (1997) (i = 28° and PA = 153°). We confirmed that the tendency of no offsets does not change, even if we adopt the same parameters as Canzian & Allen (1997).

NGC 4579 (M61)

This galaxy is classified as Type 3. The Ω_P was measured at 50 km/s/kpc in García-Burillo et al.(2009). We used the rotation curve from Daigle et al. (2006), because the rotation curve used by García-Burillo et al.(2009) was not available. The R_{CR} was estimated at 61″ from the rotation curve and Ω_P. The R_{CR} is consistent with García-Burillo et al.(2009), although our distance of 16.8 Mpc is slightly different from their distance of 19.8 Mpc. The arms we traced are located in the radial region of 50″ − 90″ which includes the corotation radius. In Figure D.3, magenta lines show the estimated positions of stellar clusters with the ages of 10 Myr. The star forming regions located on the dust lanes are consistent with the distribution predicted by the magenta lines. However, the transition of θ_{offset} across the $R_{CR} \simeq 60''$ is unclear. In addition, star forming regions are distributed symmetrically with respect to the dust lanes. We note that our parameters (i = 45.7° and PA = 89.5°) are slightly different from García-Burillo et al.(2009) (i = 36° and PA = 95°). We confirmed that the tendency of no offsets does not change, even if we adopt the same parameters as García-Burillo et al.(2009).

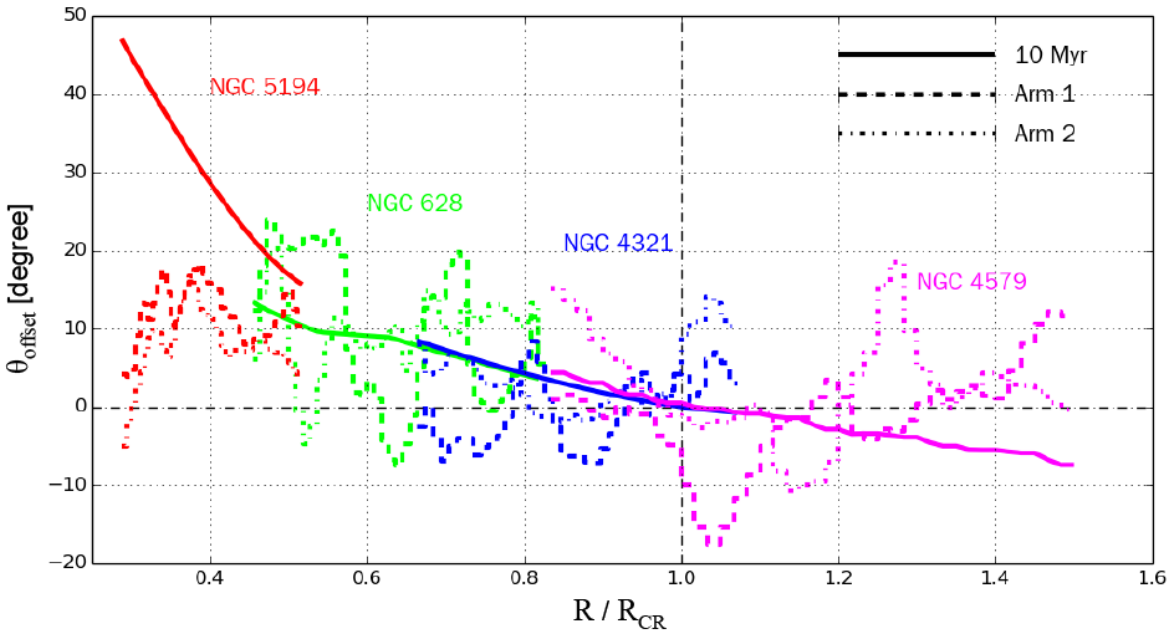

Figure 7.2: The radial dependence of the offsets for NGC 628, NGC 4321, NGC 4579 and NGC 5194. The solid lines show the estimated azimuthal offsets of stellar clusters with the ages of 10 Myr assuming that they were born in the dust lanes and rotate in a circular orbit. The dashed and dash-dotted lines show the $\theta_{\rm offset}(r)$ in each arm.

NGC 5194 (M51)

This galaxy is classified as Type 1. E09 measured the $\Omega_{\rm P}$ at 31 km/s/kpc with the rotation curve from Sofue et al. (1999). We adopted the $\Omega_{\rm P}$ and rotation curve, and used their distance of 9.6 Mpc instead of 7.7 Mpc listed in Table 4.1. The $R_{\rm CR}$ was estimated at 171″ from the rotation curve and $\Omega_{\rm P}$. The arms we traced are located in the radial region of 50″ − 90″ which is inside of the corotation radius. In Figure D.4, magenta lines show the estimated positions of stellar clusters with the ages of 10 Myr. We used the same parameters (i = 20° and PA = 22°) as E09. The star forming regions seem to be consistent with the distribution predicted by the magenta lines.

7.3.2 Radial Dependence of Offsets

We show the radial dependence of the offsets for four galaxies in Figure 7.2. The solid lines show the estimated azimuthal offsets of stellar clusters with the ages of 10 Myr. If the rotation speed is constant within the radial region where we traced dust lanes, the azimuthal offset is inversely proportional to $R/R_{\rm CR}$. The dashed and dash-dotted lines show the $\theta_{\rm offset}(r)$ in each arm. The offset estimated from rotation curves and $\Omega_{\rm P}$ is less than 10° at $R/R_{\rm CR} \gtrsim 0.6$, which is not large enough to be detected clearly in comparison with the fluctuation of the $\theta_{\rm offset}(r)$. This

result suggests that it is be difficult to detect clear offsets for Type 3 galaxies with bar structure of $R_{bar}/R_{CR} \gtrsim 0.6$ because the arms are located near the corotation resonance. On the other hand, elliptical orbits nearly parallel to the spiral arms may also affect the amount of offsets in Type 3 galaxies, because an unbarred galaxy NGC 628 has larger offsets than a barred galaxy NGC 4321 at $R/R_{CR} \gtrsim 0.6$. In either case of corotation resonance and elliptical orbits, larger offsets are expected between gas arms and older stellar populations (e.g., Dobbs & Pringle 2010, Hirota et al. 2014). Therefore, we need other methods to trace older star formation histories than Hα emission (i.e., 10 Myr) in order to find evidence for the density wave in Type 3 galaxies.

Table 7.2: Ω_P and R_{CR} from previous studies

NGC	Authority	Ω_P (km/s/kpc)	R_{CR} ($''$)	Method	Data
628	Elmegreen et al.(1992)	...	141	Morphology	B
	Fathi et al.(2007)	31^{+5}_{-3}	110^{a*}	SFE	HI, Hα
	Egusa et al.(2009)	16 ± 3	54 − 114	Offset	CO, Hα
	Martínez-García & Puerari (2014)	41.8 ± 1	89 ± 2	Phase-shift	CO, 24μm
1068	Rand & Wallin (2004)	72	50*	TW	CO
3184	Tamburro et al.(2008)	38 ± 5	127* ± 28	Offset	HI, 24μm
3631	Fridman et al.(2001)	...	42 ± 5	Kinematics	HI, Hα
4254	Elmegreen et al.(1992)	...	87*	Morphology	B
	Kranz et al.(2001)	20	77 ± 11	Simulation	K, Hα
	Egusa et al.(2009)	10 ± 3	60 − 78	Offset	CO, Hα
	Buta & Zhang (2009)	...	91^{b}	Phase-shift	H
4303	Rautiainen et al.(2008)	...	89.1 ± 8.5	Simulation	H
	Egusa et al.(2009)	24 ± 29	$\gtrsim 36$	Offset	CO, Hα
	Buta & Zhang (2009)	...	85^{b*}	Phase-shift	H
4321	Elmegreen et al.(1992)	...	118	Morphology	B
	Canzian & Allen (1997)	31	98* ± 10	Kinematics	Hα
4535	...	...	...	...	...
4548	Rautiainen et al.(2008)	...	95.2 ± 11.9	Simulation	H
	Buta & Zhang (2009)	...	75^{b*}	Phase-shift	H
4579	Rautiainen et al.(2008)	...	71.1 ± 8.4	Simulation	H
	Buta & Zhang (2009)	...	81^{b}	Phase-shift	H
	García-Burillo et al.(2009)	50 ± 10	60* ± 10	Bar length	CO, HI, K
5194	Elmegreen et al.(1992)	...	132	Morphology	B
	Egusa et al.(2009)	31 ± 5	$174^{*\ +12}_{-24}$	Offset	CO, Hα
	Martínez-García & Puerari (2014)	23.7 ± 0.5	202 ± 3	Phase shift	CO, 24μm
5248	Elmegreen et al.(1992)	...	103*	Morphology	B
	Jogee et al.(2002)	...	115^{c}	Bar length	R, K
	Buta & Zhang (2009)	...	70^{b}	Phase-shift	H

Note.

* R_{CR} adopted for this work.

[a] R_{CR} is from Cepa & Beckman (1990).

[b] Buta & Zhang (2009) derived multiple R_{CR}. We adopted the R_{CR} closest to those of other studies.

[c] R_{CR} is estimated by the relational expression (R_{CR}/R_{bar}=1.2±0.2) from Athanassoula (1992).

Chapter 8

Summary of Part I

We investigated the difference of offsets between gas arms and star forming regions in 12 nearby spiral galaxies with two prominent spiral arms. This method has been applied to a number of galaxies in previous studies, but it depends on tracers of gas and galaxies whether the offsets predicted by the density wave theory are observed. We traced dust lanes as a sign of molecular gas with I−H or I−K color images whose resolution is higher than that of radio data used by previous studies. We selected 11 galaxies capable of extracting dust lanes from an optical and near-infrared imaging survey of 57 nearby spiral galaxies by Knapen et al. (2003) besides NGC 5194 with the HST data.

We measured $\theta_{\rm offset}$ which is the average position of the Hα emission intensity with respect to dust lanes within the azimuth angle from -50° to $+50^\circ$. We found that the bar structure is related to the offset. We classified 12 galaxies into three types based on the bar structure. (Type 1;) galaxies without bar structure (NGC 628, NGC 3631, NGC 4254, and NGC 5194). (Type 2;) galaxies with bar structure of the radii smaller than 3 kpc (NGC 1068, NGC 3184, and NGC 4303). (Type 3;) galaxies with bar structure of the radii larger than 3 kpc (NGC 4321, NGC 4535, NGC 4548, NGC 4579, and NGC 5248). The average values of $\theta_{\rm offset}$ for Type 1, 2, and 3 galaxies were 10°, 7° and 1°, respectively. Type 3 galaxies with no offsets tended to have the arms farther from the center and have stronger m=2 spiral structures than the others.

Seven of 12 galaxies were included in the sample of E09, which have investigated the offsets between molecular clouds and star forming regions. Our results were consistent with those of E09. We newly found three galaxies with no offsets in addition to two galaxies in E09. Considering the properties of Type 3 galaxies, there is a possibility that the reason for no offsets can be explained by the effects of corotation resonance and elliptical orbits nearly parallel to the spiral arms. In order to test the density wave theory in Type 3 galaxies, we need other methods to trace older star formation histories than Hα emission (i.e., 10 Myr).

Part II

The Distributions of Young and Old Stellar Clusters in NGC 4321

Chapter 9

Introduction of Part II

In Part II, we verify the density wave theory in NGC 4321 with high resolution imaging data. In the density wave theory for quasi-stationary spiral structures, sequential stellar age gradient across the spiral arm is predicted as illustrated in Figure 9.1 (Dobbs & Pringle 2010). On the other hand, in the recent theoretical studies for non-stationary spiral structures, sequential stellar age gradient across spiral arms is not predicted as illustrated in Figure 9.2 (Grand et al. 2012b).

NGC 4321 is considered to be a representative galaxy against the density wave theory. E09 and Part I suggested that the spiral arms show no offsets between molecular gas arms and star forming regions. In addition, Ferreras et al. (2012) found no offsets between HII regions and UV star-forming sources with the ages over 100 Myr. These results seem to strongly support that this galaxy has non-stationary spiral structure. However, in Part I, we suggested that the effects of corotation resonance and elliptical orbits nearly parallel to the spiral arms may explain no offsets between molecular gas arms and star forming regions. In addition, since Ferreras et al. (2012) used unresolved stellar cluster complexes, it is worth testing the density wave with resolved stellar clusters. The southern spiral arm has been observed using the HST with multiband filters including Hα. We can detect resolved stellar clusters and investigate the difference between the distributions of young and old stellar clusters.

In this part, we explain the advantages of this work in comparison with Ferreras et al. (2012) in Chapter 10. We use the imaging data obtained with the HST Wide Field Camera 3 (WFC3) and Wide Field and Planetary Camera 2 (WFPC2). The details of the data and the analysis are described in Chapter 11 and Chapter 12. We investigate the age distributions of young and old stellar clusters in Chapter 13. The results are discussed in Chapter 14. Then, we give a summary in Chapter 15.

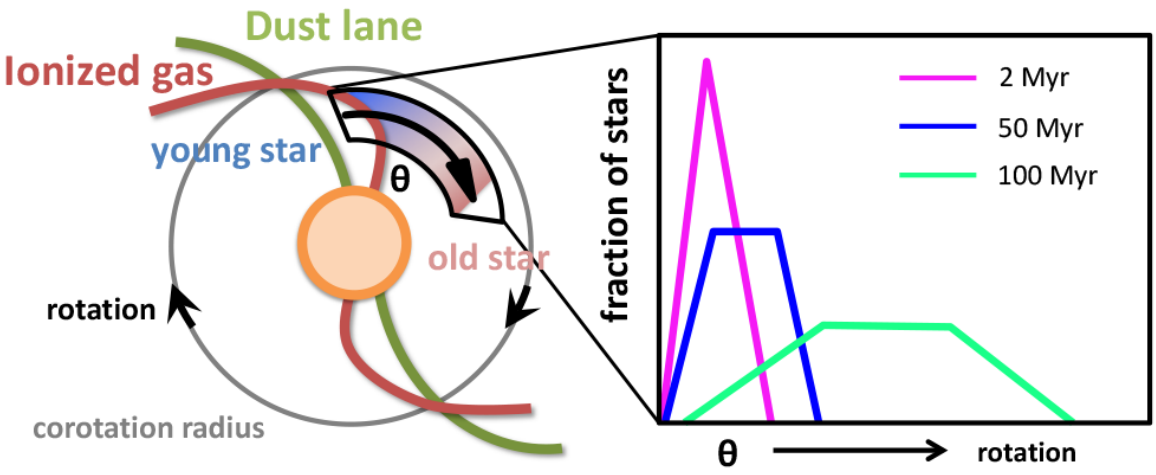

Figure 9.1: *(Left);* The positions of dust lanes, ionized gas and young/old stars in a spiral disk predicted by the density wave theory. *(Right);* A schematic view of the predicted distributions of stars with given ages against the angular distance across a spiral arm (for more details, see Figure 4 of Dobbs & Pringle 2010).

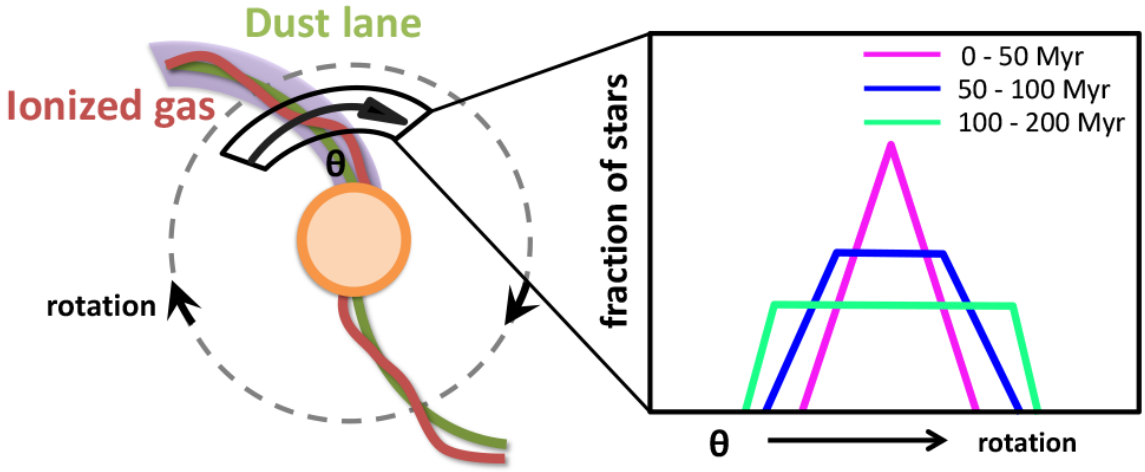

Figure 9.2: *(Left);* The positions of dust lanes, ionized gas and young/old stars in a spiral disk predicted by the recent time-dependent multi-dimensional numerical simulations of spiral structures. *(Right);* A schematic view of the predicted distributions of stars with given ages against the angular distance across a spiral arm (for more details, see Figure 21 of Grand et al. 2012b).

Chapter 10

Approach

Ferreras et al. (2012, hereafter F12) investigated the offset between a very young component (an HII region) and an older component (a UV star-forming source) with deep UV imaging data which can trace stellar populations with the ages over 100 Myr. However, they gave negative evidence for density wave spirals. Here, after a brief description of F12, we describe the arm region where the offsets are predicted and the importance of high resolution imaging.

10.1 Brief Description of F12

F12 used the UV imaging data taken with the Ultra-Violet/Optical Telescope (UVOT) on board the Swift spacecraft (Gehrels et al. 2004). It has a 30 cm Ritchey-Chrétien telescope with micro-channel plate intensified charge coupled device detectors that record the arrival time of individual photons and provide sub-arcsecond positioning of sources (Roming et al. 2005). They used images obtained with three filters of UVW1, UVM2, and UVW2. The λ_c [nm]/ FWHM [nm] are 251/70, 217/51, and 188/76 for UVW1, UVM2, and UVW2 respectively. The FWHM of the point spread function (PSF) are $2''.4$, $2''.5$, and, $2''.9$ (Breeveld et al. 2010). The total exposure times are 9.74 ks, 11.95 ks, and 21.28 ks. They also used the Hα imaging data from the SINGS.

They detected 787 sources on the UVW2 image by Sextractor (Bertin & Arnouts 1996). We show the detected UVW2 sources with crosses in Figure 10.1. The catalog of the sources was downloaded through the VizieR[*1]. They divided sources by Hα luminosity L^0_α, which was defined by the equation $\log L^0_\alpha$ (erg s^{-1}) $\equiv 37.9 - 0.4 \times (\mathrm{UVW2}_{AB} - 20)$ with the Hα and UVW2 imaging data. The blue crosses show sources of Hα luminosity $L^0_\alpha > 0$ (young population), and the red crosses show sources of Hα luminosity $L^0_\alpha < 0$ (old population). They traced three arms, which

[*1] http://vizier.nao.ac.jp/viz-bin/VizieR?-source=J/MNRAS/424/1636

are shown by green solid lines in the left panel of Figure 10.1, based on detected sources. They compared the distributions of young and old sources within ± 2 kpc from the traced arms shown by green dashed lines. The thick solid ellipse shows the corotation radius R_{CR} = 98″ (Canzian & Allen 1997). The dashed ellipses have the deprojected radii of h and 1.5h, where h is the scale length of the disk, i.e., h = 83″.4 (Kodaira et al. 1986). They chose two radial areas of R < h and R > 1.5h to investigate the distributions of stellar populations with different ages.

They also used the Sloan Digital Sky Survey (SDSS) u, g, r, i, z-band images, and the Spitzer/IRAC 3.6, 4.5, 5.8, 8 μm images. They compared the distributions of young and old sources by dividing sources with UVW2 − SDSS g color and age of a young population derived from the model fitting of the NUV/optical/IR photometry, in addition to the Hα luminosity L_{α}^{0}. They found no significant offsets in three cases (see the right panel of Figure 11 in F12).

10.2 Arm Region where Offsets Are Predicted

In Part I, we estimated positions of stellar clusters with the ages of 10 Myr from rotation curves and Ω_P. Here, we show the arm regions where the offsets between young and old stellar populations are predicted.

We traced two dust lanes with an I − K color image in Part I. In the right panel of Figure 10.1, we show the dust lanes with green lines. We estimated positions of stellar clusters with the age of 10 Myr and 100 Myr assuming that they were born in the dust lanes and rotate in a circular orbit. The rotation curve from Sofue et al. (1999) and the Ω_P = 31 km/s/kpc from Canzian & Allen (1997) were used for the calculation. From here on we refer to the estimated age as "kinematic age". We show the estimated positions of stellar clusters with the kinematic age of 10 Myr and 100 Myr with magenta and cyan lines, respectively. We adopted an inclination of 27° and a position angle of 146° (Sofue et al. 1999) instead of an inclination of 38° and a position angle of 151° (Chemin et al. 2006) which were adopted by F12. The dashed ellipses show the region of the deprojected radii from 65″ to 105″, where we traced dust lanes. We see that the areas, where the distribution of the stellar clusters younger than 100 Myr is predicted, are small in comparison with those investigated by F12. Therefore, in this work, we investigate arm regions close to the dust lanes in order to verify the density wave theory accurately.

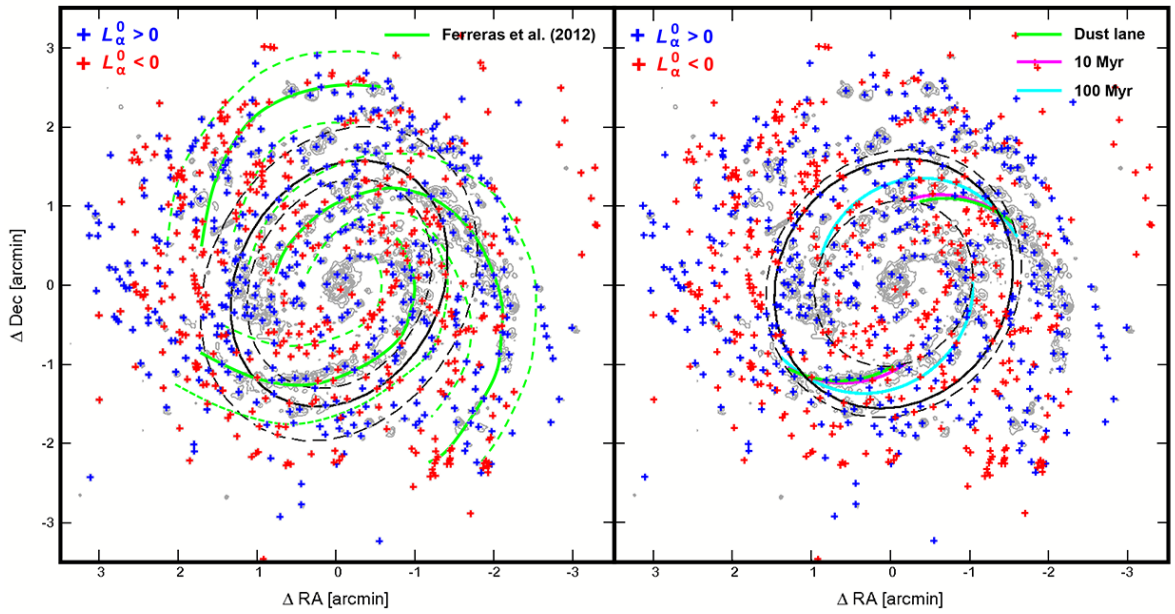

Figure 10.1: The comparison of arm regions between F12 (left panel) and this work (right panel). The crosses indicate sources detected with the UVW2 image in F12. The blue crosses show sources of Hα luminosity $L_\alpha^0 > 0$ (young component), and the red crosses show sources of Hα luminosity $L_\alpha^0 < 0$ (old component). The L_α^0 is defined by the equation $\log L_\alpha^0$ (erg s^{-1}) $\equiv 37.9 - 0.4 \times (\mathrm{UVW2}_{AB} - 20)$. The contour map shows the Hα image from the SINGS. *(Left);* The green lines show three arms traced by F12. The green dashed lines show the positions of ± 2 kpc from the arms. We note that their positions were roughly traced from Figure 10 in F12. They chose two radial areas of R < h and R > 1.5h to compare the distributions of young and old sources (h is the scale length of the disk from Kodaira et al. 1986, i.e., $h = 83''.4$). The dashed ellipses show the deprojected radii of R = h and R = 1.5h. The thick solid ellipse shows $\mathrm{R_{CR}} = 98''$ (Canzian & Allen 1997). They adopted an inclination of 38° and a position angle of 151° (Chemin et al. 2006). *(Right);* The dust lanes we traced in Part I are shown with green lines, and the estimated positions of stellar clusters with given ages are shown with magenta and cyan lines. We used a rotation curve from Sofue et al. (1999) and a pattern speed of Ω_P = 31 km/s/kpc from Canzian & Allen (1997) to calculate their positions. The thick solid ellipse shows $\mathrm{R_{CR}} = 98''$ (Canzian & Allen 1997). The dashed ellipses show the region of the deprojected radii from 65″ to 105″, where we traced dust lanes in Part I. We adopted an inclination of 27° and a position angle of 146° (Sofue et al. 1999).

10.3 Importance of High Resolution Imaging

To investigate the effect of angular resolution, we constructed the same UVW2 image as F12. We downloaded the data through the MAST[*1]. The details of the data are summarized in Table 1 of F12. We combined the images into one frame with the total exposure time of 21.28 ks. We

[*1] https://archive.stsci.edu/

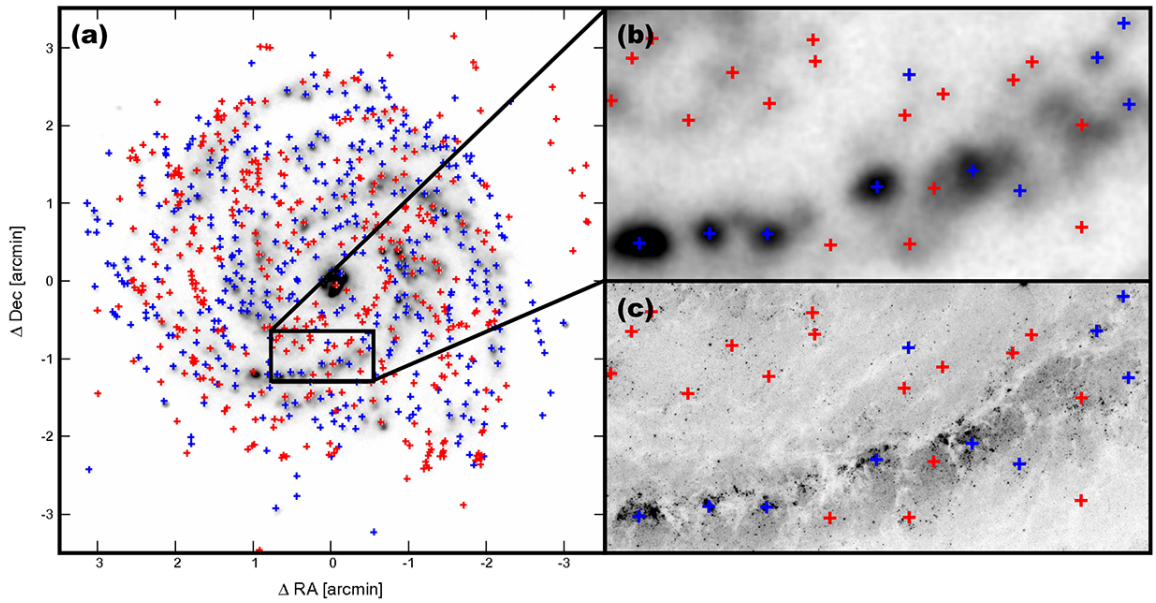

Figure 10.2: The comparison between the UV image used by F12 and the HST V-band image used by this work. (a) The Swift/UVOT UVW2 image. The blue crosses show sources of Hα luminosity $L_\alpha^0 > 0$ (young component), and the red crosses show sources of Hα luminosity $L_\alpha^0 < 0$ (old component). (b) The enlarged image of the southern spiral arm shown by a black rectangle in (a). The image size is $80'' \times 40''$. (c) The HST WFC3/UVIS F555W image which shows the same region as (b).

show the UVW2 image in Figure 10.2 (a) and the enlarged image of the southern arm in Figure 10.2 (b). On the other hand, we display the HST WFC3 UVIS F555W image (Section 11.2.1) in Figure 10.2 (c).

In Figure 10.2, we plotted the young (blue cross) and old (red cross) sources which were divided by Hα luminosity in F12. Comparing Figure 10.2 (b) and (c), we see that there are a number of small sources in the sources detected by F12. The angular resolution of $2''.5$ FWHM of the UV image used by F12 corresponds to the physical size of about 200 pc in NGC 4321 assuming the distance of 16.8 Mpc (Tully 1988). The size is not suitable for the detection of resolved stellar clusters considering that the median effective radius ($R_{\rm eff}$) of stellar clusters is 2.1 pc in NGC 5194 (Scheepmaker et al. 2007) and 2.5 pc in NGC 5236 (Ryon et al. 2015). Therefore, in this work, we use the HST imaging data with the angular resolution of $0''.04$ ($\sim$ 3 pc) to detect resolved stellar clusters and investigate the difference between the distributions of young and old stellar clusters.

Chapter 11

Galaxy & Data

11.1 NGC 4321

NGC 4321 (M100) is a face-on late-type spiral galaxy classified as the Hubble class SAB(s)bc. It is located at RA = 12h 22m 54.8s, Dec = +15° 49′ 19″ according to NED. We adopted an inclination of 27° and a position angle of 146° from Sofue et al. (1999). The angular scale is estimated at 81.4 pc arcsec^{-1} assuming the distance of 16.8 Mpc (Tully 1988).

11.2 HST WFC3/UVIS and WFPC2 Data

We used the imaging data obtained with the HST WFC3/UVIS F555W (V) filter and WFPC2 F336W (U), F439W (B), F555W (V), F675W (R), F814W (I) and F658N (Hα) filters. We retrieved the data through the Hubble Legacy Archive (HLA)[*1]. We show the properties of the data in Table 11.1 and the observation fields in the left panel of Figure 11.1.

11.2.1 WFC3/UVIS

The WFC3 (Dressel 2015) is a fourth generation imaging instrument which was installed on the HST in May 2009. The UVIS is the UV/optical channel of WFC3, which covers wavelengths from 200 to 1000 nm. It has two 4096 × 2051 thinned, back-illuminated CCDs manufactured by E2V Technologies Limited (formerly Marconi Applied Technologies Limited). Two detectors are located with a gap of about 30 pixels. The field of view projected onto the sky is rhomboidal, 162″ × 162″, with the acute angle between the x and y axes of the detector of about 86°. The pixel scale projected onto the sky is also rhomboidal, ∼ 0″.04 × 0″.04.

[*1] http://hla.stsci.edu/hlaview.html

We used the imaging data obtained with the WFC3/UVIS F555W filter. The observation was carried out on November 12, 2009 (HST Proposal ID: Cycle 17 GO 11646, PI: Crotts, Title: Light Echoes as Probes of Supernova Type Ia Environments). The target was Supernova SN 2006X located at RA = 12h 22m 54.0s, Dec = +15° 48′ 33″. We show the image in the right panel of Figure 11.1. The total exposure time was 970 seconds. The F555W filter is similar to the Johnson-Cousins V-band filter.

11.2.2 WFPC2

The WFPC2 (McMaster et al. 2008) is a second generation imaging instrument which was installed on the HST in December 1993 and was replaced by the WFC3 in May 2009. It has four 800 × 800 thick, front-side illuminated CCDs manufactured by Loral Aerospace, which cover wavelengths from 115 to 1100 nm. The incident light is divided by a four-faceted pyramid mirror and relayed by four sets of optics. The optics of three cameras called as the Wide Field Camera (WF2, WF3, and WF4) have a focal ratio of F/12.9 which gives a pixel scale of 0″.1. The fourth camera called as the Planetary Camera (PC1) has a focal ratio of F/28.3 which gives a pixel scale of 0″.046. Three cameras of the WF2, WF3, and WF4 with a field of view of 80″ × 80″ have an L-shaped field of view of 2′.5 × 2′.5. On the other hand, the PC1 has a field of view of 34″ × 34″.

We used the imaging data obtained with the WFPC2 F336W, F439W, F555W, F675W, F814W and F658N filters. They were obtained on July 29, 1996 (HST Proposal ID: Cycle 6 GO 6584, PI: Filippenko, Title: Interaction of Supernovae with Circumstellar Material). SN 1979C, which is located at RA = 12h 22m 58.6s, Dec = +15° 47′ 52″, was targeted on the PC1. We show the images in Figure 11.2. The total exposure times for the F336W, F439W, F555W, F675W, F814W and F658N filters were 2600, 2400, 800, 1000, 1200, and 3900 seconds, respectively. The F336W, F439W, F555W, F675W and F814W filters are similar to the Johnson-Cousins U, B, V, R and I-band filters, respectively. The F658N filter (λ_c: 6590.8 Å, Width: 28.5 Å) is used as an Hα + [NII] filter.

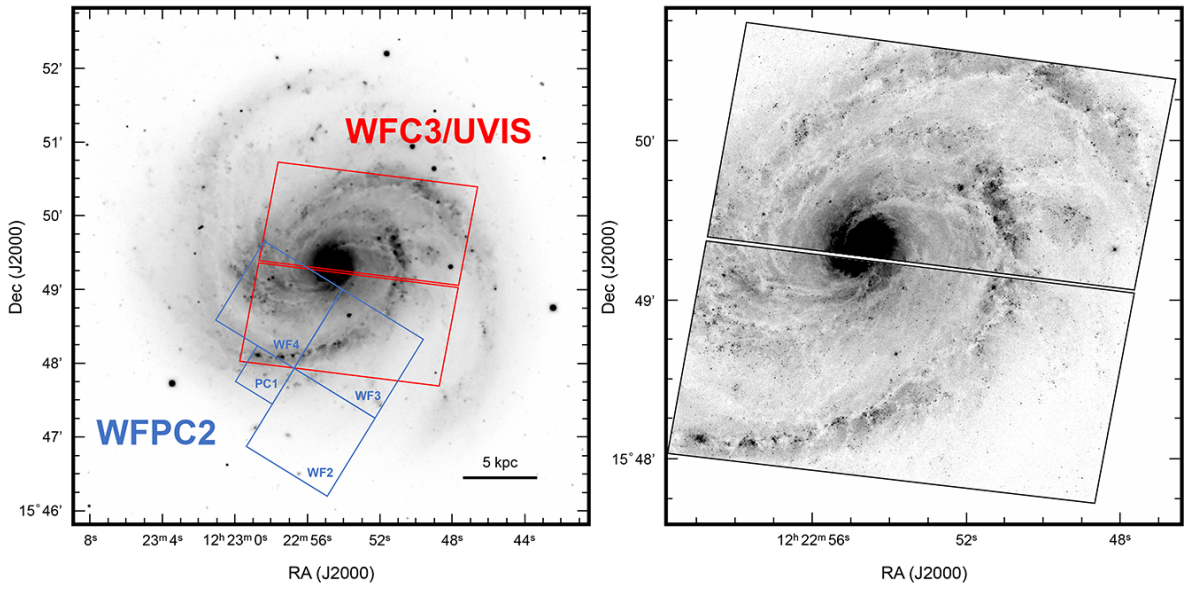

Figure 11.1: *(Left);* The observation fields of the HST WFC3/UVIS and WFPC2 imaging data. The red rhomboids indicate the field of the WFC3/UVIS. The blue squares indicate the field of the WFPC2. The background image is the R-band image from the SINGS. *(Right);* The WFC3/UVIS F555W (V) image.

Table 11.1: Properties of the HST data

Instrument	Filter	Central Wavelength (Å)	Width (Å)	Exposure Time (second)	Proposal ID
WFC3	F555W	5308[a]	1562[c]	970	11646
WFPC2	F336W	3344.4[b]	374.3[d]	2600	6584
WFPC2	F439W	4311.3[b]	473.2[d]	2400	6584
WFPC2	F555W	5439.0[b]	1228.4[d]	800	6584
WFPC2	F675W	6717.4[b]	866.8[d]	1000	6584
WFPC2	F814W	8012.2[b]	1539.4[d]	1200	6584
WFPC2	F658N	6590.8[b]	28.5[d]	3900	6584

Note.

[a] The pivot wavelength cited from Table 6.2 of Dressel (2015).

[b] The pivot wavelength cited from Table 6.1 of McMaster et al. (2008).

[c] The passband rectangular width cited from Table 6.2 of Dressel (2015).

[d] The effective width of the bandpass cited from Table 6.1 of McMaster et al. (2008).

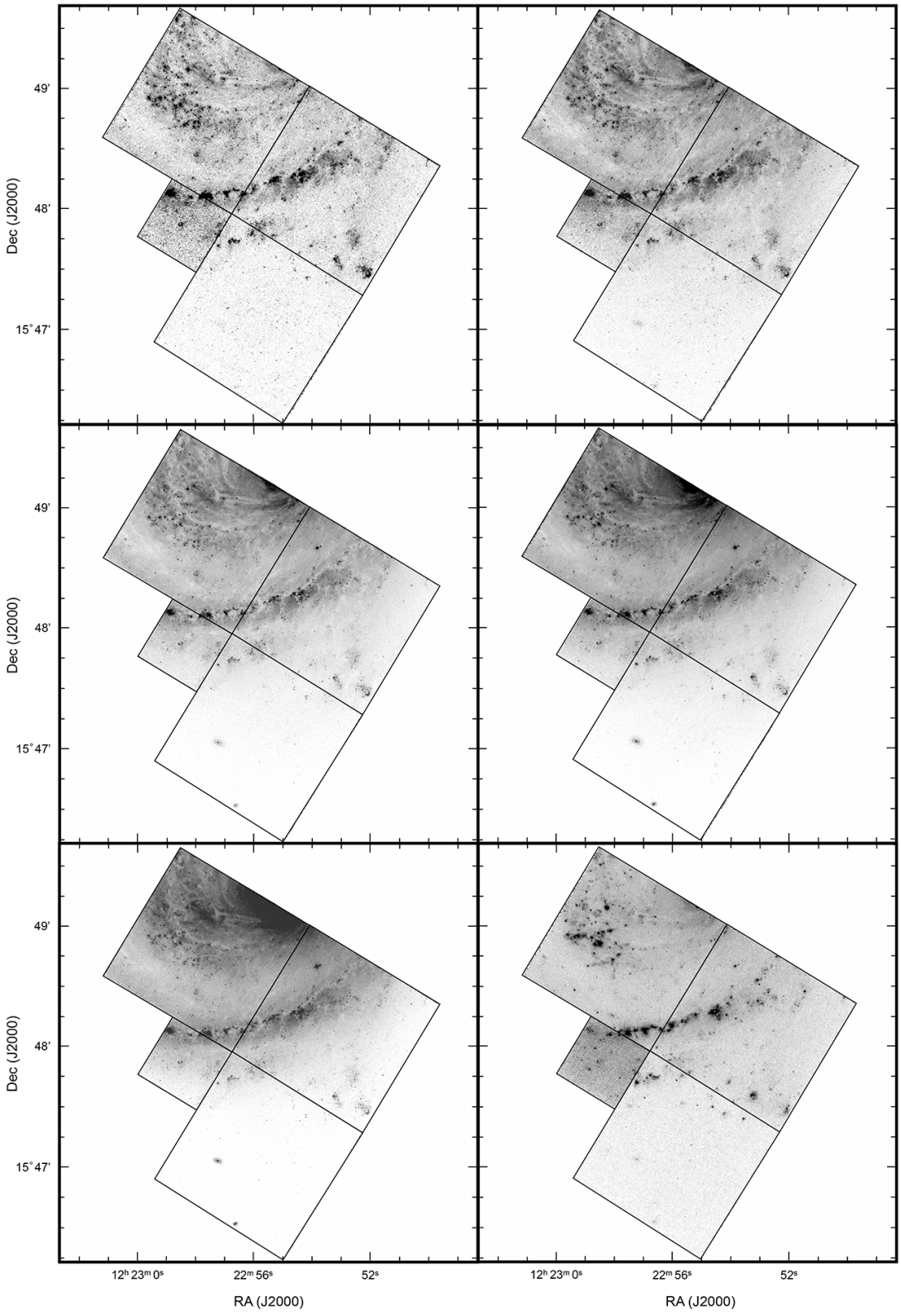

Figure 11.2: *(Top Left);* The WFPC2 F336W (U) image. *(Top Right);* The WFPC2 F439W (B) image. *(Middle Left);* The WFPC2 F555W (V) image. *(Middle Right);* The WFPC2 F675W (R) image. *(Bottom Left);* The WFPC2 F814W (I) image. *(Bottom Right);* The WFPC2 F658N (Hα) image.

Chapter 12

Data Analysis

12.1 Cluster Detection

We used the WFC3/UVIS F555W (V) image to detect stellar clusters. The angular resolution of $0''.04$ is equal to the physical size of ~ 3 pc in NGC 4321, which enables us to distinguish between individual stars and stellar clusters. We used a calibrated, geometrically-corrected, combined image. The image was created from two images obtained at the same position of the galaxy with the exposure time of 300 seconds and 670 seconds. We have not corrected the image for charge transfer efficiency (CTE) degradation, because the background level of more than 30 electrons per pixel is above the critical level where CTE losses are significant (Noeske et al. 2012).

12.1.1 Source Detection

We have used the DAOPHOT/DAOFIND package/task in IRAF (Stetson 1987) to extract both point-like and slightly extended sources with the parameters of a 3 sigma detection threshold and a background standard deviation of 0.05 in units of counts per second. In order to remove a rapidly varying background and detect sources on bright backgrounds, we used the image divided by itself with a 3×3 pixel median filter as the detection image (Miller et al. 1997). We used the detection parameter of the FWHW from 1 pixel to 5 pixels. We have not restricted sources by roundness or by sharpness in order to include elliptical and marginally resolved clusters. We chose the brightest source when there were multiple sources within an aperture radius of $0''.15$. The total list includes $\sim$ 63,000 source candidates, which consist of individual stars, stellar clusters, and background galaxies.

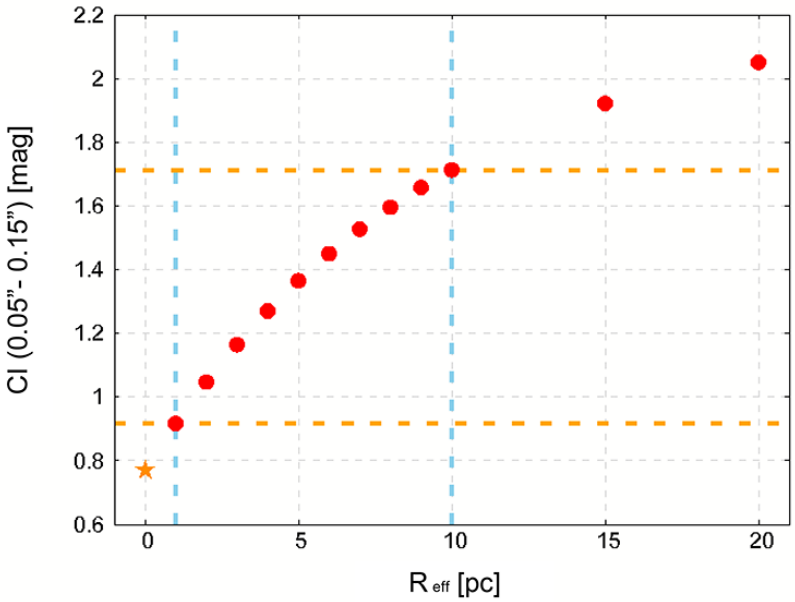

Figure 12.1: CI for artificial clusters with different R_{eff}. The orange star symbol shows the CI for an empirical PSF constructed from isolated stars. The red dots represent CI for artificial clusters of various R_{eff} generated with the MKCMPPSF task in BAOLAB by the EFF profile with a power index of 1.5. The horizontal dashed lines denote the upper and lower limits of CI for stellar clusters.

12.1.2 Extracting Clusters

The concentration index (CI) has been used for a method to distinguish between individual stars and stellar clusters (e.g., Chandar et al. 2010, Whitmore et al. 2010, Konstantopoulos et al. 2013, Ryon et al. 2014, Whitmore et al. 2014, Simanton et al. 2015). We defined the CI as the magnitude difference between aperture radii of 0″.05 and 0″.15. We performed circular aperture photometry using the DAOPHOT/PHOT package/task in IRAF with the background estimation within annuli of 0″.5 to 1″.0. We adopted the AB-magnitude photometric system, with the zeropoint of 25.78 mag from the header keywords of PHOTFLAM and PHOTPLAM (Rajan et al. 2011).

In order to define the range of acceptable CI for stellar clusters at the distance of NGC 4321, we generated artificial clusters with various R_{eff} using BAOLAB[*1] (Larsen 1999). An empirical stellar PSF was built from 17 isolated stars with the DAOPHOT/PSF package/task in IRAF. We used the MKCMPPSF[*2] task in BAOLAB to convolve the EFF profile with a power index of 1.5 with the empirical stellar PSF. This profile was successfully fitted to the luminosity profiles of young clusters in the Large Magellanic Cloud (Elson et al. 1987). Figure 12.1 shows the CI for

[*1] http://baolab.astroduo.org/

[*2] MKCMPPSF task can construct the new PSF file as a convolution product of two profiles, either of which may be given by an analytic model or supplied by the user as a FITS file.

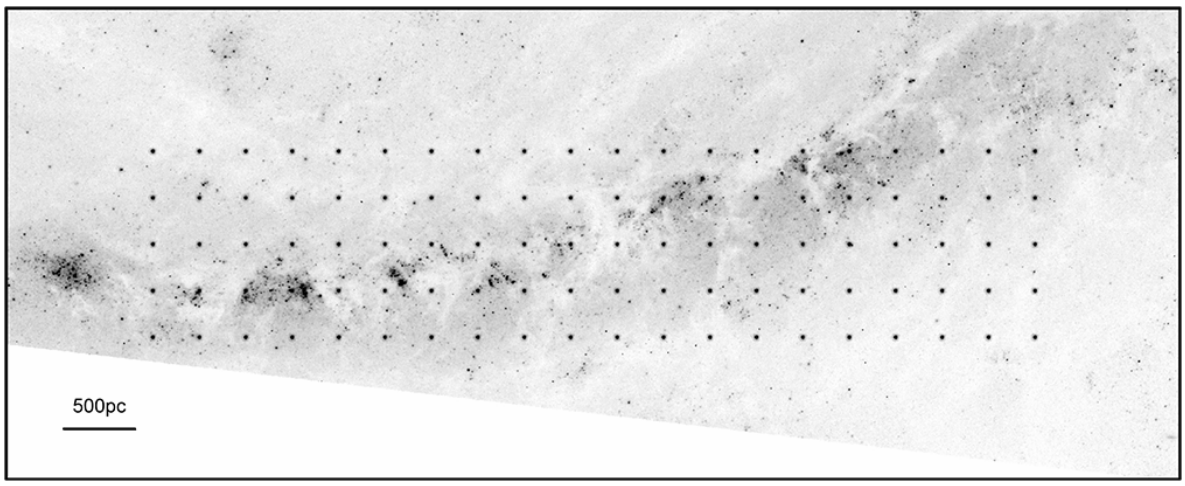

Figure 12.2: A set of artificial stars in a 20×5 object grid, which have the magnitude of 20th and are located $4''$ apart, created by the MKSYNTH task in BAOLAB on the WFC3/UVIS F555W image. The image with the size of $100'' \times 40''$ or 8.1×3.3 kpc covers the southern spiral arm.

artificial clusters with different R_{eff}. The CI for an empirical PSF constructed from isolated stars was about 0.8 mag. We set the lower and upper limits of R_{eff} for stellar clusters to 1 pc and 10 pc, considering cluster size distributions measured by previous studies (e.g., Larsen 2004, Lee et al. 2005, Barmby et al. 2006, Scheepmaker et al. 2007, Mayya et al. 2008, Bastian et al. 2012, Ryon et al. 2015). The corresponding lower and upper limits of CI for stellar clusters are 0.9 mag and 1.7 mag.

12.1.3 Completeness

We created a set of artificial stars in a 20×5 object grid with the interval of $4''$, using the MKSYNTH[*1] task in BAOLAB. The artificial objects were built using the empirical PSF generated in the above section. Objects with a fixed magnitude in the range from 20 to 30 mag in a step of 0.5 mag were added to a blank image. Then we added the output image containing the artificial objects to the science image using the IRAF IMARITH task. An example of the combined image is shown in Figure 12.2. We chose the field that covers the southern spiral arm because the completeness varies with the background level as well as crowding and confusion (e.g., Scheepmaker et al. 2007, Mora et al. 2007). The results are presented in Figure 12.3, which shows the 90% recovery fraction at 26 mag. We note that we did not correct the measured magnitude for the aperture and the extinction.

[*1] MKSYNTH task can generate a purely synthetic image, consisting of background signals including Poisson noise and a number of point-like sources.

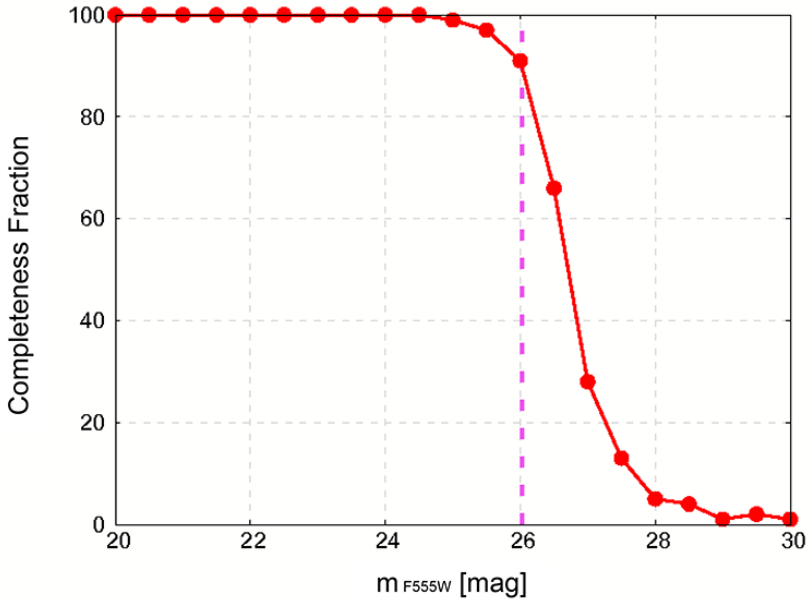

Figure 12.3: Completeness test tracing the fraction of artificial stars recovered at a range of source magnitude. The dashed vertical line indicates the 90% completeness fraction for the field that covers the southern spiral arm displayed in Figure 12.2. The horizontal axis shows the magnitude measured within the aperture radius of 0″.15 without the aperture and extinction corrections. We estimate the 90% completeness level at 26 mag.

12.1.4 Cluster Candidate

We show the CI versus the source magnitude in Figure 12.4 and the photometric error versus the source magnitude in Figure 12.5. In both figures, we plotted the detected sources on the area overlapped with the WFPC2 WF3 and WF4 chips where we used for the following analysis. In addition, we excluded the sources with the photometric errors $\sigma \geq 0.3$ mag. The orange circles indicate stellar cluster candidates selected by the upper and lower limits of CI for stellar clusters (Figure 12.1) and the completeness limit (Figure 12.3). We display the distribution of the stellar cluster candidates on the WFC3/UVIS F555W image in Figure 12.6. In 12,771 stellar cluster candidates on the WFC3/UVIS F555W image, 3,910 sources are located on the area overlapped with the WFPC2 WF3 and WF4 chips. From here on we refer to the stellar cluster candidates simply as ”clusters”.

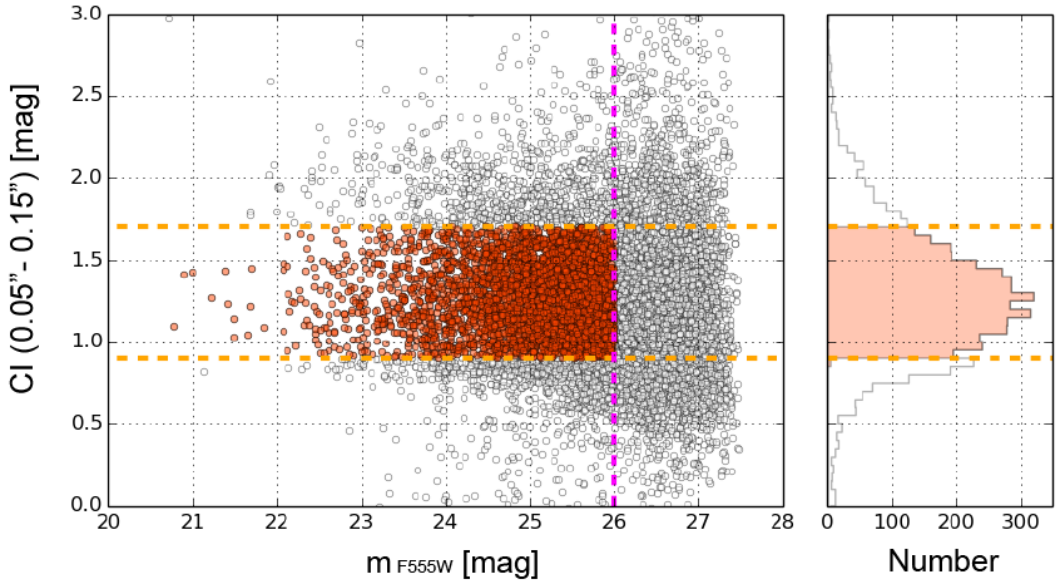

Figure 12.4: Concentration index (CI) versus source magnitude measured within the aperture radius of 0″.15 without the aperture and extinction corrections. We plotted sources on the area overlapped with the WFPC2 WF3 and WF4 chips. The orange circles indicate stellar cluster candidates. The horizontal lines denote the range of the adopted CI for stellar clusters. The vertical line shows the 90% completeness limit.

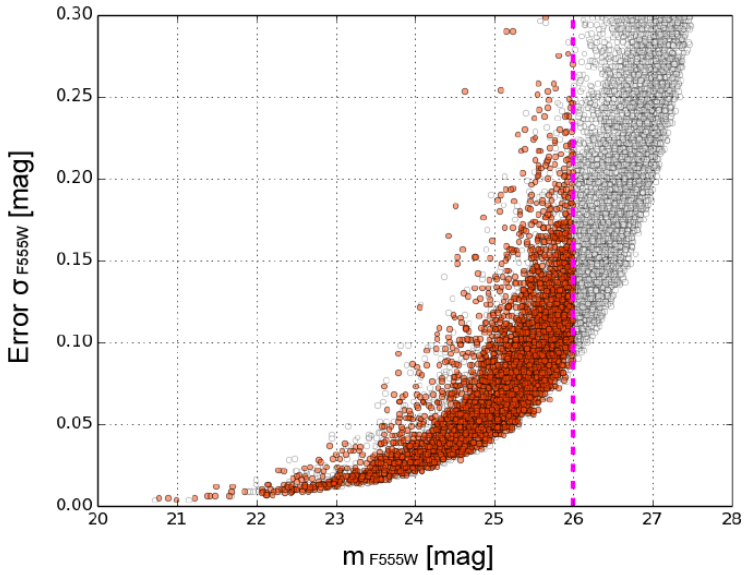

Figure 12.5: Photometric error versus source magnitude measured within the aperture radius of 0″.15 without the aperture and extinction corrections. We plotted sources on the area overlapped with the WFPC2 WF3 and WF4 chips. The orange circles indicate stellar cluster candidates. The vertical line shows the 90% completeness limit.

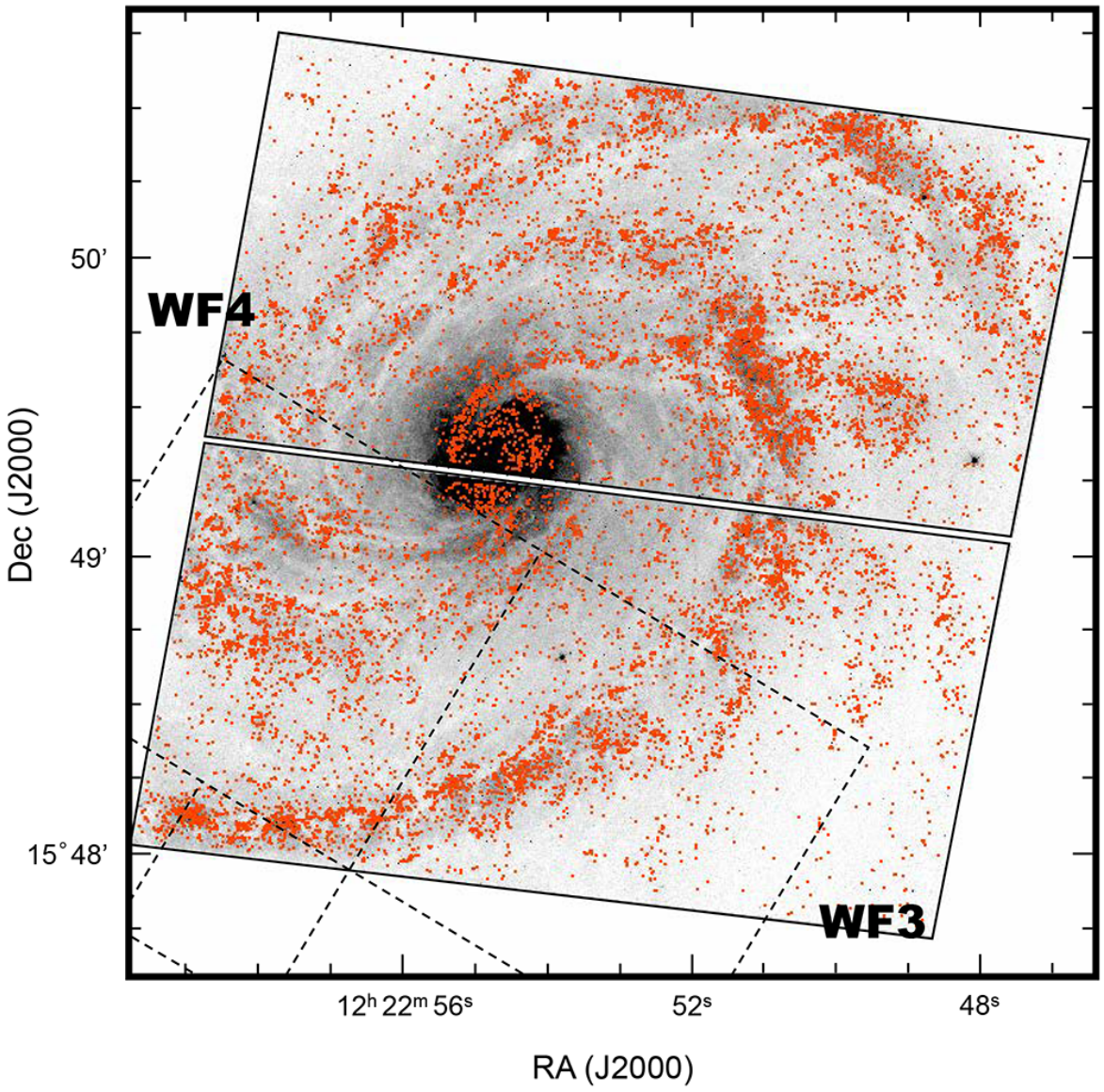

Figure 12.6: The distribution of stellar cluster candidates shown by orange dots on the WFC3/UVIS F555W image. The solid lines indicate the WFC3/UVIS field. The dashed lines indicate the WFPC2 field. We used stellar cluster candidates on the area overlapped with the WFPC2 WF3 and WF4 chips for the following analysis.

12.2 Selection of Young and Old Clusters

We used the imaging data obtained with the WFPC2 F675W (R) and F658N (Hα) filters to separate clusters into three samples with different ages. The imaging data obtained with the F336W (U), F439W (B), F555W (V) and F814W (I) filters are used to estimate average ages of three samples in Section 13.2. We analyzed the images taken with the WF3 and WF4 chips whose angular resolution of 0″.1 is equal to the physical size of ∼ 8 pc in NGC 4321.

12.2.1 WFPC2 Data Analysis

We used the calibrated science images for the WFPC2 imaging data. There are two frames for F336W, F439W, F555W, F675W and F814W, and three frames for F658N. All frames were obtained at the same position of the galaxy. We combined the images to make a cosmic ray free image using the STSDAS/CRREJ package/task in IRAF after we applied the pixel area corrections and the 34th row corrections. We arranged the four WF/PC frames into one frame using the STSDAS/WMOSAIC package/task in IRAF that corrects for geometric distortion in each chip, as well as rotation, offsets, and scale differences among the chips. The coordinate transformation functions between the WFC3 F555W image and the WFPC2 F675W mosaic frame were calculated with 510 bright resolved sources by the IRAF GEOMAP task. The root-mean-square (rms) accuracy was about 0.3 pixel in X and Y coordinates. The IRAF GEOXYTRAN task was used to transform coordinates of clusters on the WFC3 F555W image to those on the WFPC2 mosaic frame. We measured the magnitude of 3,910 clusters with the circular aperture radius of 0″.15 and the background estimation within annuli of 1″.0 to 1″.5 using the DAOPHOT/PHOT package/task in IRAF. We adopted the AB-magnitude zeropoint of 20.59, 20.74, 22.55, 22.29, 22.08 and 18.45 mag for F336W, F439W, F555W, F675W, F814W and F658N from the header keyword PHOTFLAM and PHOTPLAM (Gonzaga et al. 2010).

The CTE loss becomes significant in the data obtained before April 1994 when the operating temperature of the CCDs was lowered. In addition, the loss was getting larger throughout the mission because of the radiation damage to the CCDs. Our data were obtained in July 1996, so the effect is considered to be not so strong. However, in the F336W and F658N frames with faint targets and the low background level, there is a possibility that the amount becomes significant. Therefore, we corrected the CTE loss for all frames. The CTE loss was calculated using the correction formulae by Dolphin (2009), and the correction applied to the aperture-corrected counts with a radius of 0″.5. We derived a factor for the aperture correction by running the DAOPHOT/PHOT package/task in IRAF to isolated stars using two aperture radii of 0″.15 and

0″.5. Then we applied the aperture correction from 0″.15 to 0″.5 with a factor of 2.0 in all filters. Even in the F336W and F658N frames, most of the clusters have the CTE losses less than 0.1 mag.

12.2.2 Separating Clusters by Hα Luminosity

We show the photometric error versus the cluster magnitude of all filters in Figure 12.7. The magnitude of cluster was corrected for the aperture radius of 0″.5. We selected clusters with the photometric errors $\sigma < 0.3$ mag for the F675W (R) filter and $\sigma < 1.0$ mag for the other filters. In addition, we excluded clusters out of the color range -1.0 mag < F336W (U) − F439W (B) < 2.5 mag.

We separated clusters into the following three samples with different ages by comparing the F658N (Hα) and F675W (R) magnitude.

Young : $m_R - m_{H\alpha} > 1.5$ mag. Age $\lesssim$ 6 Myr.
Middle : 0.5 mag < $m_R - m_{H\alpha} \leq 1.5$ mag. 6 Myr $\lesssim$ Age $\lesssim$ 10 Myr.
Old : $m_R - m_{H\alpha} \leq 0.5$ mag. Age $\gtrsim$ 10 Myr.

We show the color magnitude diagram in Figure 12.8. The horizontal dashed lines indicate the boundaries of colors among three cluster samples. We estimated the ages corresponding to the boundaries with an evolutionary track of a single-burst stellar population (SSP) from Starburst99 (Leitherer et al. 1999, hereafter SB99) model. We show the time evolution of Hα equivalent width (EW) in Figure 12.9. We assumed a stellar population with a Salpeter initial mass function (IMF) with slope $\alpha = 2.35$ (Salpeter 1955), and an upper mass limit $M_{up} = 100\ M_\odot$. We plotted models with 0.4, 1, and 2 × the solar metallicity ($Z_\odot$).

As for the metallicity, Pilyugin et al. (2004) have measured the radial oxygen abundance distribution using 10 HII regions observed in McCall et al.(1985) and Shields et al.(1991). The radial oxygen abundance distribution was fitted by the following equation:

$$12 + \log(O/H) = 8.86 - 0.37 \times (R/R_{25})$$

where R/R_{25} is the fractional radius and R_{25} is located at 3′.79. The oxygen abundance in the arm region from 1′ to 1′.5, where we traced dust lanes in Part I, is estimated at 8.71 − 8.76. The metallicity is regarded as almost the solar value by adopting the solar oxygen abundance of $12 + \log(O/H)_\odot = 8.69$ (Allende Prieto et al. 2001).

As for the Hα EW, the F658N filter contains [NII]λ6548 emission line as well as Hα emission line assuming the recession velocity of 1571 km/s (redshift z = 0.005240) from NED. The theoretical intensity of the [NII]λ6584 emission line is about 3 times that of the [NII]λ6548, but

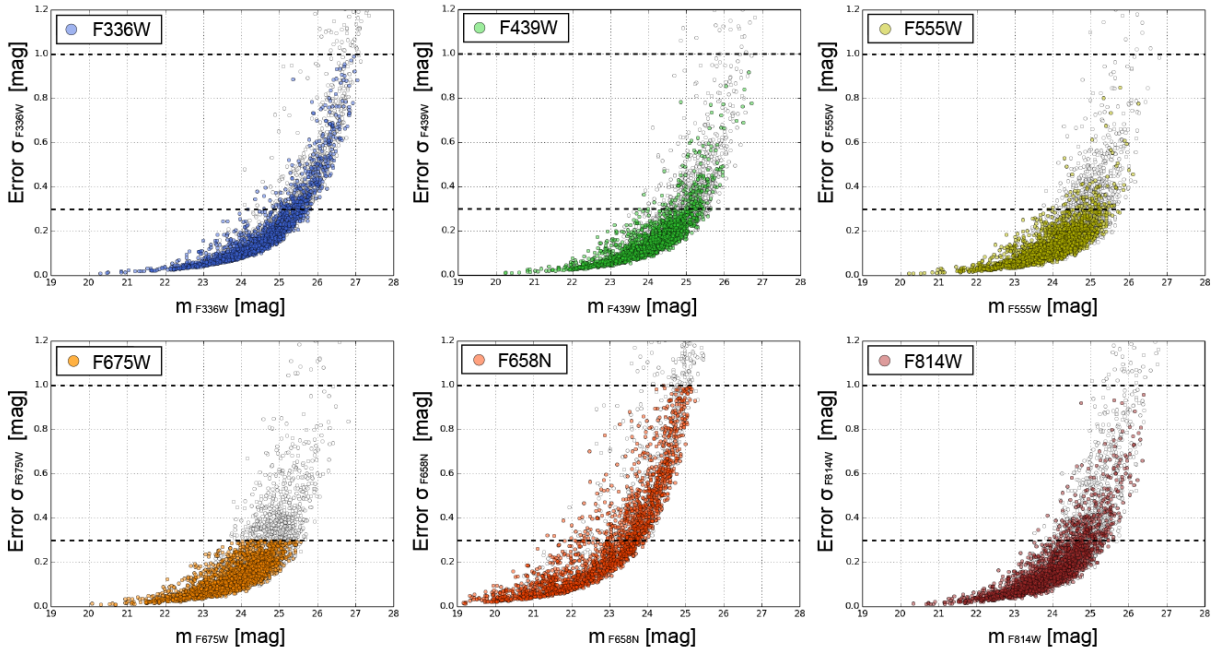

Figure 12.7: Photometric error versus cluster magnitude. The magnitude of cluster was corrected for the aperture radius of 0″.5.

the contamination by [NII]λ6584 emission line is significantly weaker than [NII]λ6548 emission line in the combination of this galaxy and the F658N filter. Prescott et al. (2007) have measured the flux ratio of [NII]λ6584 to Hα ([NII]λ6584/Hα) = 0.395 in this galaxy. We adopted this value and the solar metallicity to calculate Hα EWs corresponding to the boundaries of colors among three cluster samples, which are shown with the horizontal solid lines in Figure 12.9. The color of $m_R - m_{H\alpha}$ = 1.5 mag between the young and the middle cluster samples corresponds to the EW of 91 Å and the age of 6.2 Myr. The color of $m_R - m_{H\alpha}$ = 0.5 mag between the middle and the old cluster samples corresponds to the EW of 16 Å and the age of 7.8 – 10.3 Myr.

The age is not so sensitive to the change in the metallicity and [NII]λ6584/Hα, since the Hα EW exponentially decreases as clusters become old. For example, Hoopes & Walterbos (2003) showed that [NII]λ6584/Hα covers a wide range from 0.1 (individual HII regions) to 2.0 (diffuse Hα component) in nearby galaxies. We show the Hα EWs corresponding to the extreme cases of [NII]λ6584/Hα with the horizontal dashed lines in Figure 12.9. Considering such extreme cases, the ages are 6.2 – 6.3 Myr for the color of $m_R - m_{H\alpha}$ = 1.5 mag and 7.6 – 11.3 Myr for the color of $m_R - m_{H\alpha}$ = 0.5 mag.

We display the distributions of three cluster samples on the WFPC2 F675W image in Figure 12.10. The young, middle, and old cluster samples contain 578, 636, and 828 clusters respectively.

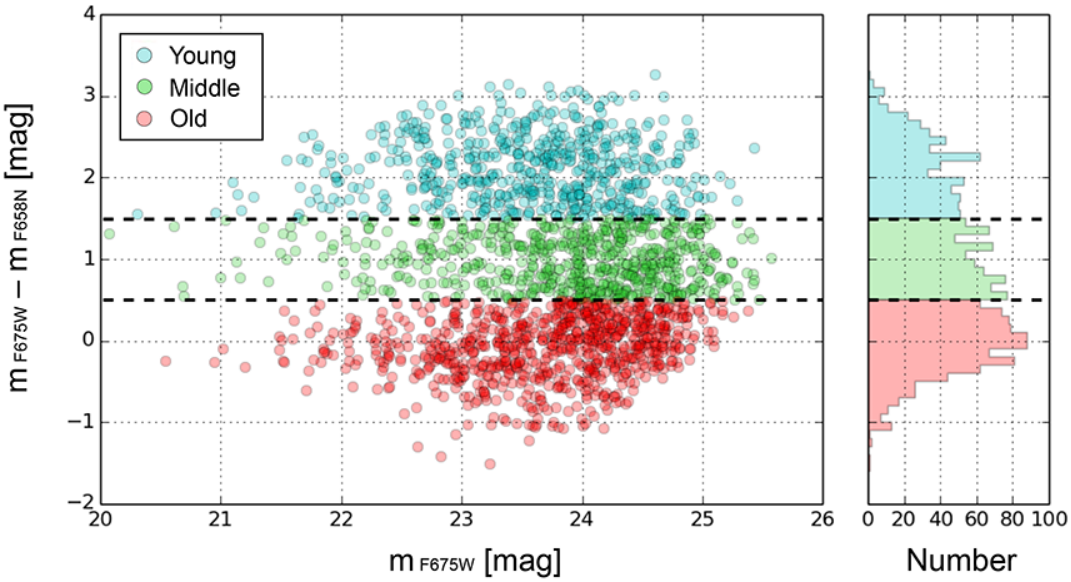

Figure 12.8: Color-magnitude diagram: F675W (R) − F658N (Hα) versus F675W (R). The horizontal dashed lines indicate the boundaries of colors among three cluster samples.

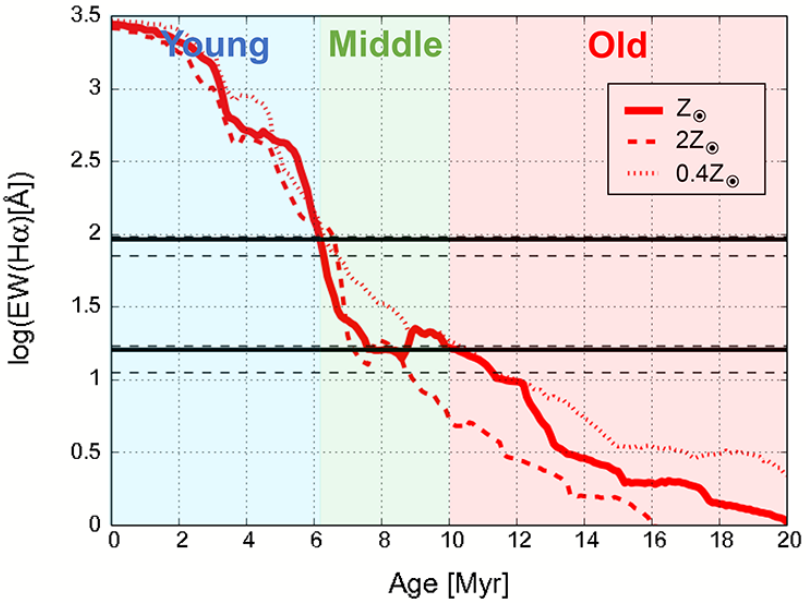

Figure 12.9: Time evolution of Hα EW from SB99 SSP models assuming a Salpeter IMF. The red solid line shows the model for solar metallicity ($Z_{\odot}$). The horizontal solid lines indicate Hα EWs corresponding to the boundaries of F675W (R) − F658N (Hα) among three cluster samples assuming a flux ratio [NII]λ6584/Hα = 0.395. The horizontal dashed lines indicate Hα EWs assuming extreme cases of [NII]λ6584/Hα = 0.1 and 2.0.

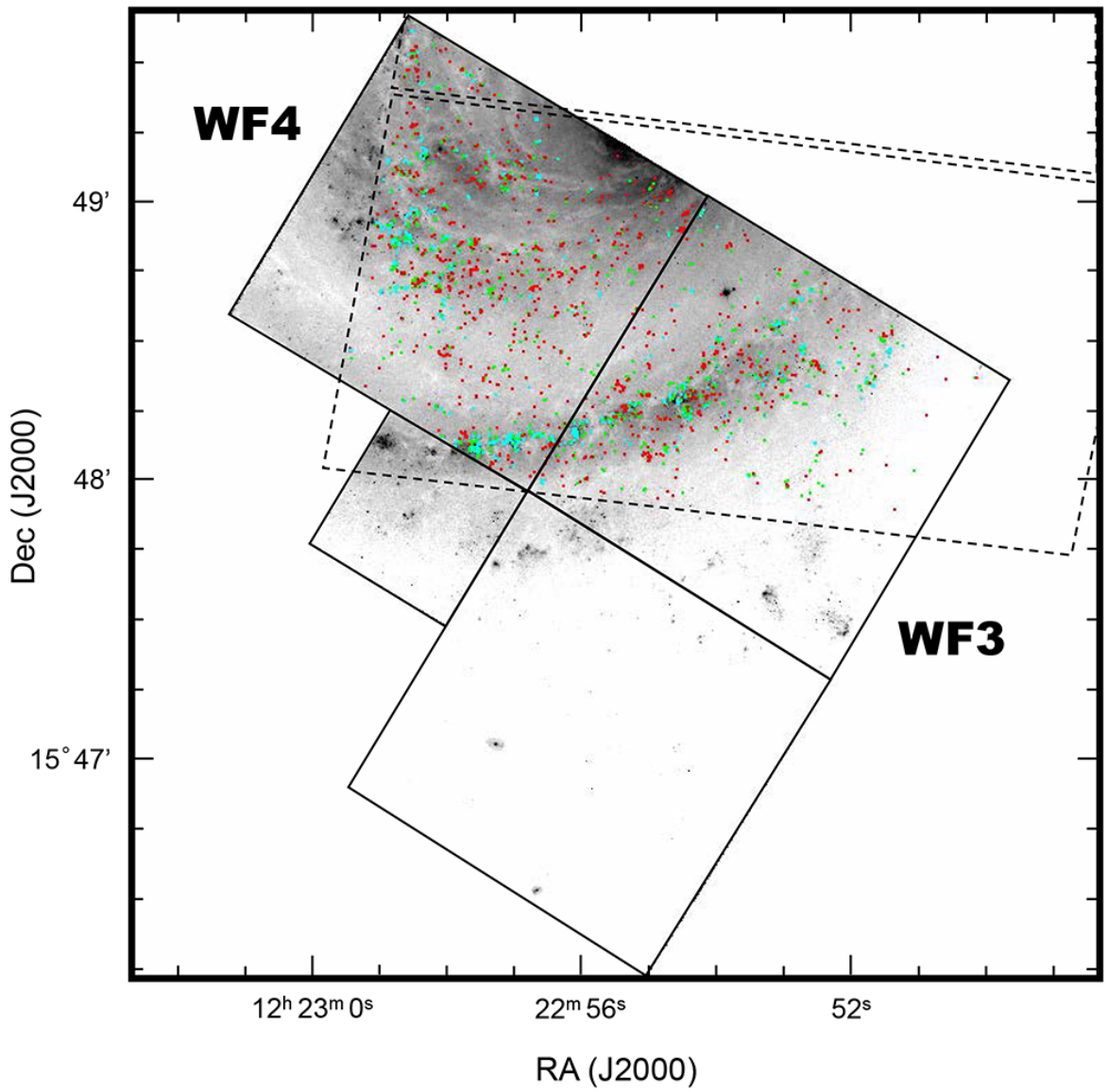

Figure 12.10: The distributions of the young, middle, and old cluster samples with cyan, green, and red dots on the WFPC2 F675W image. The sold lines indicate the WFPC2 field. The dashed lines indicate the WFC3/UVIS field.

Chapter 13

Age Distribution of Stellar Clusters

13.1 Azimuthal Distributions of Cluster Samples

We investigated the azimuthal distributions of three cluster samples in the southern spiral arm. In Figure 13.1, we show the arm region on the WFC3/UVIS F555W image. The dust lane traced with an I − K color image in Part I is shown with a magenta line. The estimated positions of stellar clusters with the kinematic age from −50 Myr to 50 Myr with an interval of 10 Myr are shown with black solid lines. We used the same rotation curve, pattern speed, inclination, and position angle as the right panel of Figure 10.1. In Figure 13.2, we show the distribution of clusters on the (Radius, azimuth θ) plane. In both figures, we plotted the young, middle, and old cluster samples with cyan, green, and red dots respectively.

We show the azimuthal distributions of three cluster samples in units of the kinematic age from the dust lane in Figure 13.3. We counted clusters within the area between the deprojected radii of 65″ and 85″ which is located inside the corotation radius. The total number of clusters are 219 for the young cluster sample, 168 for the middle cluster sample and 177 for the old cluster sample. We show the normalized and cumulative distributions in Figure 13.4.

We see that the distribution of the old cluster sample has a peak at the kinematic age of ~ 20 Myr compared to that of the young cluster sample which has a peak at the kinematic age of ~ 0 Myr. This is in agreement with the density wave theory which predicts the age gradient of stellar clusters across the spiral arm as illustrated in Figure 9.1. The Kolmogorov-Smirnov test (K-S test) indicated a statistically significant difference ($P < 0.0001$) between the distributions of the young and the old cluster samples.

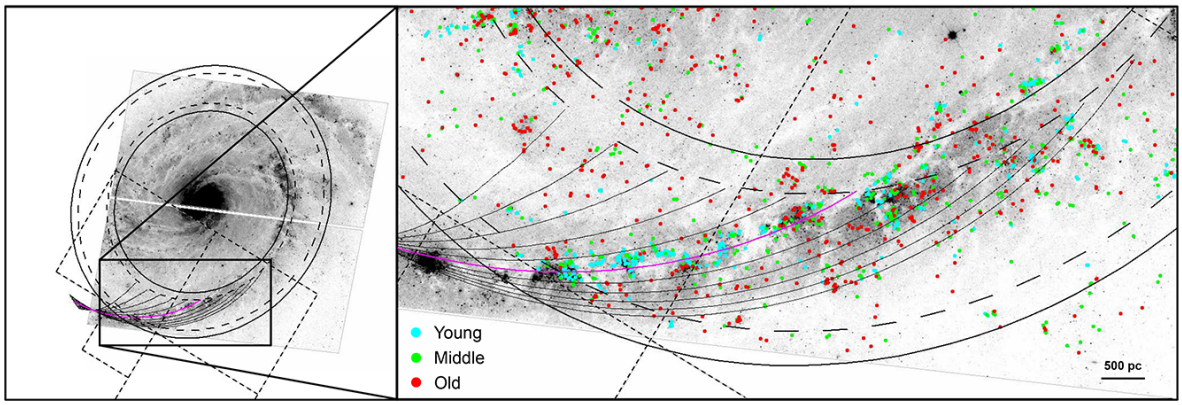

Figure 13.1: *(Left);* The arm region on the WFC3/UVIS F555W image. The dashed squares indicate the WFPC2 field. The dust lane traced in Part I is shown with a magenta line. The estimated positions of stellar clusters with the kinematic age from −50 Myr to 50 Myr with an interval of 10 Myr are shown with black solid lines. We used the same rotation curve, pattern speed, inclination, and position angle as the right panel of Figure 10.1. The dashed ellipses show the region of the deprojected radii from 65″ to 85″ within which we investigated the distributions of three cluster samples. On the other hand, the solid ellipses have the deprojected radii of 60″ and 90″ which show the whole radial region of Figure 13.2. *(Right);* A zoomed image of the southern spiral arm region shown by a black rectangle in the left panel. We plotted the young, middle, and old cluster samples with cyan, green, and red dots respectively. The frame size is 110″ × 55″ or 9.0 kpc × 4.5 kpc.

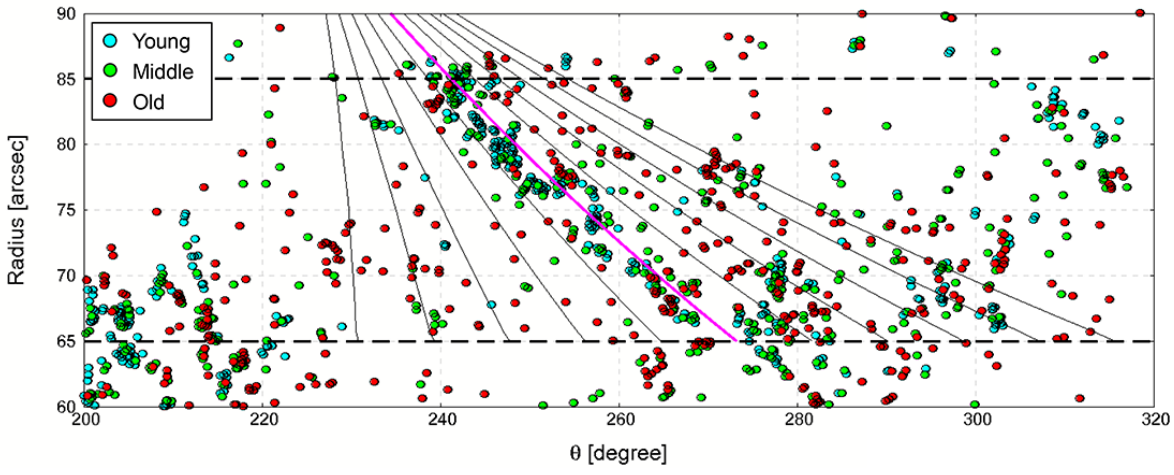

Figure 13.2: The distribution of clusters on the (Radius, azimuth θ) plane. The θ increases counterclockwise from the west in the image of the galaxy. We plotted the young, middle, and old cluster samples with cyan, green, and red dots respectively. The dust lane is shown with a magenta line. The estimated positions of stellar clusters with the kinematic age from −50 Myr to 50 Myr with an interval of 10 Myr are shown with black solid lines. The dashed lines show the range of the deprojected radius from 65″ to 85″ within which we investigated the distributions of three cluster samples.

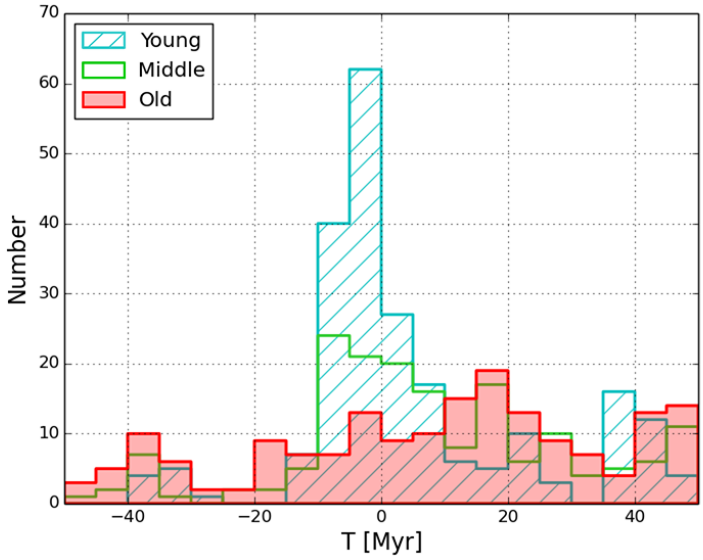

Figure 13.3: Azimuthal distributions of three cluster samples in units of the kinematic age from the dust lane within the area between the deprojected radii of 65″ and 85″. We show the distributions of the young, middle, and old cluster samples with cyan, green, and red colors respectively.

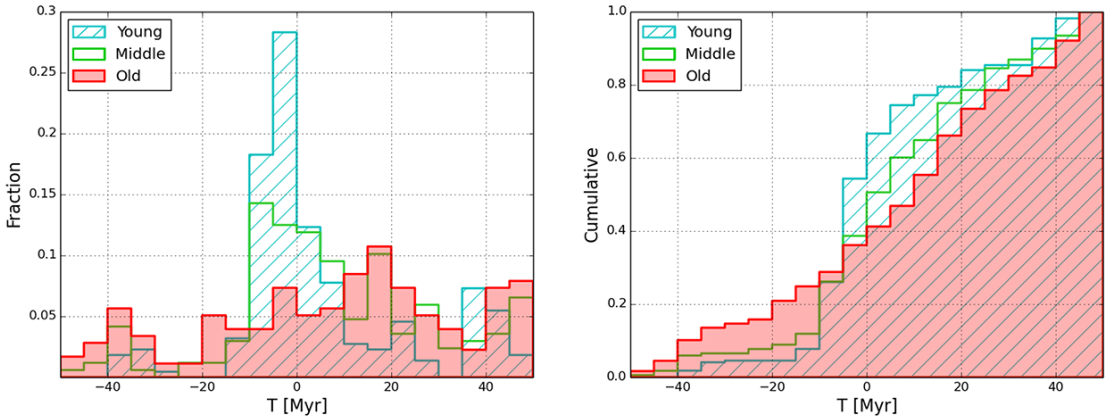

Figure 13.4: Normalized (left panel) and cumulative (right panel) distributions of Figure 13.3.

13.2 Age Estimates from Multicolor Photometry

There are multi-color images taken with the WFPC2 F336W, F439W, F555W and F814W filters as well as F658N and F675W filters. In this section, we examined average ages of three cluster samples from the colors. Then, we investigated the effect of very old clusters on the azimuthal distribution of the old cluster sample.

13.2.1 Color-Color Diagram

We show the color-color diagram of F336W − F439W (U − B) against F555W − F814W (V − I) for three cluster samples in Figure 13.5 − 13.7. We corrected the foreground Galactic extinctions of 0.02 mag for E(U−B) and 0.03 mag for E(V−I) from NED (R_V[*1] = 3.1; Schlegel et al. 1998, Fitzpatrick 1999, Schlafly & Finkbeiner 2011). In these figures, the black solid line shows an evolutionary track of a SSP model with solar metallicity and a Kroupa (2001) IMF from Maraston (2005) that broad-band colors are computed for the same filter combinations. The black arrow shows the reddening vector for visual absorption A_V[*2] = 1 mag (R_V = 3.1: Cardelli et al. 1989). The clusters seem to follow the evolutionary track well, considering that younger clusters suffer from large amounts of extinction than older clusters.

We estimated the average age of each cluster sample from the U − B and V − I colors. In Figure 13.5 − 13.7, yellow star symbols show the average colors. We see the average colors become redder from the young cluster sample to the old cluster sample. We estimated the average age and extinction from the average colors assuming the reddening vector. We plotted the average colors corrected for the extinction with an orange star symbol. We summarize the average age and extinction of each cluster sample in Table 13.1. The average ages of the young, middle and old cluster sample are 5.3, 6.7 and 27 Myr respectively, which are consistent with the ages estimated from Hα EW. We estimated the uncertainty of the ages with different stellar population models from SB99 and Bruzual & Charlot (2003), assuming a SSP model with solar metallicity and a Salpeter IMF. We calculated the colors for the WFPC2 filters from the model spectra by using the filter throughput[*3]. The average age of the young cluster sample does not vary according to the models, while the average age of the old cluster sample may be up to 80 Myr. Even if we consider the difference among the models, the average ages of the young and old cluster samples are consistent with the ages estimated from Hα EW.

[*1] R_V [= A_V/E(B−V)]: the ratio of total to selective absorption at V

[*2] A_V: the total absorption in V magnitude

[*3] http://www.stsci.edu/hst/wfpc2/analysis/filters.html

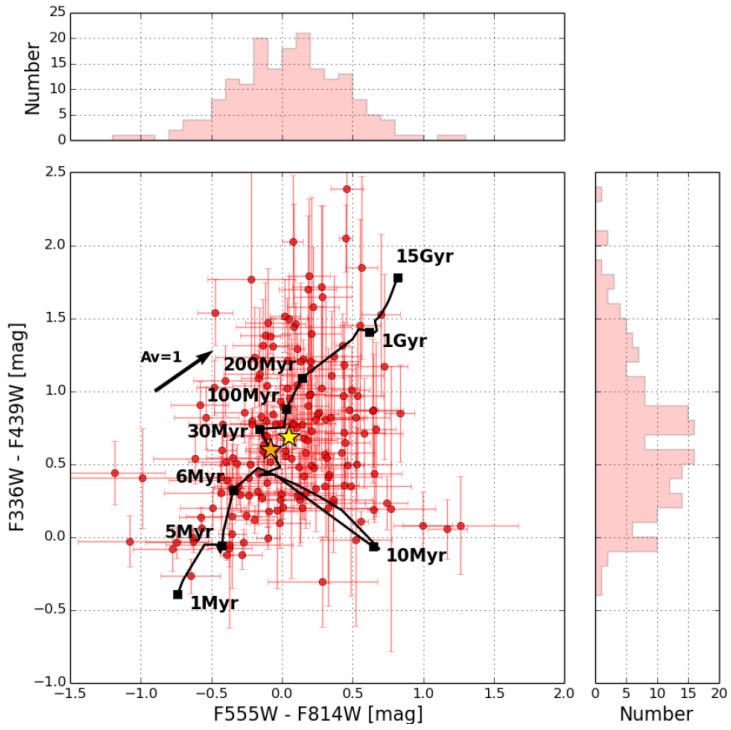

Figure 13.5: Color-color diagram of F336W − F439W (U − B) versus F555W − F814W (V − I) for the old cluster sample. The black solid line shows an evolutionary track of a SSP model with solar metallicity and a Kroupa IMF from Maraston (2005). The black arrow shows the reddening vector for visual absorption A_V = 1 mag (R_V = 3.1; Cardelli et al. 1989). The yellow star symbol shows the average colors, and the orange star symbol shows the average colors corrected for the extinction assuming the reddening vector.

Table 13.1: The average age and extinction of each cluster sample

Cluster sample	Number of clusters	Average E(B−V) (mag)	Average Age (Myr)
Young	219	0.28	$5.3\ ^{+0.7}\ _{-0.0}$
Middle	168	0.03	$6.7\ ^{+12}\ _{-1.7}$
Old	177	0.10	$27\ ^{+53}\ _{-0.0}$
Old (Age ≤ 200Myr)	145	0.04	$25\ ^{+35}\ _{-6}$

Note.
We estimated the average age with the stellar population model from Maraston (2005), and the error with different models from SB99 and Bruzual & Charlot (2003).

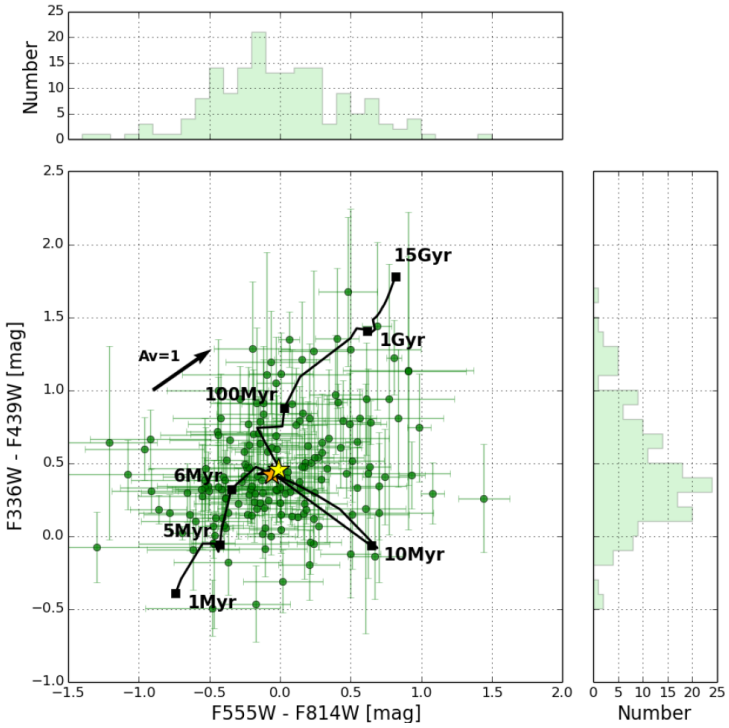

Figure 13.6: Color-color diagram of U − B versus V − I for the middle cluster sample.

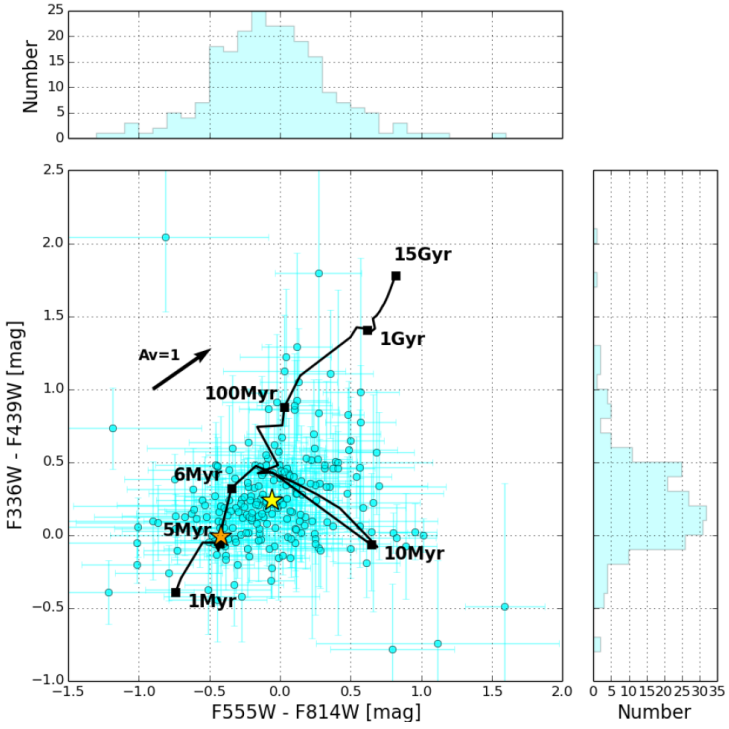

Figure 13.7: Color-color diagram of U − B versus V − I for the young cluster sample.

The average age of the young cluster sample is close to that of the middle cluster sample. The reason is considered that clusters younger than about a few Myr are embedded or obscured in dusts because of large amount of extinction (Lada & Lada 2003, Whitmore et al. 2011). On the other hand, the amount of extinction of the young cluster sample is larger than that of the middle and the old cluster samples. This trend is consistent with previous observational results that most of the dust has been expelled and ionized gas becomes larger bubbles surrounding a cluster when the cluster becomes older than about 6 Myr (Whitmore et al. 2011).

13.2.2 Effect of Very Old Clusters

The old cluster sample contains very old clusters which are not likely to be directly related with the recent star formation around the spiral arm. To investigate the effect of very old clusters on the azimuthal distribution of the old cluster sample, we constructed the cluster sample excluding clusters older than 200 Myr. We excluded clusters older than 200 Myr assuming the SSP model from Maraston (2005) and the reddening vector with R_V = 3.1 (Cardelli et al. 1989). We show the UBVI color-color diagram of the old cluster sample excluding clusters older than 200 Myr in Figure 13.8. The border line of the stellar cluster age of 200 Myr is shown by a dashed line. The cluster sample excluding clusters older than 200 Myr has 145 clusters which is about 80 % of the old cluster sample. The average age is estimated at 25 Myr with E(B−V) = 0.04 assuming the reddening vector.

We show the azimuthal distributions of the old cluster samples in Figure 13.9. The red line shows the old cluster sample which is the same as Figure 13.3. The magenta line shows the cluster sample excluding clusters older than 200 Myr. The purple line shows the distribution of the clusters older than 200 Myr. The clusters older than 200 Myr seem to be uniformly distributed around the arm, and do not significantly affect the distribution of the old cluster sample.

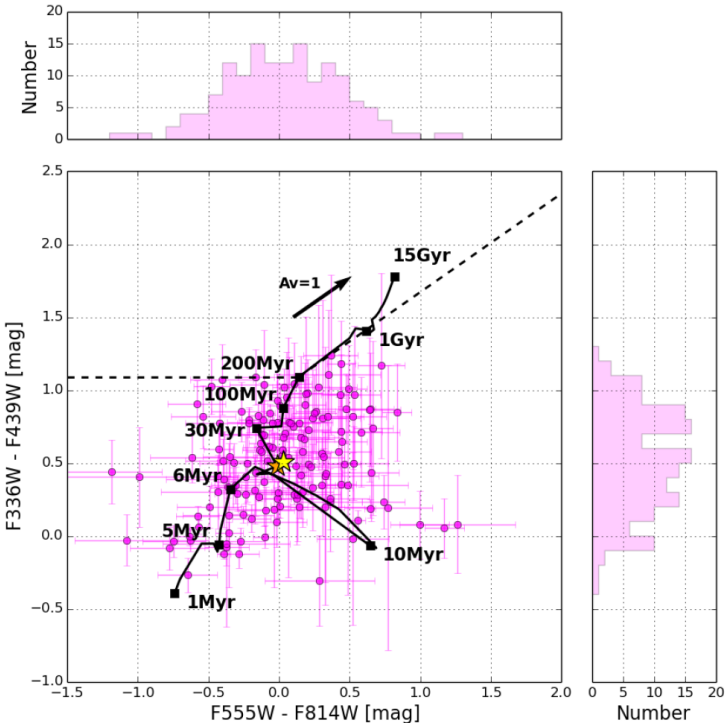

Figure 13.8: Color-color diagram of U − B versus V − I for the old cluster sample excluding clusters older than 200 Myr.

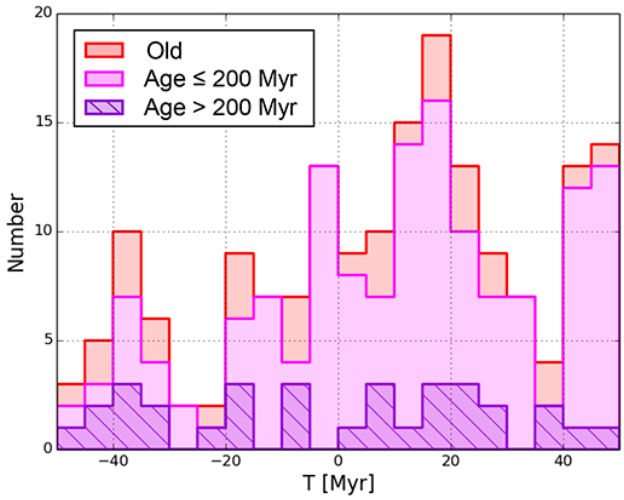

Figure 13.9: Azimuthal distributions of the old cluster samples. The red line shows the old cluster sample which is the same as Figure 13.3. The magenta line shows the cluster sample excluding clusters older than 200 Myr. The purple line shows the distribution of the clusters older than 200 Myr.

13.3 Effect of Dust Extinction

We investigated the effect of dust extinction on our cluster samples with near-infrared imaging data. Near-infrared extinction is much smaller than optical one. Grosbøl & Dottori (2012) (hereafter GD12) studied the distribution of young stellar clusters in grand design spiral galaxies including NGC 4321 with ground-based near-infrared observations. They detected complexes of young stellar clusters with the ages $\lesssim 10$ Myr that are reddened by several magnitudes of visual extinction. We compared our cluster samples with the cluster complexes detected by the near-infrared observations.

13.3.1 Near-Infrared Cluster Complexes from GD12

We used the near-infrared cluster complexes studied in GD12 whose catalog was downloaded through the VizieR[*1]. The near-infrared imaging data were obtained with the High Acuity Wide field K-band Imager (HAWK-I) on the 8.2-m Very Large Telescope (VLT), which employs a mosaic of four 2K × 2K HAWAII-2RG detectors with a pixel scale of $0''.106$ and a total field of view of $7'.5 \times 7'.5$. The observations have been carried out on March 27, 2009 (Program ID: 382.B-0331(B), PI: Grosbøl, Title: Formation of Massive Stellar Clusters triggered by Density Waves in Spiral Galaxies). The total exposure times for the Ks, H, and J filters were 9, 7, and 5 minutes, respectively.

The cluster complexes on the Ks-band image were identified by SExtractor. The seeing in the final, stacked Ks-band image was $0''.66$ (FWHM). The limiting magnitudes of J, H, and K corresponding to the completeness of around 90% were 19.32, 19.81, and 20.74 mag, respectively. The total number of cluster complexes was 1184.

13.3.2 Azimuthal Distribution of Near-Infrared Cluster Complexes

There are 47 cluster complexes with cs[*2] < 0.95 and $\sigma_{J,H,K} < 0.3$ mag in the area where we investigated the azimuthal distribution of our cluster samples in Section 13.1. We show the color-color diagram of (J − H) versus (H − K) in Figure 13.10. A first order reddening corrected color index Q has been used as an age indicator (e.g. Grosbøl & Dottori. 2009). We adopted a screen model with standard galactic extinction, which yields Q = (H − K) − 0.57 × (J − H) (Winkler 1997, Indebetouw et al. 2005). We investigated the relation of the Q index to stellar cluster ages

[*1] http://vizier.nao.ac.jp/viz-bin/VizieR?-source=J/A+A/542/A39

[*2] The *class_star* estimator provided by SExtractor. The sources with cs = 1 correspond to star-like ones and cs = 0 to diffuse ones. Sources with cs > 0.95 are assumed to be foreground stars in GD12

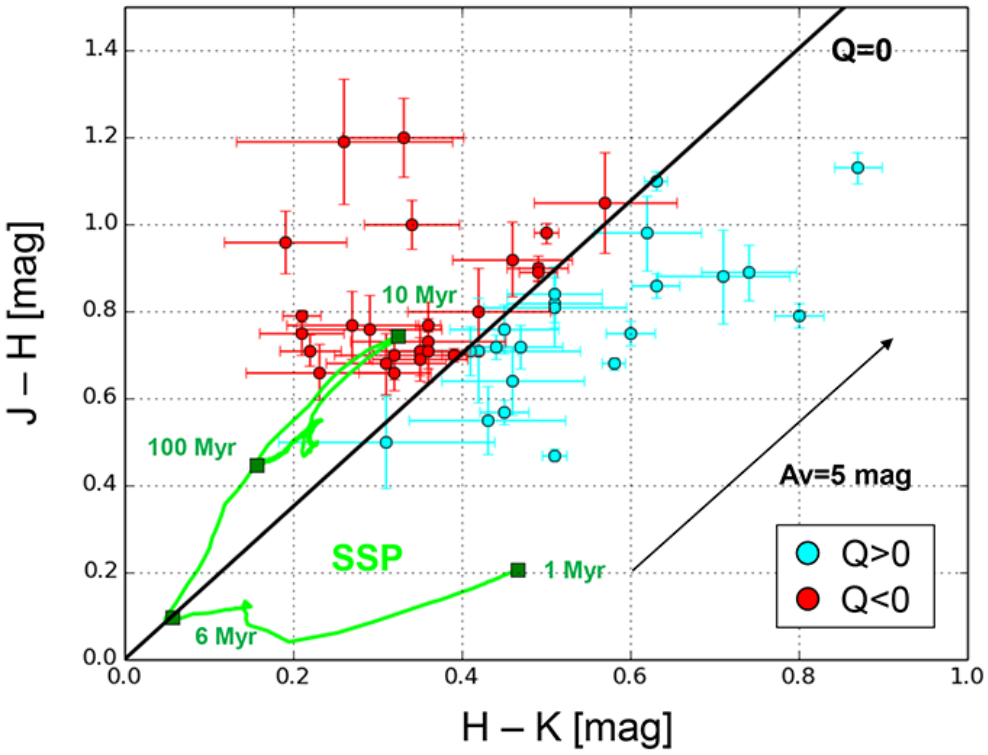

Figure 13.10: Color-color diagram of (J − H) versus (H − K) for the cluster complexes from GD12 in the southern arm field. The black solid line indicates Q = (H − K) − 0.57 × (J − H) = 0. The green line shows an evolutionary track of a SB99 SSP model assuming solar metallicity and a Salpeter IMF. The cluster complexes with Q > 0 shown by cyan circles are younger than 6 Myr and those with Q < 0 shown by red circles are older. The black arrow shows the reddening vector for visual absorption A_V = 5 mag (R_V = 3.1).

in Appendix E. In Figure 13.10, the black solid line indicates Q = 0, and the black arrow shows the reddening vector for visual absorption A_V = 5 mag assuming R_V = 3.1 (Cardelli et al. 1989). For reference, we show an evolutionary track of a SB99 SSP model by the green line, which indicates a stellar population with solar metallicity, a Salpeter IMF with slope α = 2.35, and an upper mass limit M_{up} = 100 $M_\odot$. We classified the cluster complexes with Q > 0 (cyan) as young cluster complexes (i.e., younger than 6 Myr), and those with Q < 0 (red) as old cluster complexes (i.e., older than 6 Myr).

We display the distributions of the young and the old cluster complexes with cyan and red circles on the VLT HAWK-I Ks-band image in Figure 13.11 (a). The size of the circles indicates the size of the cluster complexes measured by GD12. We show the number and area distributions of the young and the old cluster complexes in units of the kinematic age in the left panel of Figure 13.12. The old cluster complexes tend to be distributed downstream compared with the young

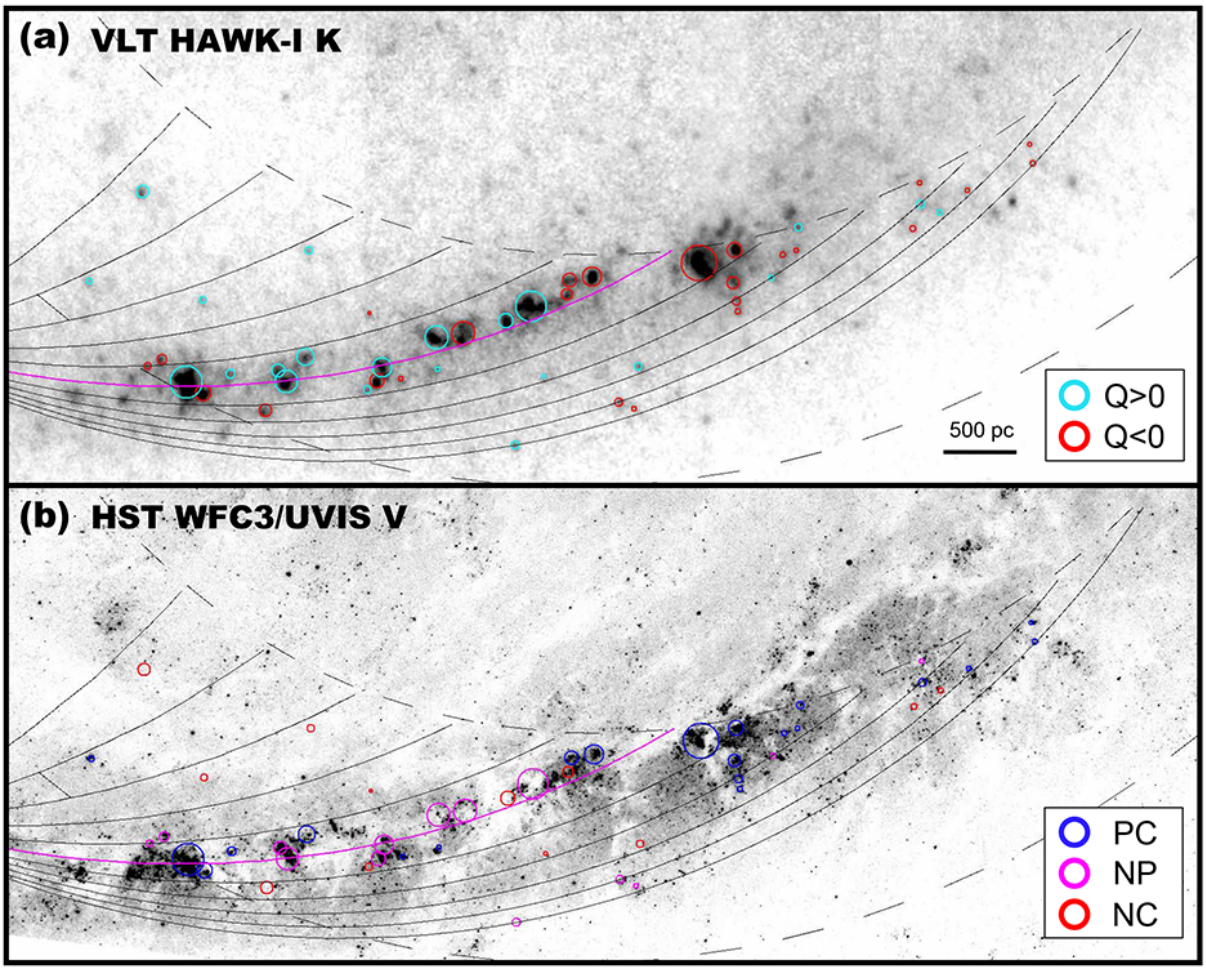

Figure 13.11: (a) The distributions of the young (Q > 0) and the old (Q < 0) cluster complexes with cyan and red circles on the VLT HAWK-I Ks-band image. (b) The distributions of the cluster complexes classified as PC (blue), NP (magenta), and NC (red) on the HST WFC3/UVIS V-band image. The black and magenta lines are the same lines as Figure 13.1. The each frame size is 100″ × 40″ or 8 kpc × 3 kpc.

cluster complexes. Their distributions are similar to the distributions of the young and the middle cluster samples shown in Figure 13.3.

13.3.3 Comparison with Near-Infrared Cluster Complexes

We classified the near-infrared cluster complexes into the following three types comparing with the optical clusters detected by the HST WFC3/UVIS V-band data. In most of the near-infrared cluster complexes, more than one clusters were detected with the HST optical imaging data. Therefore, we examined whether there exist optical clusters corresponding to the peak of the near-infrared cluster complex.

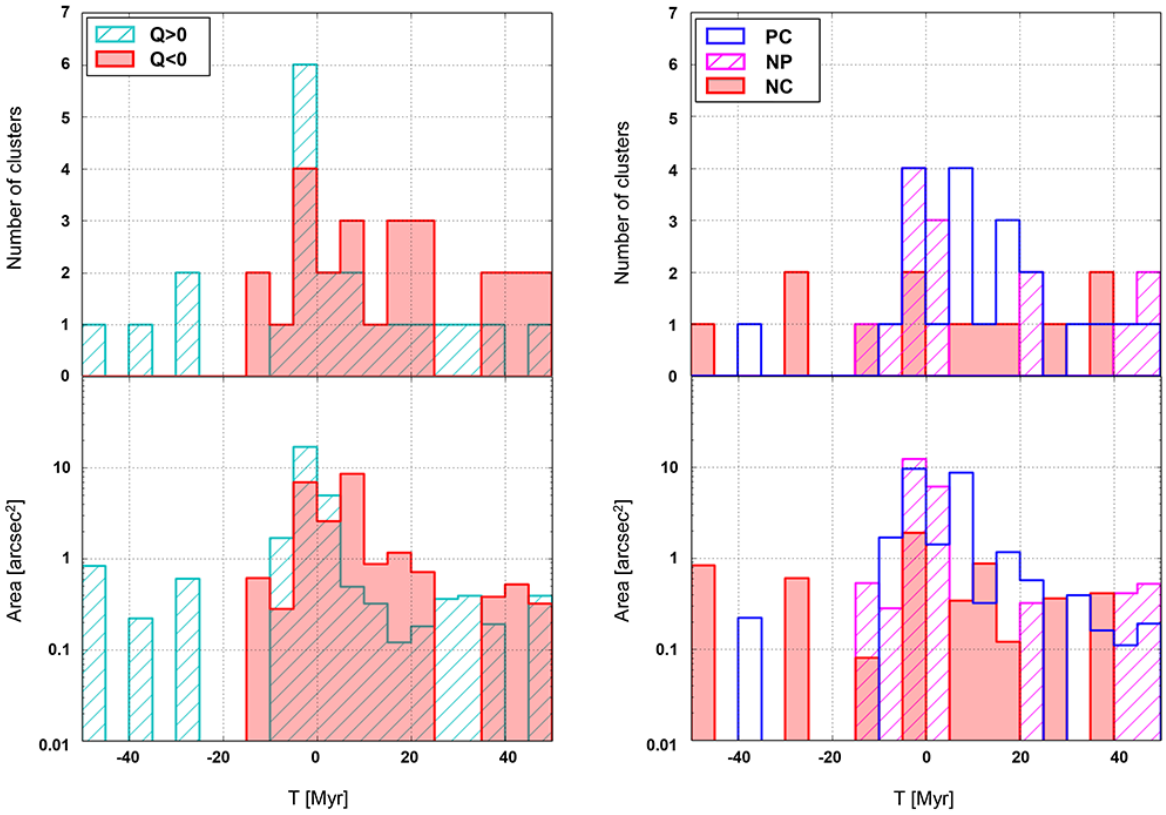

Figure 13.12: *(Left);* Number and area distributions of the young and the old cluster complexes in units of the kinematic age from the dust lane within the area between the deprojected radii of 65″ and 85″. *(Right);* Number and area distributions of the cluster complexes classified as PC, NP and NC.

PC : There exist optical clusters corresponding to the peak of the near-infrared cluster complex.

NP : There is no optical cluster corresponding to the peak of the near-infrared cluster complex due to the strong dust extinction although there exist some optical clusters in the complex.

NC : There is no optical cluster in the near-infrared cluster complex.

We display the distributions of the cluster complexes classified as PC, NP, and NC on the HST WFC3/UVIS V-band image in Figure 13.11 (b). We show the number and area distributions in the right panel of Figure 13.12. The distribution of the cluster complexes classified as PC is similar to that of the old (Q < 0) cluster complexes. On the other hand, the distribution of the cluster complexes classified as NP and NC is similar to that of the young (Q > 0) cluster complexes. The majority of the cluster complexes classified as NP and NC is the young (Q > 0) cluster complexes (58% in number, 71% in area). They are considered to have dust-embedded clusters younger than about a few Myr. The distributions of the cluster complexes classified as NP and NC are concentrated around the dust lane and have several small peaks in both sides, which are

similar to the distribution of the young cluster sample shown in Figure 13.3. Hence, the young cluster sample should be significantly affected by dust extinction, especially in the vicinity of the dust lane. However, the effect of dust extinction is much less in the upstream and downstream sides than on the dust lane. Consequently, the dust extinction does not significantly affect the normalized distribution of the young and the old cluster samples shown in the left panel of Figure 13.4.

Chapter 14

Discussion

14.1 Comparison with Density Wave Theory

14.1.1 Azimuthal Distributions of Young and Old Clusters

In Section 13.1, we showed that the old cluster sample is distributed downstream compared with the young cluster sample (Figure 13.3 and 13.4). This is in better agreement with cluster age distributions predicted by the density wave theory as illustrated in Figure 9.1 than those predicted by the recent numerical simulations as illustrated in Figure 9.2. The distribution of the old cluster sample has a peak at the kinematic age of $\sim$ 20 Myr in comparison with that of the young cluster sample which has a peak at the kinematic age of $\sim$ 0 Myr. On the other hand, the average age of the old cluster sample, which was estimated from the UBVI photometry (Section 13.2), is more than $\sim$ 20 Myr older than that of the young cluster sample. The difference of the kinematic ages that they have peaks is consistent with or younger than the difference of their average ages. The stellar clusters in the old cluster sample are considered to have been formed in the dust lane, given that gas and stellar clusters rotate in non-circular orbits (i.e., elliptical orbits nearly parallel to the spiral arm).

We investigated two effects capable of changing the distributions of the young and the old cluster samples: (1) very old clusters (Section 13.2), and (2) dust extinction (Section 13.3). The clusters older than 200 Myr seem to be uniformly distributed around the arm, and do not significantly affect the distribution of the old cluster sample (Figure 13.9). On the other hand, the young cluster sample is significantly affected by dust extinction in the vicinity of the dust lane. However, the effect of dust extinction is much less in the upstream and downstream sides than on the dust lane (Figure 13.12). Therefore, we conclude that both of (1) and (2) do not change the result that clusters older than 10 Myr are distributed downstream compared with younger clusters.

These results indicate that the star formation in the southern spiral arm of NGC 4321 is mainly

induced by the density wave. However, we note that the star formation around the spiral arm cannot be explained only by the density wave. The young cluster sample has several small peaks around the kinematic ages of −40, 20, and 40 Myr (Figure 13.3). In the vicinity of the peaks, the middle and the old cluster samples also have peaks, which are as high as or higher than those of the young cluster sample. The similar trend is also found in the distributions of near-infrared cluster complexes (Figure 13.12). We consider that such clusters were formed by other origins than the density wave, e.g., secondary star formation.

14.1.2 Importance of Old Stellar Population

We found the difference between the distributions of the young and the old cluster samples, but no difference between the distributions of the dust lane and the young cluster sample (Figure 13.3 and 13.4). We suggest that the main reason for no offset between the dust lane and HII regions in this galaxy is because the arms are located near the corotation resonance due to the large bar structure. The dust lane of this galaxy seems to have the width of about 300 pc in the radial region where we investigated the azimuthal distribution of clusters. The width corresponds to the kinematic age from −10 Myr to 10 Myr. The range of the kinematic age is longer than the time scale of star formation and the age of clusters with strong Hα emission ($\lesssim$ 6 Myr).

E09 found almost no offsets between molecular clouds and HII regions in the arm region, but found small offsets in the bar structure. They estimated the pattern speed of $\Omega_{\rm P} = 31 \pm 20$ km/s/kpc which is consistent with the pattern speed derived kinematically by Canzian & Allen (1997). In their results, galaxies with clear offsets also tend to show no offsets near the corotation resonance (see their Figure 6). Our and E09's results indicate that it is difficult to detect clear offsets between molecular clouds (dust lane) and star forming regions traced by Hα emission near the corotation resonance. Therefore, tracing older star formation histories than Hα emission (i.e., 10 Myr) is essential to verify the density wave in the arm region of this galaxy.

14.1.3 Importance of High Resolution Imaging

F12 found no clear difference between the distribution of HII regions and UV star-forming regions by using the deep UV imaging data with the angular resolution of 2″.5. However, when we focus on the arm region where the offsets between young and old stellar populations are predicted, the old sources tend to be distributed downstream of the dust lane compared with the young sources (Figure 10.1 and 10.2). This is also the case with the near-infrared imaging data with the angular resolution of 0″.7 from GD12. We see that cluster complexes older than 6 Myr tend to be distributed downstream compared with younger ones (Figure 13.11). However, in both cases, the

number of sources is too small to verify the difference between the distributions of young and old ones statistically.

In the HST high resolution imaging data, the spatial distribution of the old cluster sample is not concentrated, but sparse in comparison with the young and the middle cluster samples (Figure 13.1). The lower resolution imaging data we use, the more difficult it is to detect clusters in the old cluster sample. Therefore, the high resolution imaging data, which are capable of detecting individual clusters with a few parsec in radius, are essential to investigate the distribution of clusters older than 10 Myr.

14.2 Origin of Spiral Structures

14.2.1 Spiral Structure of NGC 4321

We succeeded in discovering an observational evidence to support the density wave that old stellar clusters are distributed downstream of young stellar clusters in NGC 4321. This result seems to support the quasi-stationary spiral structure rather than non-stationary spiral structure predicted by recent theoretical studies. However, we cannot deny that the density wave is induced by companions (e.g., NGC4323) and temporary (Toomre 1981). Considering that there is a possibility that a galactic shock is formed in less than 1 Gyr (Woodward 1975), it is difficult to confirm whether the spiral structure is sustained over 1 Gyr only by using methods to investigate the morphological features predicted by the density wave theory.

The systematic radial dependence of offsets among different tracers of star formation histories is strong evidence for the density wave theory. However, our method to investigate the age distribution of stellar clusters is not appropriate for verifying the systematic offsets, because a relatively wide radial range is needed to investigate the difference between the distributions of young and old stellar clusters statistically. Recently, Baba et al. (2015) presented a new observational test from numerical simulations of spiral structures. They found that the spiral models of quasi-stationary spiral structures show systematic radial dependence of offsets between dust lanes and stellar spiral arms (i.e., potential minima). On the other hand, the spiral models of non-stationary spiral structures show no systematic offsets. This method may be suitable for detecting the systematic offsets because the tracers are not affected by the recent star formation histories in principle. However, it is observationally difficult to obtain maps of stellar mass density accurately by excluding the effect of young stellar populations (e.g., Kendall et al. 2011). It should be studied in future work.

14.2.2 Spiral Structure of Other Spiral Galaxies

In Part I, spiral galaxies with the bar structures ($R_{bar} > 3$ kpc), which were classified as Type3, showed almost no offsets between dust lanes and HII regions. NGC 4321 is one of the Type 3 galaxies, and has the bar structure of $R_{bar}/R_{CR} \simeq 0.6$. Figure 7.1 shows that the other Type3 galaxies (NGC 4548, NGC 4579, NGC 5248) show the bar structure of $R_{bar}/R_{CR} \gtrsim 0.6$. Therefore, there is a possibility that it is difficult to detect clear offsets between dust lanes and HII regions for spiral galaxies with $R_{bar}/R_{CR} \gtrsim 0.6$ because the arms are located near the corotation resonance.

This study focused on galaxies close to grand design spiral galaxies, i.e., the two-arm mode is the strongest. Considering that we found offsets between dust lanes and HII regions for galaxies without and with bar structure smaller than 3 kpc, we infer that the origin of spiral structures in grand design spiral galaxies may be generally explained by the density wave theory. However, we found the difference between the distributions of young and old stellar clusters in only one of the galaxies with bar structure larger than 3 kpc. We need to verify the density wave by investigating the age distribution of resolved stellar clusters in other large barred spiral galaxies. In addition, we should examine whether the offsets (e.g., between dust lanes and stellar spiral arms) depend on the radius systematically to verify the density wave with higher accuracy.

Recently, Choi et al. (2015) found no evidence of the density wave theory with resolved stellar populations in a grand design spiral galaxy NGC 3031. As for this galaxy, the morphological classification is SA(s)ab, and the inclination is large ($i = 59°$; de Blok et al. 2008). The star formation activity is relatively weak and the dust lanes seem to be not prominent in comparison with our sample galaxies in Part I. Furthermore, Choi et al. (2015) used the HST/ACS imaging data taken with only two broad-band filters (F435W and F606W) to derive the spatially resolved SFHs. We suggest that further studies are needed to investigate whether the spiral arms are against the density wave.

In addition to grand design spiral galaxies, it is also unclear whether flocculent and multiple-arm spiral galaxies have quasi-stationary or non-stationary spiral structures. The nearby galaxy surveys with the HST (e.g., SHUCS; The Snapshot Hubble U-band Cluster Survey; Konstantopoulos et al. 2013, LEGUS; Legacy ExtraGalactic UV Survey; Calzetti et al. 2015) will provide a number of spiral galaxies for such studies. Applying this method to spiral galaxies with various arm types from grand design to flocculent will help us to understand the origin of spiral structures.

Chapter 15

Summary of Part II

The grand design spiral galaxy NGC 4321 is a representative galaxy against the density wave theory of quasi-stationary spiral structures. In the spiral arms, no significant differences have been found not only in the distribution of molecular gas and HII regions, but also in the distribution of HII regions and UV star-forming sources. Previous studies inferred that this galaxy has material arms, i.e., non-stationary spiral structure. However, the angular resolution of a few arcseconds might not be high enough to reject the density wave theory. Therefore, we used the HST high resolution imaging data to investigate the difference between the distributions of young and old stellar clusters.

We detected cluster candidates with the HST WFC3/UVIS F555W image, whose angular resolution of $0''.04$ is equal to the physical size of ~ 3 pc in NGC 4321. We used the HST WFPC2 F675W and F658N images to separate the clusters into the following three samples with different ages; young (Age $\lesssim$ 6 Myr), middle (6 Myr $\lesssim$ Age $\lesssim$ 10 Myr) and old (Age $\gtrsim$ 10 Myr). We investigated the azimuthal distributions of three cluster samples around the southern spiral arm. We found that the old cluster sample is distributed downstream of the young cluster sample. This was in agreement with the density wave theory which predicts the age gradient of stellar clusters across the spiral arm.

We investigated the effects of very old clusters and dust extinction on the distributions of the young and the old cluster samples. The clusters older than 200 Myr selected from the UBVI colors seemed to be uniformly distributed around the arm, and did not significantly affect the distribution of the old cluster sample. In addition, the effect of dust extinction estimated from ground-based near-infrared observations was significant on the young cluster sample in the vicinity of the dust lane, but not significant in the upstream and downstream sides of the dust lane. Therefore, we concluded that very old clusters and dust extinction do not affect the result that the old cluster sample is distributed downstream of the young cluster sample.

We found the difference between the distributions of the young and the old cluster samples, but no difference between the distributions of the dust lane and the young cluster sample. This result indicated that it is difficult to detect clear offsets between the dust lane and star forming regions traced by Hα emission because this galaxy has the arms near the corotation resonance due to the large bar structure. Therefore, tracing old star formation histories than 10 Myr was essential to verify the density wave in this galaxy. In addition, the spatial distribution of the old cluster sample was not concentrated, but sparse in comparison with the young and the middle cluster samples. The high resolution imaging data, which are capable of detecting resolved stellar clusters, were essential to investigate the distribution of stellar clusters older than 10 Myr.

NGC 4321 is one of the Type 3 galaxies which showed almost no offsets between dust lanes and HII regions in Part I. This galaxy has the bar structure of $R_{bar}/R_{CR} \simeq 0.6$. Regarding the other Type 3 galaxies with $R_{bar}/R_{CR} \gtrsim 0.6$, there is also a possibility that it is difficult to detect clear offsets between dust lanes and HII regions because the arms are located near the corotation resonance. The new method of investigating the distribution of resolved stellar clusters older than 10 Myr is essential to verify the density wave theory in such galaxies.

Chapter 16

Conclusions

In this study, we have verified the density wave theory with two approaches.

In Part I, we investigated the difference of offsets between gas arms and star forming regions in 12 nearby spiral galaxies with two prominent spiral arms. We traced dust lanes as a sign of molecular gas arms with I−H or I−K color images. We measured the offset $\theta_{\rm offset}$, i.e., the average position of the Hα emission intensity with respect to dust lanes within the azimuth angle from -50° to $+50^\circ$. We summarize our main results in Part I below.

- We found that the bar structure is related to the offset. Twelve galaxies were classified into three types based on the bar structure. (Type 1;) galaxies without bar structure (NGC 628, NGC 3631, NGC 4254, and NGC 5194). (Type 2;) galaxies with bar structure of the radii smaller than 3 kpc (NGC 1068, NGC 3184, and NGC 4303). (Type 3;) galaxies with bar structure of the radii larger than 3 kpc (NGC 4321, NGC 4535, NGC 4548, NGC 4579, and NGC 5248). The average values of $\theta_{\rm offset}$ for Type 1, 2, and 3 galaxies were 10°, 7° and 1°, respectively. Type 3 galaxies showed almost no offsets.

- We newly found three galaxies with no offsets in addition to two galaxies which have been found no offsets between molecular clouds and HII regions in Egusa et al. (2009).

- There is a possibility that the reason for no offsets can be explained by the effects of corotation resonance and elliptical orbits nearly parallel to the spiral arms. To test the density wave in Type 3 galaxies, we need other methods to trace older star formation histories than Hα emission (i.e., 10 Myr).

In Part II, we investigated the difference between the distributions of young and old stellar clusters in NGC 4321 with the HST high resolution imaging data. In this galaxy, no significant differences have been found in the distribution of HII regions and UV star-forming sources with the ages over 100 Myr in Ferreras et al. (2012). We detected cluster candidates with the HST WFC3/UVIS F555W image, whose angular resolution of $0''.04$ is equal to the physical size of ~ 3 pc. We used the HST WFPC2 F675W and F658N images to separate the clusters into the following three samples with different ages; young (Age $\lesssim 6$ Myr), middle (6 Myr $\lesssim$ Age $\lesssim 10$ Myr) and old (Age $\gtrsim 10$ Myr). We investigated the azimuthal distributions of three cluster samples around the southern spiral arm. We summarize our main results in Part II below.

- We succeeded in discovering an observational evidence in support of the density wave theory that the old cluster sample is distributed downstream of the young cluster sample.
- The ground-based near-infrared observations suggested that dust extinction is significant for the young cluster sample, but the effect is not significant in the upstream and downstream sides of the dust lane. Therefore, it does not affect the result that the old cluster sample is distributed downstream of the young cluster sample.
- There is a possibility that it is difficult to detect the offsets between molecular gas and star forming regions for spiral galaxies with relatively large bar structures ($R_{bar}/R_{CR} \gtrsim 0.6$), because the arms are located near the corotation resonance.
- The new method of investigating the distribution of resolved stellar clusters older than 10 Myr is essential to verify the density wave theory in such galaxies.

Appendix A

Tracing Dust Lanes

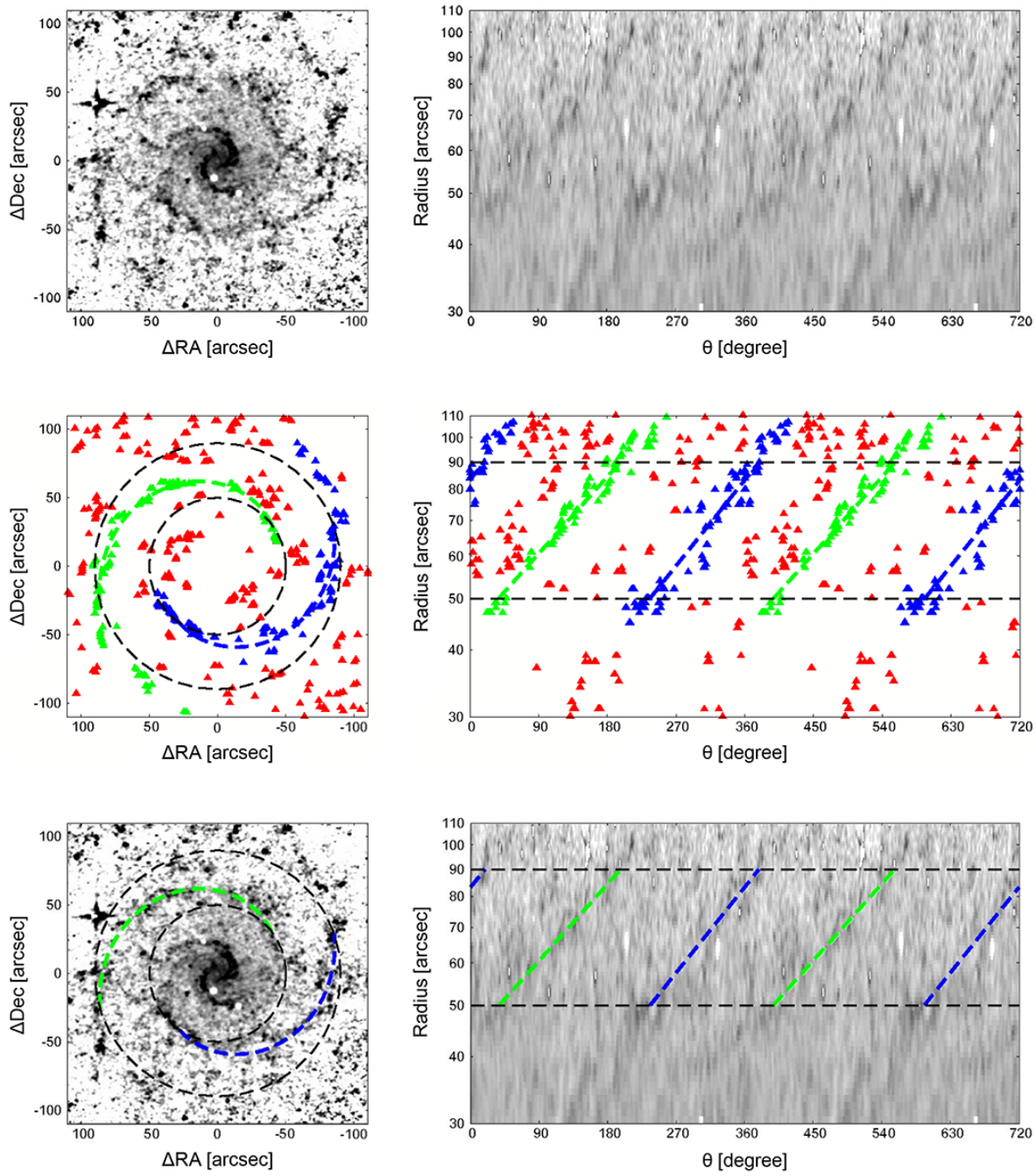

Figure A.1: [NGC 628] *(Top);* The deprojected I−K color images on the (ΔRA, ΔDec) and (log R, θ) planes. *(Middle);* The detected peaks are shown with triangles on the same planes as top panels. The peaks used for tracing dust lanes are shown with green and blue triangles, and the dust lanes we traced are shown with green and blue dashed lines. *(Bottom);* The dust lanes we traced are shown with green and blue dashed lines on the same images as top panels.

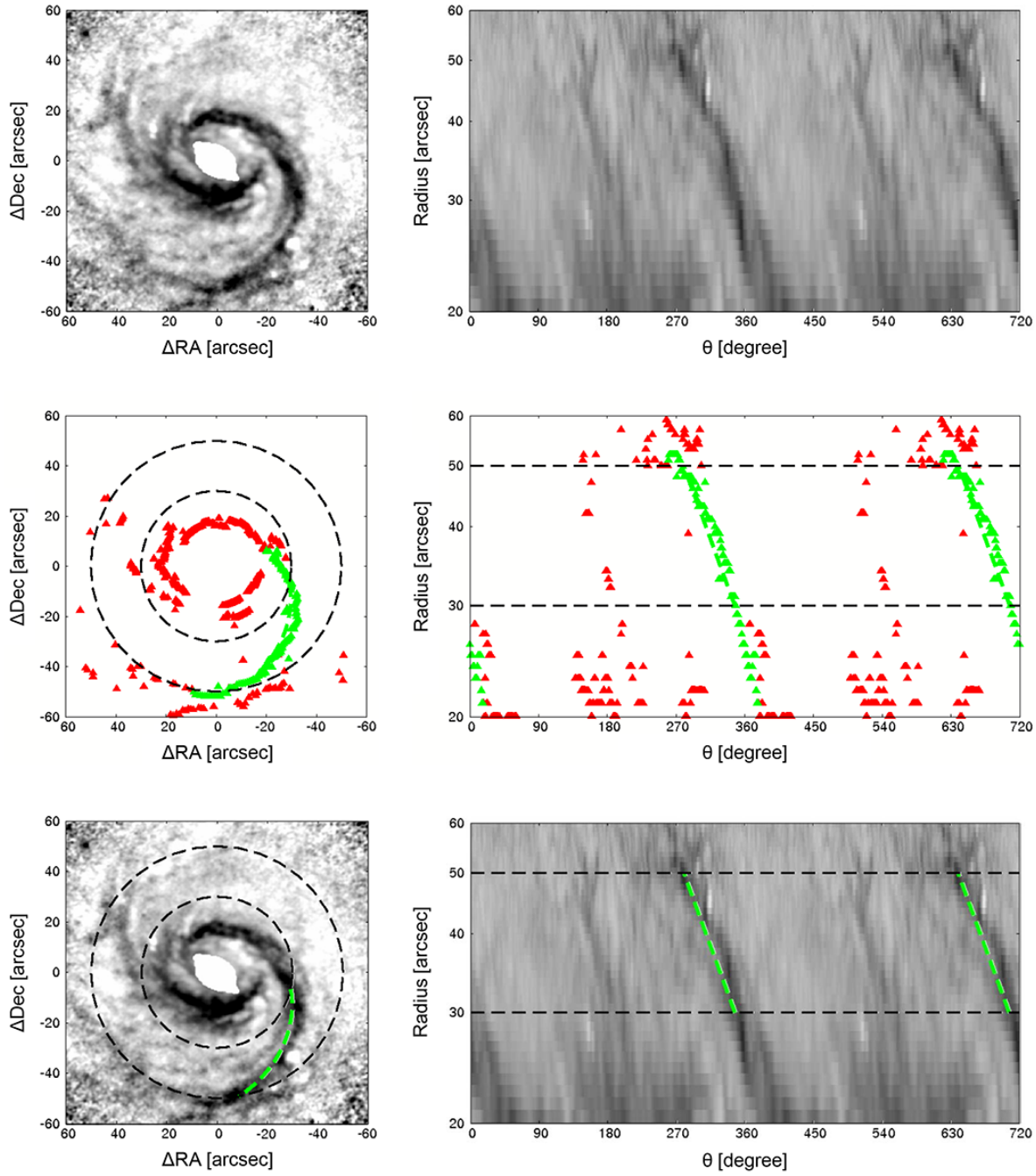

Figure A.2: [NGC 1068] *(Top);* The deprojected I−K color images on the (ΔRA, ΔDec) and (log R, θ) planes. *(Middle);* The detected peaks are shown with triangles on the same planes as top panels. The peaks used for tracing a dust lane are shown with green triangles, and the dust lane we traced is shown with green dashed lines. *(Bottom);* The dust lane we traced is shown with green dashed lines on the same images as top panels.

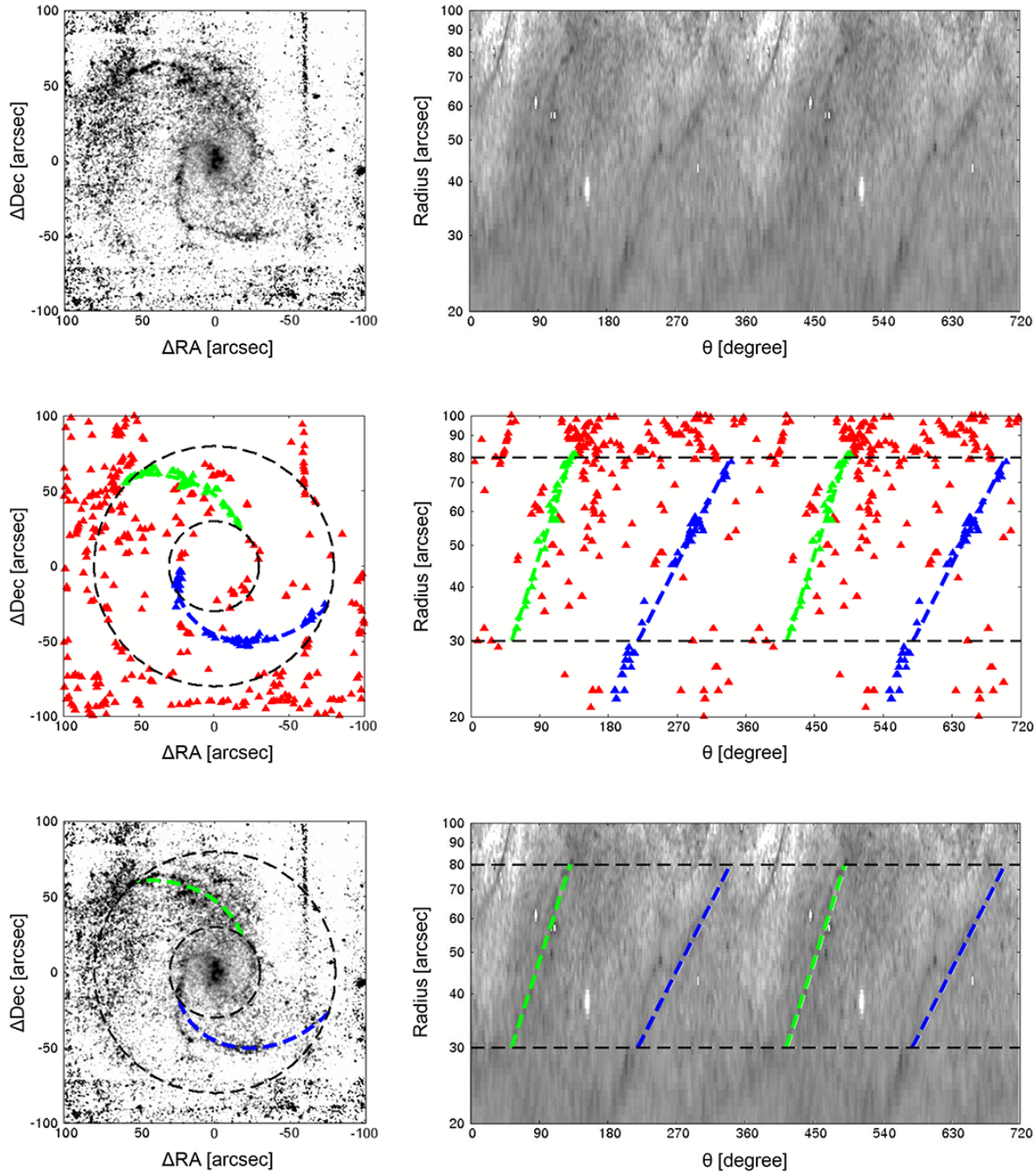

Figure A.3: [NGC 3184] *(Top);* The deprojected I−K color images on the (ΔRA, ΔDec) and (log R, θ) planes. *(Middle);* The detected peaks are shown with triangles on the same planes as top panels. The peaks used for tracing dust lanes are shown with green and blue triangles, and the dust lanes we traced are shown with green and blue dashed lines. *(Bottom);* The dust lanes we traced are shown with green and blue dashed lines on the same images as top panels.

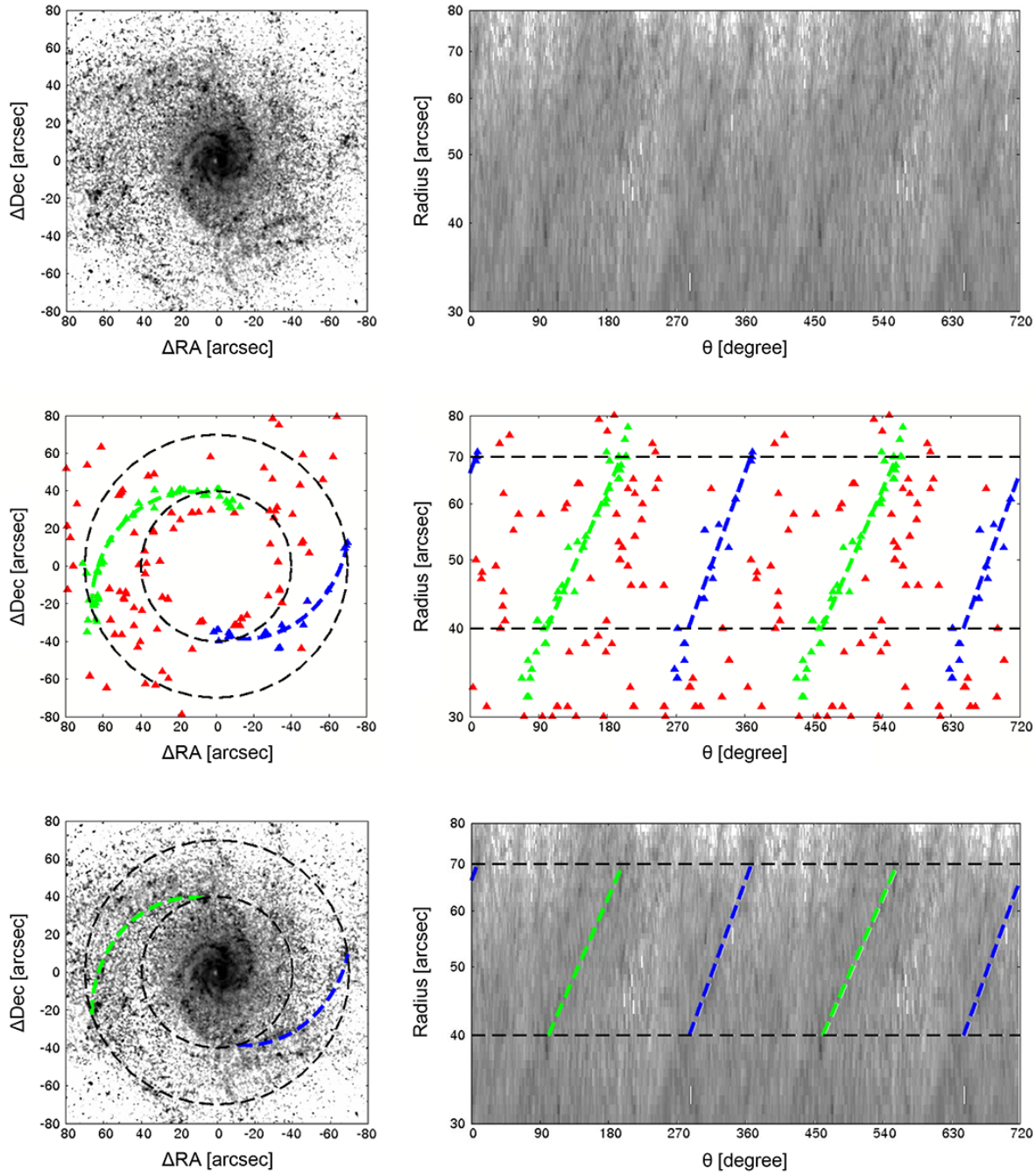

Figure A.4: [NGC 3631] *(Top);* The deprojected I−K color images on the (ΔRA, ΔDec) and (log R, θ) planes. *(Middle);* The detected peaks are shown with triangles on the same planes as top panels. The peaks used for tracing dust lanes are shown with green and blue triangles, and the dust lanes we traced are shown with green and blue dashed lines. *(Bottom);* The dust lanes we traced are shown with green and blue dashed lines on the same images as top panels.

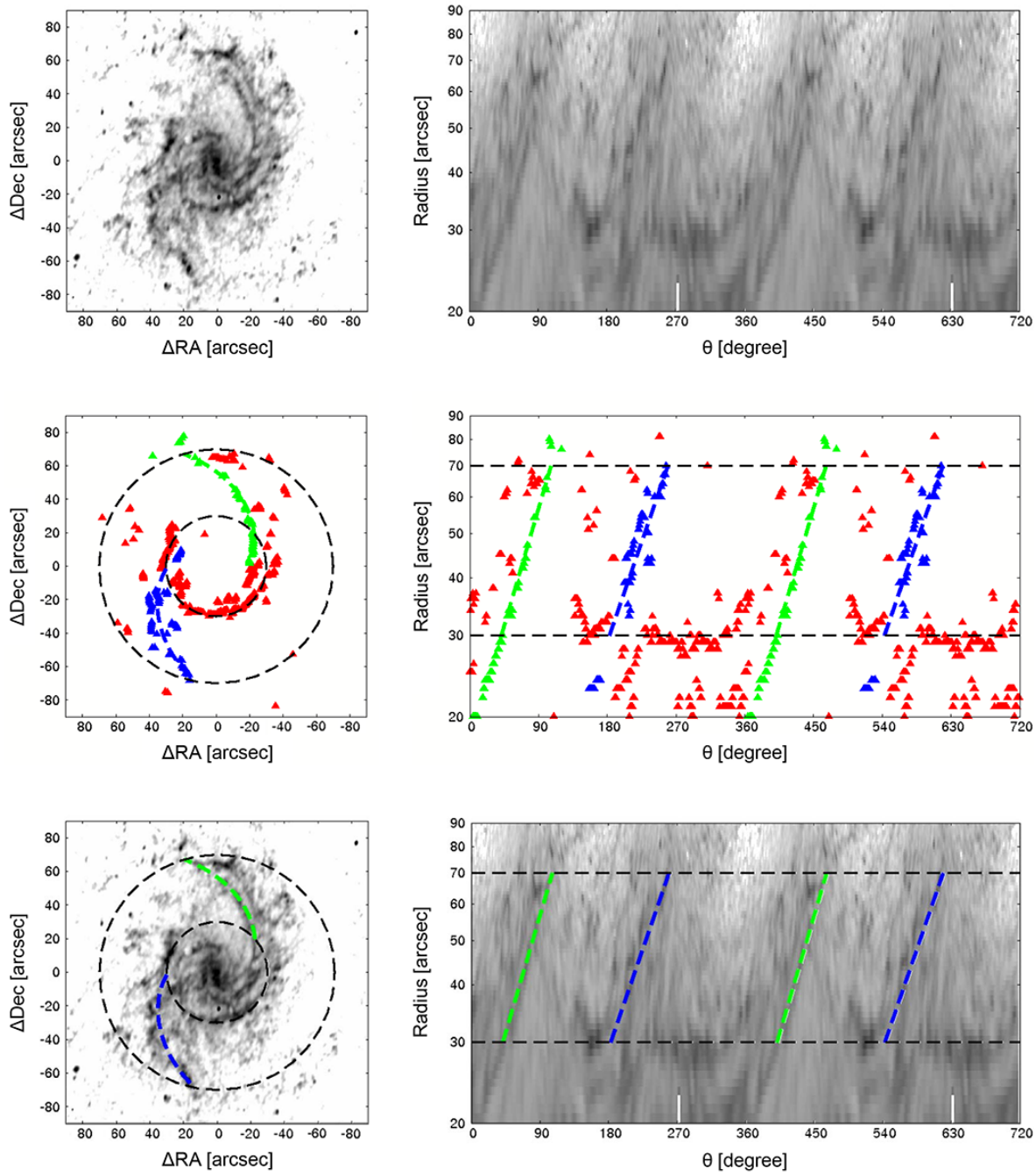

Figure A.5: [NGC 4254] *(Top);* The deprojected I−K color images on the (ΔRA, ΔDec) and (log R, θ) planes. *(Middle);* The detected peaks are shown with triangles on the same planes as top panels. The peaks used for tracing dust lanes are shown with green and blue triangles, and the dust lanes we traced are shown with green and blue dashed lines. *(Bottom);* The dust lanes we traced are shown with green and blue dashed lines on the same images as top panels.

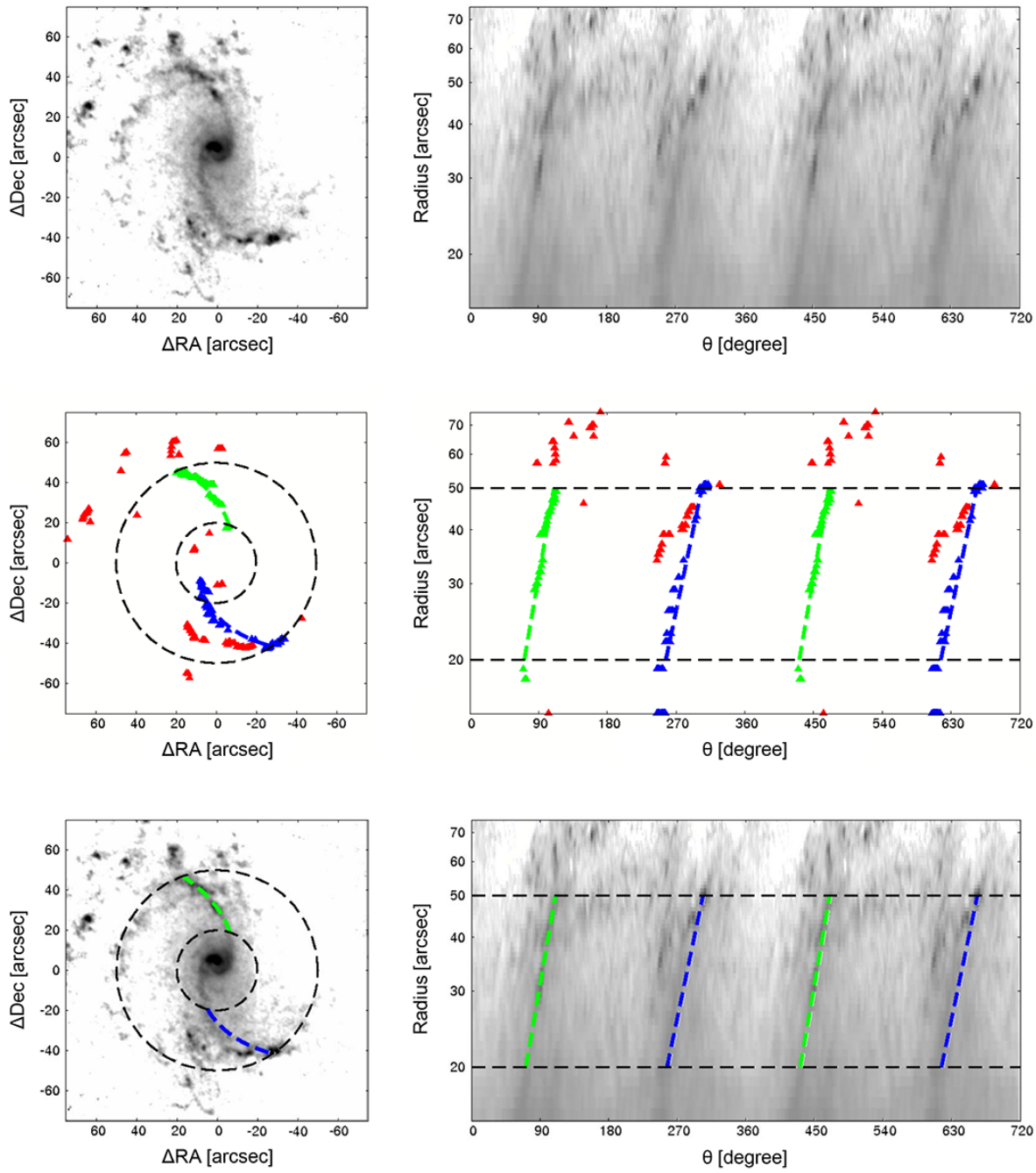

Figure A.6: [NGC 4303] *(Top);* The deprojected I−K color images on the (ΔRA, ΔDec) and (log R, θ) planes. *(Middle);* The detected peaks are shown with triangles on the same planes as top panels. The peaks used for tracing dust lanes are shown with green and blue triangles, and the dust lanes we traced are shown with green and blue dashed lines. *(Bottom);* The dust lanes we traced are shown with green and blue dashed lines on the same images as top panels.

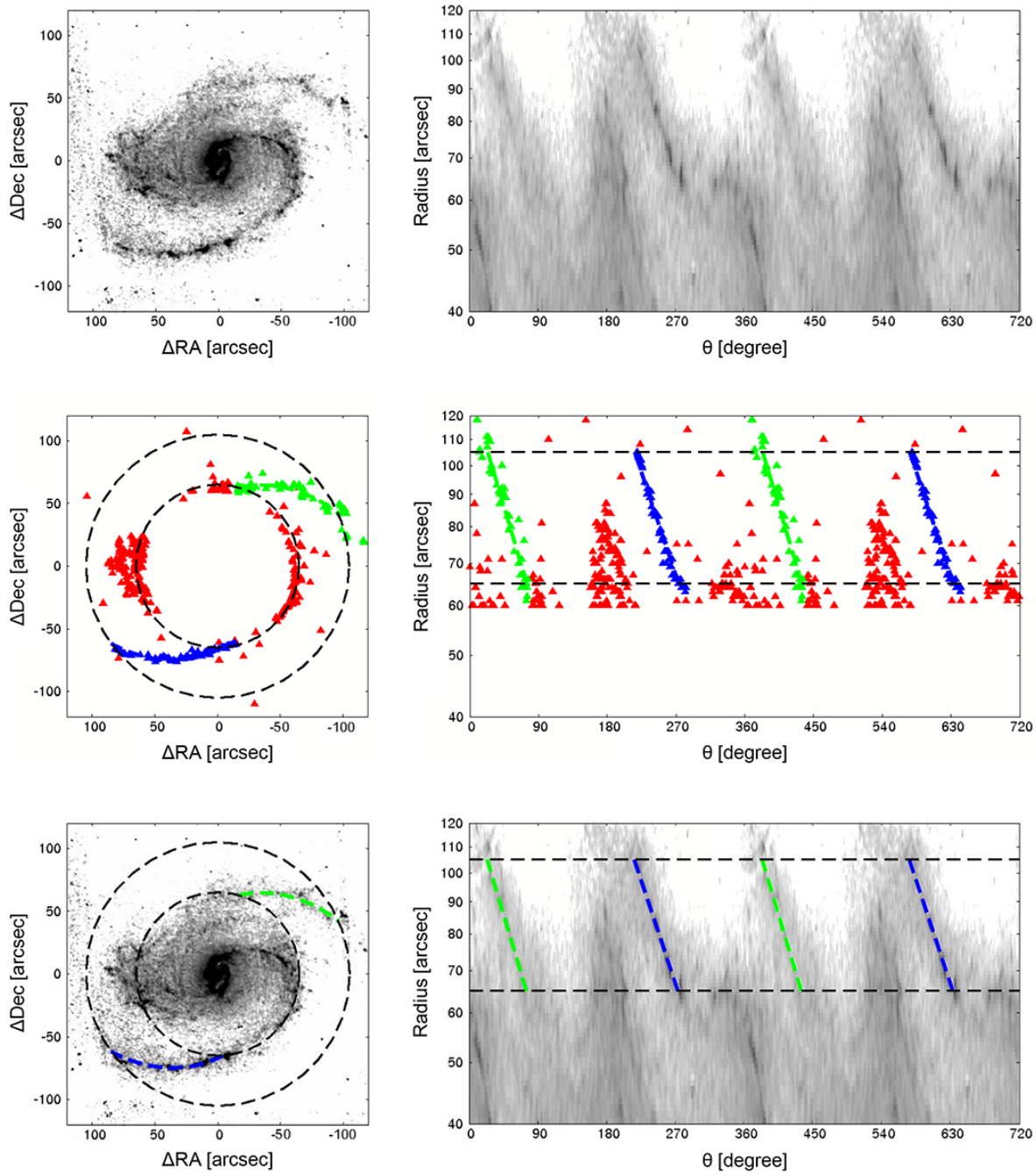

Figure A.7: [NGC 4321] *(Top);* The deprojected I−K color images on the (ΔRA, ΔDec) and (log R, θ) planes. *(Middle);* The detected peaks are shown with triangles on the same planes as top panels. The peaks used for tracing dust lanes are shown with green and blue triangles, and the dust lanes we traced are shown with green and blue dashed lines. *(Bottom);* The dust lanes we traced are shown with green and blue dashed lines on the same images as top panels.

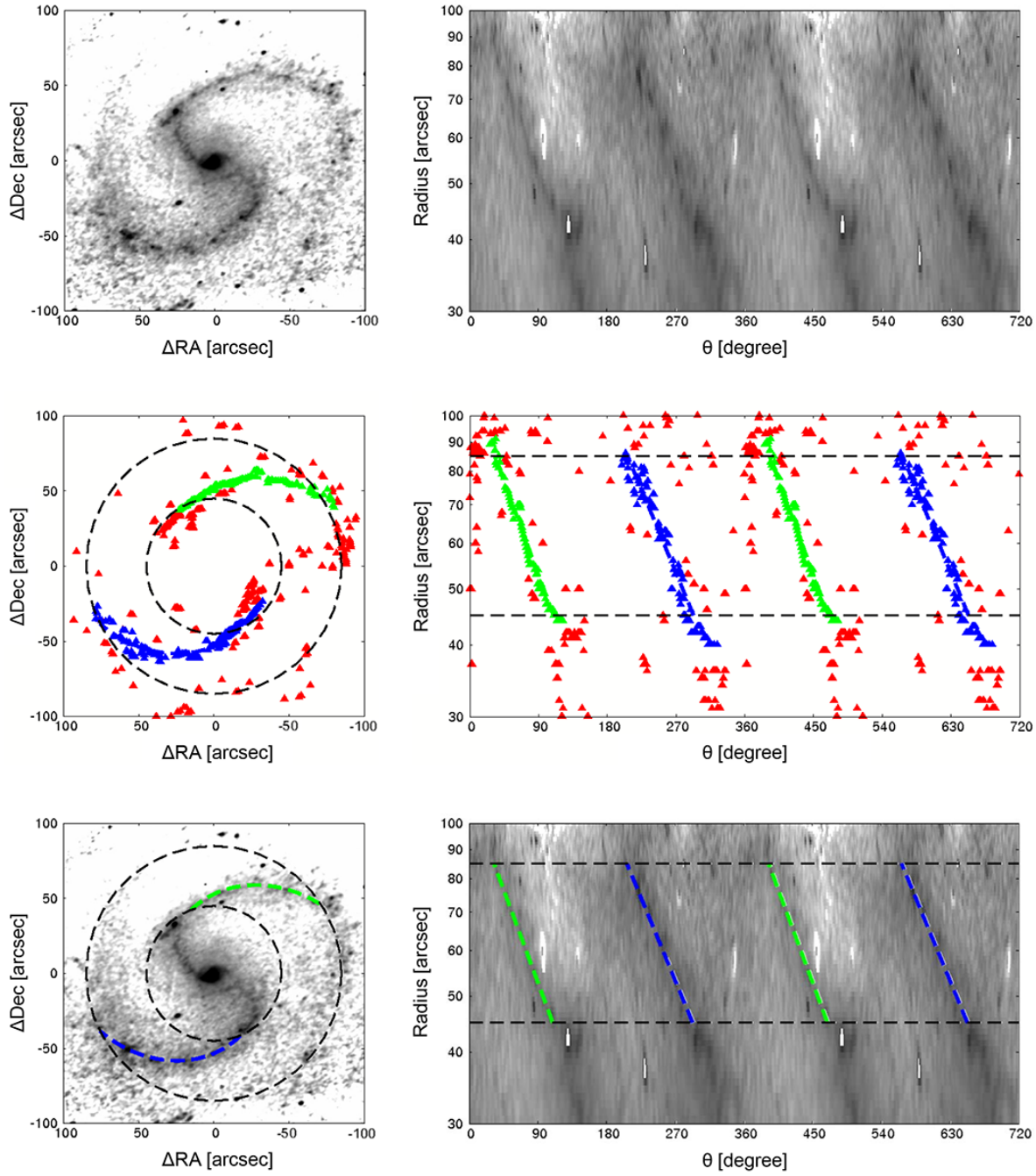

Figure A.8: [NGC 4535] *(Top);* The deprojected I−K color images on the (ΔRA, ΔDec) and (log R, θ) planes. *(Middle);* The detected peaks are shown with triangles on the same planes as top panels. The peaks used for tracing dust lanes are shown with green and blue triangles, and the dust lanes we traced are shown with green and blue dashed lines. *(Bottom);* The dust lanes we traced are shown with green and blue dashed lines on the same images as top panels.

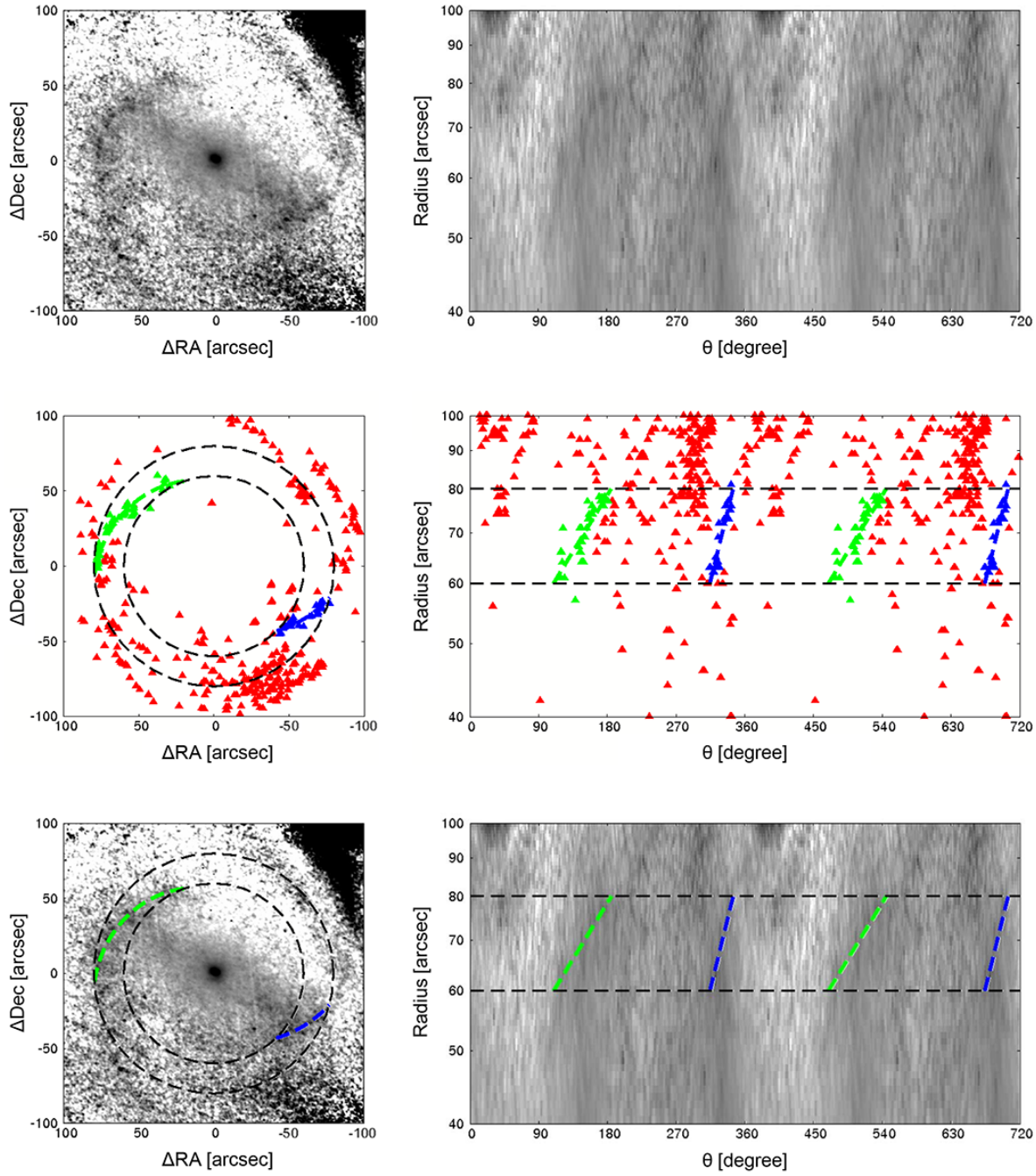

Figure A.9: [NGC 4548] *(Top);* The deprojected I−K color images on the (ΔRA, ΔDec) and (log R, θ) planes. *(Middle);* The detected peaks are shown with triangles on the same planes as top panels. The peaks used for tracing dust lanes are shown with green and blue triangles, and the dust lanes we traced are shown with green and blue dashed lines. *(Bottom);* The dust lanes we traced are shown with green and blue dashed lines on the same images as top panels.

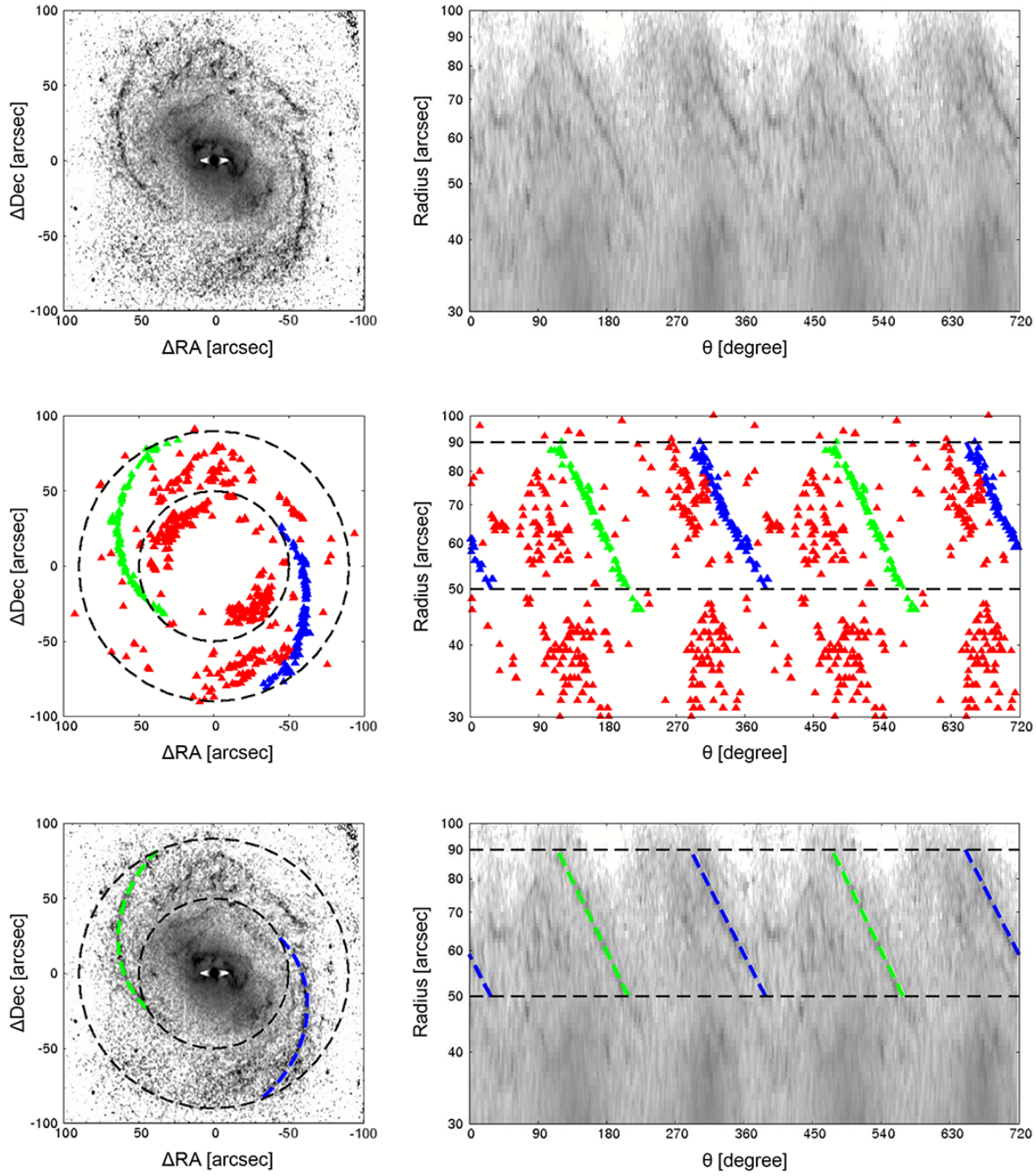

Figure A.10: [NGC 4579] *(Top);* The deprojected I−K color images on the (ΔRA, ΔDec) and (log R, θ) planes. *(Middle);* The detected peaks are shown with triangles on the same planes as top panels. The peaks used for tracing dust lanes are shown with green and blue triangles, and the dust lanes we traced are shown with green and blue dashed lines. *(Bottom);* The dust lanes we traced are shown with green and blue dashed lines on the same images as top panels.

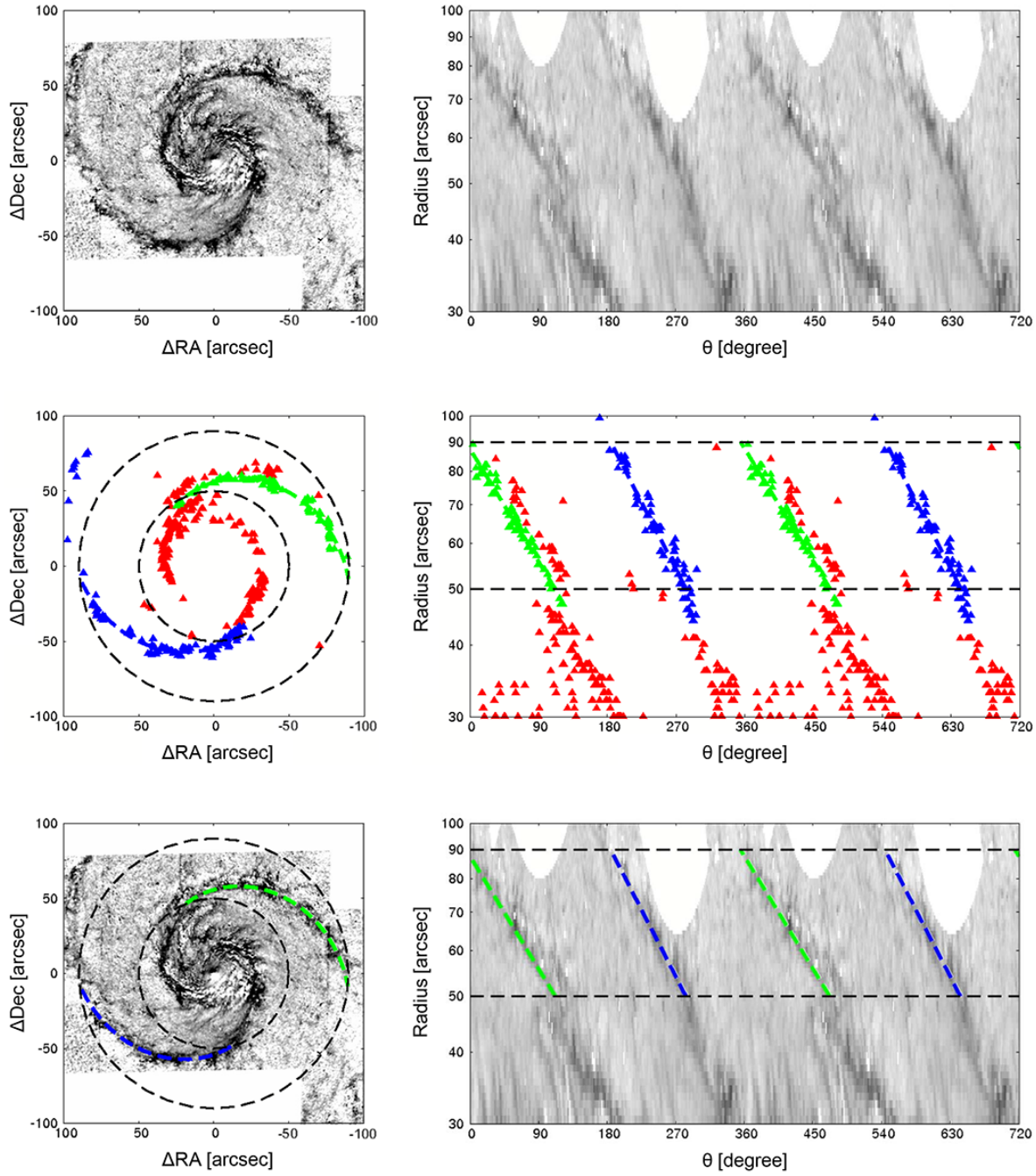

Figure A.11: [NGC 5194] *(Top);* The deprojected I−H color images on the (ΔRA, ΔDec) and (log R, θ) planes. *(Middle);* The detected peaks are shown with triangles on the same planes as top panels. The peaks used for tracing dust lanes are shown with green and blue triangles, and the dust lanes we traced are shown with green and blue dashed lines. *(Bottom);* The dust lanes we traced are shown with green and blue dashed lines on the same images as top panels.

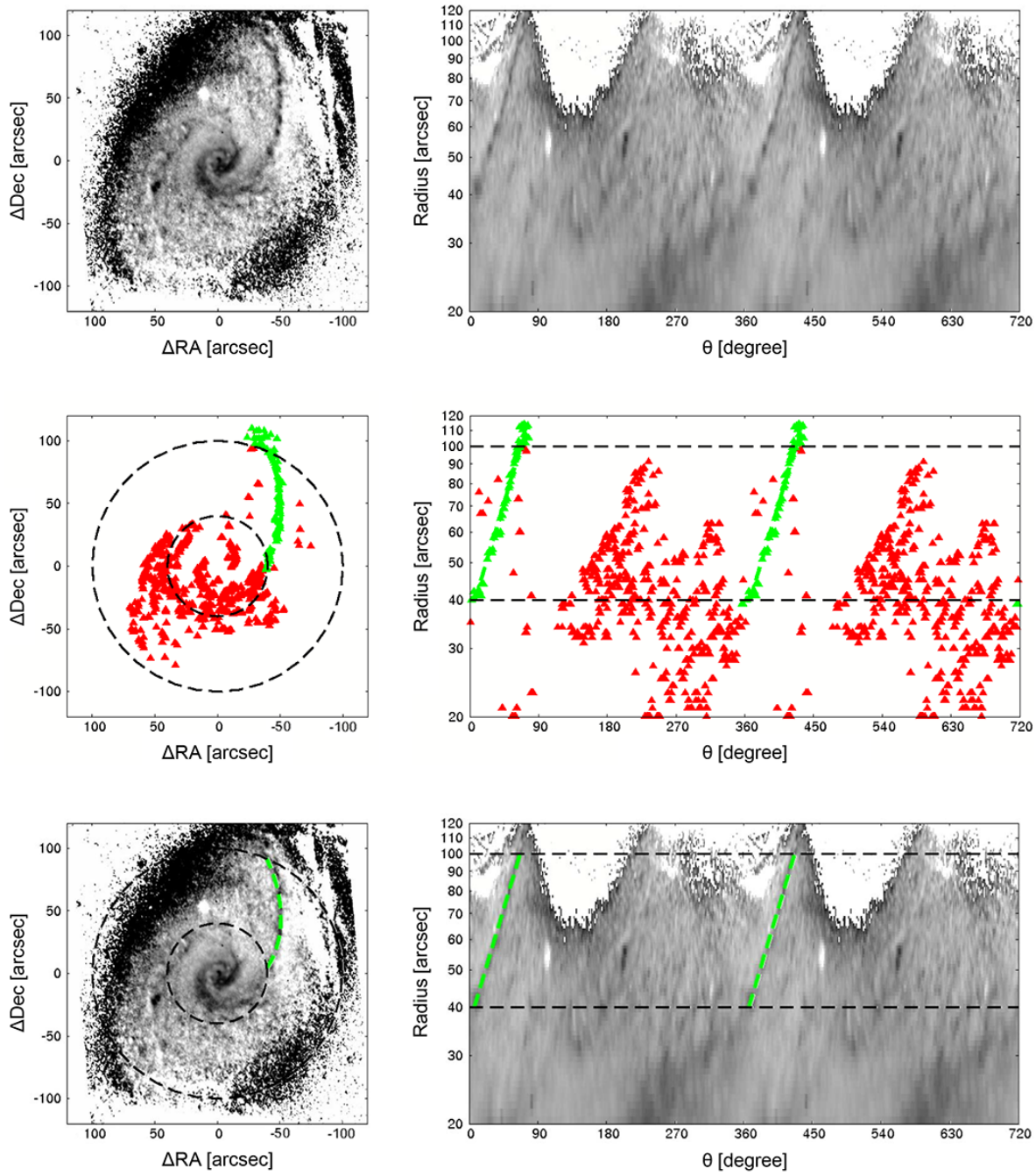

Figure A.12: [NGC 5248] *(Top);* The deprojected I−K color images on the (ΔRA, ΔDec) and (log R, θ) planes. *(Middle);* The detected peaks are shown with triangles on the same planes as top panels. The peaks used for tracing a dust lane are shown with green triangles, and the dust lane we traced is shown with green dashed lines. *(Bottom);* The dust lane we traced is shown with green dashed lines on the same images as top panels.

Appendix B

Distribution of Star Forming Regions with Respect to Dust Lanes

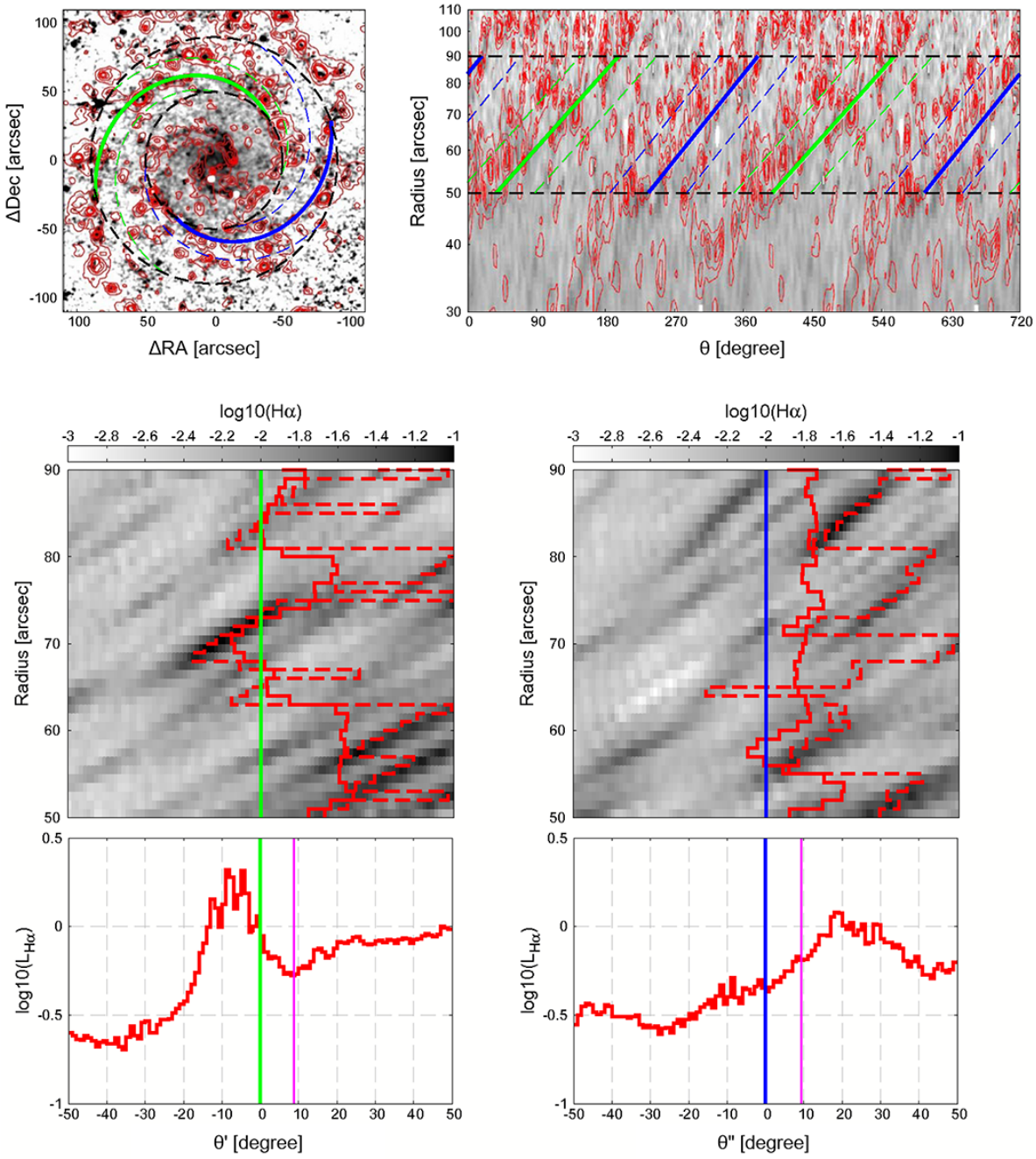

Figure B.1: [NGC 628] *(Top);* The red contour lines for the Hα emission on the deprojected I−K color images on the (ΔRA, ΔDec) and (log R, θ) planes. The dust lanes are shown with green and blue lines. The positions at the azimuth angle ± 50° with respect to the dust lanes are shown with green and blue dashed lines. *(Bottom);* The upper panels show the continuum-subtracted Hα images on the (R, θ') and (R, θ'') planes in negative representation. The average and the peak azimuth angle of the Hα emission intensity according to the radius are shown with red solid lines and red dashed lines respectively. The lower panels show the distribution of the sum of the Hα emission intensity within the radial region where we traced dust lanes according to the azimuth angle (θ', θ''). The magenta lines show the $\theta_{\rm offset}$.

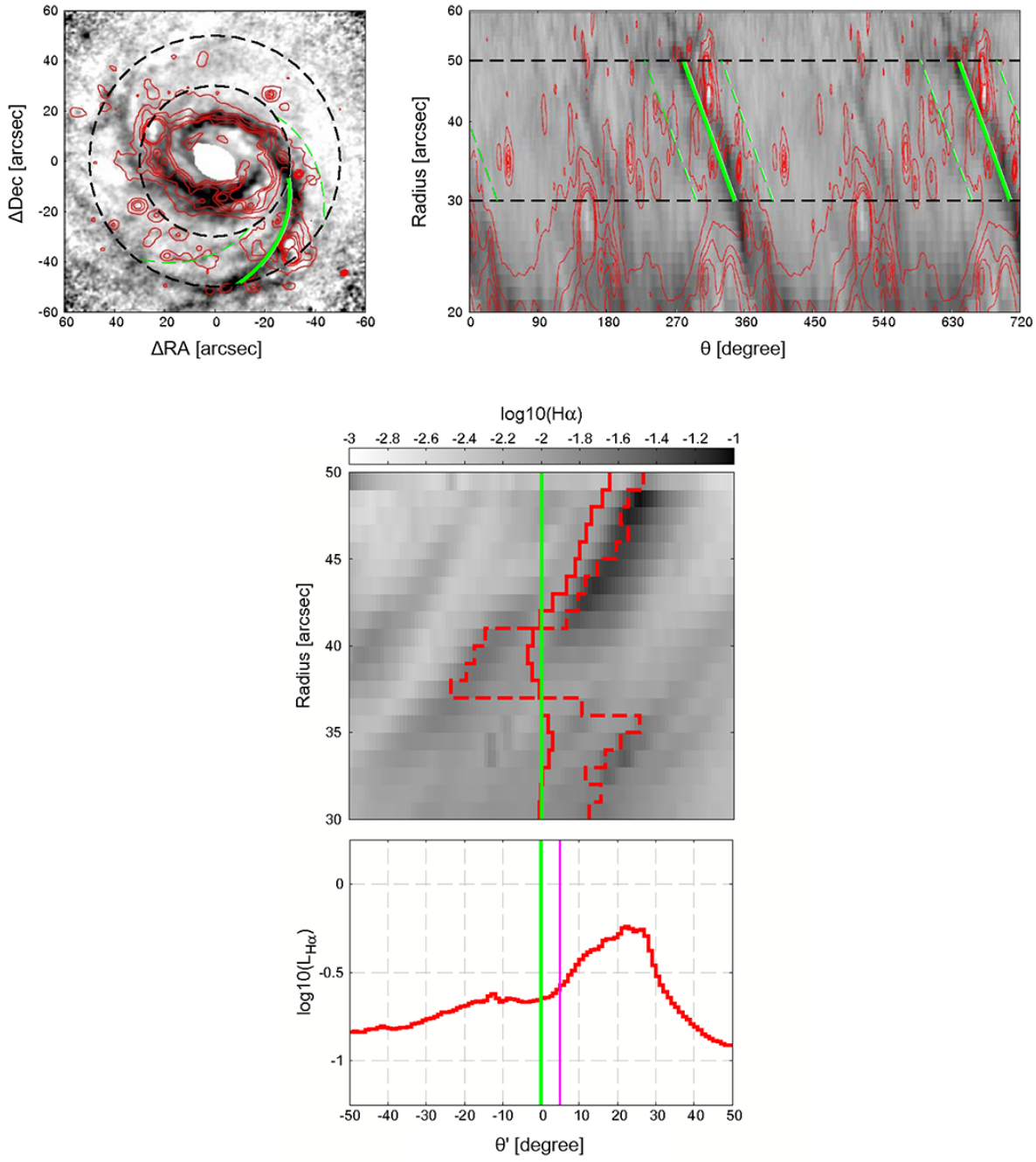

Figure B.2: [NGC 1068] *(Top);* The red contour lines for the Hα emission on the deprojected I−K color images on the (ΔRA, ΔDec) and (log R, θ) planes. The dust lane is shown with green lines. The positions at the azimuth angle ± 50° with respect to the dust lane are shown with green dashed lines. *(Bottom);* The upper panel shows the continuum-subtracted Hα image on the (R, θ') plane in negative representation. The average and the peak azimuth angle of the Hα emission intensity according to the radius are shown with a red solid line and a red dashed line respectively. The lower panel shows the distribution of the sum of the Hα emission intensity within the radial region where we traced dust lane according to the azimuth angle (θ'). The magenta line shows the $\theta_{\rm offset}$.

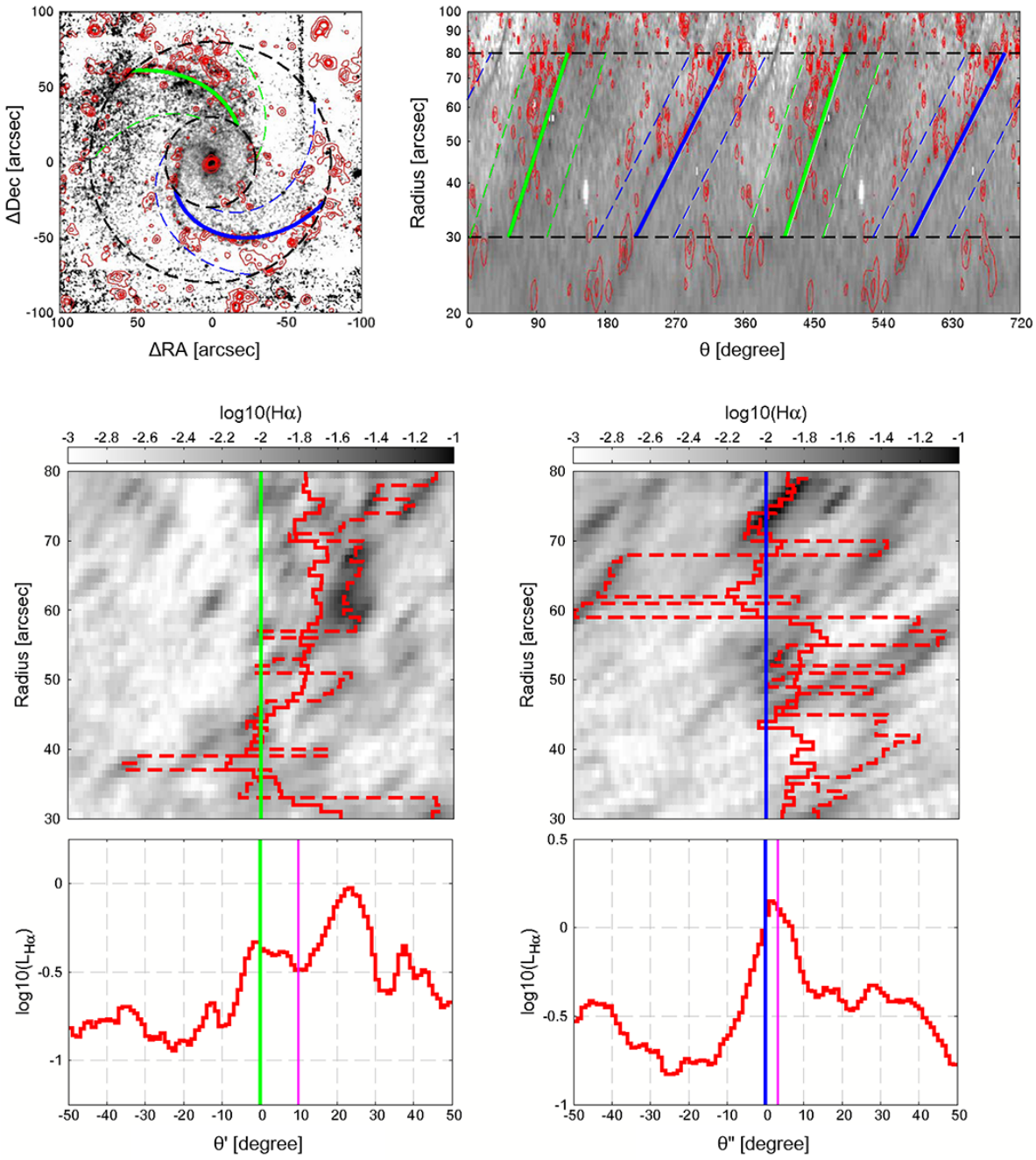

Figure B.3: [NGC 3184] *(Top);* The red contour lines for the Hα emission on the deprojected I−K color images on the (ΔRA, ΔDec) and (log R, θ) planes. The dust lanes are shown with green and blue lines. The positions at the azimuth angle ± 50° with respect to the dust lanes are shown with green and blue dashed lines. *(Bottom);* The upper panels show the continuum-subtracted Hα images on the (R, θ') and (R, θ'') planes in negative representation. The average and the peak azimuth angle of the Hα emission intensity according to the radius are shown with red solid lines and red dashed lines respectively. The lower panels show the distribution of the sum of the Hα emission intensity within the radial region where we traced dust lanes according to the azimuth angle (θ', θ''). The magenta lines show the $\theta_{\rm offset}$.

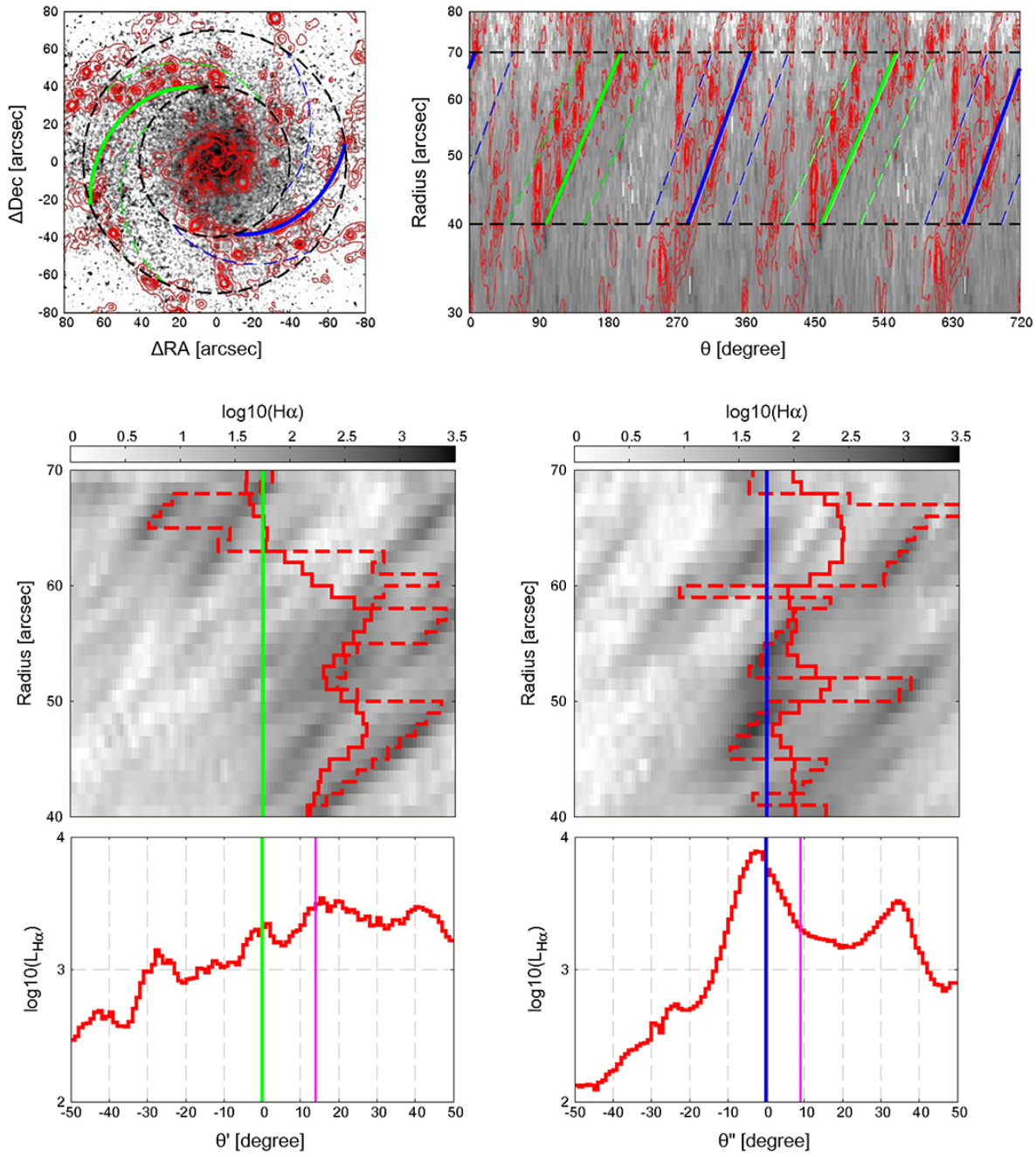

Figure B.4: [NGC 3631] *(Top);* The red contour lines for the Hα emission on the deprojected I−K color images on the (ΔRA, ΔDec) and (log R, θ) planes. The dust lanes are shown with green and blue lines. The positions at the azimuth angle ± 50° with respect to the dust lanes are shown with green and blue dashed lines. *(Bottom);* The upper panels show the continuum-subtracted Hα images on the (R, θ') and (R, θ'') planes in negative representation. The average and the peak azimuth angle of the Hα emission intensity according to the radius are shown with red solid lines and red dashed lines respectively. The lower panels show the distribution of the sum of the Hα emission intensity within the radial region where we traced dust lanes according to the azimuth angle (θ', θ''). The magenta lines show the $\theta_{\rm offset}$.

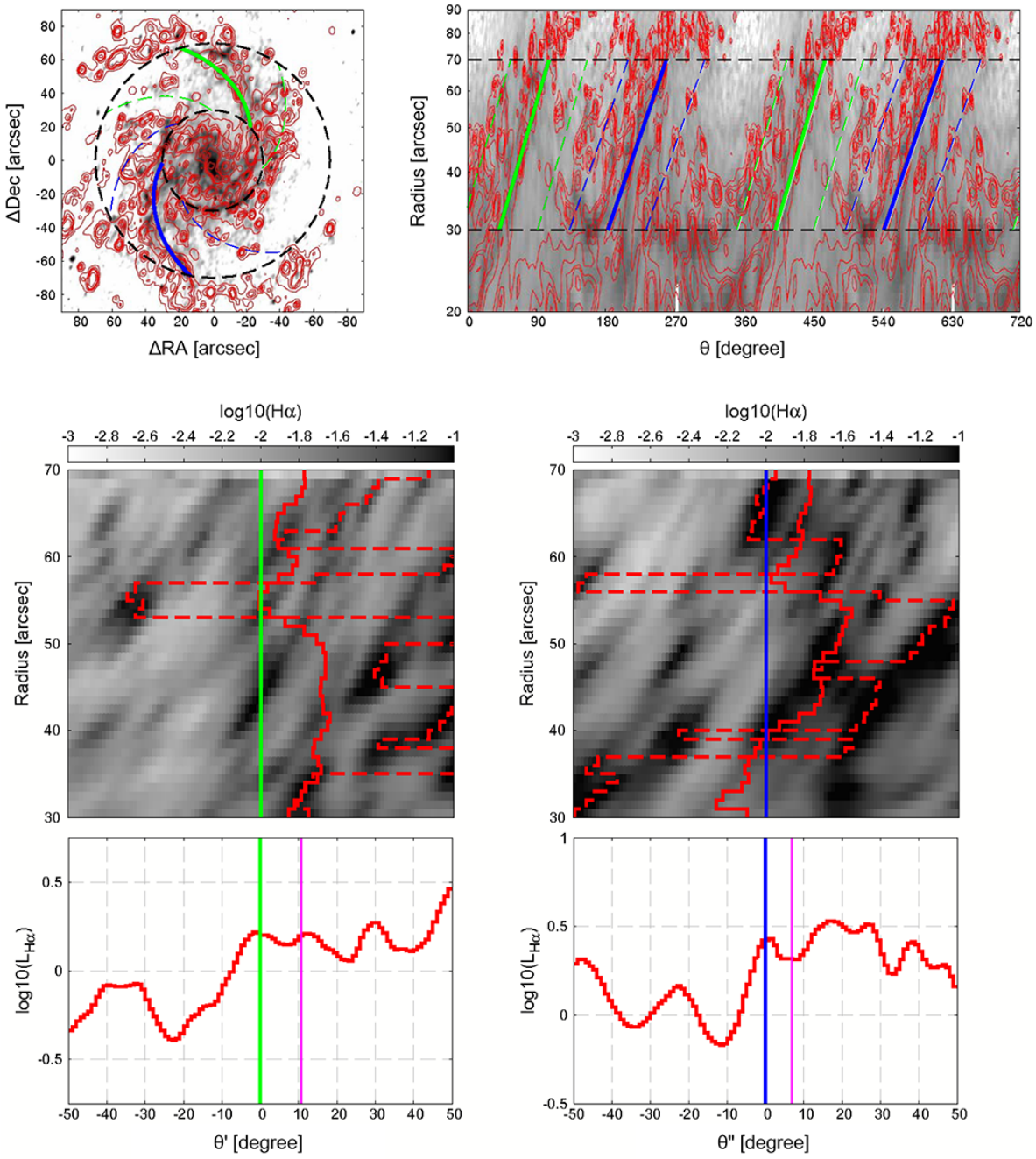

Figure B.5: [NGC 4254] *(Top);* The red contour lines for the Hα emission on the deprojected I−K color images on the (ΔRA, ΔDec) and (log R, θ) planes. The dust lanes are shown with green and blue lines. The positions at the azimuth angle ± 50° with respect to the dust lanes are shown with green and blue dashed lines. *(Bottom);* The upper panels show the continuum-subtracted Hα images on the (R, θ') and (R, θ'') planes in negative representation. The average and the peak azimuth angle of the Hα emission intensity according to the radius are shown with red solid lines and red dashed lines respectively. The lower panels show the distribution of the sum of the Hα emission intensity within the radial region where we traced dust lanes according to the azimuth angle (θ', θ''). The magenta lines show the $\theta_{\rm offset}$.

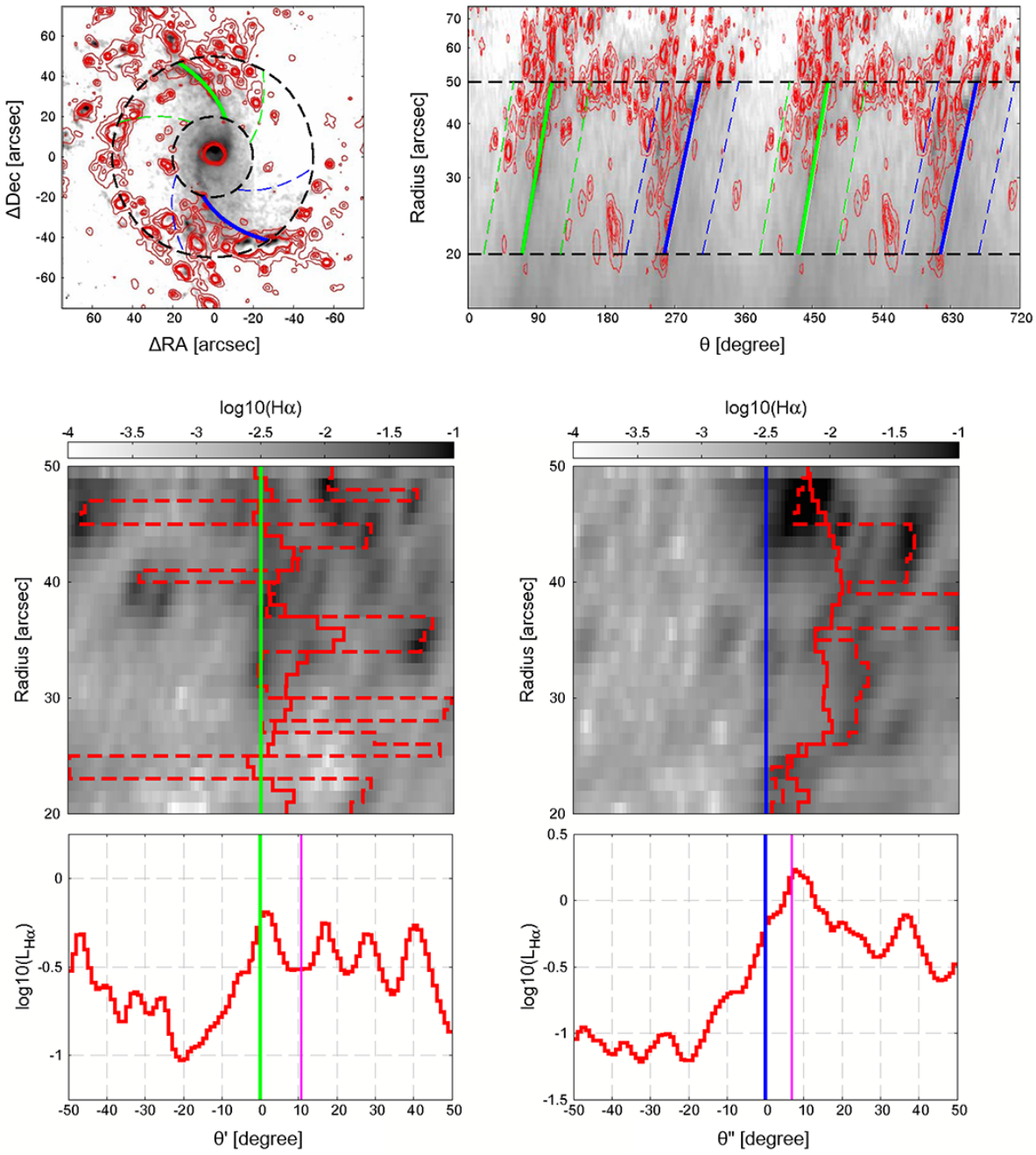

Figure B.6: [NGC 4303] *(Top);* The red contour lines for the Hα emission on the deprojected I−K color images on the (ΔRA, ΔDec) and (log R, θ) planes. The dust lanes are shown with green and blue lines. The positions at the azimuth angle ± 50° with respect to the dust lanes are shown with green and blue dashed lines. *(Bottom);* The upper panels show the continuum-subtracted Hα images on the (R, θ') and (R, θ'') planes in negative representation. The average and the peak azimuth angle of the Hα emission intensity according to the radius are shown with red solid lines and red dashed lines respectively. The lower panels show the distribution of the sum of the Hα emission intensity within the radial region where we traced dust lanes according to the azimuth angle (θ', θ''). The magenta lines show the $\theta_{\rm offset}$.

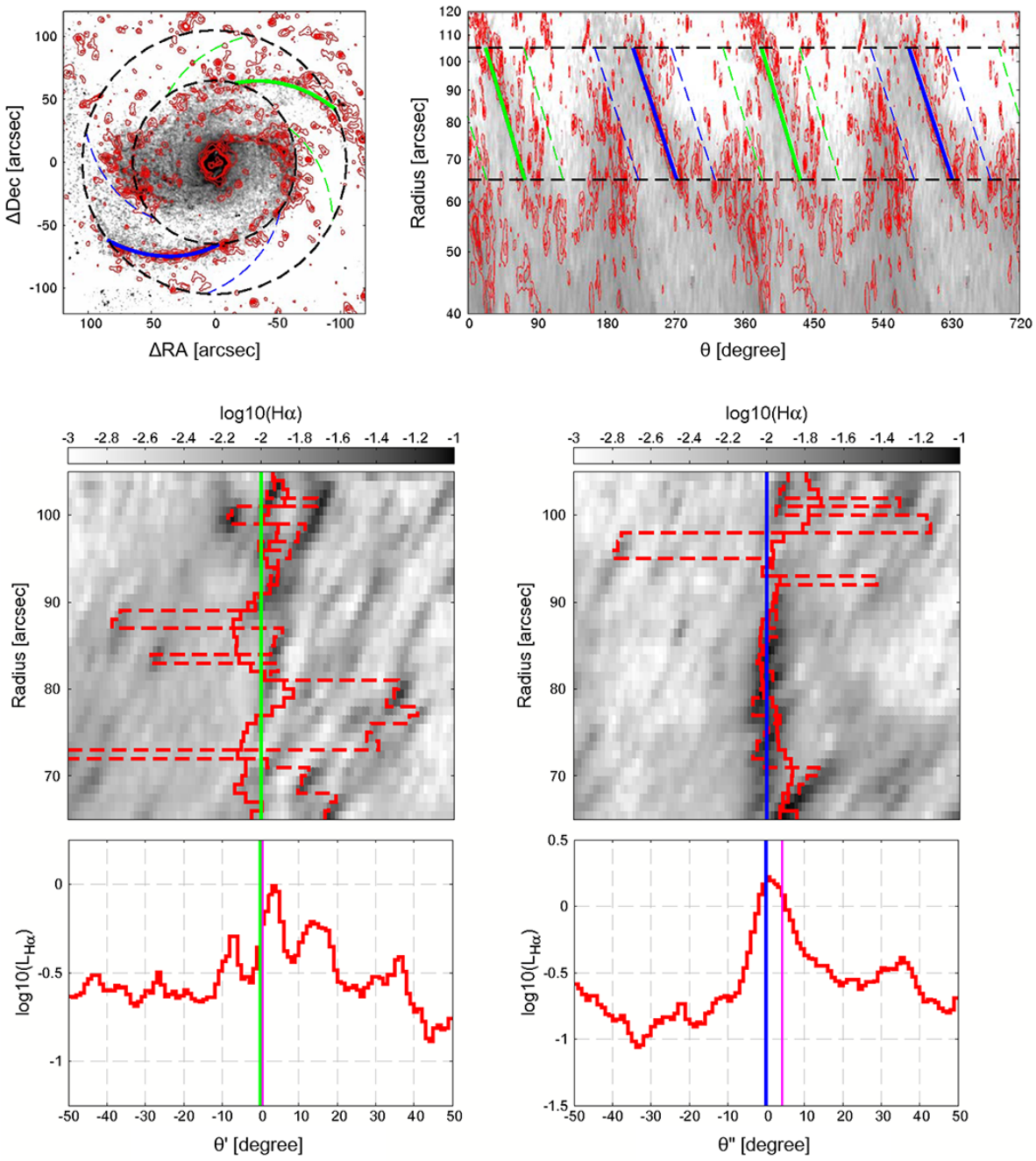

Figure B.7: [NGC 4321] *(Top);* The red contour lines for the Hα emission on the deprojected I−K color images on the (ΔRA, ΔDec) and (log R, θ) planes. The dust lanes are shown with green and blue lines. The positions at the azimuth angle ± 50° with respect to the dust lanes are shown with green and blue dashed lines. *(Bottom);* The upper panels show the continuum-subtracted Hα images on the (R, θ') and (R, θ'') planes in negative representation. The average and the peak azimuth angle of the Hα emission intensity according to the radius are shown with red solid lines and red dashed lines respectively. The lower panels show the distribution of the sum of the Hα emission intensity within the radial region where we traced dust lanes according to the azimuth angle (θ', θ''). The magenta lines show the $\theta_{\rm offset}$.

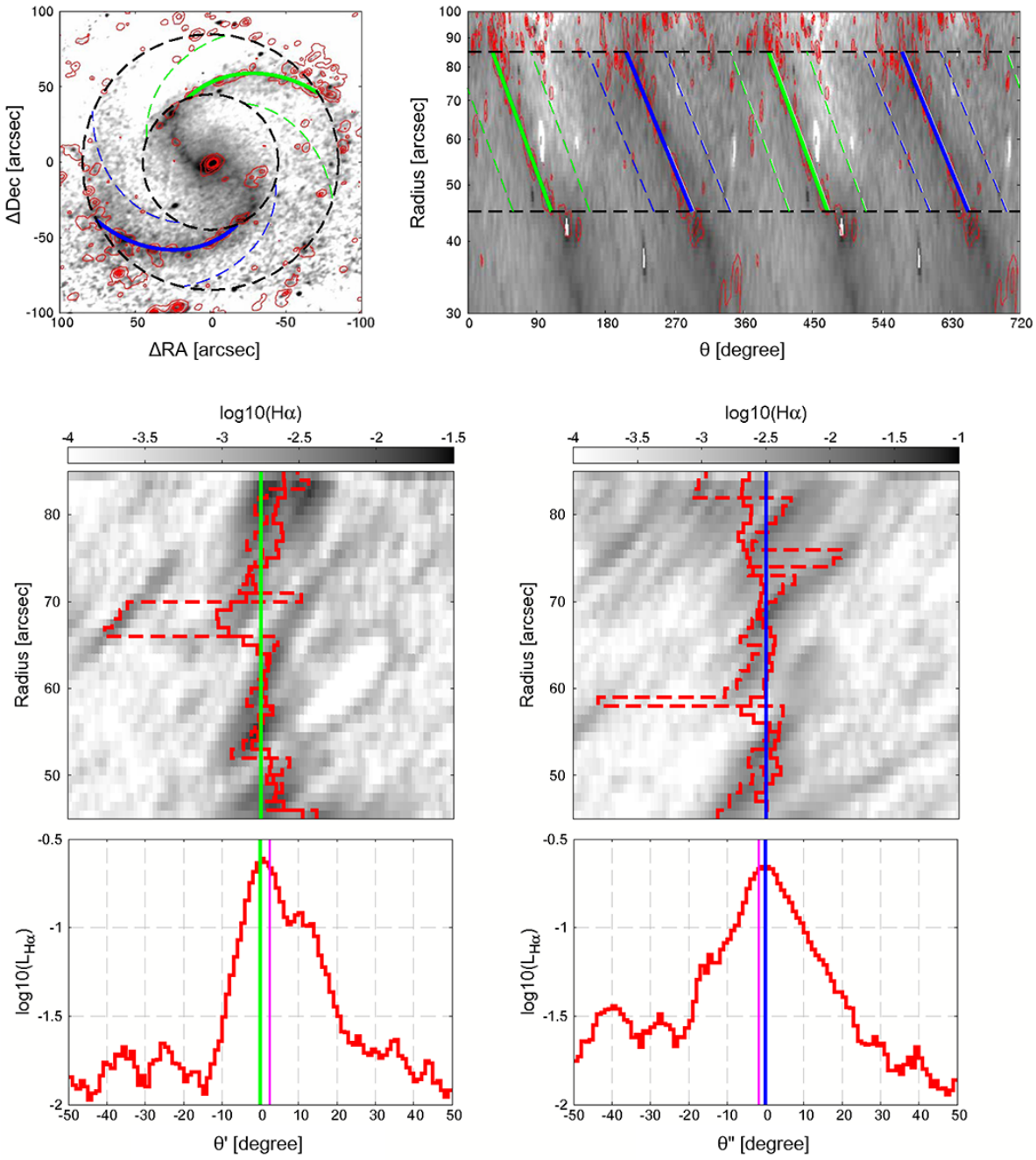

Figure B.8: [NGC 4535] *(Top);* The red contour lines for the Hα emission on the deprojected I−K color images on the (ΔRA, ΔDec) and (log R, θ) planes. The dust lanes are shown with green and blue lines. The positions at the azimuth angle ± 50° with respect to the dust lanes are shown with green and blue dashed lines. *(Bottom);* The upper panels show the continuum-subtracted Hα images on the (R, θ') and (R, θ'') planes in negative representation. The average and the peak azimuth angle of the Hα emission intensity according to the radius are shown with red solid lines and red dashed lines respectively. The lower panels show the distribution of the sum of the Hα emission intensity within the radial region where we traced dust lanes according to the azimuth angle (θ', θ''). The magenta lines show the $\theta_{\rm offset}$.

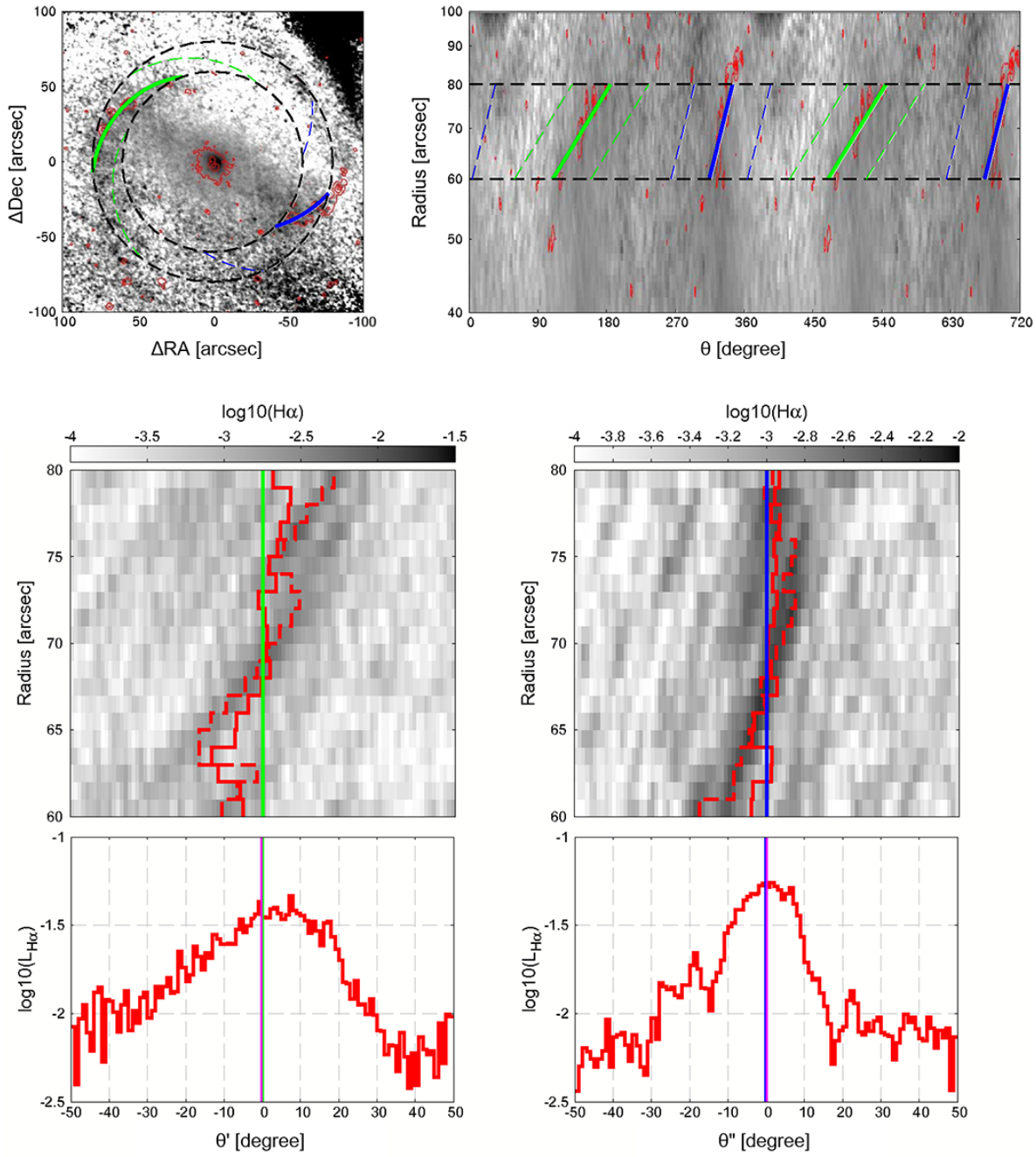

Figure B.9: [NGC 4548] *(Top);* The red contour lines for the Hα emission on the deprojected I−K color images on the (ΔRA, ΔDec) and (log R, θ) planes. The dust lanes are shown with green and blue lines. The positions at the azimuth angle ± 50° with respect to the dust lanes are shown with green and blue dashed lines. *(Bottom);* The upper panels show the continuum-subtracted Hα images on the (R, θ') and (R, θ'') planes in negative representation. The average and the peak azimuth angle of the Hα emission intensity according to the radius are shown with red solid lines and red dashed lines respectively. The lower panels show the distribution of the sum of the Hα emission intensity within the radial region where we traced dust lanes according to the azimuth angle (θ', θ''). The magenta lines show the $\theta_{\rm offset}$.

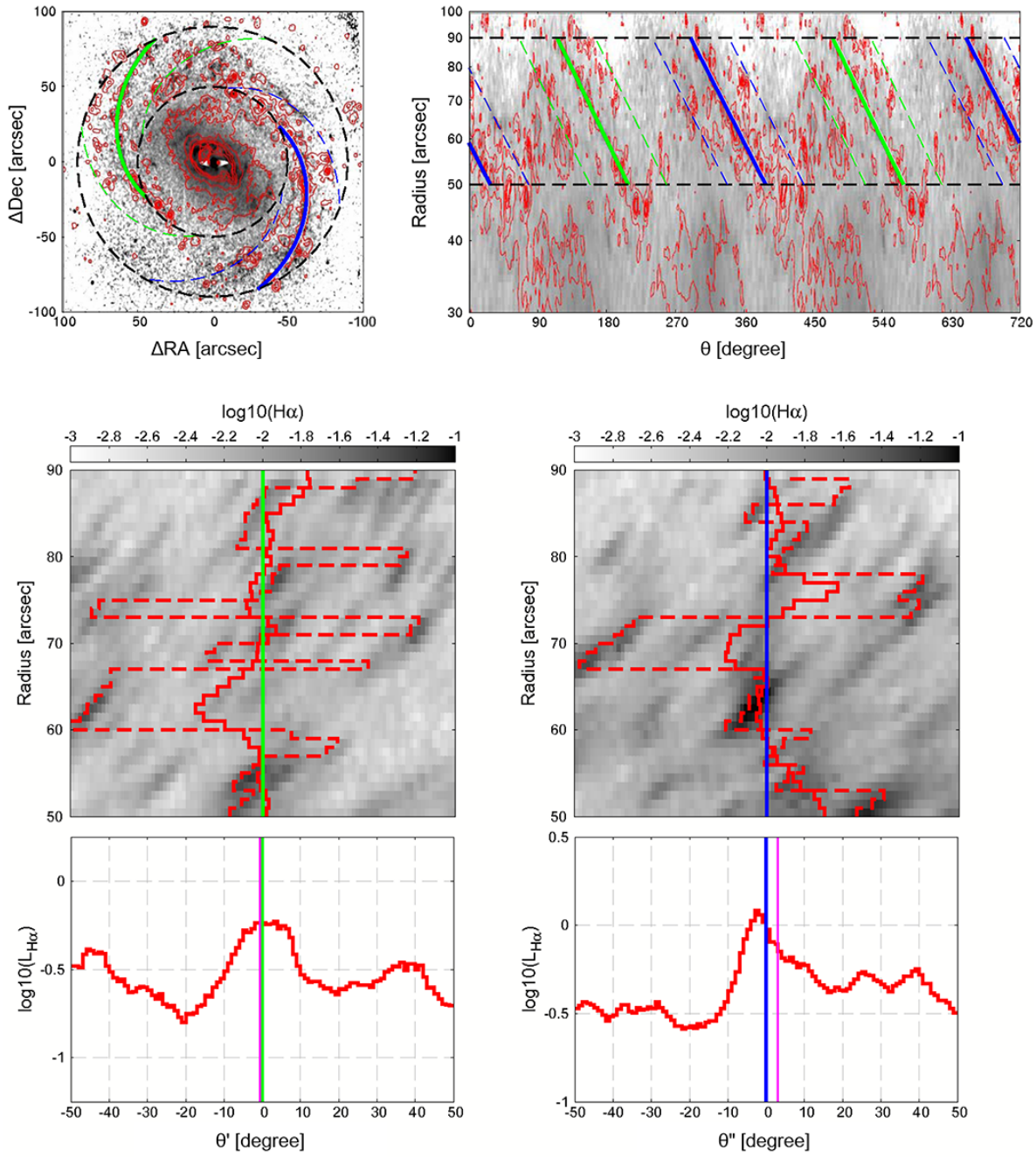

Figure B.10: [NGC 4579] *(Top);* The red contour lines for the Hα emission on the deprojected I−K color images on the (ΔRA, ΔDec) and (log R, θ) planes. The dust lanes are shown with green and blue lines. The positions at the azimuth angle ± 50° with respect to the dust lanes are shown with green and blue dashed lines. *(Bottom);* The upper panels show the continuum-subtracted Hα images on the (R, θ') and (R, θ'') planes in negative representation. The average and the peak azimuth angle of the Hα emission intensity according to the radius are shown with red solid lines and red dashed lines respectively. The lower panels show the distribution of the sum of the Hα emission intensity within the radial region where we traced dust lanes according to the azimuth angle (θ', θ''). The magenta lines show the $\theta_{\rm offset}$.

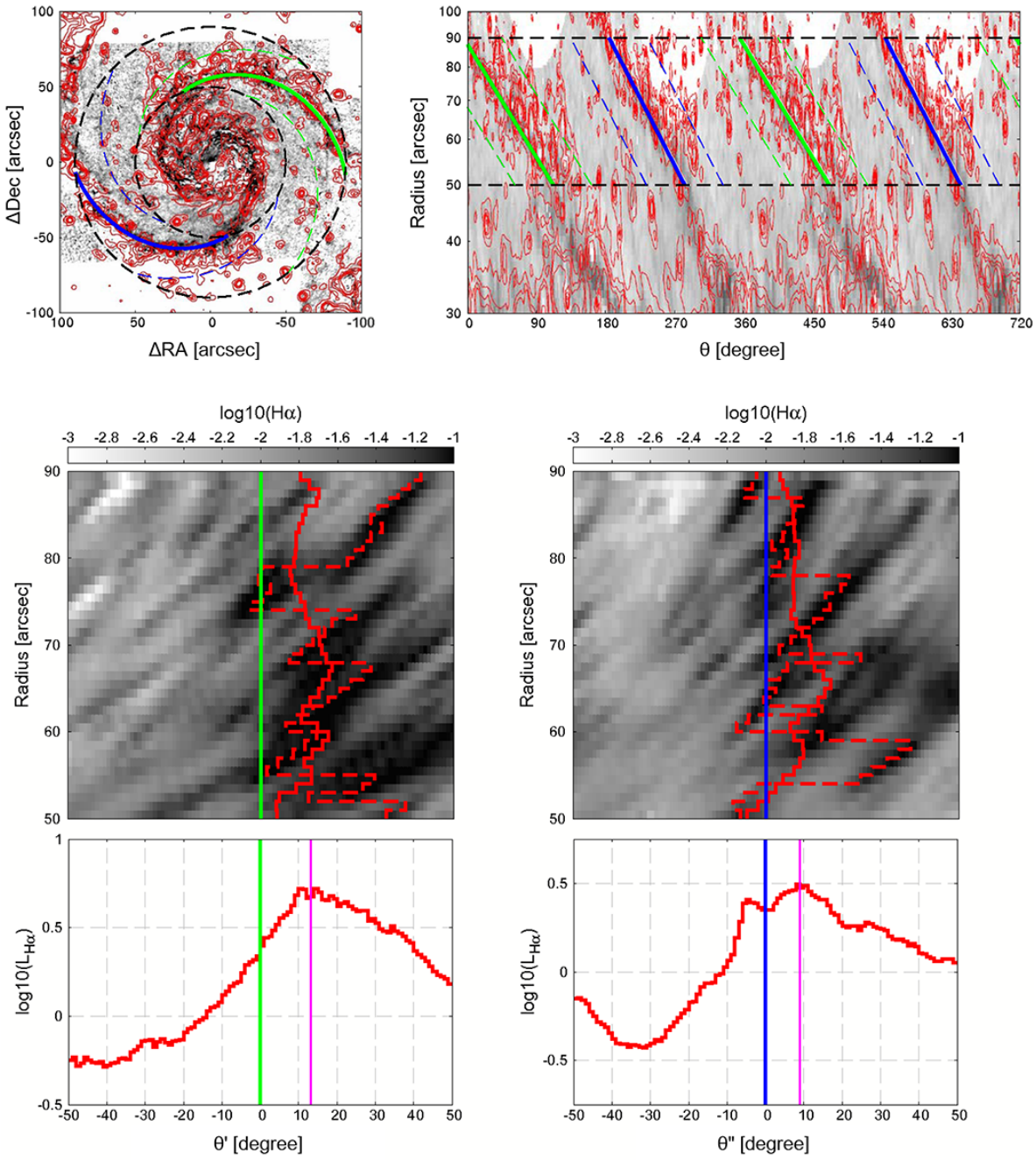

Figure B.11: [NGC 5194] *(Top);* The red contour lines for the Hα emission on the deprojected I−H color images on the (ΔRA, ΔDec) and (log R, θ) planes. The dust lanes are shown with green and blue lines. The positions at the azimuth angle ± 50° with respect to the dust lanes are shown with green and blue dashed lines. *(Bottom);* The upper panels show the continuum-subtracted Hα images on the (R, θ') and (R, θ'') planes in negative representation. The average and the peak azimuth angle of the Hα emission intensity according to the radius are shown with red solid lines and red dashed lines respectively. The lower panels show the distribution of the sum of the Hα emission intensity within the radial region where we traced dust lanes according to the azimuth angle (θ', θ''). The magenta lines show the $\theta_{\rm offset}$.

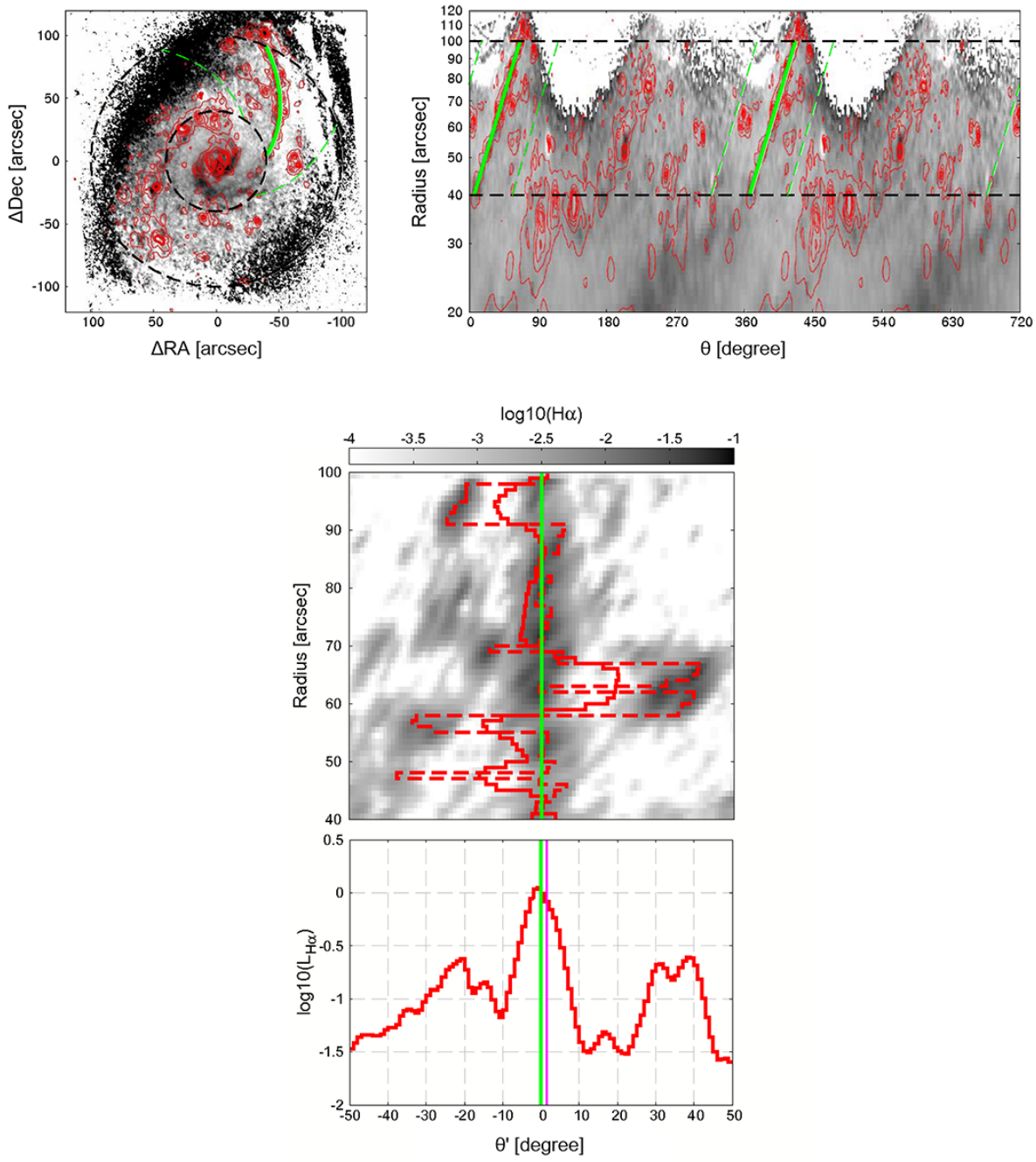

Figure B.12: [NGC 5248] *(Top);* The red contour lines for the Hα emission on the deprojected I−K color images on the (ΔRA, ΔDec) and (log R, θ) planes. The dust lane is shown with green lines. The positions at the azimuth angle ± 50° with respect to the dust lane are shown with green dashed lines. *(Bottom);* The upper panel shows the continuum-subtracted Hα image on the (R, θ') plane in negative representation. The average and the peak azimuth angle of the Hα emission intensity according to the radius are shown with a red solid line and a red dashed line respectively. The lower panel shows the distribution of the sum of the Hα emission intensity within the radial region where we traced dust lane according to the azimuth angle (θ'). The magenta line shows the $\theta_{\rm offset}$.

Appendix C

Description of Individual Galaxies

NGC 628 (M74)

NGC 628 belongs to the Hubble class SA(s)c and the spiral arms are classified as AC 9. This galaxy is considered to be an unbarred and isolated spiral galaxy. Kamphuis & Briggs (1992) found no evidence that this galaxy has had encounters with satellites or other galaxies in the last 10 Gyr. On the other hand, it is reported that there is a circumnuclear ring (Wakker & Adler 1995, James & Seigar 1999), and that the near-infrared images show a nuclear bar with a radius of 2″.1 (Laine et al. 2002) and an oval structure with a radius of about 50″ (Seigar 2002).

We traced two dust lanes over a radial region of 50″ − 90″ (2.4 − 4.2 kpc) as shown in Figure A.1. Both dust lanes seem to be disconnected and distributed with a large scatter. We defined the arm indicated by green dashed lines which starts from the west as Arm1 and that indicated by blue dashed lines which starts from the east as Arm2. The pitch angles are similar in both arms; 11.9° ± 0.2° for Arm1 and 13.3° ± 0.3° for Arm2. We show the distribution of Hα emission in Figure B.1. The star forming regions with strong Hα emission tend to be located downstream of the dust lanes in both arms. The $\theta_{\rm offset}$ were measured at 8.8° in Arm1 and 9.8° in Arm2.

E09 classified this galaxy as "C" galaxies with clear offsets. They measured 33 offsets between CO and Hα over a radial region of 12″ − 102″, which includes the radial region we traced the dust lanes. They estimated the corotation radius at $R_{\rm CR} \simeq 54'' - 114''$. The $R_{\rm CR}$ has been also measured at ∼ 141″ in Elmegreen et al. (1992), ∼ 110″ in Cepa & Beckman (1990), and 89″ ± 2″ in Martínez-García & Puerari (2014). Considering their results, the radial region we traced the dust lanes is located within the corotation radius, and our result with positive $\theta_{\rm offset}$ is consistent with the density wave theory.

NGC 1068 (M77)

NGC 1068 belongs to the Hubble class SA(rs)b and the spiral arms are classified as AC 3. This galaxy has an active galactic nucleus classified as Seyfert 2 (Khachikian & Weedman 1974). Although this galaxy is normally considered as an unbarred spiral galaxy, Scoville et al. (1988) found a bar with a radius of 16" at K-band. In addition, there is a bright oval structure with a diameter of 180″ and an eccentricity of 0.8 (Bland-Hawthorn et al. 1997). Schinnerer et al. (2000) represented the sketch of the outer disk, outer oval structure, near-infrared bar and CO arms in their Figure 6. Elmegreen & Elmegreen (1987) classified this galaxy as a flocculent spiral galaxy, but two dust lanes are prominent in the disk, which is the reason why we included this galaxy in our sample.

We traced only one dust lane which starts from the west over a radial region of 30″ − 50″ (2.1 − 3.5 kpc) as shown in Figure A.2. There is a possibility that the background subtraction of the I-band image was not accurate because the field of view was smaller than the angular size of this galaxy. This might make it hard to trace the other dust lane in the I−K image. We show the distribution of Hα emission in Figure B.2. The star forming regions with strong Hα emission are distributed around the dust lane. The $\theta_{\rm offset}$ was measured at 4.9°, which is mainly due to HII regions in a large bubble surrounding stellar clusters located at the radius of $\sim$ 45″.

Rand & Wallin (2004) argued for the presence of two different corotation radii for the near infrared inner bar and the spiral arms. They estimated the $R_{\rm CR}$ at 16″ − 19″ for the inner bar and roughly 50″ for the spiral arms by the Tremaine−Weinberg method. Assuming the $R_{\rm CR}$ = 50″, the radial region we traced the dust lane is located within the corotation radius, and our result with positive $\theta_{\rm offset}$ is consistent with the density wave theory.

NGC 3184

NGC 3184 belongs to the Hubble class SAB(rs)cd and the spiral arms are classified as AC 9. This galaxy has a bar whose radius is measured at 25″ from optical observations (Elmegreen et al. 1996) and 21″ from CO observations (Das et al. 2003). Knapen (2005) reported that there is a faint nuclear ring with a radius of 41″, but it is regarded as an inner ring rather than a nuclear ring (Comerón et al. 2010).

We traced two dust lanes over a radial region of 30″ − 80″ (1.3 − 3.4 kpc) as shown in Figure A.3. We traced the dust lanes as long as possible, although they seem to be deviated from a logarithmic spiral in some regions. We defined the arm indicated by green dashed lines which starts from the northwest as Arm1 and that indicated by blue dashed lines which starts from the southeast as Arm2. The pitch angles are relatively different in both arms; 36.1° ± 0.7° for Arm1 and 24.8° ± 0.3° for Arm2. We show the distribution of Hα emission in Figure B.3. The star

forming regions with strong Hα emission tend to be located downstream of the dust lanes in both arms. On the other hand, the HII regions in Arm2 are more concentrated on the dust lane than those in Arm1. The $\theta_{\rm offset}$ were measured at 9.9° in Arm1 and 3.2° in Arm2.

E09 classified this galaxy as "A" galaxies with ambiguous offsets. They measured 19 offsets between CO and Hα over a radial region of 36″ − 84″, which includes almost the entire radial region we traced the dust lanes. They found positive offsets at the radius of about 80″, although they derived a negative correlation i.e., $t_{\rm SF} < 0$. On the other hand, Tamburro et al. (2008) detected the systematic offsets between HI and 24 μm emission and estimated the corotation radius at $R_{\rm CR}$ = 127″ ± 28″. Assuming the $R_{\rm CR}$ = 127″, the radial region we traced the dust lanes is located within the corotation radius, and our result with positive $\theta_{\rm offset}$ is consistent with the density wave theory.

NGC 3631

NGC 3631 belongs to the Hubble class SA(s)c and the spiral arms are classified as AC 9. There is no bar and no nearby obvious companion. This galaxy has two main spiral arms with branches, which were described in Boeshaar & Hodge (1977) with a survey of the HII regions.

We traced two dust lanes over a radial region of 40″ − 70″ (3.4 − 5.9 kpc) as shown in Figure A.4. Both dust lanes are not prominent and seem to be distributed disconnectedly. We defined the arm indicated by green dashed lines which starts from the north as Arm1 and that indicated by blue dashed lines which starts from the south as Arm2. The pitch angles are similar in both arms; 18.1° ± 0.5° for Arm1 and 21.4° ± 1.5° for Arm2. We show the distribution of Hα emission in Figure B.4. The star forming regions with strong Hα emission tend to be located downstream of the dust lanes in both arms. We measured the $\theta_{\rm offset}$ at 14.0° in Arm1 and 8.9° in Arm2. Some of the HII regions belong to the branches, which make the $\theta_{\rm offset}$ large.

Boeshaar & Hodge (1977) reported that the distribution of HII regions over a radial region of ∼ 30″ − 70″ agreed with the distribution predicted by the density wave theory, which is consistent with our result. On the other hand, Fridman et al. (2001) estimated the corotation radius at $R_{\rm CR}$ = 42″ ± 5″. However, the $R_{\rm CR}$ is located around the lower end of the radial region we traced the dust lanes and inconsistent with our result of positive $\theta_{\rm offset}$. Therefore, we suggest that this galaxy has another corotation radius larger than 42″.

NGC 4254 (M99)

NGC 4254 belongs to the Hubble class SA(s)c and the spiral arms are classified as AC 9. This galaxy is a member of the Virgo Cluster. The optical images show that this galaxy is dominated by a three-arm structure with m = 1 and m = 3 Fourier components (Iye et al. 1982, Elmegreen et

al. 1992, González & Graham 1996). The strong m = 1 spiral structure which extends from the south-to-western region is also seen in the HI gas distribution (e.g., Phookun et al. 1993). Haynes et al. (2007) reported a long HI tail extending ∼ 250 kpc northward from the strong m = 1 spiral arm, which could be explained by tidal interactions with another Virgo cluster member (Minchin et al. 2007, Duc et al. 2008, Chyży 2008, Weżgowiec et al. 2012).

We traced two dust lanes over a radial region of 30″ − 70″ (2.4 − 5.7 kpc) as shown in Figure A.5. We excluded one out of three arms, because the dust lane does not extend over the radius of about 30″. We defined the arm indicated by green dashed lines which starts from the northwest as Arm1 and that indicated by blue dashed lines which starts from the southeast as Arm2. The dust lane of Arm1 is well fitted with a logarithmic spiral, but that of Arm2 is distributed with a large scatter. The pitch angles are similar in both arms; 36.7° ± 0.4° for Arm1 and 32.4° ± 1.1° for Arm2. We show the distribution of Hα emission in Figure B.5. The star forming regions with strong Hα emission tend to be located downstream of the dust lanes in both arms. The $\theta_{\rm offset}$ were measured at 10.7° in Arm1 and 6.9° in Arm2. There is a possibility that the HII regions located upstream of Arm2 were formed in the arm we excluded. This could explain the difference of the $\theta_{\rm offset}$ between Arm1 and Arm2.

E09 classified this galaxy as "C" galaxies with clear offsets. They measured 18 offsets between CO and Hα over a radial region of 24″ − 78″, which includes the radial region we traced the dust lanes. They estimated the corotation radius at $R_{\rm CR} \simeq 60'' - 78''$. The $R_{\rm CR}$ has been also measured at ∼ 87″ in Elmegreen et al. (1992), 77″ ± 11″ in Kranz et al. (2001) and ∼ 91″ in Buta & Zhang (2009). Considering their results, the radial region we traced the dust lanes is located within the corotation radius, and our result with positive $\theta_{\rm offset}$ is consistent with the density wave theory.

NGC 4303 (M61)

NGC 4303 belongs to the Hubble class SAB(rs)bc and the spiral arms are classified as AC 9. This galaxy has an active galactic nucleus classified as LINER/Seyfert 2 (e.g., Kennicutt et al. 1989, Colina et al. 1997) and a nuclear ring (Buta & Crocker 1993). This galaxy is considered to be a double barred galaxy. The radius of the primary bar was estimated at $R_{\rm bar} \sim 47''$ in Laine et al. (2002), 30″ in Laurikainen et al. (2004), and 52.5″ ± 12.0″ in Rautiainen et al. (2008) and that of the secondary bar was estimated at $R_{\rm bar} \sim 2''$ (Colina & Wada 2000, Schinnerer et al. 2002).

We traced two dust lanes over a radial region of 20″ − 50″ (1.5 − 3.7 kpc) as shown in Figure A.6. The dust lanes are well fitted with a logarithmic spiral within the radius of 50″ and folded around the radius. The end of the primary bar is located within the radial region we traced the dust lanes when we assume $R_{\rm bar}$ = 30″ (Laurikainen et al. 2004). We defined the arm indicated by green dashed lines which starts from the north as Arm1 and that indicated by blue dashed lines

which starts from the south as Arm2. The pitch angles are similar in both arms; 53.6° ± 1.3° for Arm1 and 48.0° ± 0.8° for Arm2. We show the distribution of Hα emission in Figure B.6. The star forming regions with strong Hα emission are distributed beyond the radius of 30″ which corresponds to the R_{bar}. They also tend to be located downstream of the dust lanes in both arms. We measured the θ_{offset} at 4.5° for Arm1 and 13.7° for Arm2. The HII regions in the folding arm which extends from Arm1 seem to be distributed upstream of Arm1 and downstream of Arm2. This could explain the difference of the θ_{offset} between Arm1 and Arm2.

E09 classified this galaxy as "C" galaxies with clear offsets. They measured 8 offsets between CO and Hα over a radial region of 30″ − 54″, which includes the radial region we traced the dust lanes except for the range of 20″ − 30″. They estimated the corotation radius at $R_{CR} \gtrsim 54''$. The R_{CR} has been also measured at 89″.1 ± 8″.5 in Rautiainen et al. (2008) and ∼ 85″ in Buta & Zhang (2009). Considering their results, the radial region we traced the dust lanes is located within the corotation radius, and our result with positive θ_{offset} is consistent with the density wave theory.

NGC 4321 (M100)

NGC 4321 belongs to the Hubble class SAB(s)bc and the spiral arms are classified as AC 12. This galaxy is a member of the Virgo Cluster. There is a circumnuclear ring and a moderately strong bar with a radius of ∼ 60″ (Knapen et al. 1995, Kuno et al. 2007).

We traced two dust lanes over a radial region of 65″ − 105″ (5.3 − 8.6 kpc) as shown in Figure A.7. The radial region is located outside of the bar. We defined the arm indicated by green dashed lines which starts from the north as Arm1 and that indicated by blue dashed lines which starts from the south as Arm2. The pitch angles are similar in both arms; 28.2° ± 0.9° for Arm1 and 25.7° ± 0.6° for Arm2. We show the distribution of Hα emission in Figure B.7. The star forming regions with strong Hα emission tend to be distributed around the dust lane in Arm1. On the other hand, the star forming regions are concentrated on the dust lane in Arm2. We measured the θ_{offset} at 0.6° in Arm1 and 4.1° in Arm2.

E09 classified this galaxy as "N" galaxies with no offsets. They measured 34 offsets between CO and Hα over a radial region of 18″ − 84″. They found that offsets in the radial region of ∼ 60″ − 84″ are almost zero, while those close to the bar region $\lesssim 55''$ are about 10°. The result of no offsets in the radial region of ∼ 60″ − 84″ is consistent with our result. They mentioned several possible reasons for no offsets: (1) material arms, (2) corotation resonance, and (3) elliptical orbits nearly parallel to the spiral arms. They suggested that (1) would be the most plausible reason because the offsets were found close to the bar region where orbits should have higher ellipticity than in the arm region, and the radial region where they measured offsets was within the corotation

radii calculated in previous studies (e.g., ∼ 118″ in Elmegreen et al. 1992, 98″ ± 10″ in Canzian & Allen 1997). In addition to E09, Ferreras et al. (2012), which investigated the offsets between a very young component (an HII region) and an old component (a UV star-forming source) with the ages over 100 Myr, also gave negative evidence for density wave spirals. Thus, this galaxy is considered to be a representative galaxy against the density wave theory.

NGC 4535

NGC 4535 belongs to the Hubble class SAB(s)c and the spiral arms are classified as AC 9. This galaxy is a member of the Virgo Cluster. There is a nuclear ring (Benedict et al. 1977, Buta & Crocker 1993) and a bar with a radius of 41″ in Kuno (2007). This galaxy has two spiral arms in the inner disk, but the arms break up into multiple arms in the outer disk.

We traced two dust lanes over a radial region of 45″ − 85″ (3.7 − 6.9 kpc) as shown in Figure A.8. The radial region is located outside of the bar. We defined the arm indicated by green dashed lines which starts from the north as Arm1 and that indicated by blue dashed lines which starts from the south as Arm2. The pitch angles are similar in both arms; 25.3° ± 0.3° for Arm1 and 22.9° ± 0.4° for Arm2. We show the distribution of Hα emission in Figure B.8. The star forming regions with strong Hα emission tend to be concentrated on the dust lanes in both arms. In addition, the distributions of the HII regions are almost symmetric with respect to the dust lanes. We measured the $\theta_{\rm offset}$ at 2.5° in Arm1 and −1.8° in Arm2.

There is no study to be compared with our result, but the dust lanes over a radial region of 45″ − 85″ seem to be located at the center of the stellar arms in optical images.

NGC 4548 (M91)

NGC 4548 belongs to the Hubble class SB(rs)b and the spiral arms are classified as AC 5. This galaxy is a member of the Virgo Cluster. There is an active galactic nucleus classified as LINER (e.g., Ho et al. 1997) and a relatively large bar with a radius of 67″.5 in Laurikainen et al. (2004), 62″ in Kuno et al. (2007), and 75″.8 ± 6″.8 in Rautiainen et al. (2008). Two main spiral arms seem to begin from the ends of the bar with offsets in the leading side.

We traced two dust lanes over a radial region of 60″ − 80″ (4.9 − 6.5 kpc) as shown in Figure A.9. The radial region is located outside of the bar when we assume $R_{\rm bar}$ = 62″ (Kuno et al. 2007). We defined the arm indicated by green dashed lines which starts from the northeast as Arm1 and that indicated by blue dashed lines which starts from the southwest as Arm2. The quality of the flatness around the edge of the K-band image is poor, which makes it difficult to trace the dust lane of Arm2 in the region beyond the radius of 80″. The pitch angles are different in both arms; 12.3° ± 1.3° for Arm1 and 28.4° ± 2.3° for Arm2. We show the distribution of Hα emission in

Figure B.9. The star forming regions with strong Hα emission tend to be concentrated on the dust lanes in both arms. In addition, the distributions of the HII regions are almost symmetric with respect to the dust lanes. We measured the $\theta_{\rm offset}$ at -0.3° in Arm1 and 0.2° in Arm2.

The $R_{\rm CR}$ has been measured at $95''.2 \pm 11''.9$ in Rautiainen et al. (2008) and $\sim 75''$ in Buta & Zhang (2009). The reason for no offsets may be explained by the effect of corotation resonance, because the radial region we traced the dust lanes includes the corotation radius when we assume $R_{\rm CR} = 75''$ (Buta & Zhang 2009).

NGC 4579 (M58)

NGC 4579 belongs to the Hubble class SAB(rs)b and the spiral arms are classified as AC 9. This galaxy is a member of the Virgo Cluster. There is an active galactic nucleus classified as LINER/Seyfert 1.9 (e.g., Ho et al. 1997) and a prominent bar with a radius of $45''$ in Laurikainen et al. (2004), $48''.8 \pm 5''.2$ in Rautiainen et al. (2008), and $50'' - 60''$ in García-Burillo et al.(2009).

We traced two dust lanes over a radial region of $50'' - 90''$ (4.1 − 7.3 kpc) as shown in Figure A.10. The radial region is located outside of the bar when we assume $R_{\rm bar} = 45''$ (Laurikainen et al. 2004). They are symmetric and well fitted with a logarithmic spiral. We defined the arm indicated by green dashed lines which starts from the east as Arm1 and that indicated by blue dashed lines which starts from the west as Arm2. The pitch angles are similar in both arms; $19.9^\circ \pm 0.4^\circ$ for Arm1 and $18.9^\circ \pm 0.4^\circ$ for Arm2. We show the distribution of Hα emission in Figure B.10. The star forming regions with strong Hα emission are located on the dust lanes in both arms. In addition, the star forming regions are distributed symmetrically with respect to the dust lanes. There is a possibility that most of the star forming regions located away from the dust lanes were formed there because there seem to be small and weak dust lanes around the arms. We measured the $\theta_{\rm offset}$ at -0.6° in Arm1 and 3.1° in Arm2.

The $R_{\rm CR}$ has been measured at $71''.1 \pm 8''.4$ in Rautiainen et al. (2008), $\sim 81''$ in Buta & Zhang (2009) and $60'' \pm 10''$ in García-Burillo et al.(2009). The reason for no offsets may be explained by the effect of corotation resonance, because the radial region we traced the dust lanes includes the corotation radius considering their results.

NGC 5194 (M51)

NGC 5194 belongs to the Hubble class SA(s)bc and the spiral arms are classified as AC 12. There is an active galactic nucleus classified as Seyfert 2 (Kohno et al. 1996) and a nuclear ring (Buta & Crocker 1993). This galaxy is interacting with its companion galaxy NGC 5195.

We traced two dust lanes over a radial region of $50'' - 90''$ (1.9 − 3.4 kpc) as shown in Figure

A.11. The radial region was limited by the observation field of the HST/NICMOS H-band imaging data. The dust lanes seem to be disconnected at the radius of 50″. Meidt et al. (2008) with the radial Tremaine-Weinberg method have derived different pattern speeds between inside and outside of the radius. We defined the arm indicated by green dashed lines which starts from the north as Arm1 and that indicated by blue dashed lines which starts from the south as Arm2. The pitch angles are similar in both arms; 16.0° ± 0.3° for Arm1 and 18.8° ± 0.3° for Arm2. We show the distribution of Hα emission in Figure B.11. The star forming regions with strong Hα emission tend to be located downstream of the dust lanes in both arms. We measured the $\theta_{\rm offset}$ at 13.2° in Arm1 and 9.0° in Arm2.

E09 classified this galaxy as "C" galaxies with clear offsets. They detected 41 offsets between CO and Hα over a radial region of 54″ − 132″, which includes almost the entire radial region we traced the dust lanes. They estimated the corotation radius at $\rm R_{CR} = 174^{+12}_{-24}$ arcsec. They measured the $\rm R_{CR}$ only with the offsets in Arm2, because the offsets in Arm1, which is connected to the companion galaxy NGC 5195, showed negative dependence on $\Omega_{\rm gas}$ i.e., $\rm t_{SF} < 0$. The $\rm R_{CR}$ has been also measured at ∼ 132″ in Elmegreen et al. (1992) and 202″ ± 3″ in Martínez-García & Puerari (2014). Considering their results, the radial region we traced the dust lanes is located within the corotation radius, and our result with positive $\theta_{\rm offset}$ is consistent with the density wave theory.

NGC 5248

NGC 5248 belongs to the Hubble class SB(rs)bc and the spiral arms are classified as AC 9. It is reported that this galaxy has two circumnuclear rings (e.g., Laine et al. 2001, Maoz et al. 2001, van der Laan et al. 2013). In addition, there is a bar with a radius of 22″ in Martin (1995), 71″ in Elmegreen & Elmegreen (1985), and 95″ in Jogee et al. (2002).

We traced only one dust lane which starts from the west over a radial region of 40″ − 100″ (2.5 − 6.2 kpc) as shown in Figure A.12. The radial region includes the bar when we assume $\rm R_{bar}$ = 71″ (Elmegreen & Elmegreen 1985). There is a possibility that the background subtraction of the K-band image was not accurate because the field of view was smaller than the angular size of this galaxy. This might make it hard to trace the other dust lane in the I − K image. We show the distribution of Hα emission in Figure B.12. The star forming regions with strong Hα emission tend to be concentrated on the dust lane. On the other hand, the star forming regions with weak Hα emission seem to be distributed upstream of the dust lane. In addition, there is a clump of young stellar clusters located downstream of the dust lane at the radial region of 60″ − 70″. We measured the $\theta_{\rm offset}$ at 1.5°.

E09 classified this galaxy as "N" galaxies with no offsets. They measured 13 offsets between

CO and Hα over a radial region of $36'' - 84''$ and found that the offsets are almost zero. With an improved nonlinear asymptotic theory of spiral density waves, Yuan & Yang (2006) has calculated strong inward streaming motions along the spiral arm up to the radius of about $70''$ assuming that the disk is predominantly driven by a large-scale bar of Jogee et al. (2002). E09 suggested that such noncircular orbit can partially explain the reason for no offsets. The R_{CR} has been measured at $\sim 103''$ in Elmegreen et al. (1992), $\sim 115''$ in Jogee et al. (2002) and $\sim 70''$ in Buta & Zhang (2009). Assuming the $R_{CR} = 103''$, the corotation radius is located around the upper end of the radial region we traced the dust lanes. We infer that the reasons for no offsets can be explained by both effects of elliptical orbits nearly parallel to the spiral arms and corotation resonance.

Appendix D

Star Forming Regions Predicted by Rotation Curve and Ω_P

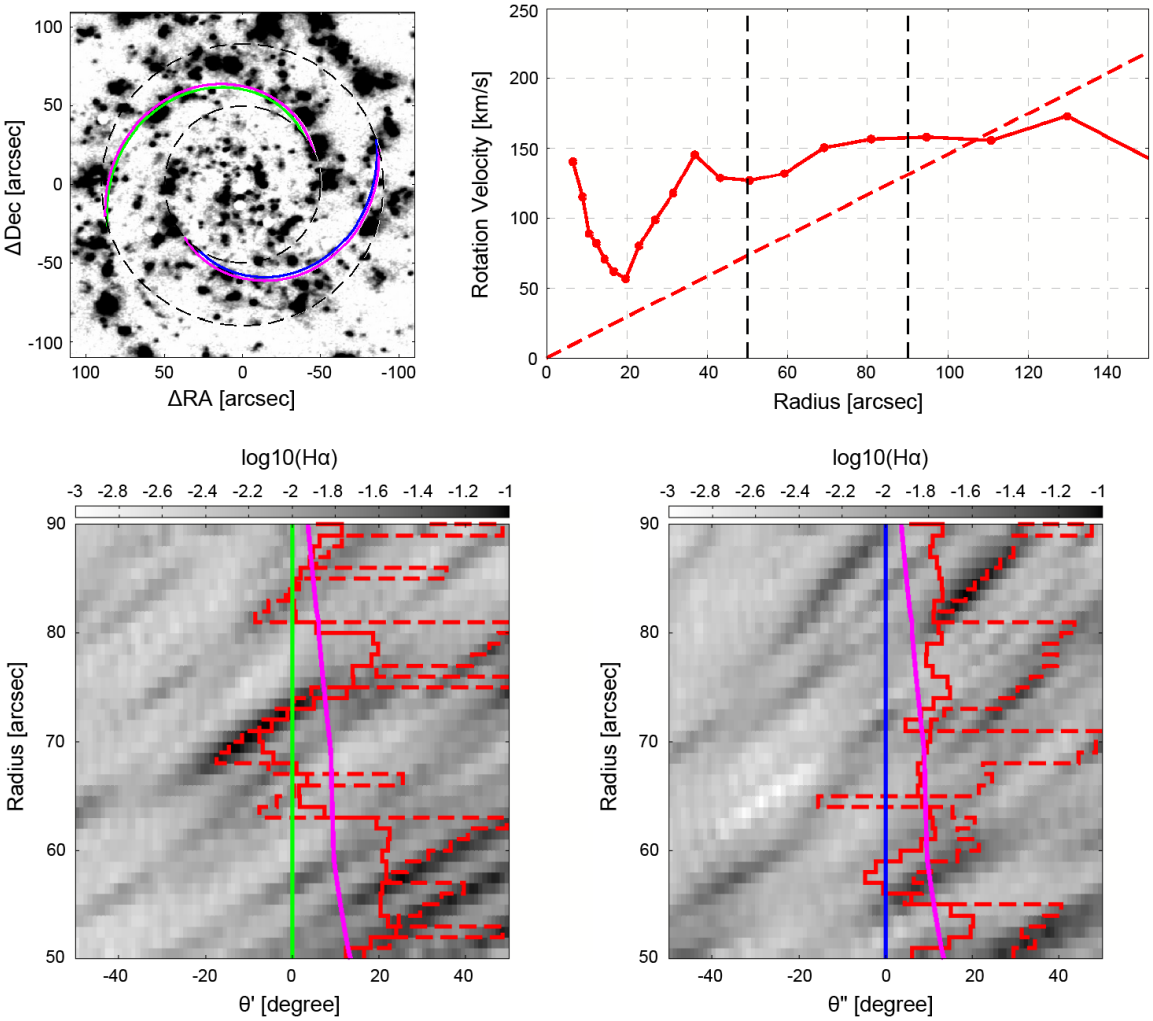

Figure D.1: [NGC 628] *(Top Left);* The deprojected continuum-subtracted Hα image in negative representation. The dust lanes we traced are shown with green and blue lines. The magenta lines show the estimated positions of stellar clusters with the ages of 10 Myr assuming that they were born in the dust lanes and rotate in a circular orbit. *(Top Right);* The rotation curve and the pattern speed of Ω_P = 31 km/s/kpc from Fathi et al. (2007) are shown with a red solid line and a red dashed line respectively. *(Bottom);* The continuum-subtracted Hα image on the (R, θ') and (R, θ'') planes in negative representation. The average and the peak azimuth angle of the Hα emission intensity according to the radius are shown with red solid lines and red dashed lines respectively. The magenta lines show the estimated positions of stellar clusters with the ages of 10 Myr.

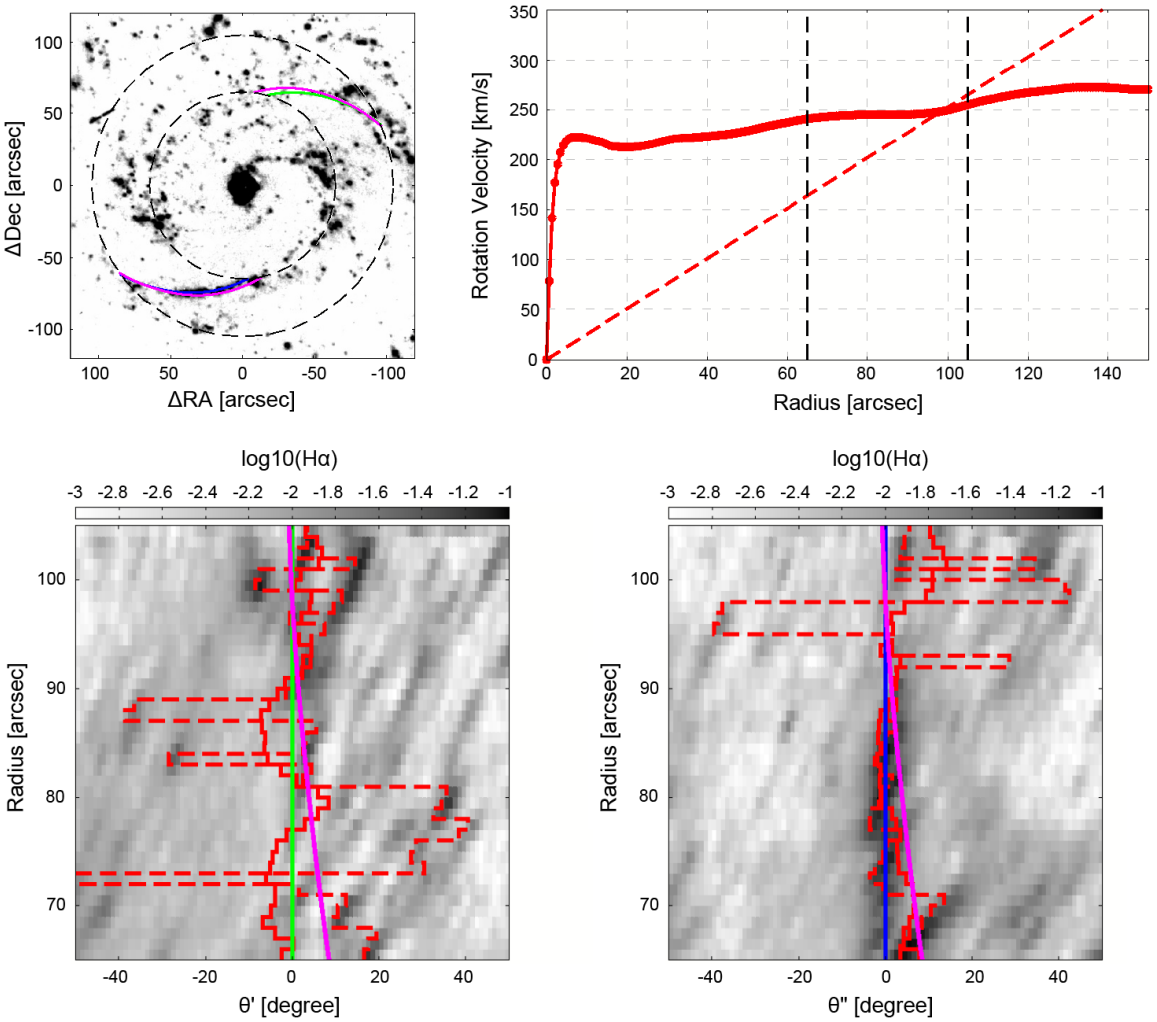

Figure D.2: [NGC 4321] *(Top Left);* The deprojected continuum-subtracted Hα image in negative representation. The dust lanes we traced are shown with green and blue lines. The magenta lines show the estimated positions of stellar clusters with the ages of 10 Myr assuming that they were born in the dust lanes and rotate in a circular orbit. *(Top Right);* The rotation curve from Sofue et al. (1999) is shown with a red solid line, and the pattern speed of Ω_P = 31 km/s/kpc from Canzian & Allen (1997) is shown with a red dashed line. *(Bottom);* The continuum-subtracted Hα image on the (R, θ') and (R, θ'') planes in negative representation. The average and the peak azimuth angle of the Hα emission intensity according to the radius are shown with red solid lines and red dashed lines respectively. The magenta lines show the estimated positions of stellar clusters with the ages of 10 Myr.

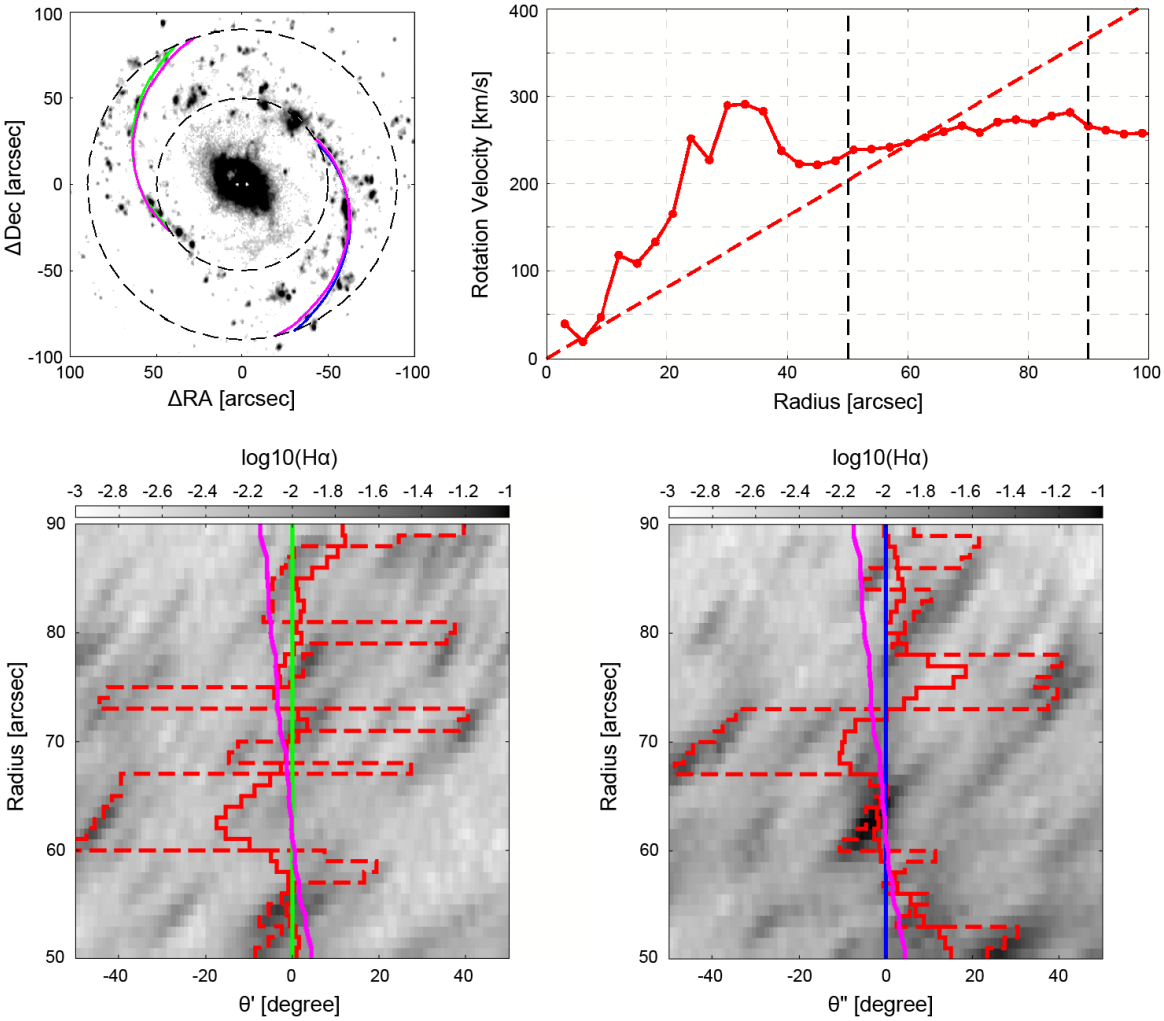

Figure D.3: [NGC 4579] *(Top Left);* The deprojected continuum-subtracted Hα image in negative representation. The dust lanes we traced are shown with green and blue lines. The magenta lines show the estimated positions of stellar clusters with the ages of 10 Myr assuming that they were born in the dust lanes and rotate in a circular orbit. *(Top Right);* The rotation curve from Daigle et al. (2006) is shown by a red solid line, and the pattern speed of Ω_P = 50 km/s/kpc from García-Burillo et al.(2009) is shown by a red dashed line. *(Bottom);* The continuum-subtracted Hα image on the (R, θ') and (R, θ'') planes in negative representation. The average and the peak azimuth angle of the Hα emission intensity according to the radius are shown with red solid lines and red dashed lines respectively. The magenta lines show the estimated positions of stellar clusters with the ages of 10 Myr.

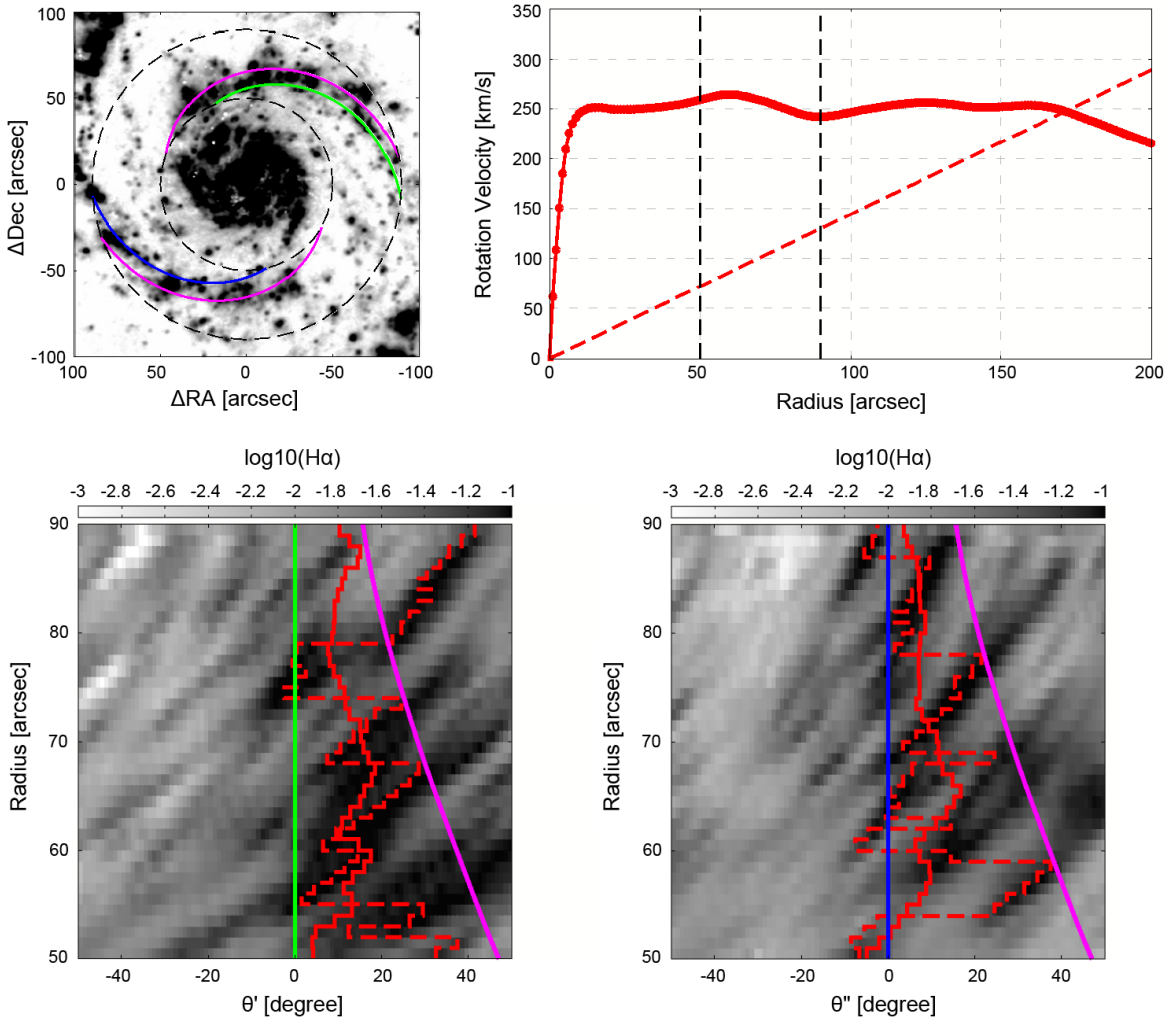

Figure D.4: [NGC 5194] *(Top Left);* The deprojected continuum-subtracted Hα image in negative representation. The dust lanes we traced are shown with green and blue lines. The magenta lines show the estimated positions of stellar clusters with the ages of 10 Myr assuming that they were born in the dust lanes and rotate in a circular orbit. *(Top Right);* The rotation curve from Sofue et al. (1999) is shown by a red solid line, and the pattern speed of Ω_P = 31 km/s/kpc from Egusa et al. (2009) is shown by a red dashed line. We assumed the distance of 9.7 Mpc instead of 7.7 Mpc. *(Bottom);* The continuum-subtracted Hα image on the (R, θ') and (R, θ'') planes in negative representation. The average and the peak azimuth angle of the Hα emission intensity according to the radius are shown with red solid lines and red dashed lines respectively. The magenta lines show the estimated positions of stellar clusters with the ages of 10 Myr.

Appendix E

Reddening Corrected Color Index Q

We carried out spectroscopic observations of 29 near-infrared cluster complexes in NGC 4321 to investigate the relation of the reddening corrected color index Q to stellar cluster ages.

E.1 Observation with Subaru/MOIRCS

E.1.1 Observation

We conducted multi-object spectroscopic (MOS) observations with the Multi-Object InfraRed Camera and Spectrograph (MOIRCS; Ichikawa et al. 2006, Suzuki et al. 2008) on the 8.2-m Subaru Telescope. The MOIRCS has two 2K × 2K HAWAII-2 detectors with a pixel scale of $0''.117$ and a total field of view of $4' \times 7'$. The field of view is divided into two areas by a roof mirror and then re-focused onto two arrays through two sets of identical optics.

We selected 29 objects from the near-infrared cluster complexes studied in GD12. We summarize the RA, Dec and JHK magnitudes of the objects in Table E.1, which are quoted from the catalog presented by GD12[*1]. We show a layout of the multi-object slit mask and the distribution of the objects in Figure E.1. We arranged 19 slits for 29 objects. Each slit was either 15 or 20 arcsec in length and 1.0 arcsec in width. We set the PA to $-135°$.

The observation was carried out on April 16, 2014 (PI: Iwata). We used the medium resolution R1300 grism and K-band filter with the wavelength range of $2.0 - 2.4\,\mu$m. The resolution is about 1000 for the 0.5 arcsec slit width, and the dispersion is 3.88 Å/pixel. The total exposure for object frames was 2 hours. The individual frames with 600 second exposure time were taken with a dither offset of 2.0, 2.5 or 3.0 arcsec. In addition, sky frames with 4×600 second exposure times were taken with an offset of about 8.5 arcmin in RA.

[*1] http://vizier.nao.ac.jp/viz-bin/VizieR?-source=J/A+A/542/A39

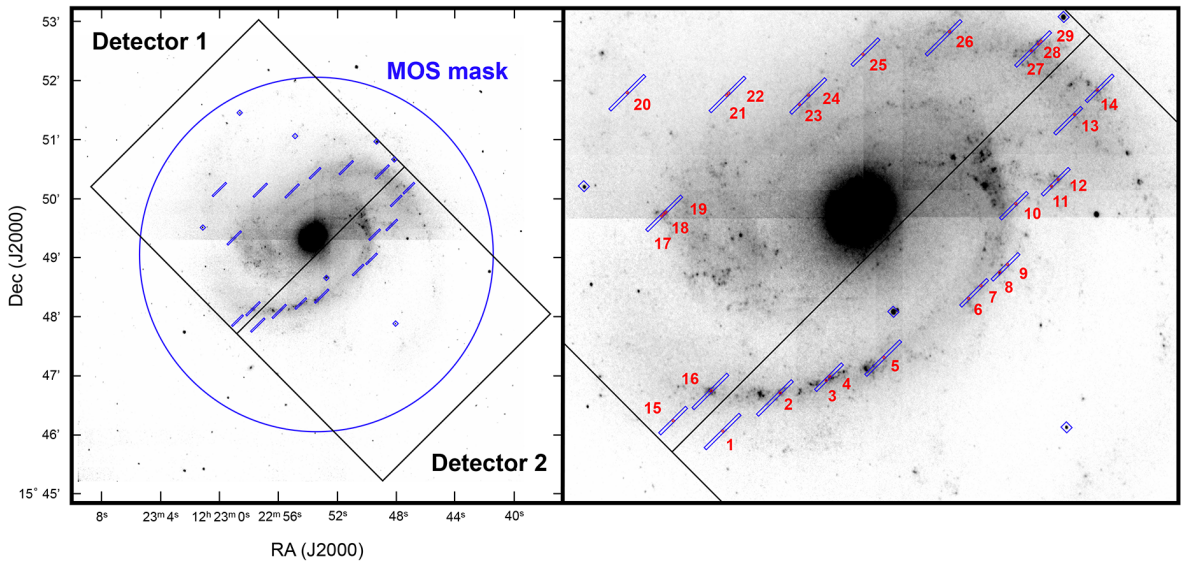

Figure E.1: *(Left);* A layout of the MOIRCS multi-object slit mask on the Ks-band image of NGC 4321 taken with the VLT/HAWK-I. The blue lines show the slit mask. The black rectangles show the field of view of the MOIRCS. *(Right);* The distribution of 29 objects on the enlarged image of the left. The red circles show the positions of the objects. The image size is 250″ × 200″.

E.1.2 Data Reduction

The data reduction was carried out with the MOIRCS MOS Data Pipeline (MCSMDP; Yoshikawa et al. 2010) which is a PyRAF script package for the MOIRCS MOS data reduction. First of all, the flat-fielding by dome flats, rejection of bad pixels and cosmic-rays, sky-subtraction with sky frames, and distortion correction were performed. Next, each 2D spectrum was cut out based on the mask design file. The wavelength calibration was done using the thorium-argon (ThAr) comparison lamp lines and the OH sky emission lines. The residual sky background was subtracted by polynomial interpolation of sky signals around the object. Then, all frames were combined with appropriate offsets. The flux calibration was done using the A0V-type standard star HIP 50133. Finally, we extracted 1D spectra from the flux calibrated 2D spectra.

We measured the Brγ EW by the IRAF SPLOT task. We derived the Brγ EW larger than 10Å in 13 objects. We estimated their stellar ages by using a SB99 SSP model with solar metallicity, a Salpeter IMF with slope α = 2.35, and an upper mass limit M_{up} = 100 $M_{\odot}$. We show the time evolution of Brγ EW in the left panel of Figure E.2. The objects with the Brγ EW larger than 10Å are estimated to be younger than about 6 Myr. We summarize the Brγ EWs and ages for 13 objects in Table E.1.

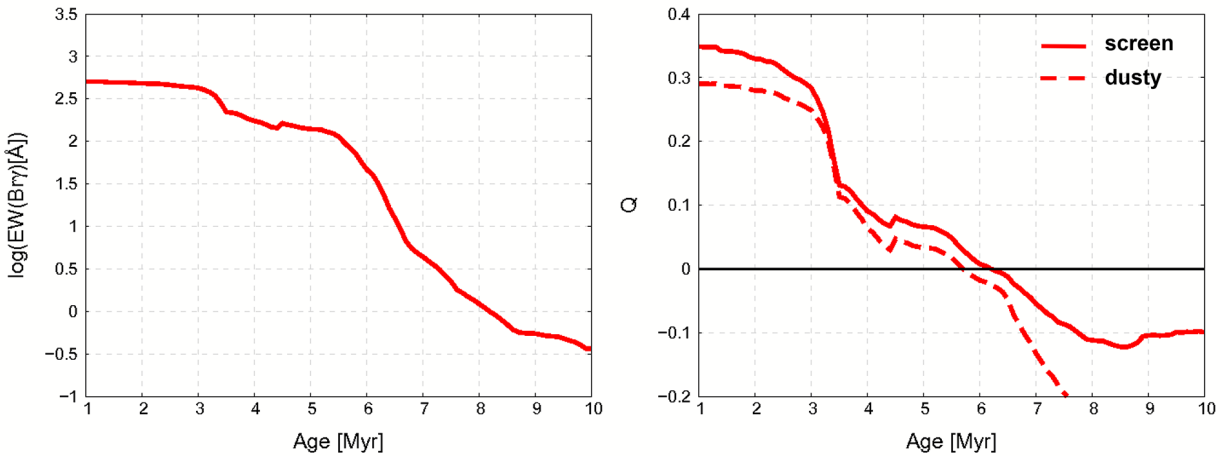

Figure E.2: *(Left);* Time evolution of Brγ EW from a SB99 SSP model assuming solar metallicity and a Salpeter IMF. *(Right);* Time evolution of the reddening corrected color index Q. The red solid line indicates a screen model of the dust, which is expressed with Q = (H − K) − 0.57 × (J − H). The red dashed line indicates a dusty model, which is expressed with Q = (H − K) − 0.85 × (J − H). We assumed a SB99 SSP model with solar metallicity and a Salpeter IMF for the JHK colors. The black solid line shows Q = 0.

E.2 Relation of Q Index to Stellar Cluster Ages

A first order reddening corrected color index Q serves as an age indicator. We consider two extreme cases for Q index. One is a screen model of the dust with standard galactic extinction, which is expressed with Q = (H − K) − 0.57 × (J − H) (Winkler 1997, Indebetouw et al. 2005). The other is a dusty model, which is expressed with Q = (H − K) − 0.85 × (J − H) (e.g., Israel et al. 1998, Witt et al. 1992). We show the time evolution of the Q indices in the right panel of Figure E.2. The red solid line indicates the screen model, and the red dashed line indicates the dusty model. For the JHK colors, we adopted the SB99 SSP model with solar metallicity and a Salpeter IMF. We see that stellar clusters with Q > 0 are estimated to be younger than about 6Myr in both models.

We show the color-color diagram of (J − H) versus (H − K) for 29 objects in Figure E.3. The objects, whose ages were estimated by the Brγ EW, are plotted by using cyan, blue and magenta circles according to the ages. The other objects, whose ages were estimated to be older than about 6.5 Myr (i.e., Brγ EW < 10 Å), are plotted by using red circles. The black solid line indicates Q = 0 for the screen model of the dust, and the black dashed line indicates Q = 0 for the dusty model. Both black lines show the positions of stellar clusters with the ages about 6 Myr, when the SB99 SSP model is assumed. The screen model of the dust is in better agreement with the distribution of objects whose ages are about 6 Myr than the dusty model.

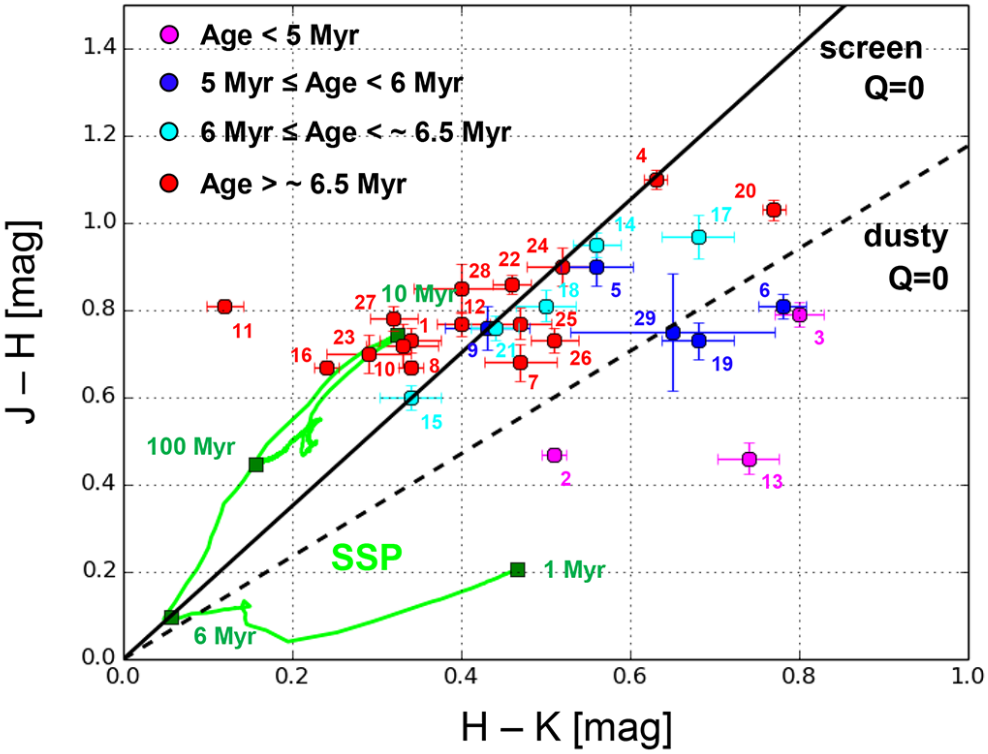

Figure E.3: Color-color diagram of (J − H) versus (H − K) for 29 objects. The objects, whose ages were estimated by the Brγ EW, are shown by using cyan, blue and magenta circles according to the ages. The other objects older than about 6.5 Myr are shown by using red circles. The black solid line indicates Q = 0 for the screen model of the dust, and the black dashed line indicates Q = 0 for the dusty model. The green line shows an evolutionary track of a SB99 SSP model assuming solar metallicity and a Salpeter IMF.

There are some objects classified as Q > 0, i.e., younger than about 6Myr, although their ages were estimated to be older than about 6.5 Myr by the Brγ EW. Bastian et al. (2014) reported that clusters younger than about 10 Myr become redder due to contamination of neighboring clusters as larger apertures are used for the photometry. Therefore, the reason for the discrepancy between the ages estimated by the Brγ EW and the Q index is probably because the colors of the Q index were measured with considerably large apertures in comparison with the cluster size. Our observations show that the number of such objects is relatively small.

We conclude that the reddening corrected color index Q = (H − K) − 0.57 × (J − H) for the screen model of the dust serves as a good age indicator of stellar clusters in NGC 4321. The Q index enables us to divide young clusters (age < ~ 6 Myr) from old clusters (age > ~ 6 Myr) based on whether Q > 0 or Q < 0.

Table E.1: List of 29 objects observed with Subaru/MOIRCS

Object No.	RA (J2000)	Dec (J2000)	K (mag)	H (mag)	J (mag)	EW Brγ (Å)	Age (Myr)
1	185.74474	+15.79759	18.98	19.32	20.05	-	-
2	185.73807	+15.80193	17.78	19.00	18.76	171.7 ± 5.5	$4.05^{+0.08}_{-0.07}$
3	185.73276	+15.80336	18.03	18.83	19.62	141.9 ± 5.8	$4.93^{+0.29}_{-0.62}$
4	185.73216	+15.80369	17.72	18.35	19.45	-	-
5	185.72596	+15.80587	18.65	19.21	20.11	52.2 ± 3.6	$5.96^{+0.03}_{-0.03}$
6	185.71613	+15.81245	17.99	18.77	19.58	81.9 ± 2.2	$5.73^{+0.02}_{-0.02}$
7	185.71468	+15.81399	18.65	19.12	19.80	-	-
8	185.71250	+15.81548	17.47	17.81	18.48	-	-
9	185.71154	+15.81629	18.48	18.91	19.67	71.6 ± 4.3	$5.81^{+0.03}_{-0.03}$
10	185.71050	+15.82314	18.31	18.64	19.36	-	-
11	185.70631	+15.82508	18.03	18.15	18.96	-	-
12	185.70553	+15.82585	18.36	18.76	19.53	-	-
13	185.70361	+15.83322	18.66	19.40	19.86	259.0 ± 25.1	$3.45^{+0.04}_{-0.04}$
14	185.70093	+15.83593	18.15	18.71	19.66	22.6 ± 1.2	$6.33^{+0.02}_{-0.02}$
15	185.75059	+15.79879	18.79	19.13	19.73	16.5 ± 1.0	$6.41^{+0.02}_{-0.02}$
16	185.74613	+15.80212	17.72	17.96	18.63	-	-
17	185.75194	+15.82191	18.60	19.28	20.25	40.3 ± 2.0	$6.11^{+0.03}_{-0.03}$
18	185.75165	+15.82218	18.41	18.91	19.72	24.0 ± 0.9	$6.31^{+0.02}_{-0.02}$
19	185.75140	+15.82227	18.39	19.07	19.80	64.8 ± 2.7	$5.86^{+0.02}_{-0.02}$
20	185.75585	+15.83577	18.28	19.05	20.08	-	-
21	185.74424	+15.83552	18.63	19.07	19.83	19.0 ± 0.9	$6.37^{+0.02}_{-0.02}$
22	185.74400	+15.83573	18.52	18.98	19.84	-	-
23	185.73578	+15.83436	18.62	18.91	19.61	-	-
24	185.73476	+15.83549	18.43	18.95	19.85	-	-
25	185.72837	+15.84004	18.92	19.39	20.16	-	-
26	185.71817	+15.84249	18.51	19.02	19.75	-	-
27	185.70864	+15.84042	18.45	18.77	19.55	-	-
28	185.70778	+15.84119	18.28	18.68	19.53	-	-
29	185.70749	+15.84146	19.00	19.65	20.40	112.2 ± 10.6	$5.52^{+0.06}_{-0.10}$

Acknowledgements

First of all, I would like to express the deepest appreciation to my supervisor, Prof. Mamoru Doi for giving me a lot of opportunities and advice during my graduate course. Without his persistent help, this thesis would not have been finished. I am also very grateful to Dr. Tomoki Morokuma for always giving me valuable comments on my works. I would like to thank Dr. Ikuru Iwata and Dr. Ichi Tanaka (NAOJ) for offering me a precious opportunity to participate in the MOIRCS Upgrade Project. I also thank them for supporting my research by giving me a chance for observations and meaningful advice.

Prof. Mamoru Doi gave me a valuable opportunity to engage in development of the Line Imager and Slit Spectrograph (LISS) from the initial design, which was mounted on the 1.6-m Pirka telescope of the Hokkaido University at Nayoro in Hokkaido (2012-2013) and the 2.0-m NAYUTA telescope at the Nishi-Harima Astronomical Observatory (2014-present). I would like to thank Dr. Shigeyuki Sako for his constructive guidance. I learned a lot of valuable skills from this experience. I also thank members of the development team: Dr. Hanindyo Kuncarayakti, Mitsuru Kokubo and Kazuma Mitsuda. I am proud to have been able to work together with them. I also would like to acknowledge many people and organizations that provided opportunities and support for the commissioning observations.

I was financially supported by the Japan Society for the Promotion of Science (JSPS) Research Fellowships for Young Scientists. I would like to thank my colleagues and friends for their moral support. Finally I would like to express my deepest gratitude to my family for their understanding, support, and encouragement.

References

[Aalto et al. (1999)] Aalto, S., Huetemeister, S., Scoville, N. Z., & Thaddeus, P. 1999, ApJ, 522, 165

[Allen (2002)] Allen, R. J. 2002, in ASP Conf. Ser. 276, Seeing Through the Dust: The Detection of HI and the Exploration of the ISM in Galaxies, ed. A. R. Taylor, T. L. Landecker, & A. G. Willis (San Francisco, CA: ASP), 288

[Allende Prieto et al. (2001)] Allende Prieto, C., Lambert, D. L., & Asplund, M. 2001, ApJ, 556, L63

[Ann & Lee (2013)] Ann, H. B., & Lee, H. R. 2013, JKAS, 46, 141

[Athanassoula (1992)] Athanassoula, E. 1992, MNRAS, 259, 345

[Avila et al. (2015)] Avila, R., et al. 2015, ACS Instrument Handbook, Version 14.0

[Baba et al. (2013)] Baba, J., Saitoh, T. R., & Wada, K. 2013, ApJ, 763, 46

[Baba et al. (2015)] Baba, J., Morokuma-Matsui, K., & Egusa, F. 2015, PASJ, 67, L4

[Barmby et al. (2006)] Barmby, P., Kuntz, K. D., Huchra, J. P., & Brodie, J. P. 2006, AJ, 132, 883

[Bastian et al. (2012)] Bastian, N., Adamo, A., Gieles, M., et al. 2012, MNRAS, 419, 2606

[Bastian et al. (2014)] Bastian, N., Adamo, A., Schirmer, M., et al. 2014, MNRAS, 444, 3829

[Beckman & Cepa (1990)] Beckman, J. E., & Cepa, J. 1990, A&A, 229, 37

[Benedict et al. (1977)] Benedict, G. F., van Citters, G. W., McGraw, J. T., & Rybski, P. M. 1977, BAAS, 9, 629

[Bertin et al. (1989)a] Bertin, G., Lin, C. C., Lowe, S. A., & Thurstans, R. P. 1989, ApJ, 338, 78

[Bertin et al. (1989)b] Bertin, G., Lin, C. C., Lowe, S. A., & Thurstans, R. P. 1989, ApJ, 338, 104

[Bertin & Arnouts (1996)] Bertin, E., & Arnouts, S. 1996, A&AS, 117, 393

[Bland-Hawthorn et al. (1997)] Bland-Hawthorn, J., Gallimore, J. F., Tacconi, L., et al. 1997, Ap&SS, 248, 9

[Boeshaar & Hodge (1977)] Boeshaar, G., & Hodge, P.W. 1977, ApJ, 213, 361

[Breeveld et al. (2010)] Breeveld, A. A., Curran, P. A., Hoversten, E. A., et al. 2010, MNRAS, 406, 1687

[Bruzual & Charlot (2003)] Bruzual, A. G., & Charlot, S. 2003, MNRAS, 344, 1000
[Buta & Crocker (1993)] Buta, R. J., & Crocker, D. A. 1993, AJ, 105, 1344
[Buta & Zhang (2009)] Buta, R. J., & Zhang, X. 2009, ApJS, 182, 559
[Calzetti et al. (2015)] Calzetti, D., Lee, J. C., Sabbi, E. et al. 2015, AJ, 149, 51
[Canzian & Allen (1997)] Canzian, B., & Allen, R. J. 1997, ApJ, 479, 723
[Cardelli et al. (1989)] Cardelli, J. A., Clayton, G. C., & Mathis, J. S. 1989, ApJ, 345, 245
[Cedrés et al. (2013)] Cedrés, B., Cepa, J., Bongiovanni, Á., et al. 2013, A&A, 560, A59
[Cepa & Beckman (1990)] Cepa, J., & Beckman, J. E. 1990, ApJ, 349, 497
[Chandar et al. (2010)] Chandar, R., Whitmore, B. C., Kim, H., et al. 2010, ApJ, 719, 966
[Chemin et al. (2006)] Chemin, L., Balkowski, C., Cayatte, V., et al. 2006, MNRAS, 366, 812
[Choi et al. (2015)] Choi, Y., Dalcanton, J. J., Williams, B. F., et al. 2015, ApJ, 810, 9
[Chyży (2008)] Chyży, K. T. 2008, A&A, 482, 755
[Colina et al. (1997)] Colina, L., Garcia Vargas, M. L., Mas-Hesse, J. M., et al. 1997, ApJ, 484, L41
[Colina & Wada (2000)] Colina, L., & Wada, K. 2000, ApJ, 529, 845
[Comerón et al. (2010)] Comerón, S., Knapen, J. H., Beckman, J. E., et al. 2010, MNRAS, 402, 2462
[Daigle et al. (2006)] Daigle, O., Carignan, C., Amram, P., et al. 2006, MNRAS, 367, 469
[Das et al. (2003)] Das, M., Vogel, S. N., Teuben, P. J., et al. 2003, ApJ, 582, 190
[de Blok et al. (2008)] de Blok, W. J. G., Walter, F., Brinks, E., et al. 2008, AJ, 136, 2648
[de Vaucouleurs (1959)] de Vaucouleurs, G. 1959, Handbuch der Physik, 53, 275
[de Vaucouleurs et al. (1976)] de Vaucouleurs, G., de Vaucouleurs, A., & Corwin, J. R. 1976, Second reference catalogue of bright galaxies, 1976, Austin: University of Texas Press (RC2)
[de Vaucouleurs et al. (1991)] de Vaucouleurs, G., de Vaucouleurs, A., Corwin, J. R., et al. 1991, Third reference catalogue of Bright galaxies, 1991, New York : Springer-Verlag (RC3)
[Dobbs & Pringle (2010)] Dobbs, C. L., & Pringle, J. E. 2010, MNRAS, 409, 396
[Dolphin (2009)] Dolphin, A. E. 2009, PASP, 121, 655
[D'Onghia et al. (2013)] D'Onghia, E., Vogelsberger, M., & Hernquist, L. 2013, ApJ, 766, 34
[Dressel (2015)] Dressel, L. 2015, Wide Field Camera 3 Instrument Handbook, Version 7.0
[Duc et al. (2008)] Duc, P.-A., & Bournaud, F. 2008, ApJ, 673, 787
[Egusa et al. (2004)] Egusa, F., Sofue, Y., & Nakanishi, H. 2004, PASJ, 56, L45
[Egusa et al. (2009)] Egusa, F., Kohno, K., Sofue, Y., et al. 2009, ApJ, 697, 1870
[Elmegreen & Elmegreen (1985)] Elmegreen, B. G., & Elmegreen, D. M. 1985, ApJ, 288, 428
[Elmegreen & Elmegreen (1987)] Elmegreen, D. M., & Elmegreen, B. G. 1987, ApJ, 314, 3
[Elmegreen & Elmegreen (1989)] Elmegreen, B. G., & Elmegreen, D. M. 1989, ApJ, 342, 677

[Elmegreen et al. (1992)] Elmegreen, B. G., Elmegreen, D. M., & Montenegro, L. 1992, ApJS, 79, 37

[Elmegreen et al. (1996)] Elmegreen, B. G., Elmegreen, D. M., Chromey, F. R., et al. 1996, AJ, 111, 2233

[Elmegreen (2007)] Elmegreen, B. G. 2007, ApJ, 668, 1064

[Elmegreen et al. (2011)] Elmegreen, D. M., Elmegreen, B. G., Yau, A., et al. 2011, ApJ, 737, 32

[Elson et al. (1987)] Elson, R. A. W., Fall, S. M., & Freeman, K. C. 1987, ApJ, 323, 54

[Fathi et al. (2007)] Fathi, K., Beckman, J. E., Zurita, A., et al. 2007, A&A, 466, 905

[Ferreras et al. (2012)] Ferreras, I., Cropper, M., Kawata, D., et al. 2012, MNRAS, 424, 1636

[Fitzpatrick (1999)] Fitzpatrick, E. L. 1999, PASP, 111, 63

[Foyle et al. (2011)] Foyle, K., Rix, H.-W., Dobbs, C. L., et al. 2011, ApJ, 735, 101

[Fridman et al. (2001)] Fridman, A. M., Khoruzhii, O. V., Polyachenko, E. V., et al. 2001, MNRAS, 323, 651

[Fujii et al. (2011)] Fujii, M. S., Baba, J., Saitoh, T. R., et al. 2011, ApJ, 730, 109

[Fujimoto (1968)] Fujimoto, M. 1968, in Non-stable Phenomena in Galaxies, IAU Symp., 29, 453

[García-Burillo et al. (1993)] García-Burillo, S., Guelin, M., & Cernicharo, J. 1993, A&A, 274, 123

[García-Burillo et al. (2009)] García-Burillo, S., Fernández-García, S., Combes, F., et al. 2009, A&A, 496, 85

[Gehrels et al. (2004)] Gehrels, N., Chincarini, G., Giommi, P., et al. 2004, ApJ, 611, 1005

[Gonzaga et al. (2010)] Gonzaga, S., & Biretta, J., et al. 2010, in HST WFPC2 Data Handbook, v. 5.0

[Gonzaga (2014)] Gonzaga, S. 2014, ACS Data Handbook, Version 7.2

[González & Graham (1996)] González, R. A., & Graham, J. R. 1996, ApJ, 460, 651

[Gott et al. (2005)] Gott, J. R., III, Jurić, M., Schlegel, D., et al. 2005, ApJ, 624, 463

[Grand et al. (2012)a] Grand, R. J. J., Kawata, D., & Cropper, M. 2012, MNRAS, 421, 1529

[Grand et al. (2012)b] Grand, R. J. J., Kawata, D., & Cropper, M. 2012, MNRAS, 426, 167

[Grosbøl et al. (1999)] Grosbøl, P. J., Block, D. L., & Patsis, P. A. 1999, Ap&SS, 269, 423

[Grosbøl & Dottori (2009)] Grosbøl, P., & Dottori, H. 2009, A&A, 499, L21

[Grosbøl & Dottori (2012)] Grosbøl, P., & Dottori, H. 2012, A&A, 542A, 39

[Haynes et al. (2007)] Haynes, M. P., Giovanelli, R., & Kent, B. R. 2007, ApJ, 665, L19

[Helfer et al. (2003)] Helfer, T. T., Thornley, M. D., Regan, M.W., et al. 2003, ApJS, 145, 259

[Hirota et al. (2014)] Hirota, A., Kuno, N., Baba, J., et al., 2014, PASJ, 66, 46

[Ho et al. (1997)] Ho, L. C., Filippenko, A. V., & Sargent, W. L. W. 1997, ApJS, 112, 315

[Hoopes & Walterbos (2003)] Hoopes, C. G., & Walterbos, R. A. M. 2003, ApJ, 586, 902
[Hubble (1926)] Hubble, E. 1926, ApJ, 64, 321
[Ichikawa et al. (2006)] Ichikawa, T., Suzuki, R., Tokoku, C., et al. 2006, in Proc. of SPIE, Vol. 6269, 38
[Indebetouw et al. (2005)] Indebetouw, R., Mathis, J. S., Babler, B. L., et al. 2005, ApJ, 619, 931
[Israel et al. (1998)] Israel, F. P., van der Werf, P. P., Hawarden, T. G., & Aspin, C. 1998, A&A, 336, 433
[Iye et al. (1982)] Iye, M., Okamura, S., Hamabe, M., & Watanabe, M. 1982, ApJ, 256, 103
[James & Seigar (1999)] James, P. A., & Seigar, M. S. 1999, A&A, 350, 791
[Jogee et al. (2002)] Jogee, S., Knapen, J. H., Laine, S., et al. 2002, ApJ, 570, L55
[Kamphuis & Briggs (1992)] Kamphuis, J., & Briggs, F. 1992, A&A, 253, 335
[Kendall et al. (2011)] Kendall, S., Kennicutt, R. C., & Clarke, C. 2011, MNRAS, 414, 538
[Kennicutt et al. (1989)] Kennicutt, R. C., Jr., Keel, W. C., & Blaha, C. A. 1989, AJ, 97, 1022
[Kennicutt et al. (2003)] Kennicutt, R. C., Jr., Armus, L., Bendo, G., et al. 2003, PASP, 115, 928
[Khachikian & Weedman (1974)] Khachikian, E. Y., & Weedman, D. W. 1974, ApJ, 192, 581
[Kim et al. (2012)] Kim, H., Whitmore, B. C., Chandar, R., et al. 2012, ApJ, 753, 26
[Knapen et al. (1995)] Knapen, J. H., Beckman, J. E., Heller, C. H., et al. 1995, ApJ, 454, 623
[Knapen (1997)] Knapen, J. H. 1997, MNRAS, 286, 403
[Knapen et al. (2003)] Knapen, J. H., de Jong, R. S., Stedman, S., & Bramich, D. M. 2003, MNRAS, 344, 527 (Erratum MNRAS, 346, 333, 2003)
[Knapen et al. (2004)] Knapen, J. H., Stedman, S., Bramich, D. M, et al. 2004, A&A, 426, 1135
[Knapen (2005)] Knapen, J. H. 2005, A&A, 429, 141
[Kodaira et al. (1986)] Kodaira, K., Watanabe, M., & Okamura, S. 1986, ApJS, 62, 703
[Kohno et al. (1996)] Kohno, K., Kawabe, R., Tosaki, T., & Okumura, S. K. 1996, ApJ, 461, L29
[Konstantopoulos et al. (2013)] Konstantopoulos, I. S., Smith, L. J., Adamo, A., et al. 2013, AJ, 145, 137
[Kranz et al. (2001)] Kranz, T., Slyz, A., & Rix, H.-W. 2001, ApJ, 562, 164
[Kroupa (2001)] Kroupa, P. 2001, MNRAS, 322,231
[Kuno & Nakai (1997)] Kuno, N., & Nakai, N. 1997, PASJ, 49, 279
[Kuno et al. (2007)] Kuno, N., Sato, N., Nakanishi, H., et al. 2007, PASJ, 59, 117
[Lada & Lada (2003)] Lada, C. J., & Lada, E. A. 2003, ARA&A, 41, 57
[Laine et al. (2001)] Laine, S., Knapen, J. H., Pérez-Ramírez, D., et al. 2001, MNRAS, 324, 891
[Laine et al. (2002)] Laine, S., Shlosman, I., Knapen, J.H., & Peletier, R.F. 2002, ApJ, 567, 97
[Larsen (1999)] Larsen, S. S. 1999, A&AS, 139, 393
[Larsen (2004)] Larsen, S. S. 2004, A&A, 416, 537

[Laurikainen et al. (2004)] Laurikainen, E., Salo, H., Buta, R., & Vasylyev, S. 2004, MNRAS, 355, 1251

[Lee et al. (2005)] Lee, M. G., Chandar, R., & Whitmore, B. C. 2005, AJ, 130, 2128

[Leitherer et al. (1999)] Leitherer, C., Schaerer, D., Goldader, J. D., et al. 1999, ApJSS, 123, 3

[Leroy et al. (2009)] Leroy, A. K., Walter, F., Bigiel, F., et al. 2009, AJ, 137, 4670

[Lin & Shu (1964)] Lin, C. C., & Shu, F. H. 1964, ApJ, 140, 646

[Lintott et al. (2011)] Lintott, C., Schawinski, K., Bamford, S., et al. 2011, MNRAS, 410, 166

[Liu et al. (2011)] Liu, G., Koda, J., Calzetti, D., et al. 2011, ApJL, 735, 63

[Loinard et al. (1996)] Loinard, L., Dame, T. M., Koper, E., et al. 1996, ApJ, 469, L101

[Lord & Kenney (1991)] Lord, S. D., & Kenney, J. D. P. 1991, ApJ, 381, 130

[Louie et al. (2013)] Louie, M., Koda, J., & Egusa, F. 2013, ApJ, 763, 94

[Lynden-Bell & Kalnajs (1972)] Lynden-Bell, D., & Kalnajs, A. J. 1972, MNRAS, 157, 1

[Lynds (1970)] Lynds, B. T. 1970, in IAU Symp. 38, The Spiral Structure of Our Galaxy, ed. W. Becker & G. I. Kontopoulos (Dordrecht: Reidel), 26

[Maoz et al. (2001)] Maoz, D., Barth, A. J., Ho, L. C., et al. 2001, AJ, 121, 3048

[Maraston (2005)] Maraston, C. 2005, MNRAS, 362, 799

[Martin (1995)] Martin, P. 1995, AJ, 109, 2428

[Martínez-García et al. (2009)] Martínez-García, E. E., González-López lira, R. A., & Bruzual-A, G. 2009, ApJ, 694, 512

[Martínez-García & González-López lira (2013)] Martínez-García, E. E., & González-López lira, R. A. 2013, ApJ, 765, 105

[Martínez-García & Puerari (2014)] Martínez-García, E. E., & Puerari, I. 2014, ApJ, 790, 118

[Mathewson et al. (1972)] Mathewson, D. S., van der Kruit, P. C., & Brouw, W. N. 1972, A&A, 17, 468

[Mayya et al. (2008)] Mayya, Y. D., Romano, R., Rodríguez-Merino, L. H., et al. 2008, ApJ, 679, 404

[McCall et al. (1985)] McCall, M. L., Rybski, P. M., & Shields, G. A. 1985, ApJS, 57, 1

[McCarthy et al. (2001)] McCarthy, D. W., Ge, J., Hinz, J. L., et al. 2001, PASP, 113, 353

[McMaster et al. (2008)] McMaster, M., & Biretta, J., et al. 2008, Wide Field and Planetary Camera 2 Instrument Handbook, Version 10.0

[Meidt et al. (2008)] Meidt, S. E., Rand, R. J., Merrifield, M. R., et al. 2008, ApJ, 676, 899

[Meidt et al. (2009)] Meidt, S. E., Rand, R. J., & Merrifield, M. R. 2009, ApJ, 702, 277

[Merrifield et al. (2006)] Merrifield, M. R., Rand, R. J., & Meidt, S. E. 2006, MNRAS, 366, L17

[Miller et al. (1997)] Miller, B., Whitmore, B. C., Schweizer, F., & Fall, S. M. 1997, AJ, 114, 2381

[Minchin et al. (2007)] Minchin, R., Davies, J., Disney, M., et al. 2007, ApJ, 670, 1056

[Möllenhoff & Heidt (2001)] Möllenhoff, C., & Heidt, J. 2001, A&A, 368, 16

[Mora et al. (2007)] Mora, M. D., Larsen, S. S., & Kissler-Patig, M. 2007, A&A, 464, 495

[Mutchler et al. (2005)] Mutchler, M., Beckwith, S. V. W., Bond, H., et al. 2005, AAS, Vol.37, No.2

[Noeske et al. (2012)] Noeske, K., Baggett, S., Bushouse, H., et al. 2012, WFC3 UVIS Charge Transfer Eciency October 2009 to October 2011

[Packham et al. (2003)] Packham, C., Thompson, K., Zurita, A., et al. 2003, MNRAS, 345, 395

[Phookun et al. (1993)] Phookun, B., Vogel, S. N., & Mundy, L. G. 1993, ApJ, 418, 113

[Pilyugin et al. (2004)] Pilyugin, L. S., Vílchez, J. M., & Contini, T. 2004, A&A, 425, 849

[Prescott et al. (2007)] Prescott, M. K. M., Kennicutt, Jr., R. C., Bendo, G. J., et al. 2007, ApJ, 668, 182

[Rajan et al. (2011)] Rajan, A., et al. 2011, WFC3 Data Handbook, Version 2.1

[Rand & Kulkarni (1990)] Rand, R. J., & Kulkarni, S. R. 1990, ApJ, 349, L43

[Rand (1995)] Rand, R. J. 1995, AJ, 109, 2444

[Rand & Wallin (2004)] Rand, R. J., & Wallin, J. F. 2004, ApJ, 614, 142

[Rautiainen et al. (2008)] Rautiainen, P., Salo, H., & Laurikainen, E. 2008, MNRAS, 388, 1803

[Rix & Rieke (1993)] Rix, H.-W., & Rieke, M. J. 1993, ApJ, 418, 123

[Roberts (1969)] Roberts, W. W. 1969, ApJ, 158, 123

[Roming et al. (2005)] Roming, P. W. A., Kennedy, T. E., Mason, K. O., et al. 2005, Space Sci. Rev., 120, 95

[Rots (1975)] Rots, A. H. 1975, A&A, 45, 43

[Rozas et al. (1996)] Rozas, M., Beckman, J. E., & Knapen, J. H. 1996, A&A, 307, 735

[Ryon et al. (2014)] Ryon, J. E., Adamo, A., Bastian, N., et al. 2014, AJ, 148, 33

[Ryon et al. (2015)] Ryon, J. E., Bastian, N., Adamo, A., et al. 2015, MNRAS, 452, 525

[Salo et al. (2010)] Salo, H., Laurikainen, E., Buta, R., & Knapen, J. H. 2010, ApJL, 715, L56

[Salpeter (1955)] Salpeter, E. E. 1955, ApJ, 121, 161

[Sánchez-Gil et al. (2011)] Sánchez-Gil, M. C., Jones, D. H., Pérez, E., et al. 2011, MNRAS, 415, 753

[Scheepmaker et al. (2007)] Scheepmaker, R. A., Haas, M. R., Gieles, M., et al. 2007, A&A, 469, 925

[Scheepmaker et al. (2009)] Scheepmaker, R. A., Lamers, H. J. G. L. M., Anders, P., & Larsen, S. S. 2009, A&A, 494, 81

[Schinnerer et al. (2000)] Schinnerer, E., Eckart, A., Tacconi, L. T., et al. 2000, ApJ, 533, 850

[Schinnerer et al. (2002)] Schinnerer, E., Maciejewski, W., Scoville, N., & Moustakas, L. A.

2002, ApJ, 575, 826

[Schinnerer et al. (2013)] Schinnerer, E., Meidt, S. E., Pety, J., et al. 2013, ApJ, 779, 42

[Schlafly & Finkbeiner (2011)] Schlafly, E. F., & Finkbeiner, D. P. 2011, ApJ, 737, 103

[Schlegel et al. (1998)] Schlegel, D. J., Finkbeiner, D. P., & Davis, M. 1998, ApJ, 500, 525

[Scoville et al. (1988)] Scoville, N. Z., Matthews, K., Carico, D. P., & Sanders, D. B. 1988, ApJ, 327, L61

[Seigar (2002)] Seigar, M. S. 2002, A&A, 393, 499

[Sellwood & Carlberg (1984)] Sellwood, J. A., & Carlberg, R. G. 1984, ApJ, 282, 61

[Shields et al. (1991)] Shields, G. A., Skillman, E. D., & Kennicutt, R. C. 1991, ApJ, 371, 82

[Simanton et al. (2015)] Simanton, L. A., Chandar, R., & Whitmore, B. C. 2015, ApJ, 805, 160

[Sofue et al. (1999)] Sofue, Y., Tutui, Y., Honma, M., et al. 1999, ApJ, 523, 136

[Speights & Westpfahl (2011)] Speights, J. C., & Westpfahl, D. J. 2011, ApJ, 736, 70

[Speights & Westpfahl (2012)] Speights, J. C., & Westpfahl, D. J. 2012, ApJ, 752, 52

[Stedman & Knapen (2001)] Stedman, S., & Knapen, J. H. 2001, Ap&SS, 276, 517

[Stetson (1987)] Stetson, P. B. 1987, PASP, 99, 191

[Suzuki et al. (2008)] Suzuki, R., Tokoku, C., Ichikawa, T., et al. 2008, PASJ, 60, 1347

[Tamburro et al. (2008)] Tamburro, D., Rix, H.-W., Walter, F., et al. 2008, AJ, 136, 2872

[Thatte et al. (2009)] Thatte, D., & Dahlen, T., et al. 2009, NICMOS Data Handbook, Version 8.0

[Theureau et al. (2007)] Theureau, G., Hanski, M. O., Coudreau, N., et al. 2007, A&A, 465, 71

[Toomre (1981)] Toomre, A. 1981, in Structure and Evolution of Normal Galaxies, ed. S. M. Fall & D. Lynden-Bell, 111136

[Tremaine & Weinberg (1984)] Tremaine, S., & Weinberg, M. D. 1984, ApJ, 282, L5

[Tully & Fisher (1977)] Tully, R. B., & Fisher, J. R. 1977, A&A, 54, 661

[Tully (1988)] Tully, R. B. 1988, Nearby Galaxies Catalog (Cambridge: Cambridge Univ. Press)

[Tully et al. (2009)] Tully, R. B., Rizzi, L., Shaya, E. J., et al. 2009, AJ, 138, 323

[van der Laan et al. (2013)] van der Laan, T. P. R., Schinnerer, E., Emsellem, E., et al. 2013, A&A, 556, A98

[Viana et al. (2009)] Viana, A., Wiklind, T., et al. 2009, NICMOS Instrument Handbook, Version 11.0

[Vogel et al. (1988)] Vogel, S. N., Kulkarni, S. R., & Scoville, N. Z. 1988, Nature, 334, 402

[Wada et al. (2011)] Wada, K., Baba, J., & Saitoh, T. R. 2011, ApJ, 735, 1

[Wakker & Adler (1995)] Wakker, B. P., & Adler, D. S. 1995, AJ, 109, 134

[Wężgowiec et al. (2012)] Wężgowiec, M., Bomans, D. J., Ehle, M., et al. 2012, A&A, 544, A99

[Whitmore et al. (2010)] Whitmore, B. C., Chandar, R., Schweizer, F., et al. 2010, AJ, 140, 75

[Whitmore et al. (2011)] Whitmore, B. C., Chandar, R., Kim, H., et al. 2011, ApJ, 729, 78

[Whitmore et al. (2014)] Whitmore, B. C., Chandar, R., Bowers, A. S., et al. 2014, AJ, 147, 78

[Wiklind et al. (1990)] Wiklind, T., Rydbeck, G., Hjalmarson, Å., & Bergman, P. 1990, A&A, 232, Lll

[Wilczynski (1896)] Wilczynski, E. J. 1896, ApJ, 4, 97

[Willett et al. (2013)] Willett, K. W., Lintott, C. J., Bamford, S. P., et al. 2013, MNRAS, 435, 2835

[Winkler (1997)] Winkler, H. 1997, MNRAS, 287, 481

[Witt et al. (1992)] Witt, A. N., Thronson, H. A., & Capuano, Jr., J. M. 1992, ApJ, 393, 611

[Woodward (1975)] Woodward, P. R. 1975, ApJ, 195, 61

[Yoshikawa et al. (2010)] Yoshikawa, T., Akiyama, M., Kajisawa, M., et al. 2010, ApJ, 718, 112

[Yuan & Yang (2006)] Yuan, C., & Yang, C.-C. 2006, ApJ, 644, 180